Ultrafast nonlinear optical processes in metal-dielectric nanocomposites and nanostructures

Passive Mode-Locking, Slow Light, High Harmonic Generation

D I S S E R T A T I O N

zur Erlangung des akademischen Grades
doctor rerum naturalium
(Dr. rer. nat.)
im Fach Physik

eingereicht an der
Mathematisch-Naturwissenschaftlichen Fakultät I
der Humboldt-Universität zu Berlin

von
M. Sc.-Phys. Kwang-Hyon Kim

Präsident der Humboldt-Universität zu Berlin:
Prof. Dr. Jan-Hendrik Olbertz

Dekan der Mathematisch-Naturwissenschaftlichen Fakultät I:
Prof. Dr. Andreas Herrmann

Gutachter:
1. Prof. Dr. Thomas Elsässer
2. Priv.-Doz. Dr. Alejandro Saenz
3. Prof. Dr. Claus Ropers

eingereicht am: 24 Januar 2012
Tag der mündlichen Prüfung: 13 April 2012

Abstract

This work reports results of a theoretical study of nonlinear optical processes in metal-dielectric nanocomposites used for the increase of the nonlinear coefficients and for plasmonic field enhancement. The main results include the study of the transient saturable nonlinearity in dielectric composites doped with metal nanoparticles, its physical mechanism as well its applications in nonlinear optics. For the study of the transient response, a time-depending equation for the dielectric function of the nanocomposite using the semi-classical two-temperature model is derived. By using this approach, we study the transient nonlinear characteristics of these materials in comparison with preceding experimental measurements. The results show that these materials behave as efficient saturable absorbers for passive mode-locking of lasers in the spectral range from the visible to near IR. We present results for the mode-locked dynamics in short-wavelength solid-state and semiconductor disk lasers; in this spectral range other efficient saturable absorbers do not exist. We suggest a new mechanism for the realization of slow light phenomenon by using glasses doped with metal nanoparticles in a pump-probe regime near the plasmonic resonance. Furthermore, we study femtosecond plasmon generation by mode-locked surface plasmon polariton lasers with Bragg reflectors and metal-gain-absorber layered structures. In the final part of the thesis, we present results for high-order harmonic generation near a metallic fractal rough surface. The results show a possible reduction of the pump intensities by three orders of magnitudes and two orders of magnitudes higher efficiency compared with preceding experimental results by using bow-tie nanostructures.

Keywords: Surface Plasmon, Nonlinear Optics, Ultrafast Optics, Plasmonics

Zusammenfassung

Diese Arbeit ist der theoretische Untersuchung nichtlinearer optischer Prozesse in metall-dielektrischen Medien gewidmet, wobei Möglichkeiten zur Ausnutzung der erhöhten nichtlinearen Koeffizienten und der Feldüberhöhung durch metallische Nanoteilchen untersucht wurden. Die wichtigsten Ergebnisse beziehen sich auf eine Untersuchung der zeitabhängigen sättigbaren Absorption in Gläsern, die mit metallischen Nanoteilchen dotiert sind, ihrer physikalischen Ursache sowie verschiedener Anwendungen in der nichtlinearen Optik. Zur Untersuchung der Zeitabhängigkeit der nichtlinearen Rückwirkung wird unter Verwendung des semi-klassischen Zwei-Temperatur-Modells eine zeitabhängige Gleichung für die nichtlineare dielektrische Funktion der Metalle hergeleitet. Die Ergebnisse zeigen, dass solche Gläser, sich als sehr effiziente sättigbare Absorber im Spektralbereich vom sichtbaren bis nahen IR eignen. Für kurzwellige Laser im blau/violetten Spektralbereich wird die Dynamik der Modenkopplung in Festkörper- und Halbleiter-Scheibenlaser untersucht. Weiterhin wird ein neuer Mechanismus für die Realisierung von langsamem Licht vorgeschlagen und im Detail untersucht, der in solchen dotierten Gläsern in einem Pump-Probe Regime infolge der sättigbaren Absorption in der Nähe der Plasmonresonanz realisierbar ist. Weiterhin untersuchten wir die Möglichkeit einer Femtosekunden Plasmon Impulserzeugung durch Modenkopplung eines Oberflächen Plasmonlasers mit einem Bragg Resonator, der aus einer dünnen Schicht aus Silber sowie einem sättigbaren Absorbers und einem Verstärker besteht. Im letzten Teil der Arbeit werden Ergebnisse zur Erzeugung hoher Harmonischer in Edelgasen in der Nähe einer metallischen fraktalen rauen Oberfläche untersucht. Die Berechnungen zeigen eine Reduzierung der geforderten Intensität um drei Größenordnungen und eine um zwei Größenordnungen erhöhte Effizienz gegenüber der bisher experimentell realisierten HHG in der Nähe von metallischen "bow-tie"Nanostrukturen.

Schlagwörter: Oberflächenplasmon, Nichtlineare Optik, Ultraschnelle Optik, Plasmonics

Contents

1. Introduction

Surface plasmons (SPs) [1, 2] are collective oscillations of conducting electrons on the metallic surfaces. The term "plasmon" emphasizes the fact that SPs have the properties as particles including energies and momenta from the viewpoint of quantum mechanics [3]. Therefore, SPs can be defined, to be more accurate, as the quasi-particles of electronic collective oscillations or electron waves on the metallic surfaces surrounded by the materials with positive dielectric functions. Nevertheless, SPs are sufficiently well described by using classical electromagnetic theory and we apply this model everywhere in this thesis. SPs can be excited by the illumination of light, electron beams, acoustic waves and other means. In this thesis, we deal with only the SPs excited by coherent laser light.

SPs may be localized in a sufficiently small volume and also can propagate along the metallic film surfaces or the aligned metallic nanoparticles (NPs) arrays [3, 4]. For metal NPs, SPs are localized at the particle and can not propagate. Those are called localized surface plasmons. SPs excited on the surface of metallic film propagate coupled with light. These waves are called surface plasmon polaritons (SPPs) which are quasi-particles of coupled electron-photon wave.

For a certain wavelength depending on the sort of host medium, sizes and shapes of metal NPs, the amplitude of collective oscillation significantly increases and this phenomenon is called surface plasmon resonance (SPR). The significant field enhancement near the metal NPs or films, is fascinating feature for the optical purposes requiring the high intensity or sensitivity, e. g. Raman spectroscopy [5, 6] and biological sensing [7–9], the realization of negative refraction [10, 11] and optical cloaking [12], nonlinear optical wavelength conversion including second- [13, 14] and third-harmonic generation [15], high-order harmonic generation (HHG) [16], etc.

The dielectric composites doped with metal NPs have great perspectives as the nonlinear optical materials because of the high inherent nonlinearities of metal NPs [17–20] and their nonlinearity being further enhanced by the increase of the field intensity by the SPR [21] resulting significantly enhanced effective nonlinearity [21, 22]. Linear and nonlinear optical properties of the composites doped with metal NPs have been investigated for the past several decades [23, 24] and lots of theoretical and experimental results in this field have been published, mainly for very small spherical metal NPs. By using the different sizes and shapes of metal NPs, SPR wavelengths can be changed [25–27]. Wavelength tunability is of great importance for the general cases of nonlinear optics.

Saturable absorption is the typical nonlinearity useful for the ultrashort pulse generation by passive mode-locking. The experimental results published over the past decade have shown that the metal nanocomposites are very good saturable absorbers with low saturation intensity (see e. g. [28–30]) from near UV to IR range and have relatively fast response time, typically in few picoseconds range [31]. This behavior attracts a great interest to the realizability of lasers which directly generate visible coherent radiations. The important problem is to clarify the mechanism and temporal response of the materials.

Nondegenerate nonlinearity of metal nanocomposite materials has not still been clearly understood though many results of these processes on the rough metal surfaces have been reported. Generally, slow responding materials have the prominent nonlinear response and the width of the resonance is restricted by their nonlinear response time [32]. The nonlinear optical response of metal nanocomposites can be regarded as slow. In contrast to the nonlinear response, the linear response, represented by SPR, has ultrashort response time, typically below few femtoseconds [33]. On the other hand, most of the preceding saturable absorbers show the optical delay because of the transverse relaxation much slower than the longitudinal relaxation time [34]. This is similar to the case of plasmonic response and is an interesting problem though it is not reported in any other publications.

For the recent several years, a new kind of laser – SPASER (Surface plasmonic emission by stimulated emission of radiation) – has been one of the hottest subjects in the photonics [35]. This subject is interesting because of its potential for the fascinating nanophotonic applications. The huge loss of SPPs during their propagation severely limits their applications for the nanophotonic applications. To overcome this problem, the researchers have proposed to insert the gain in the dielectric layer in the plasmonic waveguide and even stimulated emission of SPPs [36]. The ultrashort pulse generation is the necessary technique for the investigations of the ultrafast processes. Naturally, the question on the possibility for the ultrashort plasmonic pulse generation may arise. If it is possible, many problems for the ultrafast surface spectroscopy and the realization of compact information processing devices can be solved.

HHG near the metallic nanostructure surrounded by the noble gases [16, 37] has been attracted by many researchers because the high threshold [38] for HHG limits its practical applications with high repetition rates, typically in the MHz scale. The experimental and theoretical results in the periodic metal nanostructure by using the strong plasmonic field enhancement, has been reported and the threshold has been revealed to be decreased to more than 3 orders [37]. However, this structure requires the expensive nanolithographic technology. It is interesting whether the low threshold HHG will be possible and if possible, how high the generation efficiency at how low pump peak intensity can be.

In this thesis, we focus on the problems of the ultrafast nonlinear optical processes accompanying the field enhancement by the plasmonic enhancement in the metal nanostructures including metal nanocomposite and metallic surfaces. Beginning from the study of the linear optical response of composite materials doped with noble metal NPs with different shapes and sizes, we study the nonlinear optical characteristics in both the temporal and spectral domain. Based on this, we study passive mode-locking of lasers by using metal nanocomposites as the saturable absorbers and all-optical delay by slow light phenomenon in those materials. Next, we suggest the possibility of femtosecond plasmon pulse generation by mode-locking surface plasmon polariton laser. In the final part, we investigate the plasmon-enhanced hihg harmonic generation on the metallic fractal rough surfaces.

Outline

The thesis is organized as follows:

Chapter 2 introduces the basic concepts, the relevant theoretical and experimental results on SPR. Nonlinear optical properties of metal NPs and composite materials are outlined.

Chapter 3 is devoted to the study of nonlinear characteristics of the composites doped

with metal NPs with different shapes and sizes. By using the discrete dipole approximation (DDA) and the conjugate gradient method, the field enhancement is studied. In combination with the effective medium approximation, in addition, the effective dielectric function and nonlinear susceptibilities as the functions of wavelengths are investigated. For higher pump intensities, the saturable nonlinearity of metal nanocomposites is studied. Based on the self-consistent approach, the field enhancement factor distribution is studied. For the different shapes and sizes, the main parameters including the saturable nonlinearities and the saturation intensities, are investigated. These nonlinear characteristics are dealt with in the steady state.

Chapter 4 focuses on the temporal nonlinear response of metal nanocomposites based on the semiclassical two-temperature model (TTM). For the weak pump fluence approximation, the direct relations between the parameters of the incident light pulse and the metal NPs are presented. By using this approach, the femtosecond pulse generation by passive mode-locking of solid state lasers and semiconductor lasers operating in visible range, is investigated.

Chapter 5 is related to the study for the nondegenerate nonlinearity and its dispersion in the metal nanocomposites. It is shown that the strong dispersion of nonlinear susceptibility enables the realization of slow light which is of great interest in the modern photonics.

Chapter 6 suggests the femtosecond plasmon pulse generation by mode-locking of SPP laser in the layered nanostructure containing gain and nonlinear absorber dye layers, simultaneously.

Chapter 7 presents the plasmon-assisted low-threshold high-order harmonic generation on the metallic fractal rough surfaces.

Chapter 8 summarizes the results in this thesis.

2. Surface plasmon resonance and optical properties of metal nanoparticles and surfaces

The surface plasmon resonance (SPR) [4, 39, 40] representing the high field enhancement near metal nanoparticles (NPs) and surfaces finds numerous applications in photonics. As typical examples, there are surface enhanced Raman spectroscopy [5], high-harmonic generation on metallic surfaces [16], strong field focusing by using metallic nanoattenae [41], etc.

The strong inherent nonlinearity of metal NPs, typically 6 orders higher than silica, attracts great interest for nonlinear optics. Metallic NPs and their composite materials have fast dephasing time, typically with a response time of a few femtoseconds. The electrons are in a strongly non-equilibrium state and plasmonic response is linear in this time scale. The nonlinear response of metal NPs arises from the electron thermalization by the collisions between electrons excited by the external field, typically in few hundreds femtoseconds, and it is attenuated by cooling of the electrons through the thermal exchange between the electrons and the lattices in metal NPs, in a temporal range of few picoseconds.

Metallic surfaces also play important roles in modern nanophotonics, mainly because of the high field enhancement and nanoconfinement. Surface plasmon polaritons [42] (SPPs) propagating along smooth metal surfaces are prospective for the next generation nanophotonics.

All the plasmon-related phenomena originate from the fact that the real part of dielectric function of metal is negative. From the Drude model [43], the dielectric function of metal is represented by

$$\varepsilon_m = 1 - \frac{\omega_p^2}{\omega^2 + i\Gamma\omega}, \tag{2.1}$$

where ω is the angle frequency of light, ω_p is plasma frequency and Γ is collision frequency. From the above expression, we have [43]

$$\mathrm{Re}\,(\varepsilon_m) = 1 - \frac{\omega_p^2}{\omega^2 + \Gamma^2}, \tag{2.2}$$

$$\mathrm{Im}\,(\varepsilon_m) = \frac{\Gamma}{\omega\,(\omega^2 + \Gamma^2)}. \tag{2.3}$$

For incident light with a frequency lower than the plasma frequency ω_p, the real part of the metal's dielectric function given by Eq. (2.2) becomes negative because the collision frequency Γ is much lower than ω_p. As an example, the plasma frequency of silver corresponds to 328 nm (3.78 eV) and $\Gamma = 3.23 \times 10^{14}$ s^{-1} [43]. The above facts shows that silver has a negative real part of the dielectric function at wavelengths longer than about

330 nm. Plasmon-induced enhancement of light field near the metallic surface has the physical origin in this optical property of metal (see Section 2.1).

In this chapter, we review the basic concept SPR as well as the preceding results for the linear and nonlinear optical properties of metal NPs (NPs) and surfaces.

2.1. Surface plasmon resonance in metal nanoparticles and surfaces

In this section, we focus on the plasmonic excitation and resonance in metal-dielectric nanostructures. For a certain wavelength, the field strength near the NPs surfaces is significantly increased and this phenomenon is called localized surface plasmon resonance (SPR).

Unlike the plasmonic excitation and resonance on the metallic NPs, surface plasmons on a surface can propagate along the surfaces of metallic films surrounded by dielectric media. This propagating plasmon waves are called SPPs. These waves always have the propagation constants larger than that in the vacuum or dielectric media because the dielectric function of metal is negative. Therefore, for the excitation of SPPs we must have a special way to match these values of incident light and propagating SPPs. Under this condition, the energy of incident light is efficiently coupled to the metallic film or waveguides, leading to the plasmonic resonance for the propagating plasmon waves.

2.1.1. Localized surface plasmon resonance

Most applications of metal nanostructures are directly related to the surface plasmon resonance (SPR), the characteristics of which depend on their structure. These metallic nanostructures are generally fabricated by using one of the two approaches - lithographic technologies and chemical synthesis. The practical technology useful for metal NPs and arrays is electron beam lithography. This technology enables very high resolution appropriate for fabrication of metal nanoparticles (NPs). The advantage of this technique is that it allows to produce relatively large numbers of NPs with different shapes. This technique has been applied to make arrays of disks [44], bow-tie structures [45], etc. Despite the flexibility of lithographic technology, difficulties are still remaining in the roughness on the NP surfaces, in obtaining nanometer-scale interparticle spacings, in variations in their sizes and shapes, and other problems. To overcome these problems, chemical synthesis approaches are applied. In particular, these techniques are very useful for isolated metal NPs with a variety of shapes and sizes. By tailoring the sizes and shapes, it is possible to change SPR wavelengths over a wide range from ultraviolet to infrared [46]. This enables countless applications of SPR (see [8] and references therein).

Metal NPs exhibit prominently different optical properties in comparison with bulk metals. Conduction electrons in metal NPs collectively oscillate in response to the incident light field. When the electron cloud is displaced from the nuclei, a strong Coulomb forces between electrons and nuclei lead to oscillation of the electron cloud relative to the nuclei (see Fig. 2.1). The collective oscillation of electrons in isolated metal NPs becomes stronger for a certain wavelengths and this corresponds to the localized SPR. Near the SPR wavelength range, as the energy of incident photons is absorbed by the metal NPs,

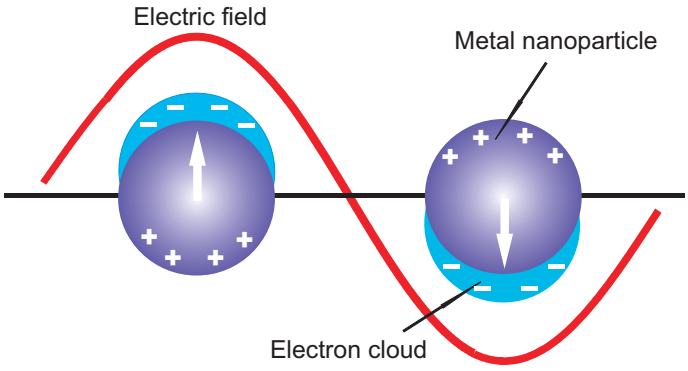

Figure 2.1.: Localized surface plasmon resonance on the metallic NP surfaces.

the medium doped with these particles shows a certain color corresponding to the inherent plasmonic absorption. This effect happens more clearly in noble metal NPs than the other metal NPs because these metals have dielectric functions, the real part of which is negative and, in particular, the magnitude of the imaginary part is much smaller than the real part [43, 47].

Below we briefly explain the physical origin of the localized SPR based on the electrostatic theory. The electromagnetic field around the particle surfaces can be determined by Laplace equation $\nabla^2\varphi = 0$, where φ is the electric potential and the electric field is given by $\mathbf{E} = -\nabla\varphi$. To solve this equation, we apply the two boundary conditions: (i) φ is continuous on the particle surface and (ii) the normal component of electric displacement $\mathbf{D} = \varepsilon\mathbf{E}$ is also continuous, where ε is dielectric function or permittivity. For spherical NP, the electric field outside of the particle is represented by [46]

$$\mathbf{E}_{out} = \mathbf{E}_0 - \alpha E_0 \left[\frac{\hat{\mathbf{x}}}{r^3} - \frac{3x}{r^5}\mathbf{r}\left(x\hat{\mathbf{x}} + y\hat{\mathbf{y}} + z\hat{\mathbf{z}}\right) \right],$$

where $\mathbf{E}_0$ is the incident field, α is the sphere polarizability, $\mathbf{r} = x\hat{\mathbf{x}} + y\hat{\mathbf{y}} + z\hat{\mathbf{z}}$, $\hat{\mathbf{x}}$, $\hat{\mathbf{y}}$ and $\hat{\mathbf{z}}$ are the common unit vectors, and $r = |\mathbf{r}|$. In the above equation, the incident field is parallel to $\hat{\mathbf{x}}$, $\mathbf{E}_0 = \hat{\mathbf{x}}|\mathbf{E}_0|$. From the Laplace equation, we obtain the dipole polarizability

$$\alpha = g_d a^3 \tag{2.4}$$

for very small nanospheres, where

$$g_d = \frac{\varepsilon_m - \varepsilon_h}{\varepsilon_m + 2\varepsilon_h}, \tag{2.5}$$

ε_m and ε_h are dielectric functions of metal and host dielectric, and a is the radius of the metal NP. The corresponding extinction and scattering efficiencies are given by [46]

$$Q_{\text{ext}} = 4x\,\text{Im}\left(g_d\right), \tag{2.6}$$

$$Q_{\text{sca}} = \frac{8}{3}x^4\left|g_d\right|^2, \tag{2.7}$$

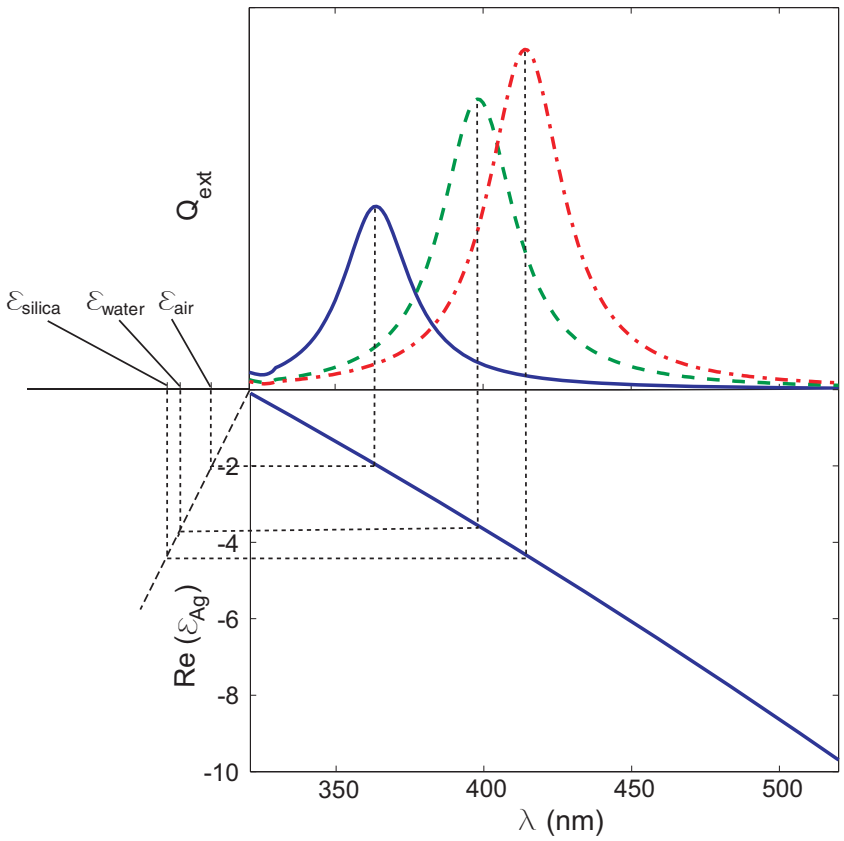

Figure 2.2.: Relation between SPR wavelength and dielectric function of host and metal for very small silver nanospheres.

where $x = 2\pi a\sqrt{\varepsilon_h}\lambda^{-1}$ andλ is light wavelength. The extinction efficiency is the ratio of the extinction cross-section to the geometrical cross-section πa^2. The scattering efficiency is also defined similarly to the extinction efficiency.

The dipole resonance wavelength depends on the dielectric functions of host medium and particles, as well as the sizes and shapes of the particles. Equations (2.5, 2.6) shows that SPR appears when the denominator $\varepsilon_m + 2\varepsilon_h$ becomes nearly zero. This situation can be realized only in the NPs with negative inherent dielectric functions like metals [43].

From Eq. (2.5), we can expect that for the host medium with larger dielectric function, the SPR wavelength becomes red-shifted for the same sort of metal consisting the NPs. Fig. 2.2 shows the dependence of SPR wavelengths on the host materials. For the metal NPs dispersed in air, the SPR wavelength is shortest of all the cases and is around 365 nm. For silica which has the dielectric function of 2.17, the SPR wavelength is 418 nm. The factor 2 in the denominator is valid only for very small nanospheres. For larger particles, the factor depends on the particle diameter. Generally, this factor increases with the particle sizes and as a result, SPR peaks are red-shifted. The shapes of the particles also show the influence on dipole SPR wavelengths but this can be approved only by experimental or

numerical approaches.

For larger particles, higher multipoles also contribute to the total extinction and scattering. Taking into account also the quadrupole term, the outside field for the larger particles written as [46]:

$$\mathbf{E}_{out} = \mathbf{E}_0 + ikE_0\left(x\hat{\mathbf{x}} + z\hat{\mathbf{z}}\right) - \alpha E_0\left(\frac{\hat{\mathbf{x}}}{r^3} - \frac{3x}{r^5}\mathbf{r}\right) - \beta E_0\left[\frac{x\hat{\mathbf{x}} + z\hat{\mathbf{z}}}{r^5} - \frac{5x}{r^7}\mathbf{r}\left(x^2\hat{\mathbf{x}} + y^2\hat{\mathbf{y}} + xz\hat{\mathbf{z}}\right)\right].$$

The corresponding quadrupole polarizability is given by

$$\beta = g_q a^5 \tag{2.8}$$

with

$$g_q = \frac{\varepsilon_m - \varepsilon_h}{\varepsilon_m + (3/2)\,\varepsilon_h}. \tag{2.9}$$

The total (dipole+quadrupole) extinction and scattering efficiencies are given by

$$Q_{\text{ext}} = 4x\text{Im}\left[g_d + \frac{x^2}{12}g_q + \frac{x^2}{30}\left(\varepsilon_m - 1\right)\right], \tag{2.10}$$

$$Q_{\text{sca}} = \frac{8}{3}x^4\left[\left|g_d\right|^2 + \frac{x^4}{240}\left|g_q\right|^2 + \frac{x^4}{900}\left|\varepsilon_m - 1\right|^2\right]. \tag{2.11}$$

An important fact in the quadrupole term is that the denominator contains the factor 3/2 in contrast to the factor 2 in Eq. (2.5) corresponding to dipole. This fact shows that the quadrupole-related SPR absorption or extinction peak appears in a wavelength range much shorter than the dipole-related SPR.

For nonspherical NPs, the sizes along the individual directions are different and the different sizes leads to the different SPR wavelengths. Therefore, several dipole SPR

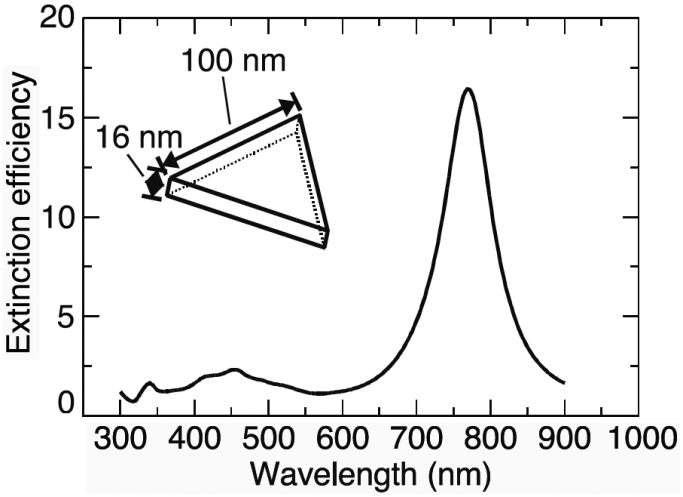

Figure 2.3.: Extinction spectrum of aqueous colloid containing Au nanoprisms (the figure taken from Ref. [48])

peaks appear simultaneously at different wavelengths. Higher-order SPR peaks also appear correspondingly. In Fig. 2.3 we show the extinction spectrum of an Au nanoprism immersed in the water [48], as an example. Four resonance peaks are visible: in-plane dipole at 779 nm, in-plane quadrupole at 460 nm, out-of-plane dipole at 420 nm, out-of-plane quadrupole at 335 nm. The figure shows that for a larger characteristic size of the NP the SPR peak becomes stronger and occurs at longer wavelength. The quadrupole peaks are placed in the range of wavelengths shorter than that of dipole peaks.

In this subsection, we qualitatively introduced the basic concept of localized SPR in metal NPs and its dependence on the material parameters of host and particles, and their sizes and shapes. Next, we briefly describe the general theory of inhomogeneous media and introduce the numerical method to solve the problems which are important for the electromagnetic simulation of metal nanostructures.

2.1.2. Electrodynamics in inhomogeneous media: theory and numerical methods

Maxwell's equations [49] describe light propagation in all kinds of materials. The electromagnetic field in inhomogeneous media can be obtained by using them in the form of

$$\nabla \times \mathbf{E}(\mathbf{r},t) = -\frac{1}{c_0}\frac{\partial \mathbf{B}(\mathbf{r},t)}{\partial t}, \tag{2.12}$$

$$\nabla \times \mathbf{B}(\mathbf{r},t) = \frac{1}{c_0}\frac{\partial \mathbf{E}(\mathbf{r},t)}{\partial t} + \frac{4\pi}{c_0}\mathbf{J}(\mathbf{r},t), \tag{2.13}$$

$$\nabla \cdot \mathbf{D}(\mathbf{r},t) = 4\pi\rho(\mathbf{r},t), \tag{2.14}$$

$$\nabla \cdot \mathbf{B}(\mathbf{r},t) = 0, \tag{2.15}$$

where **E**, **H**, **D** and **B** are electric field, magnetic field, the electric displacement, and magnetic induction, ρ and **J** are charge and current densities, respectively, and c_0 is the speed of light in vacuum. To determine the fields, it is necessary to add material equations:

$$\mathbf{D}(\mathbf{r},t) = \varepsilon(\mathbf{r})\mathbf{E}(\mathbf{r},t), \tag{2.16}$$

$$\mathbf{B}(\mathbf{r},t) = \mu(\mathbf{r})\mathbf{H}(\mathbf{r},t), \tag{2.17}$$

where ε and μ are permittivity (or dielectric function) and permeability. Combining the above equations for a monochromatic field, we obtain a vectorial Helmholtz equation:

$$\nabla \times \nabla \times \mathbf{E}(\mathbf{r}) - \frac{\omega^2}{c_0^2}k(\mathbf{r})\mathbf{E}(\mathbf{r}) = 0, \tag{2.18}$$

where $\mathbf{E}(\mathbf{r},t) = \mathbf{E}(\mathbf{r})\exp(-i\omega t)$, ω is the angle frequency of light and $k(\mathbf{r}) = \varepsilon(\mathbf{r})\mu(\mathbf{r})$ is the wavenumber of light in the medium. For a inhomogeneous medium, the wavenumber is dependent on the space coordinate and, more generally, when the medium is anisotropic, it is a tensor. The solution of the above equation is the electric field which contains the information on the incident and scattered fields.

There are several methods for solving Eq. (2.18) including analytical [50] and numer-

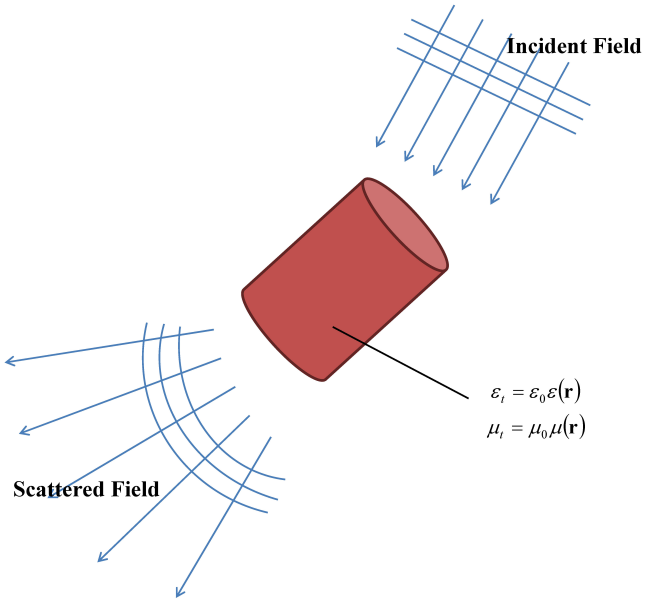

Figure 2.4.: Scattering of incident light by the object with the permittivity and permeability different from the environment

ical [51] ones. The typical analytical method is Mie theory [52] and its extensions (see e. g. [53]). This theory is suitable for the scattering by spherical particles. However, the inhomogeneous media in nature generally contain nonspherical particles. There are few cases which can be solved analytically. Therefore, many researchers have proposed numerical methods for solving the equation. Numerical methods for the scattering problems include the differential equation methods, volume integral equation methods, surface-integral equation methods and so on.

The differential equation methods calculate the scattered field by solving directly Eq. (2.18) in the frequency domain or time domain. The finite element method (FEM) [54] is a typical differential equation method in frequency domain. The principle of FEM is based on solving scattering problem by discretising Eq. (2.18) in space and solving it as a boundary value problem. This method is simple in principle, straightforward, and it can be applied for arbitrarily-shaped inhomogeneous particles. In practice, however, for very complicated particle shapes the huge cost for calculation should be elapsed. Another shortcoming is that the calculation accuracy is sensitively dependent on the sharp edge structure. The typical softwares include COMSOL [55], JCMwave [56], etc. As the time-domain differential equation methods, there are the finite difference time-domain method (FDTD) and the separation of variables method (SVM). FDTD is also a direct solution method such as FEM but in the time domain. This method is also simple and straightforward. One of the main advantages is the high flexibility for the particle shapes. The drawbacks are similar to FEM. The typical softwares are OptiFDTD, Lumerical [57], MEEP (open source), etc. The principle of SVM is to make a separation ansatz for the

solution to the scalar Helmholtz equation and to obtain a set of differential equations for each component function from the equation. The important advantage of this method is the high numerical accuracy. The another advantage is that it can be applied to compute a T-matrix and optical properties of an ensemble of randomly oriented particles analytically [51]. The main drawback is the huge computational cost.

The principles of volume integral equation methods is to solve the volume-integral equation which can be obtained from the vector Helmholtz equation by Green function method. The typical methods in this category include method of moment (MoM), discrete-dipole approximation or coupled dipole approximation (DDA or CDA) [58–64]. The two methods are similar and the only difference is that MoM uses the total fields in the volume cells as the unknown quantity, while DDA uses the incident field. The main advantage of these methods is the fast calculation speed by the application of fast Fourier transformation (FFT) for the calculation of volume integral. In addition, these can be applied for arbitrarily-shaped particles. The main drawback is that the calculation accuracy becomes low if the absolute sizes of calculation element is large. Among them, DDA is the most widely applied for solving scattering problems. This method is especially useful for the composite system containing isolated NPs [46] and rough surfaces [65].

As other methods, there are also the null-field method which is a kind of the surface-integral equation method, Fredholm integral equation method, time-domain surface integral equation method [51], etc.

In this thesis, we apply the DDA for all the electromagnetic simulations. Here, we introduce the principle of DDA in detail.

For convenience, let us assume that the medium is nonmagnetic and $\mu(\mathbf{r}) = 1$. On the other hand, Eq. (2.18) can be rewritten as follows:

$$\nabla \times \nabla \times \mathbf{E}(\mathbf{r}) - k_0^2 \mathbf{E}(\mathbf{r}) = k_0^2 [\varepsilon(\mathbf{r}) - 1] \mathbf{E}(\mathbf{r}), \tag{2.19}$$

where $k_0^2 = \omega^2/c_0^2$ is the wavenumber of light in vacuum. From the Green function theory, the integral equation for the above expression is given by

$$\mathbf{E}_0(\mathbf{r}) = \int_{V'} \mathbf{G}(\mathbf{r}, \mathbf{r}') \frac{[\varepsilon(\mathbf{r}') - 1]}{4\pi} \mathbf{E}(\mathbf{r}') \, d^3\mathbf{r}', \tag{2.20}$$

where $\mathbf{E}_0(\mathbf{r})$ is the solution of the Helmholtz equation without the source term or incident field, and $\mathbf{G}(\mathbf{r}, \mathbf{r}')$ is the tensor operator given by

$$\mathbf{G}(\mathbf{r}, \mathbf{r}') \mathbf{E}(\mathbf{r}') = \frac{e^{ik_0 r''}}{r''^3} \left\{ k_0^2 \mathbf{r}'' \times [\mathbf{r}'' \times \mathbf{E}(\mathbf{r}')] + \frac{1 - ik_0 r''}{r''^2} [r''^2 - 3\mathbf{r}''\mathbf{r}'' \cdot \mathbf{E}(\mathbf{r}')] \right\}, \tag{2.21}$$

where $\mathbf{r}'' = \mathbf{r} - \mathbf{r}'$ and $r'' = |\mathbf{r}''|$. As we can see from the above equation, it is impossible to solve directly Eq. (2.20) because the integral operator contains zero denominators for $r'' = 0$. To eliminate this problem, we consider the included particles as aggregates of very small spheres and write the self-terms in the above integral equation

$$\mathbf{E}_{self}(\mathbf{r}) = \int_{V' \to 0} \mathbf{G}(\mathbf{r}, \mathbf{r}') \frac{[\varepsilon(\mathbf{r}') - 1]}{4\pi} \mathbf{E}(\mathbf{r}') \, d^3\mathbf{r}' \tag{2.22}$$

and invoke that the field in very small sphere is enhanced by the factor $3/\left[\varepsilon\left(\mathbf{r}'\right)+2\right]$ from the Clausius-Mossotti formula or Lorentz-Lorenz formula [66]. Then, we can rewrite Eq. (2.20) as follows:

$$\mathbf{E}_0\left(\mathbf{r}\right)=\mathbf{E}_{self}\left(\mathbf{r}\right)+\mathbf{E}_{scat}\left(\mathbf{r}\right)=\mathbf{E}_{self}\left(\mathbf{r}\right)+\int_{V\notin V'}\mathbf{G}\left(\mathbf{r},\mathbf{r}'\right)\frac{3\left[\varepsilon\left(\mathbf{r}'\right)-1\right]}{4\pi\left(\varepsilon\left(\mathbf{r}'\right)+2\right)}\mathbf{E}_{self}\left(\mathbf{r}'\right)d^3\mathbf{r}'. \tag{2.23}$$

Here, we discuss the physical basis of the above equation. Let us introduce the element polarizability

$$d\alpha\left(\mathbf{r}'\right)=\frac{3\left[\varepsilon\left(\mathbf{r}'\right)-1\right]}{4\pi\left[\varepsilon\left(\mathbf{r}'\right)+2\right]}d^3\mathbf{r}'. \tag{2.24}$$

This quantity is the polarizability of an infinitely small sphere according to the Clausius-Mossotti formula [66] and its dipole moment can be written as

$$d\mathbf{d}\left(\mathbf{r}'\right)=\mathbf{E}_{self}\left(\mathbf{r}'\right)d\alpha\left(\mathbf{r}'\right).$$

Consequently, Eq. (2.23) can be rewritten as follows:

$$\mathbf{E}_0\left(\mathbf{r}\right)=\mathbf{E}_{self}\left(\mathbf{r}\right)-\int_{V\notin V'}\mathbf{G}\left(\mathbf{r},\mathbf{r}'\right)d\mathbf{d}\left(\mathbf{r}'\right). \tag{2.25}$$

This equation has the physical meaning that the local field in the inhomogeneous medium is the sum of incident field and scattered field due to the existence of particles, the dielectric function of which is different from that of the host medium. The scattered field is linear superposition of the electromagnetic field formed by the individual dipoles. In practice, the above equation should be discretised to be solved. In that case, the discretised element spheres have the volumes of their own but not equal to zero. Thus, the accuracy of the method is guaranteed only when the size of discretised element spheres can be regarded as very small compared with the light wavelength which is requested by the electric dipole approximation.

Discretising the above equation, we obtain the main equation of discrete dipole approximation:

$$\mathbf{E}_j=\mathbf{E}_{0j}-\sum_{j\neq k}\mathbf{G}_{jk}\mathbf{d}_k, \tag{2.26}$$

where $\mathbf{E}_j$ and $\mathbf{E}_{0j}$ are incident and resultant fields at j-th place, respectively, and discretised Green tensor $\mathbf{G}_{jk}$ is given by

$$\mathbf{G}_{jk}=\frac{e^{ik_0r_{jk}}}{r_{jk}}\left[k_0^2\left(\hat{r}_{jk}\hat{r}_{jk}-\mathbf{I}\right)+\frac{ik_0r_{jk}-1}{r_{jk}^2}\left(3\hat{r}_{jk}\hat{r}_{jk}-\mathbf{I}\right)\right], \tag{2.27}$$

where $r_{jk}=\left|\mathbf{r}_j-\mathbf{r}_k\right|$ and

$$\hat{r}_{jk}=\frac{\mathbf{r}_j-\mathbf{r}_k}{r_{jk}}$$

and $\mathbf{I}$ is 3×3 identity matrix. In Eq. (2.26), the dipole moment at the k-th location is given

by

$$\mathbf{d}_k = \alpha_k \mathbf{E}_k = \frac{3v_k(\varepsilon_k - 1)}{4\pi(\varepsilon_k + 2)}\mathbf{E}_k, \tag{2.28}$$

where v_k and ε_k are the element volume and local dielectric function at the k-th dipole, respectively. This formula is correct only when the volume of the dipole can be neglected. For dipoles larger than about 5 nm, the discretization error cannot be neglected. Therefore, in the DDA approach the following modified diameter-depending polarizability, which reduces the discretization error, is introduced:

$$\alpha'_k = \frac{\alpha_k}{1 + \frac{\alpha_k}{d^3}\left[(b_1 + m^2 b_2 + m^2 b_3 S)(k_0 d)^2 - \frac{2}{3}i(k_0 d)^3\right]}, \tag{2.29}$$

where $d = \sqrt[3]{v_k}$, $b_1 = -1.891531$, $b_2 = 0.1648469$, $b_3 = -1.7700004$,

$$S = \sum_{j=1}^{3} (a_j e_j)^2$$

and **a** and **e** are the unit vectors defining the incident direction and the polarization state [59].

The extinction and scattering cross-sections can be obtained by using the following expressions [59]:

$$C_{\text{ext}} = \frac{4\pi k_0}{|\mathbf{E}_0|^2} \sum_{j=1} \text{Im}\left(\mathbf{E}^*_{0j} \cdot \mathbf{d}_j\right), \tag{2.30}$$

$$C_{\text{abs}} = \frac{4\pi k_0}{|\mathbf{E}_0|^2} \sum_{j=1} \left[\text{Im}\left(\mathbf{d}_j \cdot \mathbf{E}^*_j\right) - \frac{2}{3}k_0^3 \left|\mathbf{d}_j\right|^2\right]. \tag{2.31}$$

The corresponding extinction and scattering efficiencies are calculated by the ratio of cross-sections to the effective cross-section:

$$Q_{\text{ext}} = C_{\text{ext}} / \pi r_{\text{eff}}^2, \tag{2.32}$$

$$Q_{\text{abs}} = C_{\text{abs}} / \pi r_{\text{eff}}^2, \tag{2.33}$$

where $r_{\text{eff}} = \sqrt[3]{3V/(4\pi)}$ is the effective radius of the particle and V is the volume of the particle. These two efficiencies show the strength of extinction and absorption by the corresponding metal NPs.

In Eq. (2.26), self-terms on the left hand side of the equation can be combined with the scattering term (the second term in the right side hand). Then we can rewrite the equation as a linear matrix equation:

$$\sum_{\mathbf{k}} \mathbf{A_{jk}} \mathbf{d_k} = \mathbf{E_{0j}}, \tag{2.34}$$

where $\mathbf{A_{jk}} = \mathbf{G_{jk}}$ for $\mathbf{j} \neq \mathbf{k}$ and $\mathbf{A_{jj}} = \alpha_{\mathbf{j}}^{-1}$ for every subindex $\mathbf{j}$. To directly solve the above equation is immensely time-consuming. Alternatively, the problem can be changed with the optimization which gives the vector $\{\mathbf{E_k}\}$ closest to the realistic solution. Among several methods for the solution of the equations, the conjugate gradient method is the

most widely applied. The details of this method are described in Appendix A.

In each step of optimization, we have to calculate the product $\sum_{\mathbf{k}} \mathbf{A_{jk}} \mathbf{d}'_{\mathbf{k}}$, where $\mathbf{d}'_{\mathbf{k}}$ is the approximation in each step. This calculation is the main source of calculating time. Therefore, the main point for reducing calculation time is in obtaining this product faster. For this purpose, Goodman and Draine had developed the fast Fourier-transformation-based method [60]. In physics, we frequently meet the integrals similar to this product but they are generally simpler and contain scalar quantities. If the integral can be expressed by convolution, it can be easily calculated by using fast Fourier transformation (FFT). In matrix formalism, it is necessary that the integral kernel should be so-called "Block-Toeplitz" [62]. A square matrix $\mathbf{T}$ is called Toeplitz, if matrix elements on any line parallel to the main diagonal are the same, i. e. $\mathrm{T}_{ij} = t_{i-j}$, where i and j is arbitrary number of a matrix element T_{ij}. It is clear that the product of Toeplitz matrix and a vector is the same as the convolution of the the first column of the matrix and the vector from the definition of Toeplitz matrix. The Block-Toeplitz matrix is the tensor whose elements are 3×3 tensors and each elements are arranged in the same order as in Toeplitz.

To make the product in the left hand of Eq. (2.34) identical to the product of the Block-Toeplitz matrix and the polarization vector, Goodman et al. introduced the following approach [60]. First let the lattice of the matrix $\mathbf{A}$ be doubled in each dimension, e. g.,

$$j_x \in \{1, 2, \cdots, 2N_x\},$$

and regard $\mathbf{A}'$ and $\mathbf{X}$ as periodic in each dimension, e. g.

$$X_{j_x, j_y, j_z} = X_{j_x \pm 2N_x, j_y, j_z}.$$

Set $\mathbf{X_j} = 0$ if $N_x < j_x \leq 2N_x$, $N_y < j_y \leq 2N_y$ or $N_z < j_z \leq 2N_z$. Then the product $\mathbf{Y} = \mathbf{AX}$ is represented by

$$\mathbf{Y_j} = \sum_{j_x=0}^{2N_x} \sum_{j_y=0}^{2N_y} \sum_{j_z=0}^{2N_z} \mathbf{A}'_{\mathbf{j-k}} \cdot \mathbf{X_k} \equiv \sum_{\mathbf{j}}{}' \mathbf{A}'_{\mathbf{j-k}} \cdot \mathbf{X_j}. \tag{2.35}$$

Because the above product is a convolution and identical to the product that we need to calculate in Eq. (2.34), we can apply the Fourier transform. In each step of the calculation of matrix-vector product, we can apply fast Fourier transform (FFT) by using the above method and, therefore, we can significantly reduce the calculation time.

The study of the electrodynamic field enhancement is the basis of all the optical phenomena in the metal nanostructures. The DDA is one of the most efficient simulation approaches for this purpose. In Section 3.1, we develop the DDA simulation tool for the applications of nonlinear processes accompanying SPR in metal nanostructures.

2.1.3. Surface plasmon polaritons on metallic surfaces

A surface plasmon polariton (SPP) [42, 67] is a coupled wave of photons and electrons existing on the surface of a "good" metal. Here the good metal indicates that the real part of its dielectric function is negative and the magnitude of the imaginary part is much smaller than that of the real part. These surface waves always exist in the interface of the two media, one of which has negative permittivity (metal) and the other positive (dielectric). The

amplitude of a SPP decays exponentially with the increase of distance from the interface and its energy is confined to the near vicinity of the two media. Energy confinement leads to the strong field enhancement which is useful for the detection of the surface state. High sensitivity on the surface state is widely applied for chemical or biological sensors. By using field enhancement on the surface, it is possible to significantly enhance Raman scattering, second or third-order harmonic generation (SHG or THG), fluorescence, etc. SPPs intrinsically exist on the 2D space and can propagate on the waveguide structure. This property enables their applications for optical informatics and communications. Recently, the control of SPPs by using optical signals based on nonlinear SPP optics is attracting much attention because this has a potential for purely photonic control and processing of signals.

SPPs are hard to detect because they are confined in space. To detect them, it is necessary to couple SPPs to radiative electromagnetic waves. By the development of scanning near-field microscopic (SNOM) technology, it has been possible to detect SPPs locally on the surfaces. Likewise, we have to place a certain element for coupling light to SPP to excite them.

First, we consider the simplest case: SPP on a single interface of dielectric and metal (Fig. 2.5). The electromagnetic field of a SPP can be described by Maxwell's equations with boundary conditions. The boundary conditions represents the continuity of tangential components of electric field and magnetic fields across the interface. We first consider the case of TM waves (p-polarization). From Maxwell's equations, we take the electric field as a plane wave form

$$\mathbf{E}_a = (\hat{x}E_{ax} + \hat{z}E_{az})\, e^{iKz - \alpha_a x - i\omega t},$$
$$\mathbf{E}_b = (\hat{x}E_{bx} + \hat{z}E_{bz})\, e^{iKz + \alpha_b x - i\omega t},$$

where $\hat{x}$ and $\hat{z}$ are the unit vectors along x and z axes, E_{ax}, E_{az}, E_{bx} and E_{bz} are x- and z-components of the electric field $\mathbf{E}$ in a and b layers, α_a and α_b are the attenuation coefficients in a and b layers, respectively, and ω is light frequency [68]. The boundary conditions

$$E_{az} = E_{bz}, \tag{2.36}$$
$$\varepsilon_a E_{ax} = \varepsilon_b E_{bx} \tag{2.37}$$

at the interface $z = 0$ have to be satisfied. Since $\nabla \cdot \mathbf{E} = 0$ in the both media, Eq. (2.37) is transformed into

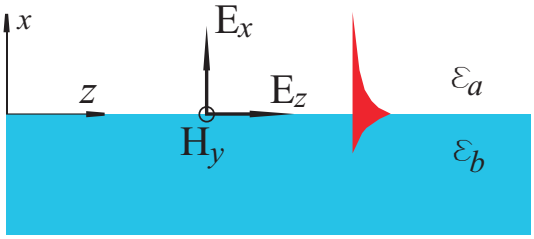

Figure 2.5.: Surface plasmon polariton at a single interface of metal and dielectric.

$$\varepsilon_a \left(\frac{iK}{\alpha_a} \right) E_{az} = \varepsilon_a \left(\frac{-iK}{\alpha_b} \right) E_{az}. \tag{2.38}$$

From Eq. (2.38), the following equation is obtained:

$$\varepsilon_a \alpha_b + \varepsilon_b \alpha_a = 0. \tag{2.39}$$

Taking into account Eq. (2.38), the dispersion relation for a SPP

$$K = k_0 \sqrt{\frac{\varepsilon_a \varepsilon_b}{\varepsilon_a + \varepsilon_b}} \tag{2.40}$$

is obtained, where $k_0 = \omega/c$ is propagation constant in vacuum. For the surface wave to exist, α_a and α_b must be positive and real and, therefore

$$(K/k_0)^2 > \varepsilon_a, \varepsilon_b. \tag{2.41}$$

This condition is satisfied only if one of the two media has a negative dielectric function and its magnitude is larger than the other. In the other word, the layers have to consist of metal and dielectric. For metals below the plasma frequency, the dielectric function is always negative [43]. The preceding calculation process is repeated for the transverse electric (TE) wave (or s-wave), but in this case, the dispersion relation for surface wave can not be obtained. This shows that no TE waves can propagate as a surface plasmon waves and SPPs are always TM waves [68].

SPPs suffer from the strong attenuation during their propagation along the interface. This is because much of their energy is concentrated in the metal layer. The typical propagation length for single-interface SPPs are tens of microns. For this reason, one of the main problems arising in their practical applications is to increase their propagation length.

The condition Eq. (2.41) shows that the SPP's wavenumber is always larger than that of electromagnetic waves in any bulk media. This also implies that any radiative light can not directly excite SPPs due to the wavevector mismatch, and conversely, SPPs can not be directly radiated. To couple SPPs to light or light to SPPs, we should have couplers, which changes the wavevectors. As the couplers, gratings and prisms can be used. One of the widely applied form of couplers is grating. When the z-component of SPP's wavevector has the same magnitude as the vectorial sum of the incident wavevector and the grating

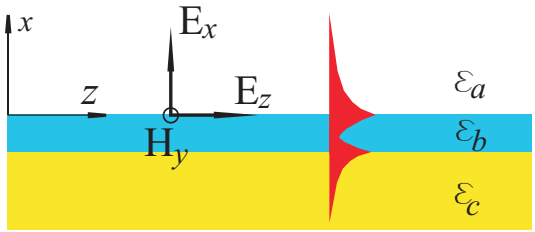

Figure 2.6.: Surface plasmon polariton propagation on a metal film surrounded by dielectric layers

vector, the light incident on the grating surface can be coupled to SPPs. A coupling efficiency of more than 10 % can be reached [69].

Next we consider the SPP propagation on the surface of metal film placed between the two dielectric layers with semi-infinitive widths (Fig. 2.6). The electric field in each layer can be written as

$$\mathbf{E}_a = (\hat{x}E_{ax} + \hat{z}E_{az})\, e^{iKz-\alpha_a x-i\omega t},$$
$$\mathbf{E}_b = \left(\hat{x}E_{bx}^{+} + \hat{z}E_{bz}^{+}\right) e^{iKz+\alpha_b x-i\omega t} + \left(\hat{x}E_{bx}^{-} + \hat{z}E_{bz}^{-}\right) e^{iKz-\alpha_b x-i\omega t},$$
$$\mathbf{E}_c = (\hat{x}E_{cx} + \hat{z}E_{cz})\, e^{iKz+\alpha_c x-i\omega t}$$

with the boundary conditions

$$E_{az}|_{x=0} = E_{bz}|_{x=0},$$
$$E_{bz}|_{x=-d} = E_{cz}|_{x=-d},$$
$$\varepsilon_a\, E_{ax}|_{x=0} = \varepsilon_b\, E_{bx}|_{x=0},$$
$$\varepsilon_b\, E_{bx}|_{x=-d} = \varepsilon_c\, E_{cx}|_{x=-d},$$

where d is thickness of metal film. From the above equations, the dispersion relation for SPPs near the metal film surface is obtained [70]:

$$(\varepsilon_a\alpha_b + \varepsilon_b\alpha_a)(\varepsilon_b\alpha_c + \varepsilon_c\alpha_b) + (\varepsilon_a\alpha_b - \varepsilon_b\alpha_a)(\varepsilon_b\alpha_c - \varepsilon_c\alpha_b)\, e^{-2\alpha_b d} = 0, \qquad (2.42)$$

where $\alpha_a^2 = K^2 - \varepsilon_a\omega^2/c^2$, $\alpha_b^2 = K^2 - \varepsilon_b\omega^2/c^2$ and $\alpha_c^2 = K^2 - \varepsilon_c\omega^2/c^2$. For very thick metal film ($d \to \infty$), we obtain the two equations

$$\begin{aligned} \varepsilon_a\alpha_b + \varepsilon_b\alpha_a &= 0 \\ \varepsilon_b\alpha_c + \varepsilon_c\alpha_b &= 0 \end{aligned},$$

which are identical to the individual dispersion relations for the two single interfaces: a-b and b-c interfaces [see Eq. (2.39)].

The dispersion relation Eq. (2.42) has two solutions, for which the energy of electromagnetic modes are concentrated near the interfaces. These two are the coupled modes of the individual modes existing at individual interfaces. Figure 2.7 shows the electromagnetic field of these modes: one has a symmetric field distribution and the other an

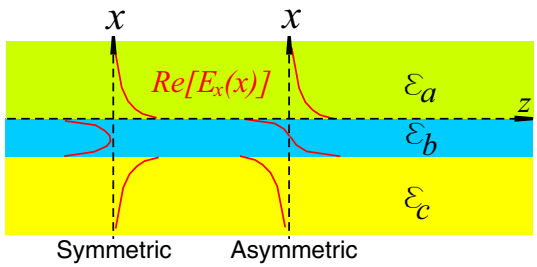

Figure 2.7.: Symmetric and asymmetric SPP modes in double-interface structure. The layer b is metallic film and the other two layers a and c are dielectrics.

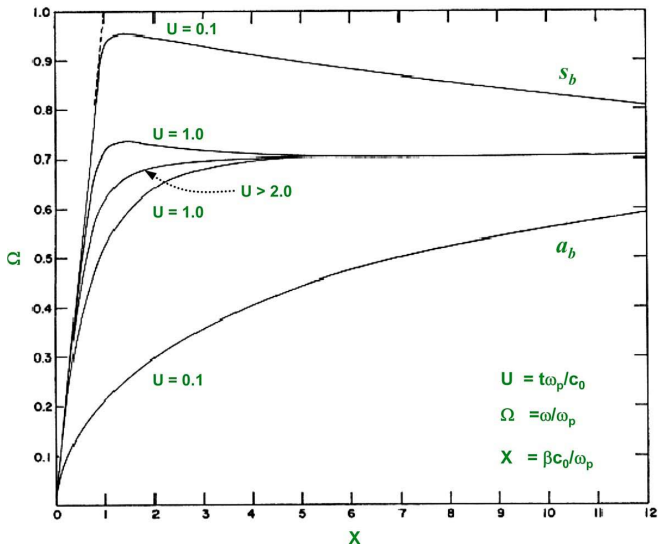

Figure 2.8.: Normalized dispersions for the symmetric and asymmetric bound modes with semiinfinite vacuum claddings for three normalized thicknesses U=0.1, 1.0, 2.0. The figure is taken from Ref. [71].

asymmetric one. For the symmetric structure consisting of the same dielectrics in a and c layers, the fields are accurately symmetric and anti-symmetric. The two SPP modes exhibit the different characteristics, in particular for very thin metal layer. For instance, mode index of the symmetric mode is generally smaller than that of the asymmetric. These facts are illustrated in Fig. 2.8. In the figure, ω_p is the plasma frequency of metal, ω is the light frequency, c_0 is the light velocity in vacuum, t is the thickness of metal film, β is the real part of propagation constant of SPP, U, Ω, and X are the normalized film thickness, frequency, and propagation constant, respectively. With the increase of metal film thickness the differences between the two modes become smaller. Moreover, the attenuation of symmetric bound mode decreases with decrease of metal film thickness and asymmetric mode increases, and former is generally much smaller than latter. From this fact, the symmetric plasmon mode is named as the long-range surface plasmon polariton (LRSPP) and the asymmetric the short range surface plasmon polariton (SRSPP) [71, 72]. The typical propagation length of LRSPP is up to ~ 300 μm. Instead, LRSPPs shows much weaker field confinement. However, the field can be, in principle, confined in a region shorter than the light wavelength even for LRSPP. In case of SRSPP the propagation length is much shorter, typically a few microns.

SPPs allow the localization of light below the diffraction limit and promise the progress in miniaturization of sophisticated compact optical devices with new functionalities. One of the main limitations for the applications of SPPs is its short propagation length (typically in the range of $30-200$ μm), even in case of LRSPP, due to the high SPP loss. Introducing gain to a dielectric adjacent to the metallic film has driven recent research to examine stimulated emission of SPPs [36, 73–76]. The next step in this development was the realization of lasers on the nanoscale by appropriate feedback [77–80]. The smallest laser reported to date has been achieved [79] by the realization of spaser, the concept of

which has been developed by Bergman and Stockman [35, 81], by using a single gold core and dye doped silica shell structure. Spaser is an acronym of Surface Plasmon Amplification by Stimulated Emission of Radiation. In this nanoscale device, the coherent plasmon radiation is generated from the photon flux amplified by gain medium embedded in the plasmonic NPs. Spasers provide a solution of the nanoscale coherent radiation through the outcoupling of light from the generated plasmon emission. Additional theoretical studies of spasers [82–88] and SPP amplification [89–91] have been published. Especially, the possibility of ultrafast plasmon amplification has been proposed in Ref. [88]. For the applications of the nanoconfined plasmon waves, ultrashort plasmon pulse generation has great significance which is still in question and will be discussed in Chapter 6.

2.1.4. Plasmonic field enhancement on metallic rough surfaces

In the above subsection, we have reviewed the optical properties of metallic smooth surfaces. In this subsection, we consider rough metallic surfaces.

Surfaces formed by deposition of atomic or molecular beams onto a substrate at low temperature have microscopically rough surface structures. It had been well known from a lot of experimental and theoretical investigations that cold-deposited metal films are self-affine fractal structures [92]. Self-affine surfaces are different from self-similar surfaces in that they require different scaling factors in the horizontal plane and in the normal direction. Fractal surfaces do not have translational invariance, and ordinary running waves like SPPs are generally not the eigenmodes of a self-affine surface. On the other hand, plasmonic oscillations associated with different roughness features are strongly coupled with each other via dipole or, more generally, multipole interactions. In this structure, a variety of dipolar eigenmodes can be excited by a homogeneous electromagnetic field. In contrast to the common roughness, there is no correlation length for self-affine surfaces. This fact describes that there are inhomogeneities of all sizes in self-affine structures. Plasmonic excitations on the self-affine surfaces are localized and there are a lot of different local geometrical structures, exhibiting the strong plasmonic enhancement over nearly all the wavelength range, unlike non-fractal rough metallic surfaces. This is one of the most important differences from the common rough surfaces [92].

It is crucial to clarify the reason for the localizations of dipolar modes on fractal rough surfaces. The physical picture for plasmonic field enhancement on self-affine surface is identical to the mechanism of random lasing in inhomogeneous gain media. There exist a lot of randomly located and arbitrarily shaped ring-resonators (closed paths on the surface through which plasmon waves propagate) and each "resonator" selectively responds to the incident light at the corresponding wavelength.

Due to the significant inhomogeneity of the local fields, there are "cold" regions with weak local fields and "hot spots" with strong local fields. Many surface nonlinear optical and scattering signals are dramatically enhanced on the self-affine surfaces by the high field enhancements at the "hot spots".

Self-affine surfaces can be simulated by using the restricted solid-on solid (RSS) model [93, 94]. In this model, a particle is incorporated onto the growing aggregate only if the newly created interface does not have steps that are higher than one lattice unit. The surface structure obtained by using this rule, is relatively simple because there are no overhangs. In this way strong corrections to scaling effects are eliminated and the true scaling behaviors

clearly appear even for small dimensions. After a large number of repetitions for deposition onto the substrate, the height-height correlation function for a self-affine surface has the form [92]

$$\left\langle [h(\mathbf{R}) - h(0)]^2 \right\rangle \sim R^{2H}, \tag{2.43}$$

where $\mathbf{R}$ is the radius vector in the plane normal to the growth direction and the scaling exponent H is related to the fractal dimension D, through the formula $H = 3 - D$. For the RSS model, fractal dimension is 2.6 and the scaling formula Eq. (2.43) is valid for large values of average height $\bar{h}$ which is proportional to deposition time, such that $h \gg l^{\zeta}$, where $\zeta = 2(d+1)/(d+2) = 2 - H$ (l is the linear size of a system and d is the dimension of the embedding space).

Figure 2.9 shows an example of height profile for a self-affine fractal surface generated by using the RSS model [65].

Enhanced local field distributions on self-affine metallic surfaces are generally modeled by using the discrete-dipole approximation (DDA). Due to the inherent randomness of the structure, there is not any perfectly defined optical parameter including the field enhancement factor. However, there are three important features of field enhancement on these surfaces distinguished from the general random surfaces [92]: (i) The "hot spots" are formed in different places on the surfaces for different wavelengths. (ii) The field enhancement steeply increases from approximately 350 nm to 500 nm and the average enhancement factor increases with the increase of wavelength in the range of visible to infrared. For instance, the averaged intensity enhancement at 700 nm has the order of 3. (iii) Field enhancement strongly depends on the polarized state of incident light. For p-polarized light that is polarized parallel to the plane of incidence, the field enhancement factor is much smaller than that for s-polarized light that is polarized perpendicular to the plane of incidence [65].

Metallic random surfaces are applied for the several photonic processes which require the enhancement of incident field intensity and signal amplitudes including surface enhanced Raman spectroscopy [95], second- [13, 14] and third-order harmonic generations [15], etc. High-order harmonic generation (HHG), one of the hot subjects in modern optics, requires high peak intensity and low threshold HHG [16] has been reported in the nanostructures fabricated by nanolithographic technology.

One of the important advantages of using these metallic rough surfaces is in that strong

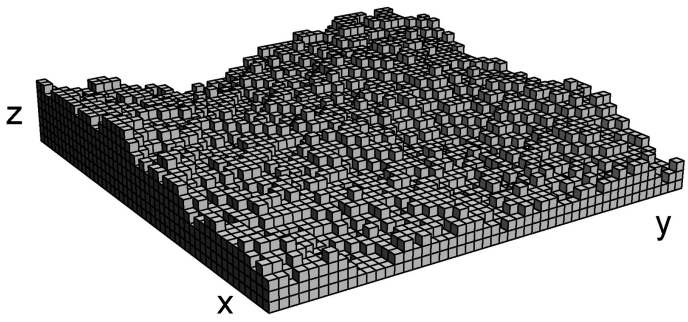

Figure 2.9.: Self-affine fractal surface obtained by solid-on-solid model (figure taken from Ref. [65])

field enhancement can be obtained with extremely low cost without the need of any expensive nanolithographic equipments. It is interesting to examine how these metallic rough surfaces can be useful for the low threshold high harmonic generation. We investigate this problem in Chapter 7.

2.2. Optical properties of composites doped with metal nanoparticles

In this section, we review preceding results on the linear and nonlinear optical characteristics of metal NPs and their nanocomposites. We briefly introduce the effective medium approximation (EMA) [96] and its variation, Maxwell-Garnett model for linear properties of metal nanocomposites. Next, we outline their quasi-static nonlinear properties (in the temporal range longer than picoseconds) including the generalized Maxwell-Garnett model [23], which is valid for dilute composite materials, and introduce the experimental data for their intensity-dependent nonlinearity and physical explanations. In the final part, we review the transient nonlinear response of these materials.

2.2.1. Effective medium approximation and Maxwell-Garnett model

The effective medium approximation (EMA) [96] is a method for treating an inhomogeneous medium, the dielectric function of which varies in space. One example of such media is a metal-dielectric composite.

We begin with the consideration of a random mixture of two types of grains denoted by A and B with relative volume fractions f and $1-f$, and different dielectric functions ε_A and ε_B. In this case, we regard the grains of volume fraction $1-f$ as the host and the other grains as guest. We are now going to obtain the effective dielectric function ε_{eff} of the composite. We assume that the composite as a whole behaves like a homogeneous medium with ε_{eff} instead of being a mixture of grains. We suppose that each grain has a spherical shape as well. From the relationship for the enhanced field in the spherical particles [17], the electric field inside the i-th particle is written as

$$E_i = E_0 \frac{3\varepsilon_{\text{eff}}}{\varepsilon_i + 2\varepsilon_{\text{eff}}},$$

where $\varepsilon_i = \varepsilon_A$ or ε_B and E_0 is the electric field far from the particle or incident field. Correspondingly, the electric displacement for i-th particle is given by

$$D_i = \varepsilon_i E_i = \varepsilon_i E_0 \frac{3\varepsilon_{\text{eff}}}{\varepsilon_i + 2\varepsilon_{\text{eff}}}.$$

The averaged electric displacement have to be identical to $\varepsilon_{\text{eff}} E_0$:

$$\langle D \rangle = f D_A + (1-f) D_B = \varepsilon_{\text{eff}} E_0, \tag{2.44}$$

leading to

$$f \frac{\varepsilon_A - \varepsilon_{\text{eff}}}{\varepsilon_A + 2\varepsilon_{\text{eff}}} + (1-f) \frac{\varepsilon_B - \varepsilon_{\text{eff}}}{\varepsilon_B + 2\varepsilon_{\text{eff}}} = 0. \tag{2.45}$$

Generalizing the above result to the multi-component composite system, we can write the equations

$$\langle D \rangle = \sum_i f_i D_i = \varepsilon_{\text{eff}} E_0, \tag{2.46}$$

$$\sum_i f_i \frac{\varepsilon_i - \varepsilon_{\text{eff}}}{\varepsilon_i + 2\varepsilon_{\text{eff}}} = 0, \tag{2.47}$$

where f_i and ε_i are filling factor and dielectric function for i-th component, respectively. This is the effective medium approximation based on Bruggeman's formalism [96].

Next, let us derive the relationship between the effective permittivity and the dielectric functions of host and inclusion particles in a different way. We assume that the filling factor is so small that the particles are separately included in the host and they are very small compared to the wavelength of light. Now we take a sphere which is also very small compared with wavelength but large enough to contain many individual particles (see Fig. 2.10). From the Clausius–Mossotti formula, the total polarizability of the sphere can be written by

$$\alpha_T = R^3 \frac{\varepsilon_{\text{eff}} - \varepsilon_h}{\varepsilon_{\text{eff}} + 2\varepsilon_h}, \tag{2.48}$$

where R is the radius of the sphere, and ε_h is dielectric function of the host medium. This polarization must be equal to the sum of the polarizabilities of the individual particles:

$$\alpha_T = N\alpha, \tag{2.49}$$

where N is the number of the particles included in the sphere.

On the other hand, the polarizability of each particle is written by

$$\alpha = r^3 \frac{\varepsilon_m - \varepsilon_h}{\varepsilon_m + 2\varepsilon_h}, \tag{2.50}$$

where ε_m and r are the dielectric function and radius of included particles, respectively. From Eqs. (2.48, 2.49, and 2.50), we obtain the relation

$$\frac{\varepsilon_{\text{eff}} - \varepsilon_h}{\varepsilon_{\text{eff}} + 2\varepsilon_h} = f \frac{\varepsilon_m - \varepsilon_h}{\varepsilon_m + 2\varepsilon_h}, \tag{2.51}$$

where filling factor is $f = Nr^3/R^3$. This is called Maxwell-Garnett equation and the model is named Maxwell-Garnett model.

The two results Eqs. (2.45) and Eq. (2.51) are very similar for small filling factor. From Eq. (2.45), we obtain

$$\frac{\varepsilon_{\text{eff}} - \varepsilon_B}{3\varepsilon_{\text{eff}}} = f \frac{\varepsilon_A - \varepsilon_B}{\varepsilon_A + 2\varepsilon_{\text{eff}}}.$$

For small filling factor $f \ll 1$, $\varepsilon_{\text{eff}} \approx \varepsilon_B$ and $\varepsilon_{\text{eff}} + 2\varepsilon_B \approx 3\varepsilon_{\text{eff}}$. Under this approximation, the above equation is identical to Maxwell-Garnett equation (2.51). This fact shows that the Maxwell-Garnett model as an approximate effective medium approach can be applied for the only case of small filling factor, typically smaller than 0.2 [23]. Actually, the result of Bruggeman's formalism can be applied for even higher filling factors because this formalism considers the constituents symmetrically.

From Eq. (2.51), we obtain the effective dielectric function in Maxwell-Garnett model

$$\varepsilon_{\text{eff}} = \varepsilon_h \frac{1+2\sigma f}{1-\sigma f}, \tag{2.52}$$

where

$$\sigma = 1 - p_0 = \frac{\varepsilon_m - \varepsilon_h}{\varepsilon_m + 2\varepsilon_h}, \tag{2.53}$$

$$p_0 = \frac{3\varepsilon_h}{\varepsilon_m + 2\varepsilon_h} \tag{2.54}$$

is field enhancement factor.

The above formula for field enhancement can be applied for very small nanospheres. For non-spherical and larger nanospheres, it is impossible to use it. A typical size limit for the applicability of Eq. (2.54) is about 10 nm. Otherwise, electrodynamic simulations tools have to be applied, as mentioned in Section 2.1. From Eq. (2.52-2.54), one can see that the effective dielectric function is mostly affected for the large value of field enhancement factor p_0, corresponding to SPR. As the dielectric function of metal is negative, this condition is fulfilled if $|\varepsilon_m + 2\varepsilon_h|$ is close to zero. To estimate the effect of plasmon resonance, it is worth to evaluate the range of absolute value of p_0. For silver nanospheres dispersed in silica, plasmonic resonance appears at 414 nm and $|p_0| = 8.86$, leading to a significant contribution to the effective dielectric function even for very small filling factor f. In contrast, e.g. at 800 nm $|p_0| = 0.27$, which is 33 times smaller than the former case. The plasmonic field enhancement far prominently contribute to the effective nonlinear susceptibilities because the nonlinear polarizations include the higher orders of field, as will be discussed in the next subsection.

The effective medium approximation can be written in general form by

$$\varepsilon_{\text{eff}} = \frac{\langle \mathbf{D} \rangle}{\langle \mathbf{E}_{\text{enh}} \rangle}, \tag{2.55}$$

where $\mathbf{E}_{\text{enh}} = p_0 \mathbf{E}_{\text{local}}$ is the enhanced field, $\mathbf{E}_{\text{local}}$ is the local field, and the $\langle\rangle$ represents

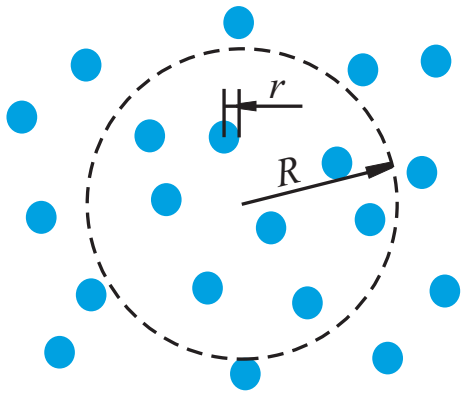

Figure 2.10.: Maxwell-Garnett model. The radii of inclusion particles r and the sphere $R \gg r$ are much smaller than the wavelength.

volume averaging.

2.2.2. Nonlinear optical susceptibilities of metal nanocomposites

The nonlinear optical susceptibility can also be evaluated by using the effective medium approach. The total electric displacement is written by

$$\mathbf{D} = \varepsilon \mathbf{E}_{\text{enh}} + \chi^{(3)} |\mathbf{E}_{\text{enh}}|^2 \mathbf{E}_{\text{enh}}. \tag{2.56}$$

The change of energy by the nonlinear optical interaction of the composite and the light field is given by [97]

$$\Delta W = \int \mathbf{P}^{NL} \cdot \mathbf{E}_{\text{enh}} dV, \tag{2.57}$$

where $\mathbf{P}^{NL} = \chi^{(3)} |\mathbf{E}_{\text{enh}}|^2 \mathbf{E}_{\text{enh}}$ is the enhanced local field-induced polarization. On the other hand, introducing the effective third-order nonlinear susceptibility $\chi^{(3)}_{\text{eff}}$ we can write the relation

$$\left\langle \mathbf{P}^{NL} \right\rangle = \chi^{(3)}_{\text{eff}} \left| \langle \mathbf{E}_{\text{enh}} \rangle \right|^2 \langle \mathbf{E}_{\text{enh}} \rangle . \tag{2.58}$$

In addition, the equation

$$\Delta W = \left\langle \mathbf{P}^{NL} \right\rangle \langle \mathbf{E}_{\text{enh}} \rangle \tag{2.59}$$

has to be satisfied. From Eqs. (2.57-2.59), we obtain the expression for the effective third-order susceptibility of the composite materials

$$\chi^{(3)}_{\text{eff}} = \frac{\left\langle \chi^{(3)} |\mathbf{E}_{\text{enh}}|^2 \mathbf{E}^2_{\text{enh}} \right\rangle}{|\langle \mathbf{E}_{\text{enh}} \rangle|^2 \langle \mathbf{E}_{\text{enh}} \rangle^2}. \tag{2.60}$$

The above equation is the rule of effective medium approximation for nonlinear third-order susceptibility in general cases. If the composite material contains very small particles with a nonlinear susceptibility much larger than the host medium with low filling factor f, the effective nonlinear third susceptibility can be approximately calculated by [97]

$$\chi^{(3)}_{\text{eff}} = f \chi^{(3)}_m \left| \frac{3\varepsilon_h}{\varepsilon_m + 2\varepsilon_h} \right|^2 \left(\frac{3\varepsilon_h}{\varepsilon_m + 2\varepsilon_h} \right)^2, \tag{2.61}$$

where $\chi^{(3)}_m$ is the nonlinear susceptibility of the included particles. The above approximation very well explains the experimental data for dilute composites doped with very small metal NPs. The enhancement factor of nonlinear susceptibility

$$G_{Kerr} = \left| \frac{3\varepsilon_h}{\varepsilon_m + 2\varepsilon_h} \right|^2 \left(\frac{3\varepsilon_h}{\varepsilon_m + 2\varepsilon_h} \right)^2$$

reflects the extent of plasmonic field enhancement to the effective third order nonlinear susceptibility. For silver nanospheres dispersed in silica $|G_{Kerr}| = |p_0|^4$ amounts 6.16×10^3 at 414 nm exhibiting SPR and 5.23×10^{-3} at 800 nm far from SPR, which is 6 orders smaller than the case at SPR.

If the nonlinearity of host medium cannot be neglected, we have to apply the following

equation of generalized Maxwell-Garnett model [23]

$$\chi_{\text{eff}}^{(3)} = f\frac{\chi_m^{(3)}}{|p|^2 p^2} + \frac{\chi_h^{(3)}\left\{1 - f\left(1 - 0.4\left[4|\sigma|^2\sigma^2 + \left(3|\sigma|^2\sigma + \sigma^3\right) + 9\left(|\sigma|^2 + \sigma^2\right)\right]\right)\right\}}{|1-\sigma f|^2 (1-\sigma f)^2}, \tag{2.62}$$

where

$$p = (1-\sigma f)\frac{\varepsilon_m + 2\varepsilon_h}{3\varepsilon_h}. \tag{2.63}$$

2.2.3. Intensity-dependent absorption in metal nanocomposites: experimental observations

In the above subsection, we introduced the theoretical basis for the nonlinear susceptibility of metal nanocomposites under perturbation conditions, i. e., for very weak pump intensity. For stronger intensities, the nonlinear optical characteristics such as nonlinear refractive index and absorption coefficient of metal nanocomposites depend on the intensity of incident light. In particular, the sign of the absorption coefficient is changed at a certain intensity, typically higher than GW/cm^2, leading to increasing absorption with the increase of intensity which is called the reverse saturable absorption (see e. g. Refs. [98, 99]). Intensity-dependent absorption also depends on the pulse duration, sort of metal and matrix, the shapes and sizes of the particles. Up to now a series of experimental results for the intensity-dependent nonlinearity of metal nanocomposites have been reported. Nevertheless, there is still no clear understanding of the mechanisms. Below, we introduce typical experimental data.

Composites doped with metal NPs exhibit saturable absorption for pump intensities below a certain value [28–30, 98–101]. In Ref. [101], the nonlinear absorption of a silicate glass doped with Ag NPs is investigated by the Z-scan technique using second harmonic radiation of a picosecond Nd:YAG laser (wavelength 532 nm, pulse duration 55 ps). The researchers have measured the nonlinear absorption coefficient depending on the pump intensity (Fig. 2.11). In the soda lime silicate glass doped with small Ag NPs, the nonlinear absorption behaves as a typical saturable absorber. Similar results are reported in Ref. [99].

The saturable absorption in these materials is explained as follows [99, 102]. The plasmon band of metal NPs as explained by the Mie theory involves dipolar oscillations of the free electrons in the conduction band that occupy energy states near the Fermi level. Once these electrons are excited by a laser pulse, they do not oscillate at the same frequency as that of the unexcited electrons, thus causing the plasmon absorption band to bleach. Experimental results shows that such a negative nonlinear absorption is observed on the long wavelength side of SPR [103]. This phenomenon shows that the saturable absorption is directly related to the plasmon resonance. For the higher pump intensities, a strong reverse saturable absorption is observed [28, 30, 98–100]. The reverse saturation absorption is attributed to the free carrier absorption of excited electrons in the particles [99]. Another process contributing to this phenomenon is the interband absorptions from d-band in noble metal atoms to the higher excited state.

Despite many experimental studies have been reported, there is still not an explicit theoretical approach for the saturable plasmonic absorption. In Refs. [104, 105] the authors

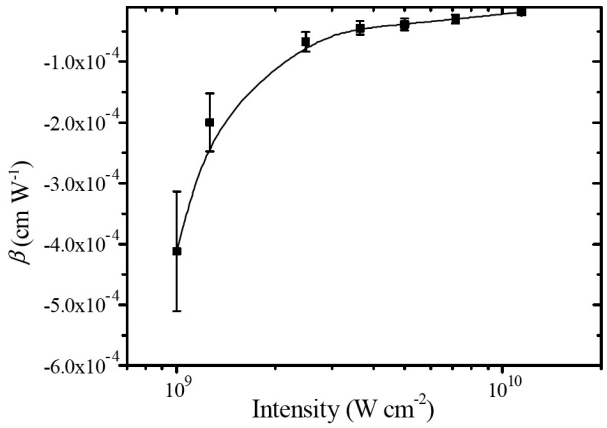

Figure 2.11.: Intensity-dependent nonlinear absorption coefficient of soda lime silicate glass doped with small Ag NPs. The negative sign of nonlinear absorption coefficient and the decrease of its magnitude with increasing pump intensity explicitly shows its saturable absorption property (the figure is taken from Ref. [101]).

have applied the T-matrix method for the derivation of high-order nonlinear susceptibilities of metal nanocomposites. However, based on these methods the effective dielectric function of metal nanocomposites is described by a power expansion with respect to the incident field. This treatment exhibits large deviations from the real values for the pump intensity of higher than ~ 10 MW/cm^2.

2.2.4. Ultrafast nonlinear optical response of metal nanocomposites

Up to now, we reviewed the quasi-static nonlinearity of metal nanocomposites. Like other optical materials, they have transient nonlinear response characteristics of their own. Numerous theoretical and experimental investigations of the transient nonlinear response of metal NPs and their composites based on this viewpoint have been reported [31, 106–128]. In metal NPs, three element processes contribute to the nonlinear response: electron thermalization, cooling of hot electrons through the thermal exchange with lattices in metal, thermal exchange between lattices in metal NPs and host medium. In the very beginning, the electrons start to oscillate collectively. This corresponds to the linear surface plasmonic response. This process happens in a time range below few femtoseconds. During the oscillation, the electrons collide with each other and they become quasiequilibrated leading to hot electron system [111]. The hot electron system loses its energy through cooling process and the phonon system (crystalline lattice in the metal NP) becomes hot. After a few picoseconds, a quasi-equilibrium state is formed between the electron system and the lattice. On a long time scale over 100 ps, the heat transfer from the NP to the host matrix becomes dominant. The temperatures of electron and lattice system as the state functions determine the dielectric function of metal NPs which is dependent on the intensity of incident light. Below we limit ourselves the consideration for the time scale shorter than ~ 10 ps.

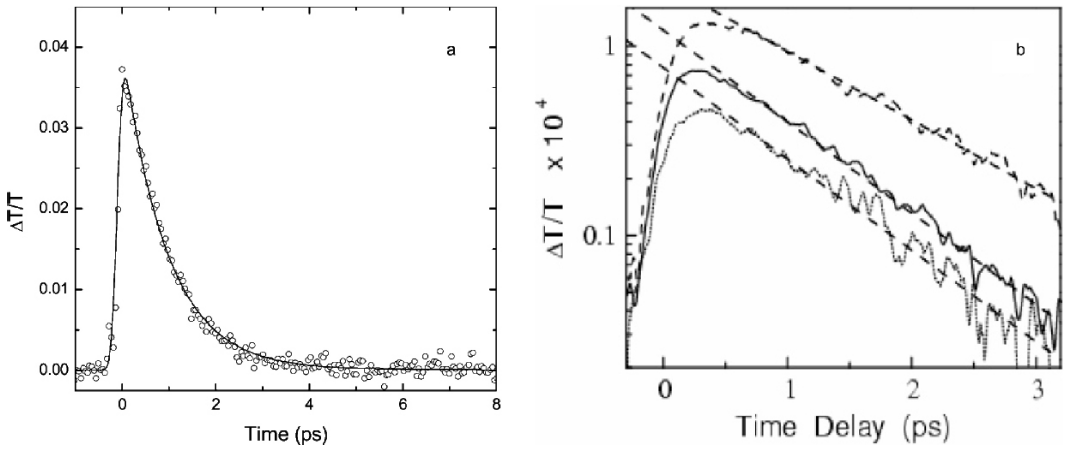

Figure 2.12.: Transient nonlinear absorption response of Au nanocolloids and a single Ag NP: (a) - transient response of an aqueous solution containing Au NPs embedded inside polyamidoamine dendrimers. Pump pulse has the fluence 0.3 mJ/cm^2, duration 150 fs at 600 nm, and the probe wavelength is tuned to SPR at 502 nm. (b) - the transient transmission changes in the single Ag nanosphere with diameter of 30 nm deposited on a cover glass for pump powers of 180 (dotted), 280 (solid), and 480 μW (upper dashed line) with 140 fs duration. Pump and probe wavelengths are 850 and 425 nm, respectively. The figures are taken from [119] (a) and [31] (b), respectively.

Dephasing time of surface plasmons determines the plasmonic absorption linewidth and is typically in the range of shorter than few femtoseconds [114, 129]. This process happens much faster than the thermalization of electrons.

After the excitation of surface plasmons in metal NPs, the electron system becomes thermalized. This process is also called electron-electron (e-e) scattering. Thermalization rate of electrons is determined by the number of the unoccupied states, which serve as the final states for this processes and it is inversely proportional to the energy above the Fermi level [114]. The experimental data reported a decade ago show that this time is in the range of hundreds of femtoseconds [130, 131]. All these results are obtained for the ensemble of metal NPs. In contrast, the recently reported ultrafast spectroscopic results for the single NP convince that the e-e scattering time is around 100 fs [31, 132–134]. During this process, the dielectric function of metal is changed by the incident laser pulse depending on the pulse duration and fluence.

Hot electron system is then cooled through the thermal exchange with the lattices in metal NPs. This process is also named as electron-phonon coupling. This time scale is mainly dependent on the pump fluence and has little relation with particle shapes and sizes. For silver NPs, it is approximately 1.23-2.37 ps [112] and for gold 0.95-1.43 ps [119]. For stronger pump fluences, the cooling time correspondingly increases.

Typical transient responses of transmittance in metal nanocomposites and a single NP are shown in Fig. 2.11. Figure 2.11(a) shows the transient response of an aqueous solution containing Au NPs with 2.5 nm diameter embedded inside polyamidoamine dendrimers. Pump wavelength is 600 nm, the central wavelength of the probe is tuned to the peak region

of the SPR (502 nm). The pump fluence is 300 μJ/cm^2 and the pulse duration is 150 fs. The rapid increase of the transmittance corresponds to the transient saturated absorption and approximately exponentially decreases with cooling time which is 0.93 ps for this case. Figure 2.11(b) shows the transient evolution of the extinction cross-section of a single silver nanosphere measured by femtosecond pump-probe spectroscopic technology. The SPR appears at 425 nm and the NP is illuminated by pump pulses with 180 (dotted line), 280 (solid line), and 480 μW (dashed line) at central wavelength 850 nm, and probe pulse at SPR wavelength (425 nm).

The transient nonlinear optical response of metal NPs is directly related with the electron and phonon temperatures. The electrons are thermalized much faster than the phonon system (lattices in the NPs and environment). In the picosecond timescale, two-temperature model (TTM) describes well the transient response of metallic NPs [106]. It is based on the assumption that there are two temperature scales: the temperature of electrons T_e and at the lattice T_L. The electron-electron interaction time is assumed to be much shorter than the cooling time. The energy transfer rate from electrons to lattices is proportional to the temperature difference. In this model, the dynamics of the two temperatures are described by [107, 121]

$$\begin{array}{l} C_e \partial T_e/\partial t = -G(T_e - T_L) + P(t) \\ C_L \partial T_L/\partial t = G(T_e - T_L) \end{array}, \tag{2.64}$$

where C_e and C_L are the heat capacities, T_e and T_L are the temperatures of electrons and lattices, respectively, and G is the cooling time constant, $P(t)$ is the absorbed laser power per unit volume. The electronic heat capacity is well approximated by a linear function of T_e: $C_e = \gamma T_e$ and depends on the density of states at the Fermi level.

The transient transmittance, an experimentally observable nonlinear quantity, is a linear function of the dielectric function of NPs [106]:

$$\frac{\Delta T}{T} = \frac{\partial \ln T}{\partial \varepsilon_1}\Delta\varepsilon_1 + \frac{\partial \ln T}{\partial \varepsilon_2}\Delta\varepsilon_2, \tag{2.65}$$

where T is the transmittance of the composite, ε_1 and ε_2 are real and imaginary parts of the dielectric functions of metal, all the Δ represent the change of the corresponding quantities. The change of dielectric functions depends on a redistribution of the electron energy at the Fermi level. Such a change is well described by a linear function of the electronic and lattice temperatures [121] for weak pump energy, and the above equation is rewritten as

$$\frac{\Delta T}{T} = aT_e(t) + bT_L(t), \tag{2.66}$$

where a and b are constants.

From Eqs. (2.65, 2.66), it can be concluded that the change of dielectric function of metal is proportional to the change of temperatures of electrons and lattices in metal NPs. The experimental results show that the influence of lattice temperature on the dielectric function change can be neglected. From these facts, the following equation can be written [117, 135]:

$$\triangle\varepsilon_m(t) = \eta\triangle T_e, \tag{2.67}$$

where η is a constant.

One of the drawbacks of the TTM is that it can not correctly describe the transient nonlinear electron dynamics below 100 fs range due to the thermalization time (e-e interaction time) being around hundreds of femtoseconds [130, 131]. Below this limit, the thermalization of electrons through e-e scattering plays a role. Even, the direct energy transfer from the nonthermalized electrons to the lattice also affects to the electron dynamics. To take into account this effect, a semiclassical TTM [25, 120] has been suggested. In the semiclassical TTM, the main source of the change in the electron and lattice temperatures, are the non-equilibrium electrons excited by the incident pulse. This process is described by the following equations:

$$\frac{\partial N}{\partial t} = -\frac{N}{\tau_{ee}} - \frac{N}{\tau_{ep}} + \delta P(t), \tag{2.68}$$

$$C_e \frac{\partial T_e}{\partial t} = -G(T_e - T_L) + \frac{N}{\tau_{ee}}, \tag{2.69}$$

$$C_L \frac{\partial T_L}{\partial t} = G(T_e - T_L) + \frac{N}{\tau_{ep}}, \tag{2.70}$$

where N is the energy density stored in the nonthermalized part of the distribution, τ_{ee} is the e-e interaction time, δ is a constant representing the contribution of light field to the generation of excited non-equilibrium electrons. This model provides an excellent agreement with the experimental results [136] as this model take into account the contributions from the non-thermalized electrons.

Another disadvantage of this model is that it can not directly account for the nonlinear optical parameters such as nonlinear refractive index and absorption. This method can only provide the fit by using the assumption that the temperatures of the thermalized electrons and lattices are proportional to the change of the dielectric function of metal NPs. This fact essentially restrict the direct application of the model to the estimation of the resultant nonlinear optical parameters.

To study the nonlinear optical processes in the metallic nanostructures, we have to obtain the direct relations between the incident light parameters and the metal NPs parameters.

The nonlinear transient response of the metal NPs resembles the temporal behaviors of saturable absorbers including semiconductor quantum dots [137, 138], semiconductor saturable absorber mirrors (SESAMs) [139], dyes [140, 141], etc., which are applied for mode-locking of lasers. One of the most fascinating point of these materials is that they exhibit prominent saturable absorption in the near UV and visible range where the traditional ones, e .g. SESAMs, semiconductor quantum dots, carbon nanotubes, and others, do not except the organic dyes that are severely suffered from the short lifetime due to the degradation. Saturable absorbers are also applied for the optical delay by all-optical technology. The fact that the metal nanocomposites show the saturable absorption, gives an inspiration for this important application. All the above promising, but not preceded, applications are available only through the careful quantitative predictions based on the correct model for the transient response.

In the following chapters (Chapter 4 and 5), we study the saturable field enhancement and absorption for the steady state. Based on this result, we establish the direct model for the transient response and apply for the study of mode-locking and slow light.

We reviewed above the interaction of laser pulses, the duration of which is tens of femtoseconds or longer, with metallic nanostructures. In some cases, we apply few femtosecond pulses for inducing nonlinear processes in the metallic nanostructures. One of the typical examples is high-order harmonic generation (HHG) near the metallic nanostructures.

In the simulation models in Refs. [16, 37], the authors neglected the interaction of few femtosecond laser pulses with metal nanostructures and the metal is dealt with as linearly responding medium. However, the physical feasibility for this approximation has to be clarified.

As we mentioned above, the metallic nanostructures can thermally respond on the time scale longer than 100 fs. In a few femtoseconds time scale, the electrons in metal nanostructures do not have any sufficient time to be heated and can not respond in this way any longer. Instead, the electrons may be escaped from the metallic surfaces because of their large kinetic energy forced by the intense light pulses. According to the Drude model for the dielectric function of metal, the electron density in metal directly exhibits an influence on the dielectric function of metal and, strictly speaking, there must be also the nonlinear response due to the electron density decrease.

If the pulse energy is so large that ponderomotive energy of electrons overcomes the work function, cold electrons can be emitted from the metallic surfaces [142]. There are many theoretical results and experimental observations on photoelectron emission from metallic surfaces [143, 144] and nanostructures [142, 145–147] under the illumination with intense few femtosecond pulses. The results show that electron emission can be neglected for peak intensity below ~ 0.5 TW/cm^2 and pulse duration of 10 fs. Actually, efficient photoemission from nanostructures including nanobots [142] has been observed for the peak intensity of incident pulse of about 1 TW/cm^2 despite the strong field enhancement by the nanostructure (pulse duration 7 fs).

All the above facts show that the change of the dielectric function of metal nanostructures can be neglected in an ultrashort temporal range of a few femtoseconds with peak intensity of about 100 GW/cm^2 which is typical value for the plasmon enhanced HHG.

The damage threshold is an important issue concerning the stable operation of HHG in the metallic nanostructures. For metallic nanostructures it decreases to 0.1 J/cm^2 and even down to 8 mJ/cm^2 for plasmonic resonance [148]. This experimental result shows that the fluence of a pulse with a peak intensity of 100 GW/cm^2 and duration of 10 fs, which is 1 mJ/cm^2, is much smaller than the damage threshold even under the condition of plasmonic resonance. However, the accumulation of heat by the illumination with a pulse train with high repetition rate may lead to permanent structural damage and the samples have to be strongly cooled for long-term protection.

3. Nonlinear optical properties of metal nanocomposites, saturable absorption

The study of the electromagnetic field and its scattering in inhomogeneous media dates for one century [149, 150]. In the inhomogeneous medium, the electromagnetic field is enhanced or decreased to a certain extent depending on the particle sizes and shapes and the sorts of host and guest media. Consequently, the averaged field is different from the incident field which shows the enhancement and scattering [50]. This aspect is discussed since the early 20th century when Mie has proposed the so called Mie-scattering theory [52, 149] based on the classical electrodynamics. The enhancement of the light field inside the inhomogeneous media essentially affects the effective linear and nonlinear optical characteristics of the composites differently from the incident light field. Therefore, we first should consider how the field is distributed in the composite and how the averaged field is enhanced depending on the inclusion nanoparticle (NP) sizes and shapes and material properties of the particles and host medium. For this purpose, we first consider the electrodynamic behavior of light propagation in inhomogeneous media.

For very weak incident light, metal NPs respond linearly and the total enhanced field can be calculated by the effective medium approximation in combination with the discrete dipole approximation (DDA). In case of very small nanospheres (typically smaller than 10 nm), the generalized Maxwell-Garnett model provides the nonlinear characteristics of the composite materials.

Table 3.1.: Theoretical methods presented in the sections

Pump intensity	Particles sizes, shapes	Field enhancement factor	Discrete dipole approximation	Maxwell–Garnett model	Effective medium approximation	Sections
Low[2]	Small[1]	Linear	–	Generalized	–	3.1
	Larger,[3] nonspherical	Linear	+	–	Generalized	3.1
Higher[4]	Small	Self-consistent	–	+	–	3.3
	Lager, nonspherical	Self-consistent	Modified	–	+	3.4

1 Nanospheres smaller than $\sim$ 10 nm, 2 Lower than $\sim$ 1 MW/cm^2, 3 Nanospheres larger than $\sim$ 10 nm, 4 Higher than $\sim$ 1 MW/cm^2

However, for higher intensities, the dielectric function itself is changed and the above perturbative approach does not work anymore. In this case, we have to self-consistently determine the field enhancement factor. In case of non-spherical and larger spherical NPs (typically larger than 10 nm), we apply the above mentioned self-consistent relation for the field enhancement factor with the DDA and obtain the intensity-dependent local field distribution in NPs. From this distribution, we can determine the effective intensity-dependent

dielectric function of the composite materials. In Table 3.1, we schematically show the theoretical methods presented in this chapter.

3.1. Linear and nonlinear optical properties of the composite doped with metal nanoparticles

In this section, we examine the linear and nonlinear optical properties of dielectric composites doped with metal nanoparticles with different shapes and sizes in the perturbative pump regime. To obtain the characteristic nonlinear parameters such as nonlinear index and absorption coefficients, we apply the effective medium approximation in combination with the discrete dipole approximation (DDA) as a simulation model for the local field enhancements near the metal nanoparticles. First of all, we develop a DDA simulation tool.

3.1.1. Discrete dipole approximation modeling

As we mentioned in Chapter 2, there are many softwares for DDA modeling but not for nonlinear optical purposes. To make the resultant DDA data such as the enhanced local field distribution, applicable for determining optical parameters, we have developed a new code for DDA modeling in MATLAB.

To examine the performance of the code, we have calculated the extinction and absorption efficiency spectrum of Ag nanoparticles suspended in air (dielectric function is 1) as shown in Fig. 3.1.

The result agrees well with the preceding study reported in Ref. [61]. The extinction and absorption efficiency spectra for the diameters of 40, 80, and 120 nm are quantitatively consistent with the result in [61].

It is worth to study the SPR behavior of non-spherical metal nanoparticles. In Fig. 3.2 we show the extinction (a) and absorption (b) spectra for Ag nanorods with diameter of 30 nm and different lengths contained in silica glass. The figure shows that the nanorods exhibit strong longitudinal (out-of-plane) dipole resonances at 557.8, 667.1, 783.3, and 901.1 nm in the order of increasing lengths of nanorods, respectively. On the other hand,

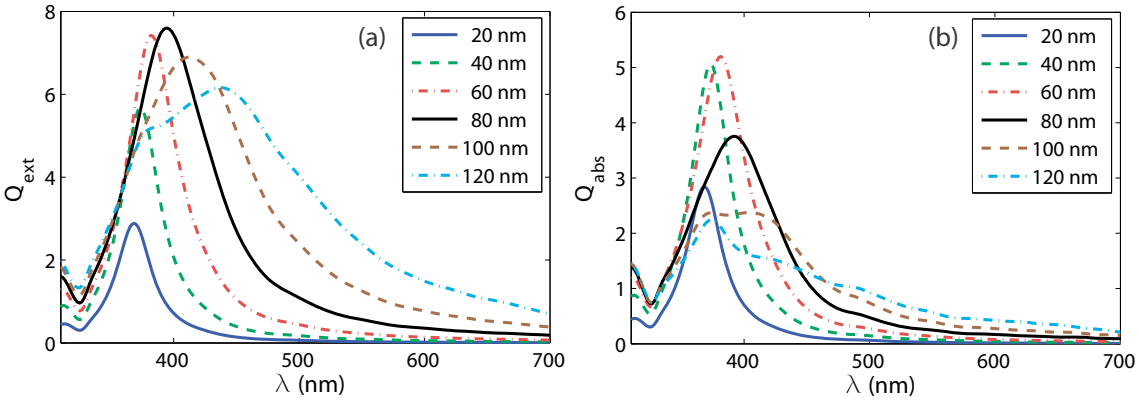

Figure 3.1.: Extinction (a) and absorption (b) efficiency spectra for Ag nanospheres in air.

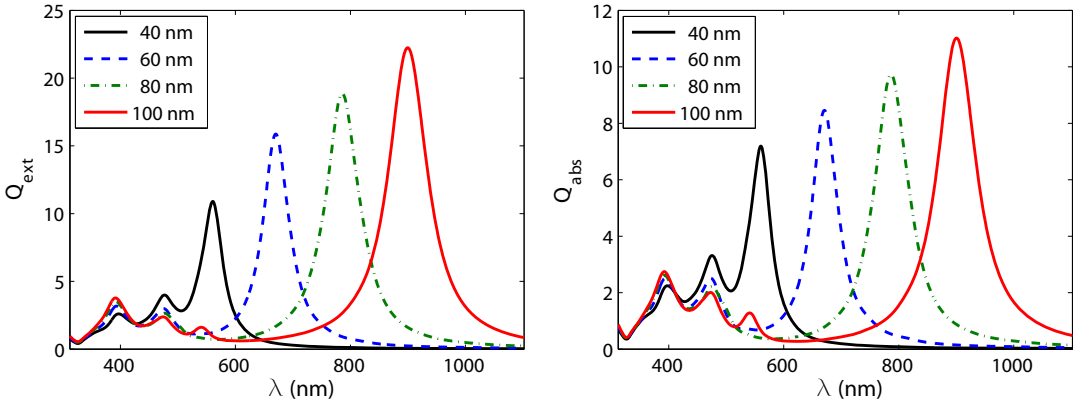

Figure 3.2.: Extinction (a) and absorption (b) efficiency spectra for Ag nanorods contained in silica glass. The diameters are 30 nm.

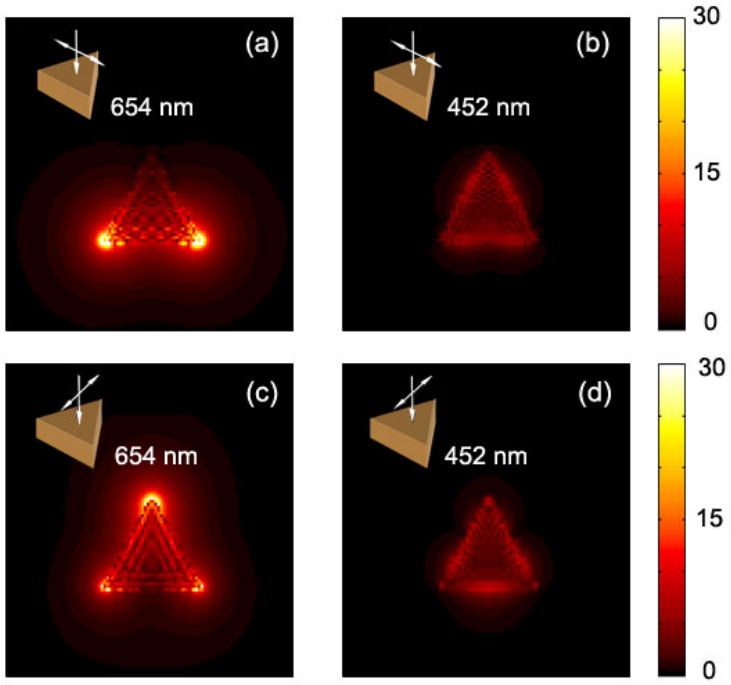

Figure 3.3.: Local field distribution near silver nanotriangles with side length and thickness of 45 nm and 15 nm, respectively, in a silica composite The polarization of the incident field as shown in the inset is parallel to one side of the nanotriangle (a), (b) and in the direction of its bisector (c), (d).

the quadrupole resonance peaks are very weak and hidden in the background of transverse (in plane) resonances except that of the nanorod with 100 nm length, at 515.2 nm. In contrast, both the dipole and quadrupole resonance peaks for out-of plane components are

equally prominent and appear at 475.2 and 389.9 nm, respectively, nearly regardless of the nanorod lengths. Among all the peaks, the strongest peaks originate from the longitudinal dipole resonances. In particular, for 80 nm long nanorods the SPR peak is located close to the central wavelength of Ti:sapphire.

The shape of the particles significantly influences the field intensity inside and outside of the particles. In particular for non-spherical NPs the field intensity at the sharp edges is strongly increased. This can be seen in Fig. 3.3 which shows the field distribution inside and outside of silver nanotriangles in silica for different polarizations and wavelengths of incident light.

3.1.2. Linear and nonlinear optical properties of the composite doped with metal nanoparticles with different sizes and shapes

First we study the permittivity ε, the absorption and extinction efficiencies Q_{ext} and Q_{abs} defined by Eqs. (2.32, 2.33), respectively, and the third-order susceptibility $\chi^{(3)}$ of an aqueous solution containing spherical silver NPs in dependence on the diameter of the NPs.

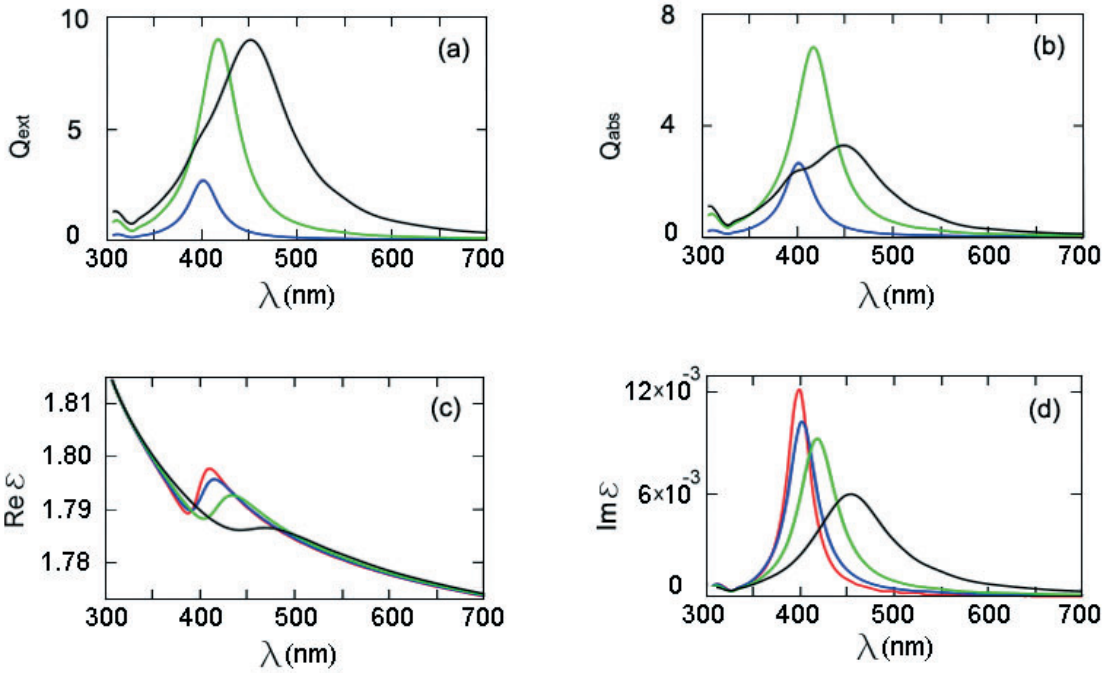

Figure 3.4.: Dependence of the effective linear optical parameters of aqueous colloid containing silver nanospheres on the particle size. In (a) the extinction efficiency Q_{ext}, in (b) the absorption efficiency Q_{abs}, in (c) the real and in (d) the imaginary part of effective permittivity are presented. The results of the generalized Maxwell-Garnett model (GMG) are presented by the red curve and numerical results are presented for NP diameters 10 nm (blue), 40 nm (green) and 70 nm (black). The filling factor is 3×10^{-4}.

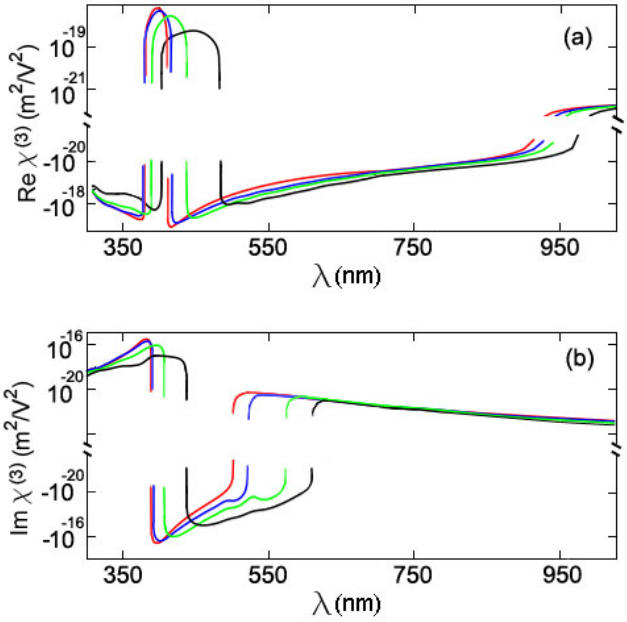

Figure 3.5.: Dependence of the real (a) and imaginary (b) part of the nonlinear optical susceptibility of aqueous colloid containing silver nanospheres on the particle size. The results of the generalized Maxwell-Garnett model (GMG) are presented by the red curve and numerical results are presented for NP diameters 10 nm (blue), 40 nm (green) and 70 nm (black). The other parameters are the same as in Fig. 3.4.

Figure 3.4 shows the extinction and absorption efficiencies and effective dielectric functions for diameters of 10 nm, 40 nm and 70 nm, respectively. Besides, results of the generalized Maxwell-Garnett (GMG) model which corresponds to an infinitely small size of the NPs are presented for comparison. The dielectric functions of silver and water are taken from [151, 152]. The figure shows that the smaller the particle, the smaller the difference between the simulation and the GMG model. All curves show a resonant behavior in the vicinity of the wavelength of the surface plasmon resonance (SPR), where the imaginary part of the permittivity is significantly enhanced. Around the SPR, the effective permittivity exhibits anomalous dispersion that is characteristic for an absorption resonance. The width is nearly the same as the width of the SPR [Fig. 3.4(c)].

In Fig. 3.5, we show the degenerate third-order nonlinear susceptibility as a function of wavelength for different diameters of silver nanospheres. The nonlinear optical susceptibilities of silver and water are taken from [24, 153–155], respectively. Fig. 3.5(a) and (b) show that even for low filling factors the nonlinearity of the metal NPs dominates over that of the host medium in a broad spectral region even rather far from the plasmon resonance. Only in the spectral range above 950 nm the nonlinearity of the host medium dominates the nonlinear response, resulting in positive total nonlinearity. This only weakly depends on the host material, because the nonlinear susceptibilities of dielectric media are typically in the range of 10^{-20} ~ 10^{-22} m^2/V^2 which is several orders smaller than the

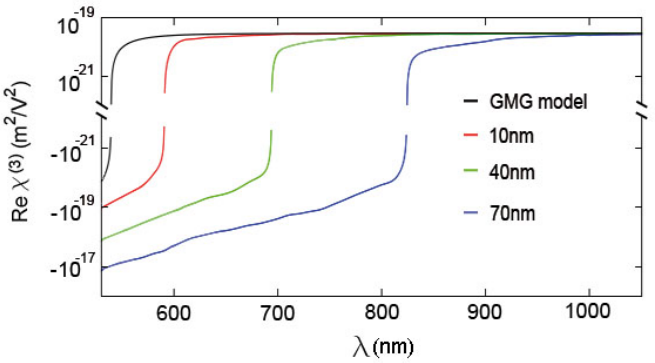

Figure 3.6.: Effective nonlinear optical susceptibility of CS_2 colloid containing silver nanospheres with various diameters with a filling factor of 3×10^{-5}.

inherent nonlinear susceptibility of metals. We find that the maximum effective nonlinear susceptibility $\chi^{(3)}$ is larger in those cases for which the ratio of peak absorption to the peak extinction is larger (at the parameters Q_{abs}/Q_{ext}= 0.989, 0.769 and 0.428 for particle diameters of 10, 40 and 70 nm, respectively). We relate this finding to the fact that both high absorption and high nonlinearity are associated with significant field enhancement in the metal nanoparticles.

Figures 3.4 and 3.5 show that the peaks of linear and nonlinear parameters become wider and lower and are red-shifted with the increase of the particle size due to the red-shift of the SPR wavelength. Because the real part of the nonlinear susceptibility of metal is negative while that of dielectric material is positive, the sign of the real part of the nonlinear susceptibility in Fig. 3.5(a) is changed at a certain wavelength which is red-shifted with decreasing filling factor and increasing particle size. To study the influence of the host media we present in Fig. 3.6 the results for the nonlinear coefficient Re $\left[\chi^{(3)}\right]$ of a colloid of carbon disulphide (CS_2) with a higher nonlinear coefficient and silver nanospheres for different diameters in dependence on the wavelengths. In Fig. 3.6 the permittivity and third-order nonlinear susceptibility of carbon disulphide is taken from [155]. In the figure, the results of the generalized Maxwell-Garnett (GMG) model describe the case of an infinitely small size of the particles. At 532 nm, the generalized Maxwell-Garnett model yields a real part of the third-order susceptibility of -1.42×10^{-20} m^2/V^2 corresponding to a nonlinear refractive index of -2.01×10^{-14} cm^2/W. This value agrees well with the experimental data (see Fig. 5(a) of reference [155]).

The effective nonlinear coefficient changes the sign at a wavelength which increases with increasing particle size: at 590 nm, 693 nm and 824 nm for particle diameters of 10 nm, 40 nm and 70 nm respectively, while the GMG model predicts a sign change at 539 nm. For longer wavelengths the nonlinear coefficient approaches that of the host material. Because the nonlinear susceptibility of carbon disulphide is much larger than that of water, the sign of the effective nonlinear susceptibility is changed at shorter wavelengths compared to such wavelength in the case of aqueous colloids. These results can be used to design a composite system with desirable wavelength-dependent nonlinear properties by the choice of appropriate host materials and diameters of the nanospheres.

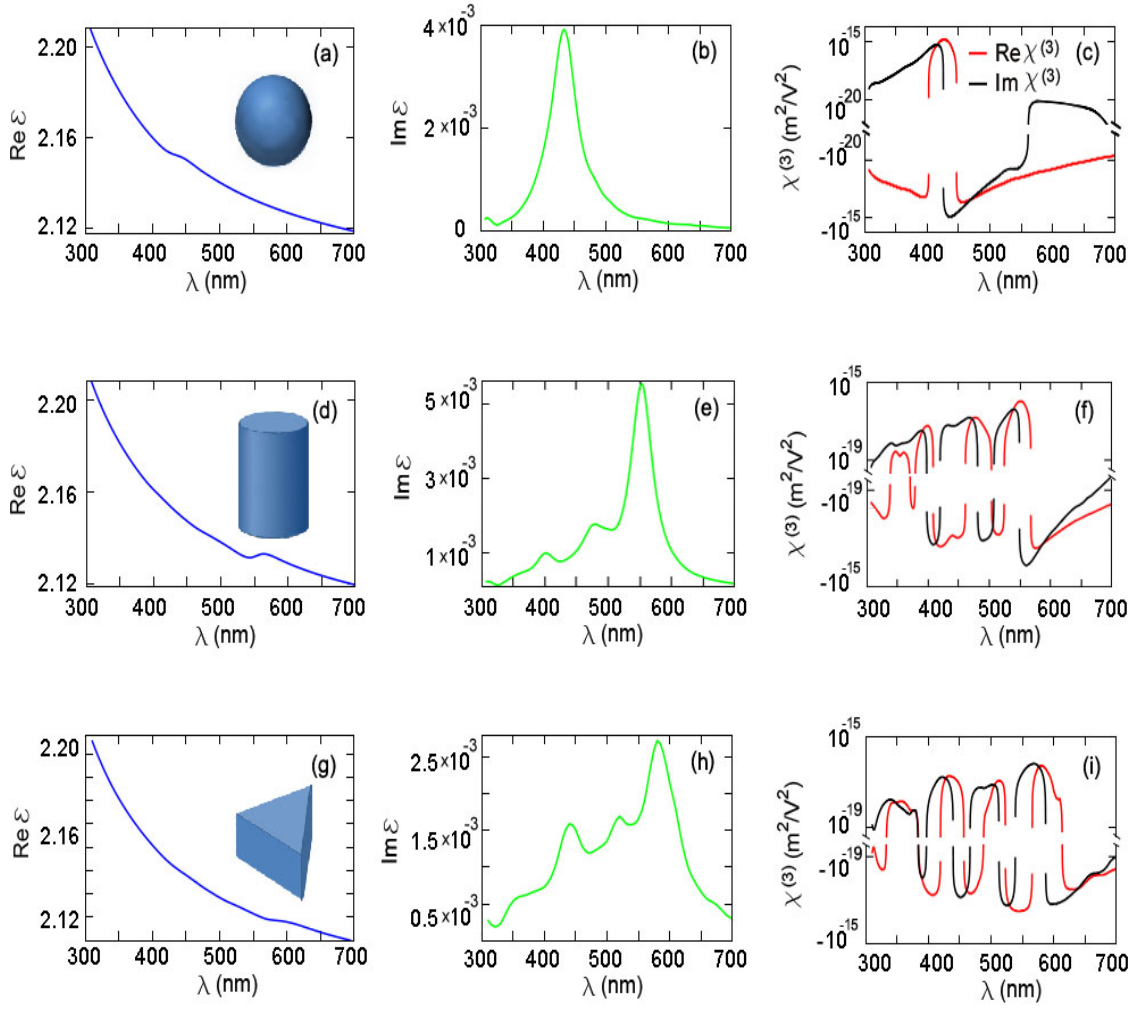

Figure 3.7.: Linear and nonlinear optical parameters of fused silica doped with silver nanoparticles with different shapes, as nanospheres (a)-(c), nanorods (d)-(f) and nanotriangles (g)-(i). The diameters and side lengths are all the same and as much as 30 nm, the length of the nanorods is 40 nm, the thickness of the nanotriangles is 15 nm and the filling factor is 10^{-4}. All the quantities are averaged for all the possible polarization directions versus the orientations of nanoparticles in space.

Let us now study the optical properties of composites containing non-spherical NPs with different shapes. As shown in Fig. 3.7, the number of peaks of the nonlinear susceptibility increases for the nanoparticles with many sharp edges, which offer the possibility of control of the nonlinear properties. The amplitude of the resonance peaks of the susceptibility decreases for particles with several sharp edges, but the non-resonant susceptibility in the long-wavelength tail is enhanced for such particles. The field redistribution and enhancement in this case results from excitation of both dipole resonances and quadrupole

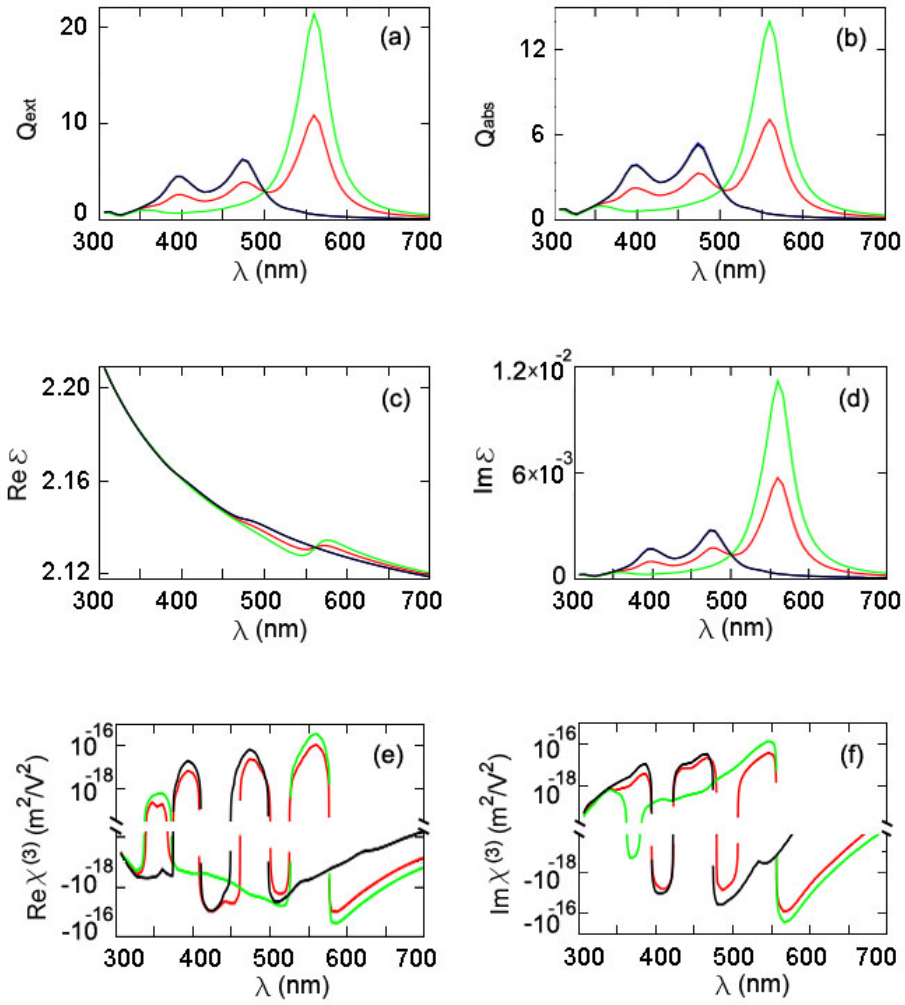

Figure 3.8.: Dielectric function and nonlinear optical susceptibilities of fused silica doped with silver nanorods for different polarization of the incident light. The black curves represent the result for in-plane polarization (polarization is perpendicular to the axis of nanorod), the green curves refer to out-of-plane polarization (polarization is parallel to the axis), and the red curves are direction averaged quantities. The parameters are the same as in Fig. 3.7(d)–5(f).

resonances. The complicated nature of the excitation results in a sensitive dependence of the field distribution on the wavelength and polarization, as well as in the field variation inside of the nanoparticles. In the case of nanotriangles and nanorods, their height is different from their side length and diameter, respectively. Therefore, in- and out-of-plane SPR wavelengths are different from each other contrary to the case of nanospheres. Correspondingly, the effective optical characteristics exhibit more than two peaks induced from the different dipole and quadrupole resonances arising from the different arrangement of nanoparticles versus polarization direction of the incident light. To clarify this

phenomenon, in Fig. 3.8 the linear and nonlinear optical susceptibilities of silver nanorods are calculated for different polarization of the incident light. The geometry and material parameters are the same as in Fig. 3.7. In the case of a polarization perpendicular to the axis of the nanorods (in-plane polarization) the SPR wavelengths are at 475 nm (dipole resonance) and 399 nm (quadrupole resonance) while, in case of polarization parallel to the axis (out-of-plane polarization) they are at 562 nm (dipole-resonance) and at 357 nm (quadrupole-resonance). Near the corresponding wavelengths, the linear and nonlinear optical parameters are greatly increased. As a result, arbitrarily oriented nanoparticles in the composites exhibit an SPR-induced enhancement with lower and smoothed peaks.

In this subsection, we presented the approach for the calculation of the effective linear and nonlinear optical parameters of materials doped with noble silver nanoparticles, using the effective medium theory combined with the discrete dipole approximation. We numerically evaluated the absorption and extinction cross-sections, the permittivity and the third-order nonlinear susceptibility of composites containing silver NPs in dependence on their size and shape and compared it with results calculated by using the generalized Maxwell-Garnett model. The effective dielectric function and the nonlinear susceptibility is significantly enhanced by the plasmon resonance which is shifted to longer wavelengths with increasing diameter of spherical NPs. The nonlinear susceptibility is mainly determined by the NPs even for very small filling factors, it has a frequency-dependent sign and is only weakly influenced by the host material. The linear and nonlinear optical parameters are also calculated for non-spherical NPs, such as rods and triangles. In this case the plasmon resonance is red-shifted and different dipole and quadrupole resonances are excited, with optical parameters exhibiting several peaks and depending on the polarization of the incident light. The results reported here demonstrate the possibility for a significant enhancement of the nonlinearity in a desired frequency range with a promising potential for applications in nonlinear optics.

3.1.3. Limit in the applicability of perturbative model

The results of the preceding subsection show that a nonlinear susceptibility of metal nanocomposites can be reached above the order of 10^{-15} m^2/V^2) even for very low filling factor. This fact show that a total change of the effective dielectric function can have the same order as the linear one even for a light intensity of hundreds of MW/cm^2 or GW/cm^2. In particular, near the SPR the imaginary part of the effective nonlinear susceptibility has the minus sign. Correspondingly, the total effective dielectric function may have the negative imaginary part leading to a physical artifact because these materials are not gain media. This problem originates from the fact that the local field is considered to be constant regardless to the intensity of the incident light. For strong intensity, the inherent dielectric function of metal is dramatically changed. We can predict that the field enhancement is correspondingly changed.

In the linear case, the SPR corresponds to the wavelength where the field enhancement factor (2.54) becomes maximum, in the other word, its denominator $\varepsilon_m + 2\varepsilon_h$ minimum. For strong intensity of the incident light, the dielectric function is changed and the magnitude of the denominator increases. Therefore, the magnitude of the field enhancement decreases leading to the plasmonic saturable absorption. Then, we have to find out what will the spectral behavior of field enhancement factor be like and how the field enhance-

ment factor decreases near SPR. Before doing that, we consider the effect of SPR shift by nonlinearity of metal NPs.

3.2. SPR shift by nonlinearity of metal nanoparticles

The spectral shift of the SPR peak is the main origin of nonlinear optical response of metal NPs and their nanocomposites. Below, we clarify the reason for this phenomenon.

For simplicity, we consider only very small spherical metal nanoparticles. The nonlinear optical susceptibility of dilute composite is approximately given by

$$\chi_{\text{eff}}^{(3)} = f\,|x|^2 x^2 \chi^{(3)}, \tag{3.1}$$

where f is the filling factor, $x = 3/(\varepsilon + 2)$ is the field enhancement factor, where $\varepsilon = \varepsilon_m/\varepsilon_h$ is the relative dielectric function.

The enhanced local field inside the particle can be calculated by $\mathbf{E}_{in} = x\mathbf{E}$, where $\mathbf{E}$ is the field out of the particle. The field enhancement factor x influences the enhanced field in both its magnitude and phase shift. For a complex enhancement factor, the enhanced local field undergoes the corresponding phase shift. For the detailed consideration, we apply the Drude model [43] [see Eq. (2.1)].

W consider the field enhancement factor x at the exact SPR wavelength. In this case,

$$x = 1 - \frac{i\omega_0}{\Gamma}, \tag{3.2}$$

where ω_0 is SPR frequency given by $\omega_0 = \omega_p/\sqrt{3}$. Considering the fact that the collision frequency is much less than SPR frequency, field inside the particle has a phase shift of approximately equal to and a little larger than $-\pi/2$.

The field enhancement factor can be written as

$$x = \frac{\omega^2 - \omega_0^2 + \Gamma^2 - i\Gamma(\omega - \gamma\Delta)}{(\gamma\Delta)^2 + \Gamma^2}, \tag{3.3}$$

where $\Delta = \omega - \omega_0$ is the frequency detuning from SPR frequency ω_0 and $\gamma = 1 + \omega_0/\omega$. From the above equation, we obtain the inequalities for the phase shift of the field inside the particle versus the incident field ϕ:

$$\begin{aligned} 0 < 2\phi < \pi \ \left(\omega < \sqrt{\omega_0^2 - \Gamma^2}\right) \\ \pi < 2\phi < 2\pi \ \left(\omega > \sqrt{\omega_0^2 - \Gamma^2}\right). \end{aligned} \tag{3.4}$$

In particular,

$$x \approx \omega \frac{2\Delta - i\Gamma}{(\gamma\Delta)^2 + \Gamma^2} \tag{3.5}$$

near the SPR. In this case,

$$\phi \approx \frac{\pi}{2}. \tag{3.6}$$

If the nonlinear susceptibility inherent to the metal is nearly real, like for Ag, the effective

nonlinear susceptibility changes. Therefore, the effective nonlinear absorption coefficient

$$\beta = \mathrm{Im}\frac{3\pi\chi^{(3)}_{\mathrm{eff}}}{2\lambda c\varepsilon_0\varepsilon_{\mathrm{eff}}} \tag{3.7}$$

also changes its sign near SPR and as a result, we deduce that the spectral peak of SPR is blue shifted.

3.3. Self-consistent formalism of the intensity-dependent dielectric function of the composite

In this section, we discuss the behavior of intensity-dependent nonlinear refraction and absorption in the composites doped with very small metal NPs. In the numerical simulation we use the generalized Maxwell-Garnett theory for spherical NPs with very small diameter and the discrete-dipole approximation for nanorods and spherical NPs of arbitrary diameter. The used analytical and numerical methods are similar to those in the preceding chapter but with an extension which takes into account the intensity-depending shift of the plasmon resonance leading to the saturation effects. The intensity-dependent dielectric function of the metal NPs is given by

$$\varepsilon_m \quad = \quad \varepsilon_{m0} + \chi^{(3)}_m |E_L|^2 ,$$

where ε_{m0} and $\chi^{(3)}_m$ are the (generally complex-valued) linear dielectric function and the third-order nonlinear susceptibility of the metal NPs and E_L is the field within the particle.

For spherical particles the latter is given by

$$E_L = \frac{3\varepsilon_h E_0}{\varepsilon_m + 2\varepsilon_h},$$

where E_0 is the incident field and ε_h the linear dielectric function of the host medium. Combining the above equations, we obtain the corrected field enhancement factor $x = E_L/E_0$

$$x = \frac{3\varepsilon_h}{\varepsilon_{m0} + 2\varepsilon_h + \chi^{(3)}_m |x|^2 |E_0|^2}. \tag{3.8}$$

To solve the above equation we transform it as

$$x = \frac{x_0}{1 + q|x|^2 |E_0|^2}, \tag{3.9}$$

where

$$x_0 = \frac{3\varepsilon_h}{\varepsilon_{m0} + 2\varepsilon_h} \tag{3.10}$$

is the linear field enhancement factor and

$$q = \frac{\chi^{(3)}_m}{\varepsilon_{m0} + 2\varepsilon_h}. \tag{3.11}$$

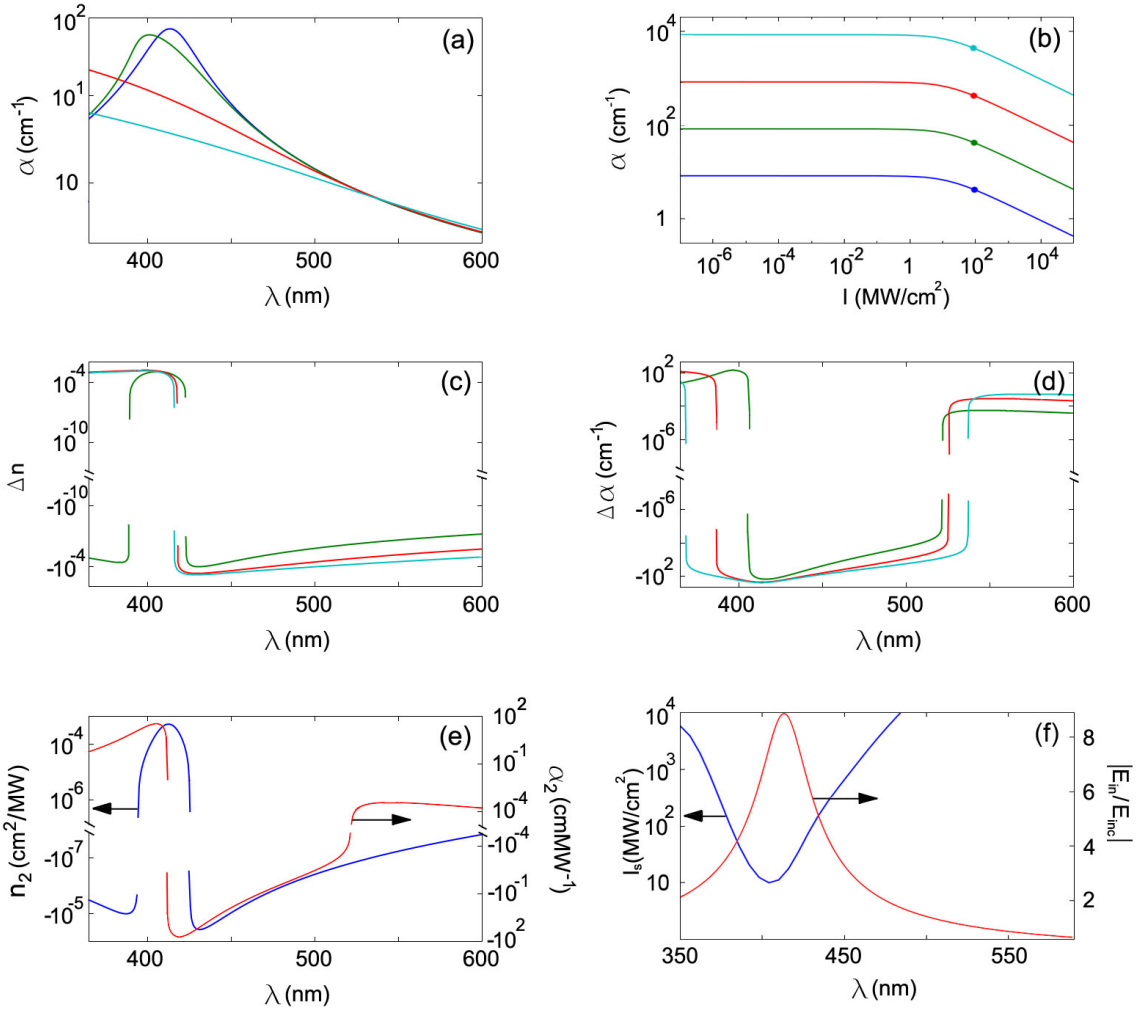

Figure 3.9.: Intensity-dependent nonlinear refraction and absorption of silica glass doped with silver nanospheres smaller than 10 nm calculated by using the generalized Maxwell-Garnett approach. Total absorption coefficient (a) and its nonlinear change (d), nonlinear refractive index change (c), the nonlinear refractive index and the absorption saturation coefficient (e), as well as the saturation intensity and the enhancement factor (f) are presented depending on the wavelength. In (b), loss is depicted as a function of intensity for different filling factors (blue, green, red and cyan curves correspond to filling factor of 10^{-5}, 10^{-4}, 10^{-3} and 10^{-2} respectively.) In (a), (c) and (d), blue, green, red and cyan curves correspond to different intensities ($I = 0$, 3.33 MW/cm^2, 106.67 MW/cm^2, and 0.81 GW/cm^2 respectively.

Equation (3.9) can be rewritten as

$$|x|^2 + (q+q^*)\,|x|^4\,|E_0|^2 + |q|^2\,|x|^6\,|E_0|^4 = |p|^2\,. \tag{3.12}$$

The above equation is a cubic equation for $|x|^2$ and can be easily calculated by numerical methods. Once $|x|^2$ is obtained, we can calculate the saturated complex field enhancement factor x by using Eq. (3.8). By solving the above equation, the dielectric function of metal nanoparticles is self-consistently obtained. The resultant intensity-dependent dielectric function of the composite ε_{eff} can the be calculated from Maxwell-Garnett equation (2.51).

For relatively low intensities, we obtain the following Taylor expansion of the effective dielectric function of the composite:

$$\varepsilon_{\text{eff}} = \varepsilon_h \frac{1+2f\sigma}{1-f\sigma} + f\chi_m^{(3)} r |E_0|^2 - f\chi_m^{(3)} r |x_0|^2 (2q+q^*) |E_0|^4 ..., \tag{3.13}$$

where $\sigma = 1 - x_0$ and $r = x_0^2 |x_0|^2$ (see Appendix B). The above equation predicts the emergence of a fifth-order nonlinearity and coincides with the result of the T-matrix method [104] and the generalized Maxwell-Garnett theory [23] [see Eq. (2.62)]. However, this Taylor expansion cannot be applied for intensities larger than 10 MW/cm^2 in the spectral range of the SPR, because the expansion diverges leading to a nonphysical transformation of loss into gain. Therefore, here we numerically solve the Eq. (3.8).

The total absorption $\alpha = 2k\text{Im}(n_{\text{eff}})$, the nonlinear refractive index $\Delta n = \text{Re}(\Delta n_{\text{eff}})$ and the absorption coefficient $\Delta\alpha = 2k\text{Im}(\Delta n_{\text{eff}})$ can be obtained from the above equations, where k is the wavenumber in free space and

$$\Delta n_{\text{eff}} = \sqrt{\varepsilon_{\text{eff}}(I)} - \sqrt{\varepsilon_{\text{eff}}(0)}$$

is the nonlinear change of effective refractive index of the composite.

In Fig. 3.9, we show the total loss (a), (b), the change of effective refractive index (c) and absorption (d), the effctive nonlinear index (e), saturation intensity and enhancement factor (f) in dependence on wavelength, light intensity and filling factor. The dielectric function and the third-order nonlinear optical susceptibility of silver and silica have been taken from [151] and [155]. The total loss presented in Fig. 3.9(a) shows a peak at the plasmon resonance and decreases with increasing intensity in the wavelength range from 412 to 520 nm. In Fig. 3.9(b) the total loss in dependence on the intensity for different filling factors at 430 nm is presented. It can be seen that with increasing intensity the loss decreases in a similar manner for all the filling factors, although the initial values of the loss differ by orders of magnitudes. The saturation intensity (defined as the intensity at which the linear loss is reduced by a factor of 2) is marked by the points in Fig. 3.9(b). At 430 nm, its value is about 100 MW/cm^2 for all filling factors. In Fig. 3.9(f) the saturation intensity (blue curve) and the field enhancement (red curve) are shown as a function of the wavelength. The saturation intensity of about 10 MW/cm^2 exhibits a minimum in the vicinity of the resonance, as expected intuitively and found in the previous experimental studies. At the same wavelength the field enhancement (red curve) shows a maximum. The nonlinear refractive index change Δn_{eff} and the nonlinear coefficient n_2 are presented in Fig. 3.9(c) and (d) and show a sign change from negative to positive around the SPR wavelength because of a phase difference between the field inside the NPs and the the external field due to the complex-valued character of the field enhancement factor [156]. For larger intensities the nonlinear contribution to the refractive index saturates, which can be seen from its reduced values in Fig. 3.9(c).

Note that for large intensities in the range of GW/cm^2 depending on the pump wavelength, the validity of the above described model is limited due to the empirically found observation that the dielectric function of metals cannot change by much more than unity.

3.4. Saturable nonlinearity in composites doped with NPs of arbitrary sizes and shapes: A modified discrete dipole approximation

In this section, we study the case of spherical NPs larger than about 10 nm and nonspherical metal NPs in the self-consistent formalism. We again use the discrete-dipole approximation (DDA) [58, 59] for the study of absorption saturation due to the intensity-dependent nonlinearity of composites doped with metal NPs with different sizes and shapes.

The difference from the conventional method is that we take polarizability of divided small dipole exchanged by the self-consistently obtained one considering the change of dielectric function of metal governed by Eqs. (3.8). For convenience, we write the local field in a way different from Eq. (2.26) [63]:

$$\mathbf{E}_j = \mathbf{E}_{0j} - \sum_{j\neq k} \frac{e^{i\beta r_{jk}}}{r_{jk}^3} \left\{ \beta^2 \mathbf{r}_{jk} \times \left(\mathbf{r}_{jk} \times \mathbf{P}_k\right) + \frac{1 - i\beta r_{jk}}{r_{jk}^2} \left[r_{jk}^2 \mathbf{P}_k - 3\mathbf{r}_{jk} \left(\mathbf{r}_{jk} \cdot \mathbf{P}_k\right) \right] \right\}, \quad (3.14)$$

where $\mathbf{E}_j$ and $\mathbf{E}_{0j}$ are local and incident fields at the position of the j-th small dipole, respectively, β is the propagation constant in the surrounding medium, and $\mathbf{P}_k = \alpha_k \mathbf{E}_k$, where

$$\alpha_k = \frac{3v_k}{4\pi} (1 - x_k), \quad (3.15)$$

v_k and x_k are the volume and the time-dependent enhancement factor for k-th dipole.

In the above equation dipole polarizabilities α_k are exchanged by the self-consistently corrected values of the k-th small nanospheres constructing the whole particle. The equation is no longer a linear matrix equation which should be solved by using nonlinear optimization method. Here we adopt nonlinear conjugate gradient method. In this method, we have to replace the residual in each step of optimization by the steepest descent direction.

We can write the evaluation function

$$\mathscr{E} = \sum_j \left| \sum_k \left(\delta_{jk} + \mathbf{G}_{jk}\alpha_k\right) \mathbf{E}_k - \mathbf{E}_{0j} \right|^2, \quad (3.16)$$

where δ_{lj} is Kronecker delta-symbol. In our case, the steepest descent direction is given by $-\partial\mathscr{E}/\partial\mathbf{E}_l^*$ because the field $\mathbf{E}_l$ is a complex function. To calculate the derivative for local field $\mathbf{E}_l$, we apply the definition of the complex derivative [157, 158]

$$\frac{\partial}{\partial z} = \frac{1}{2}\left(\frac{\partial}{\partial x} - i\frac{\partial}{\partial y}\right), \quad (3.17)$$

$$\frac{\partial}{\partial z^*} = \frac{1}{2}\left(\frac{\partial}{\partial x} + i\frac{\partial}{\partial y}\right), \quad (3.18)$$

where $z = x + iy$. The first partial derivative of the evaluation function to the field can be written by

$$\frac{\partial \mathscr{E}}{\partial \mathbf{E}_l^*} = \sum_j \left(\delta_{lj} + \mathbf{G}_{lj}^* \alpha_l^*\right) \left[\sum_k \left(\delta_{jk} + \mathbf{G}_{jk}\alpha_k\right)\mathbf{E}_k - \mathbf{E}_{0j}\right] +$$

$$+\sum_j \mathbf{G}_{lj}^* \frac{\partial \alpha_l^*}{\partial \mathbf{E}_l^*}\mathbf{E}_l^* \left[\sum_k \left(\delta_{jk} + \mathbf{G}_{jk}\alpha_k\right)\mathbf{E}_k - \mathbf{E}_{0j}\right] + \sum_j \mathbf{G}_{lj} \frac{\partial \alpha_l}{\partial \mathbf{E}_l^*}\mathbf{E}_l \left[\sum_k \left(\delta_{jk} + \mathbf{G}_{jk}\alpha_k\right)\mathbf{E}_k - \mathbf{E}_{0j}\right]^*. \tag{3.19}$$

The first term on the right hand of the above equation is the same as the residual for the linear case (see Appendix A).

Now let us calculate $\partial \alpha_l / \partial \mathbf{E}_l$. From Eqs. (3.9, 3.15, 3.17, 3.18), we obtain

$$\frac{\partial x_l}{\partial \mathbf{E}_l^*} = -r x_l^2 \left(\frac{\partial |x_l|^2}{\partial \mathbf{E}_l^*} |\mathbf{E}_l|^2 + |x_l|^2 \mathbf{E}_l\right), \tag{3.20}$$

$$\frac{\partial x_l^*}{\partial \mathbf{E}_l^*} = -r^* x_l^{*^2} \left(\frac{\partial |x_l|^2}{\partial \mathbf{E}_l^*} |\mathbf{E}_l|^2 + |x_l|^2 \mathbf{E}_l\right), \tag{3.21}$$

where $r = \chi_m^{(3)} / (3\varepsilon_h)$. Therefore,

$$\frac{\partial |x_l|^2}{\partial \mathbf{E}_l^*} = -2\mathrm{Re}\left(r x_l\right) |x_l|^2 \left(\frac{\partial |x_l|^2}{\partial \mathbf{E}_l^*} |\mathbf{E}_l|^2 + |x_l|^2 \mathbf{E}_l\right). \tag{3.22}$$

From the above equation, we obtain

$$\frac{\partial |x_l|^2}{\partial \mathbf{E}_l^*} = \frac{-2\mathrm{Re}\left(r x_l\right) |x_l|^4 \mathbf{E}_l}{1 + 2\mathrm{Re}\left(r x_l\right) |x_l|^2 |\mathbf{E}_l|^2}. \tag{3.23}$$

Substituting the above equation into Eq. (3.20),

$$\frac{\partial x_l}{\partial \mathbf{E}_l^*} = \frac{-r x_l^2 |x_l|^2 \mathbf{E}_l}{1 + 2\mathrm{Re}\left(r x_l\right) |x_l|^2 |\mathbf{E}_l|^2}. \tag{3.24}$$

Considering Eq. (3.15), we obtain

$$\frac{\partial \alpha_l}{\partial \mathbf{E}_l^*} = \frac{3\nu_l}{4\pi} \frac{r x_l^2 |x_l|^2 \mathbf{E}_l}{1 + 2\mathrm{Re}\left(r x_l\right) |x_l|^2 |\mathbf{E}_l|^2}, \tag{3.25}$$

$$\frac{\partial \alpha_l^*}{\partial \mathbf{E}_l^*} = \frac{3\nu_l}{4\pi} \frac{r^* x_l^{*^2} |x_l|^2 \mathbf{E}_l}{1 + 2\mathrm{Re}\left(r x_l\right) |x_l|^2 |\mathbf{E}_l|^2}, \tag{3.26}$$

By using the derivatives Eq. (3.25,3.26) under the self-consistency condition Eq. (3.9), we apply the standard nonlinear conjugate gradient method [159].

In Fig. 3.10 the total loss (a), the nonlinear refraction index (b) and the nonlinear change of the refraction (c) and loss (d) are shown in dependence on the wavelength for a NP diameter of 40 nm.

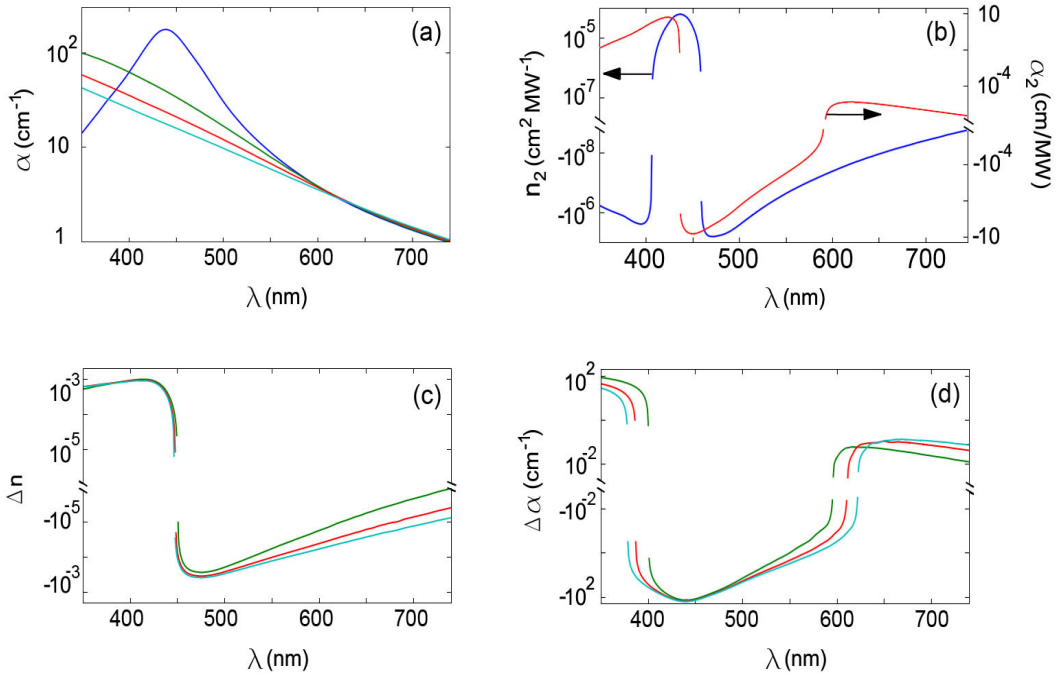

Figure 3.10.: Nonlinearity and absorption saturation of silica glass doped with Ag nanospheres. Absorption coefficient (a) and its nonlinear change (d), nonlinear change of the refractive index (c), nonlinear refractive index and the absorption saturation coefficient (b). In (a), (c) and (d), blue, green, red, and cyan curves correspond to $I = 0$, $I = 0.5$ GW/cm^2, $I = 2$ GW/cm^2, and $I = 4.5$ GW/cm^2, respectively.

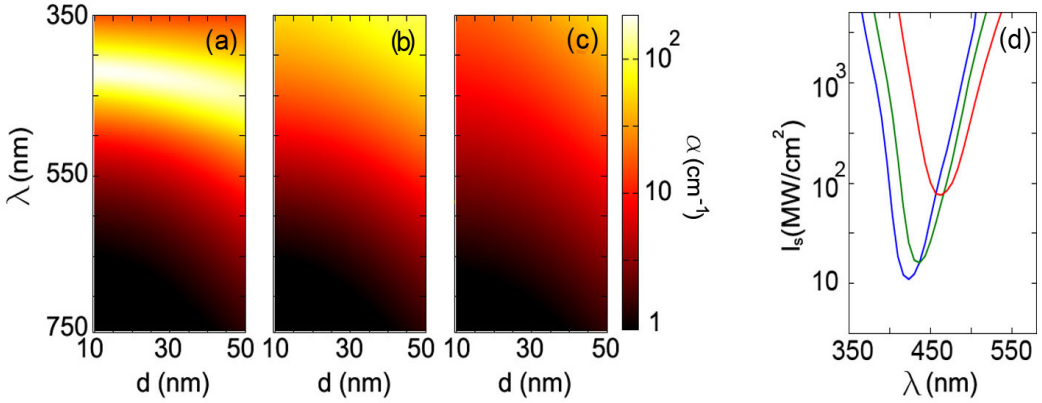

Figure 3.11.: Intensity-dependent absorption coefficient (a-c) and saturation intensity (d) depending on the particle size. In (a), (b), and (c) total loss is shown for intensities $I = 0$ (a), $I = 0.5$ GW/cm^2 (b), and $I = 2$ GW/cm^2 (c). In (d), saturation intensity is shown for different Ag particle diameters (blue: 10 nm, red: 30 nm, and magenta: 50 nm).

In Fig. 3.11(a) the maximum of the total loss (e.g. the plasmon resonance) is shifted to larger frequencies with increasing NP diameter and its dependence on intensity also differs for different particle sizes [Fig. 3.11(b) and (c)]. The smallest saturation intensity for a diameter of 10 nm is about 10 MW/cm^2. The saturation intensity, shown in Fig. 3.11(d), exhibits a sensitive dependence on the particle diameter and differs by more than one order of magnitude for a diameter of 50 nm. The behavior of these characteristics is very similar to the case of the Maxwell-Garnett approach (valid for very small NP diameter) as illustrated in Fig. 3.9.

In Fig. 3.12 we consider as an example for nonspherical metal NPs a composite containing silver nanorods with a diameter of 30 nm and a length of 48 nm. In this nanostructure three plasmon modes are excited for our conditions. In Fig. 3.12(a), the main peak for low intensities arising from the longitudinal dipole resonance is located at 602 nm while the other two peaks at shorter wavelengths are related with a quadrupole and transverse dipole mode. For low intensities, the absorption coefficient exhibits relatively sharp peaks, while

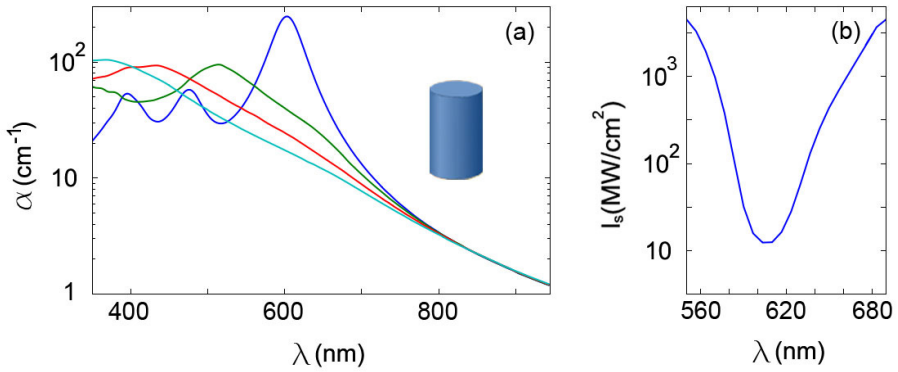

Figure 3.12.: Wavelength dependence of absorption coefficient (a) and of saturation intensity (b) of silica glass doped with Ag nanorods with the height of 48 nm and diameter of 30 nm. In (a), blue, green, red, and cyan curves correspond to $I = 0$, $I = 0.5$ GW/cm^2, $I = 2$ GW/cm^2, and $I = 4.5$ GW/cm^2 respectively.

it is smoothed and lowered with increasing intensity of the incident light. Because the quadrupole and transverse dipole SPR peaks are much weaker than that of the longitudinal dipole SPR, the saturation effect for those wavelengths is small, and at larger intensities absorption saturation is dominated by the longitudinal plasmonic dipole resonance. Figure 3.12(b) shows that the minimum saturation intensity at 615 nm is about 12 MW/cm^2 which is in the same range as for very small spherical NP in Fig. 3.9 or Fig. 3.11 for NPs with larger diameters.

For an intuitive understanding, we show the spatial field enhancement distribution for different intensities in Fig. 3.13 [for very low intensity (a) and for an intensity of 100 MW/cm^2 (b)]. The enhancement factors decrease with increasing intensity, leading to the saturation of the loss.

To conclude, in this chapter we have studied the nonlinear optical characteristics of the composites doped with metal NPs having different shapes and sizes. The results show that the effective nonlinear susceptibility of metal nanocomposites is significantly enhanced

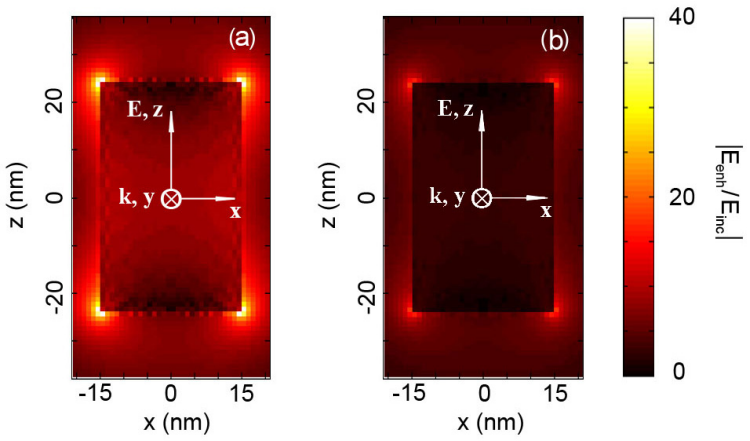

Figure 3.13.: Enhanced field distributions for the intensities of incident light of 0 (a) and 100 MW/cm^2 (b) in Ag nanorods with the height of 48 nm and diameter of 30 nm, contained in silica glass. The polarization of incident light is parallel to the axis of nanorod.

near the SPR and it can be tuned by changing the shapes and sizes of the metal NPs contained in the composites. Most importantly, we have shown the saturation of loss and the light-induced change of the refractive index in fused silica doped with silver nanoparticles. We used a self-consistent formalism in which saturation is included by the intensity-dependent intrinsic dielectric function of the metal NPs both within the frame of the generalized Maxwell-Garnet approach and a generalized discrete-dipole formalism for NPs with arbitrary shape. The numerical results show that the total absorption coefficient exhibits a strong saturation behavior near the plasmon resonance. For spherical silver NPs with a diameter smaller than 20 nm the composite acts as a saturable absorber at 400 nm with a saturation intensity of about 10 MW/cm^2. Increasing the NP diameter leads to a small shift of the plasmon resonance and a larger increase of the saturation intensity. The wavelength range of saturated absorption can be significantly shifted over the visible to infrared spectral region by using metal NPs with nonspherical shapes. As an example we studied a composite containing silver nanorods and predicted saturable absorption at 600 nm with a saturation intensity of 12 MW/cm^2. We also studied the light-induced changes of the refraction index and the field enhancement factor in the above given examples and predicted that both the nonlinear refraction index and the field enhancement factor decreases with increasing intensity.

Possible prospective applications could be passive mode locking of lasers. Over the past three decades remarkable progress has been achieved in the generation of extremely short pulses [160, 161]. Most femtosecond lasers involve a saturable absorber for passive mode-locking or the Kerr-lens mechanism. Commonly applied saturable absorbers for passive mode-locking are semiconductor multi-quantum wells [139], semiconductor quantum dots [137, 138]. Recently carbon nanotube mode-locking saturable absorbers (see e.g. [162, 163]) or graphene-based absorbers (see e.g. [164]) have gained much attention. However, these types of saturable absorbers can be used mainly for mode-locking of lasers in the spectral region above 700 nm. At least to our knowledge, in the short-wavelength

range below 700 nm attractive saturable absorbers are still missing. As an example saturable absorbers for mode locking of high-power diode lasers, solid state lasers and fiber lasers in the spectral range of 400 nm are of high interest. Composites doped with metal NPs could enable the fabrication of new types of such broadband elements with ultrafast response time. In order to realize a small linear loss, a thin layer of metal nanoparticles with small filling factors can be deposited on the surface of an appropriate substrate material both in reflection or transmission geometries yielding saturable absorbers with small modulation depth with a saturation intensity in the range of or larger than 10 MW/cm^2. Another advantage of these materials over the another saturable absorbers is their cost-effectiveness. For instance, SESAMs require the expensive epitaxial equipments. In contrast, metal NPs can be manufactured by the chemical synthesis with low cost.

4. Femtosecond transient response of metal nanocomposites for passive mode-locking of lasers

Metal nanocomposites have a relatively fast recovery time in the range of few picoseconds (see Section 2.2 and references therein). The only experimental result on the application of metal nanocomposite for mode-locking of solid-state lasers has been reported [165] and the resultant pulse duration was 5 ps. This pulse duration is much longer than the absorption recovery time of these materials. We can deduce that in this experiment IR light from Nd:glass laser is far from the SPR of metal nanocolloids and the modulation depth is very small. As we have discussed in the preceding chapter, these materials show saturable absorption most notably in the blue-visible spectral range.

Recently, visible solid state lasers [166–168] and semiconductor disk lasers [169, 170] have attracted much attention. For the mode-locking of these lasers metal nanocomposite materials are the best candidate because of their cost-effectiveness and good performance of saturable absorption.

In this chapter, we demonstrate the mode-locking of solid state lasers and semiconductor lasers with metal nanocomposites as slow saturable absorbers. To tune the SPR to the central lasing wavelength range and utilize the strong saturable absorption, we can change the host medium or tailor the sizes and shapes of metal nanoparticles (NPs). From the semiclassical two-temperature model, we obtain a direct relation of the incident pulse and the transient dielectric function of the metal. By using this approach, we can calculate the optical response of the composite materials doped with metal NPs with different sizes and shapes. Applying this methodology to the master equation for mode-locking, we study the mode-locking behavior of lasers. For this purpose, we first obtain a simplified equation for the transient nonlinear optical response of metal NPs based on the two-temperature model.

4.1. Semiclassical two-temperature model for weak pump pulse excitation

Passively mode-locked operation of lasers involves a complicated transient interaction of gain and absorber media with coherent light pulses. Therefore, we must have a direct relationship between light pulse and saturable absorber.

We begin with semiclassical two-temperature model (TTM). Subtracting Eq. (2.69) divided by C_e from Eq. (2.70) divided by C_L, we obtain

$$\frac{\partial (T_e - T_L)}{\partial t} = -G \left(\frac{1}{C_e} + \frac{1}{C_L} \right) (T_e - T_L) + \left(\frac{1}{C_e \tau_{ee}} - \frac{1}{C_L \tau_{ep}} \right) N. \tag{4.1}$$

Introducing the cooling time

$$\tau_{ep} = \frac{C_e C_L}{G(C_e + C_L)} \tag{4.2}$$

and considering that the increase of lattice temperature can be neglected compared to that of electrons and $T_e - T_L \approx T_e - T_0$, we obtain

$$\frac{\partial (T_e - T_0)}{\partial t} = -\frac{T_e - T_0}{\tau_{ep}} + \left(\frac{1}{C_e \tau_{ee}} - \frac{1}{C_L \tau_{ep}}\right) N. \tag{4.3}$$

On the other hand, integrating the equation (2.68) we have

$$N = \delta \int_{-\infty}^{t} P(t') \exp\left(-\frac{t - t'}{\tau'_{ee}}\right) dt', \tag{4.4}$$

where

$$\frac{1}{\tau'_{ee}} = \frac{1}{\tau_{ee}} + \frac{1}{\tau_{ep}}. \tag{4.5}$$

Combining Eqs. (4.3, 4.4), we obtain

$$\frac{\partial (T_e - T_0)}{\partial t} = -\frac{T_e - T_0}{\tau_{ep}} + \delta \left(\frac{1}{C_e \tau_{ee}} - \frac{1}{C_L \tau_{ep}}\right) \int_{-\infty}^{t} P(t') \exp\left(-\frac{t - t'}{\tau'_{ee}}\right) dt', \tag{4.6}$$

where T_0 is the initial temperatures of electrons and lattice.

From Eq. (2.67),

$$\frac{\partial \Delta \varepsilon_m}{\partial t} = \eta \frac{\partial (T_e - T_0)}{\partial t}, \tag{4.7}$$

By using Eqs. (4.6, 4.7), we can write

$$\frac{\partial \varepsilon_m}{\partial t} = -\frac{\varepsilon_m - \varepsilon_{m0}}{\tau_{ep}} + \delta' \left(\frac{1}{C_e \tau_{ee}} - \frac{1}{C_L \tau_{ep}}\right) \int_{-\infty}^{t} P(t') \exp\left(-\frac{t - t'}{\tau'_{ee}}\right) dt', \tag{4.8}$$

where ε_m is the dielectric function of metal as a function of time and incident intensity, and $\delta' = \delta \eta$. The absorbed energy density $P(t)$ must be proportional to the enhanced intensity in the metal NPs and, therefore,

$$\frac{\partial \varepsilon_m}{\partial t} = -\frac{\varepsilon_m - \varepsilon_{m0}}{\tau_{ep}} + \frac{\beta}{\tau_{ee}} \int_{-\infty}^{t} \left| x(t') E(t') \right|^2 \exp\left(-\frac{t - t'}{\tau'_{ee}}\right) dt', \tag{4.9}$$

where β is a constant proportional to $\delta' \left[C_e^{-1} - C_L^{-1} (\tau_{ee}/\tau_{ep})\right]$, $x(t)$ is the transient field enhancement factor and $E(t)$ is the incident field. To determine the constant β, we consider the steady state nonlinear response from Eq. (4.9). For a constant incident field intensity E_0, Eq. (4.9) gives

$$\varepsilon_{m,\text{static}} = \varepsilon_{m0} + \beta \tau_{ep} |x|^2 |E|^2. \tag{4.10}$$

From the above equation, we have

$$\beta = \chi_m^{(3)} / \tau_{ep}, \tag{4.11}$$

where $\chi_m^{(3)}$ is the inherent degenerate third-order susceptibility of the metal. Substituting Eq. (4.11) into Eq. (4.9), we obtain

$$\frac{\partial \varepsilon_m}{\partial t} = -\frac{\varepsilon_m - \varepsilon_{m0}}{\tau_{ep}} + \frac{\chi_m^{(3)}}{\tau_{ee}\tau_{ep}} \int_{-\infty}^{t} \left| x\left(t'\right) E\left(t'\right) \right|^2 \exp\left(-\frac{t-t'}{\tau_{ee}}\right) dt'. \tag{4.12}$$

Considering that the pure e-e scattering time τ_{ee} (typically around 100 fs) is much shorter than τ_{ep} (typically around or longer than 1 ps), in Eq. (4.12) we have replaced $\tau_{ee}^{'}$ with τ_{ee}.

Expression (4.12) is the main relation for all the studies of the transient nonlinear processes in the composites doped with metal NPs presented here. It has two advantages over the semiclassical TTM: It provides a direct relation between the incident pulse and $\varepsilon_m(t)$. The original semiclassical TTM does not consider the saturation effect for the absorbed energy of the incident pulse. In contrast, our model takes into account also this effect through $x(t)$.

4.2. Transient response of metal nanocomposites

In Eq. (4.12) the field enhancement factor is given by the dielectric response originating from the nanoscale nature of the particles. For very small spherical NPs, the time-dependent enhancement factor x can be calculated by $x(t) = 3\varepsilon_h / [\varepsilon(t) + 2\varepsilon_h]$. Here we consider pulses of a duration longer than ~ 30 fs, which is much longer than the dephasing time of plasmons (few femtoseconds). For few femtoseconds pulses, we cannot simply use this relation and we have to additionally consider the dispersion of dielectric function of metal. Equation (4.12) must be solved self-consistently. By using Eq. (4.12) and the equation for the time-dependent field enhancement, we can calculate the effective dielectric function by using the Maxwell-Garnett formula (2.51).

Fig. 4.1 shows an example of the transient nonlinear transmission response of the metal nanocomposites. The figure depicts $\Delta T(t)/T$ of a 0.2-μm-thick Al_2O_3 film doped with Ag NPs with diameter of 6.5 nm and a filling factor of 1 %. The duration of pump and probe pulses is 30 fs and their central wavelengths are 800 nm. The pump fluence is taken to be 100 μJ/cm^2. For the best fit with the experimental data, we take the e-e and cooling times to be $\tau_{ee} = 100$ fs and $\tau_{ep} = 0.70$ ps. Both the examples of theoretical predictions are in the excellent agreement with the preceding experimental results [171]. Although the pump pulse duration is sub-100 fs, the transmittance responds slower due to the delayed thermalization of electrons. In both cases, the time reaching to the maximum change in the transmittance is around 200 -250 fs longer than the e-e scattering time τ_{ee}. The exponential change of the transmittance depends on the cooling time τ_{ep} and also the pump fluence. In this work we approximate the two time scales by $\tau_{ee} = 100$ fs and $\tau_{ep} = 1$ ps.

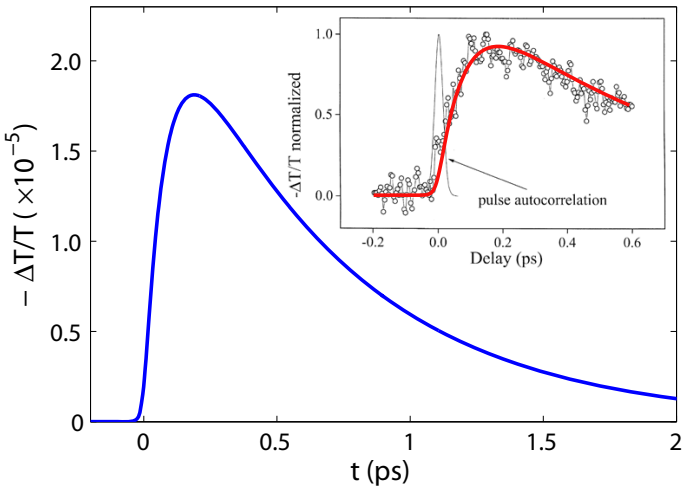

Figure 4.1.: The transient nonlinear absorption response of metal nanocomposites in the alumina film containing Ag NPs with filling factor of 1% and of the particles diameter of 6.5 nm. Pump and probe have the same central wavelength of 800 nm and pulse duration of 30 fs. The thickness of the composite film is 0.25 μm. In the inset, the experimental (black line, taken from Ref. [171]) and the theoretical (red line) results are compared with excellent agreement.

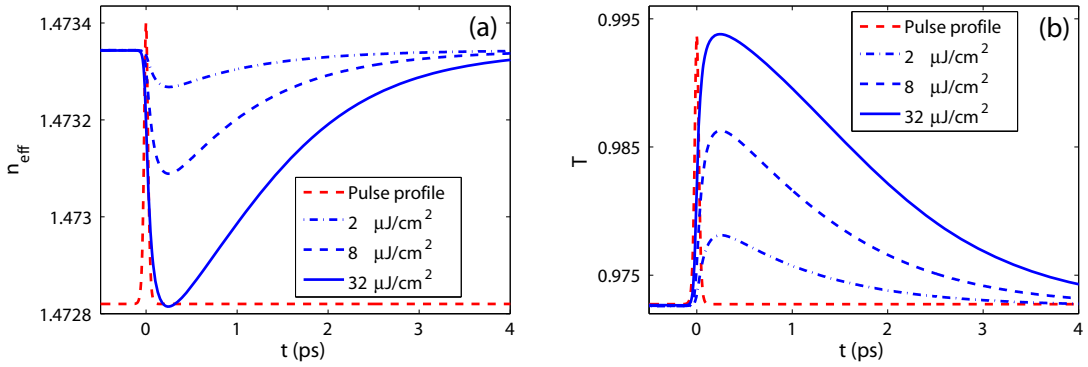

Figure 4.2.: Refractive index and transmittance of silica glass doped with Ag NPs smaller than 10 nm for different fluences of 50 fs pulses at 430 nm. Filling factor is 10^{-4} and thickness is 1 μm. The red-dashed lines in both figures show the temporal profile of pump pulse.

In Fig. 4.2 we show the dependence of the effective refractive index (a) and transmittance (b) of 1-μm-thick silica glass layer doped with very small Ag nanospheres at 430 nm. The effective index shows a different behavior. In Fig. 4.2 one can see that the relaxation of the transmittance is slower for the stronger fluence of incident light even for the fixed value of inherent cooling time for the silver as large as 1 ps.

The dependence of temporal response of metal NPs with different sizes and shapes can be considered by using the discrete dipole approximation (DDA) in combination with Eq. (4.12) for the transient nonlinear response of metal. The inherent transient dielectric function of the metal at each position split to very small element dipoles (metal NPs) can be calculated by Eq. (4.12) and the resulting local fields by using the DDA equation (2.26). The time-dependent enhancement factor x_k for k-th dipole is calculated by

$$x_k(t) = \frac{3\varepsilon_h}{\varepsilon_{mk}(t) + 2\varepsilon_h} \tag{4.13}$$

This process is iterated in the time domain. By using the effective-medium approximation, the obtained transient local field distribution and the field enhancement factor, we can calculate the resultant total response of the composites such as transient refractive index and absorption coefficient.

The composites doped with metal NPs show a similar or faster recovery compared with quantum dots, SESAMs and carbon nanotubes. This recovery time scale of a few picoseconds is suitable for the compact laser resonator for mode-locking because the stable mode-locking requires absorbers with recovery times much shorter than the pulse traveling time. The main characteristic difference from quantum dots and other semiconductor saturable absorbers is that the forefront rising time determined by the e-e scattering time is longer (200 - 400 fs).

The advantage of metal nanocomposites is that the SPR wavelength range and, therefore, saturable absorption range can easily be changed in a wide wavelength range from near UV to IR by changing the host medium, the particles sizes and shapes while the other absorbers have a restricted spectral range, generally in the IR range. In the following sections, we present the theoretical results for the passive mode-locking behaviors of solid-state lasers with metal nanocomposite absorbers. Before that, we briefly review the basic principles of passive mode-locking of lasers with saturable absorbers.

4.3. Passive mode-locking: basic principle

In this section, we briefly introduce the basic principle and the theory of passive mode-locking.

First of all, let us consider the electromagnetic field in the laser resonator. Resonator mode frequencies are determined by

$$\Omega_n = n\frac{\pi c}{L}, \tag{4.14}$$

where n is an arbitrary positive integer and L is the resonator length. The most general solution for the intracavity field is written by a superposition of mode fields

$$E(z,t) = \mathrm{Re}\left\{\sum_{n=0}^{\infty} \hat{E}_n \exp\left[i\left(\Omega_n t - K_n z\right)\right]\right\}, \tag{4.15}$$

where $K_n = n\pi/L$ and $\hat{E}_n$ are the wavenumber and the electric field of n-th mode, respec-

tively. We limit ourselves to the consideration of cases of many longitudinal modes in the laser resonator, which is the precondition for mode-locking. In this case, we can write the resonator field as a continuum:

$$E(z,t) = \frac{1}{2\pi}\int_0^\infty \hat{E}(K)\exp\{i[\Omega(K)t - Kz]\}\,dK, \tag{4.16}$$

with $\hat{E}(K) = 2L\hat{E}_n$. Now we introduce the slowly varying envelope of the pulse and the frequency and wavenumber with respect to the central frequency Ω_{n0} and wavenumber K_{n0} :

$$k = K - K_{n0},$$
$$\omega(k) = \Omega(K_{n0}+k) - \Omega_{n0},$$
$$\hat{E}(k) = \hat{E}(K_{n0}+k).$$

We introduce the wave amplitude $A(z,t)$ which is normalized to the total power of the laser beam and is written by

$$A(z,t) = \frac{1}{2\pi}\sqrt{\frac{A_{\text{eff}}}{2Z_0}}\int_0^\infty \hat{E}(k)\exp\{i[\omega(k)t - kz]\}\,dk, \tag{4.17}$$

where A_{eff} is the effective beam cross-section and Z_0 the characteristic impedance of the cavity medium. The amplitude is related with field by

$$E(z,t) = \sqrt{2Z_0/A_{\text{eff}}}A(z,t)\exp[i(\Omega_{n0}t - K_{n0}z)].$$

Let us introduce a new time variable $T = t$ and a time in a coordinate moving with the pulse

$$t' = t - \frac{z}{v_g}, \tag{4.18}$$

where v_g is group velocity given by

$$v_g = \left.\frac{\partial\omega}{\partial k}\right|_{k=0}. \tag{4.19}$$

Rewriting Eq. (4.17), we obtain

$$A(T,t') = \frac{1}{2\pi}\sqrt{\frac{A_{\text{eff}}}{2Z_0}}\int_0^\infty \hat{E}(k)\exp\left\{i\left[(\omega(k) - v_g k)T + kv_g t'\right]\right\}dk. \tag{4.20}$$

or

$$T_R\left.\frac{\partial A}{\partial T}\right|_{GDD} = i\sum_{n=2}^{\infty} D_n\left(i\frac{\partial}{\partial t'}\right)^n A \tag{4.21}$$

with the dispersion coefficients per resonator round trip $T_R = 2L/v_g$

$$D_n = -\frac{2L}{n!v_g^{n+1}}\left.\frac{\partial^{n-1}v_g(k)}{\partial k^{n-1}}\right|_{k=0}. \tag{4.22}$$

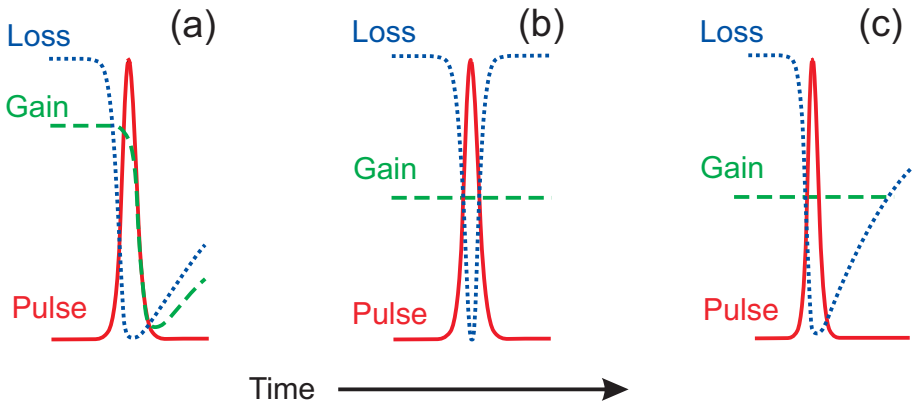

Figure 4.3.: Different passive mode-locking mechanisms: (a) slow absorber mode-locking with dynamic gain saturation, (b) fast absorber mode-locking, and (c) slow absorber mode-locking without dynamic gain saturation.

Below, we replace t' by t and remember that this is a variable for moving time scale. So far we modeled only the passive resonator. The loss can be modeled by

$$T_R \left.\frac{\partial A}{\partial T}\right|_{loss} = -lA \tag{4.23}$$

The gain can be described by

$$T_R \left.\frac{\partial A}{\partial T}\right|_{gain} = \left[g + D_g \frac{\partial^2}{\partial t^2}\right] A, \tag{4.24}$$

where g is gain and D_g is the gain dispersion given by

$$D_g = \frac{g}{\Omega_g^2} \tag{4.25}$$

and Ω_g is the gain bandwidth (HWHM) for Lorentzian gain spectral shape. Taking into account also the nonlinear terms such as saturable absorption $q(T,t)$, self-phase modulation (SPM), we can write the following master equation for mode-locking [172]

$$T_R \frac{\partial A}{\partial T} = \left\{ \left[g\left(1 + \frac{1}{\Omega_g^2}\frac{\partial^2}{\partial t^2}\right) - q - l \right] + i \sum_{n=2}^{\infty} D_n \left(i\frac{\partial}{\partial t}\right)^n - i\gamma|A|^2 \right\} A, \tag{4.26}$$

where γ is the SPM coefficient.

The above equation describes the field evolution in the laser resonator with optical elements such as saturable absorber or modulator, etc. The resonator modes have the comb-shaped spectral distribution. If these longitudinal modes have random phases, the resultant field has the complicated temporal shape. In contrast, if they have the same phases, they constructively interfere resulting in very short pulses. The pulse duration is an inverse of the total spectral width of lasing modes and the repetition rate is determined by round trip

time of pulses in the resonator.

Let us imagine that an amplitude modulator is located in the resonator and consider a longitudinal mode. This resonator is assumed to have modulation frequency exactly the same as mode spacings given by $c/2L$, where L is the resonator length. This mode generates the sidebands, the frequency offsets of which from the original mode is the same as the mode spacing, after passing through the modulator. Therefore, these sidebands have the same frequencies as that of adjacent longitudinal modes. Simultaneously, all the other modes also generate the sidebands of their own. In this way, the modulator transfers the energy of each mode to its neighboring mode and make the uniform phase distribution over all the spectral width of light field in the resonator. Correspondingly, the pulse duration is significantly shortened depending on the mode number determined by the total spectral width. The mode-locking by the action of active elements, like electro-optic modulator, is called active mode-locking. Active mode-locking can also be realized by phase modulation, and importantly synchronous pumping. The latter can be considered by gain modulation.

Mode-locking can also be realized by using saturable absorbers. In this case, saturable absorbers play the role of the modulator but the modulation is spontaneously performed unlike the active mode-locking and the mode-locking by passive elements, like saturable absorbers, are called passive-mode locking.

The passive mode-locking dynamics can be easily understood in the time domain. Passive mode-locking is categorized by three mechanisms: slow absorber mode-locking with dynamic gain saturation, fast absorber mode-locking, and slow absorber mode-locking without dynamic gain saturation (see Fig. 4.3).

Slow-absorber mode-locking with dynamic gain saturation [Fig. 4.3(a)] is typical for dye [140, 141, 173–176] and semiconductor lasers [177–182] which have gain media with a strong gain. In these gain media, the gain coefficients are so large that they are prominently saturated during one round trip of the pulses in the resonators. The precondition for the mode-locking based on this mechanism is that the saturable absorber has to be more easily saturated than the gain producing the net gain window during the pulse. Moreover, the gain medium has to have a recovery time longer than that of absorber. For self-starting operation, the initial net gain has to be positive. This mechanism is responsible for the ultrafast pulse generation in passively mode-locked dye lasers which was the first type of femtosecond pulse lasers ever developed. Due to the limited lifetime of dyes for the gain and saturable absorber and the small output power, these lasers are not widely applied nowadays. Recently, with the development of semiconductor optoelectronics, mode-locked compact semiconductor diode and disk lasers are widely investigated and they are expected to be industrialized in the near future. In particular, semiconductor disk lasers can provide high power ultrashort pulses because they have large area for pumping and lasing compared with diode lasers. Femtosecond pulse generation by passive mode-locking of optically pumped semiconductor disk lasers has been demonstrated both theoretically [179] and experimentally [177, 180–184]. Wide bandgap semiconductors are suitable for lasing in the visible or near UV range [169, 170].

Fast absorber mode-locking [Fig. 4.3(b)] is typical for solid-state lasers [185–187]. Generally, solid-state gain media have very small gain coefficient and long recovery time, so that the gain is not saturated during one round trip. For this reason, these materials does not exhibit the dynamic gain saturation behavior and pulse shaping happens only during

the net gain window where the absorber is strongly saturated. Therefore, the absorber has to simultaneously respond to the light pulse and the term fast absorber mode-locking originates from this fact. In general, the saturable absorbers cannot respond in a time range shorter than few or tens of femtoseconds and, based on this this mechanism, only picosecond pulses can be generated with real absorbers. Instead, the so-called Kerr-lens mode-locking (KLM) technology has been developed for the fast absorber mode-locked femtosecond lasers. This does not require real saturable absorbers but utilizes the passive modulation of gain through the Kerr-effect in the gain medium. The light beam with Gaussian transverse profile passing through the transparent medium with positive Kerr nonlinearity (third-order nonlinearity), exhibits self-focusing. By this phenomenon, the effective amplifying volume increases with the increase of pulse intensity and decreases with the decrease of pulse intensity. In case of hard aperture KLM, the Kerr lens reduces the optical losses at an aperture which the beam must pass in each resonator round trip and, in case of soft aperture KLM, the Kerr lens leads to a better overlap of laser and pump beam, and thus to a higher gain for the peak of the pulse [188]. This is identical to the effect of saturable absorber, even though there is not any real absorber, and is called artificial saturable absorber. In most cases, the gain media act as the Kerr-media at the same time. This nonlinear phenomenon is mostly caused far from the optically resonance and, therefore, the corresponding response is very fast, less than few femtoseconds making it suitable for the direct generation of femtosecond pulses from solid-state lasers. The disadvantage is that a long-term stable operation is difficult to achieve and the resonator design is a difficult task [188]. In addition, for the self-starting mode-locking, other measures have to be taken: synchronous oscillating end-mirror, addition of the saturable absorbers and saturable Bragg reflectors, etc.

The study on the slow-absorber mode-locking without dynamic gain saturation [Fig. 4.3(c)] has been started in the middle of 1990s. In the solid-state lasers with saturable absorbers, the net gain window has strongly asymmetric shape if the gain and absorbing media once illuminated by a femtosecond pulse circulating in the resonator. The intuition says that this will not provide any chance to shape femtosecond pulses. Nevertheless, there are still ways for pulse shaping with a duration much shorter than the absorber recovery time.

The first one is the soliton stabilization by the saturable absorber [189–191]. If the pulse energy, Kerr-nonlinearity and resonator dispersion satisfy a certain condition [190], a soliton can be generated. After several trips, the pulse can be split into the several sequent pulses or spread. However, by the existence of the saturable absorber the pulse is stabilized in the location near the very descent part of absorption if the gain and absorption is balanced so that the energy of the pulse is conserved. The theoretical limit of the achievable shortest duration, is up to 15-20 times shorter than the absorber recovery time [190]. For instance, by using an absorber with recovery time of around 1 ps, we can obtain, in principle, a pulse with a duration of about 50 fs.

The other mechanism [192, 193] responsible for passive mode-locking of solid state lasers with real absorbers still has not been clearly explained. The pulse shortening is realized by the attenuation of the leading part of the pulse in each step of travel [192–194] and the achievable pulse duration is typically in the picosecond range. However, the mechanism for the pulse stabilization in this mechanism has to be explicitly clarified. The possible shortest pulse duration was in the picosecond range.

4.4. Passive mode-locking of solid state lasers with metal nanocomposites

In the first part of this section, we present the general passive mode-locked operation taking Ho:YLF laser pumped with a diode laser as an example. Next, we study the mechanism responsible for the pulse stabilization in the non-soliton regime. In the end of the section, we show the detailed dependenceis of pulse duration and energy on the filling factor, beam are on the metal nanocomposite saturable absorber, cavity dispersion, etc.

4.4.1. Femtosecond pulse generation by slow-absorber mode-locking of solid state laser with metal nanocomposite

For convenience, we rewrite the master equation for mode-locking (4.26) equation as follows:

$$T_R \frac{\partial A(T,t)}{\partial T} = -iD\frac{\partial^2 A}{\partial t^2} + i\gamma|A|^2 A + \left[g - l + D_{g,f}\frac{\partial^2 A}{\partial t^2} - q(T,t)\right] A(T,t), \qquad (4.27)$$

where D the second order intracavity group delay dispersion (GDD), $D_{g,f} = g/\Omega_g^2 + 1/\Omega_f^2$ the gain and intracavity filter dispersion, Ω_g and Ω_f are the HWHM gain and filter bandwidth, respectively. The coefficient $\gamma = (2\pi/\lambda_0 A_L) n_2 l_L$ represents the SPM effect, where λ_0 is the central lasing wavelength, n_2 is the nonlinear index of laser active medium, A_L and l_L are the effective mode area and optical pass per round-trip. Gain is given by $g = g_0/[1 + E/(P_L T_R)]$, g_0 is the unsaturated gain or small-signal gain, E is pulse energy, P_L is the saturation power of laser material, l is linear loss inherent to passive resonator, q is loss by saturable absorber.

As an example, we study the mode-locking behavior of a Ho:YLF laser operating at 545 nm and pumped at 445 nm containing SCHOTT glass N-BAK 4 doped with Au NPs (filling factor 2×10^{-3}). In this case, the laser gain medium operates as a three level system [195]. The Ho:YLF crystal has an emission linewidth of about 18 nm in this wavelength range and a strong absorption peak around 450 nm which is suitable for pumping with high power laser diodes. We have taken the absorption cross-sections at 445 and 545 nm to be 3×10^{-21} cm^2 and 5×10^{-21} cm^2, respectively, and emission cross-section at 545 nm to be 8×10^{-21} cm^2 [195], and the fluorescence lifetime to be 110 μs [196]. The lasing transition corresponds to ${}^5S_2 - {}^5I_8$ [195]. For the Ho^{3+} concentration of 1.2×10^{20} cm^{-3}, a beam area on the crystal 1000 μm^2, pump intensity 0.6 MW/cm^2 corresponding to pump power 6 W, crystal length 10 mm, and the resonator length 1 m corresponding to repetition rate of 0.15 GHz, we have the main laser parameters of $g_0 = 0.22$, $P_L = 4.69$ W, $\Omega_g = 57.08$ THz, and $\gamma = 3.94$ MW^{-1}. We assumed a passive resonator loss to be $l = 0.02$. In the SCHOTT glass N-BAK 4 doped with Au NPs smaller than 10 nm, the plasmon resonance is located at 543 nm and we can expect strong saturable absorption as the plasmon resonance peak is located near the central lasing wavelength. Saturable absorber loss is calculated by $q(t) = -i(\omega/c)\sqrt{\varepsilon_{\text{eff}}(t)}d$, where ω is central frequency, and d is the thickness of metal nanocomposite absorber.

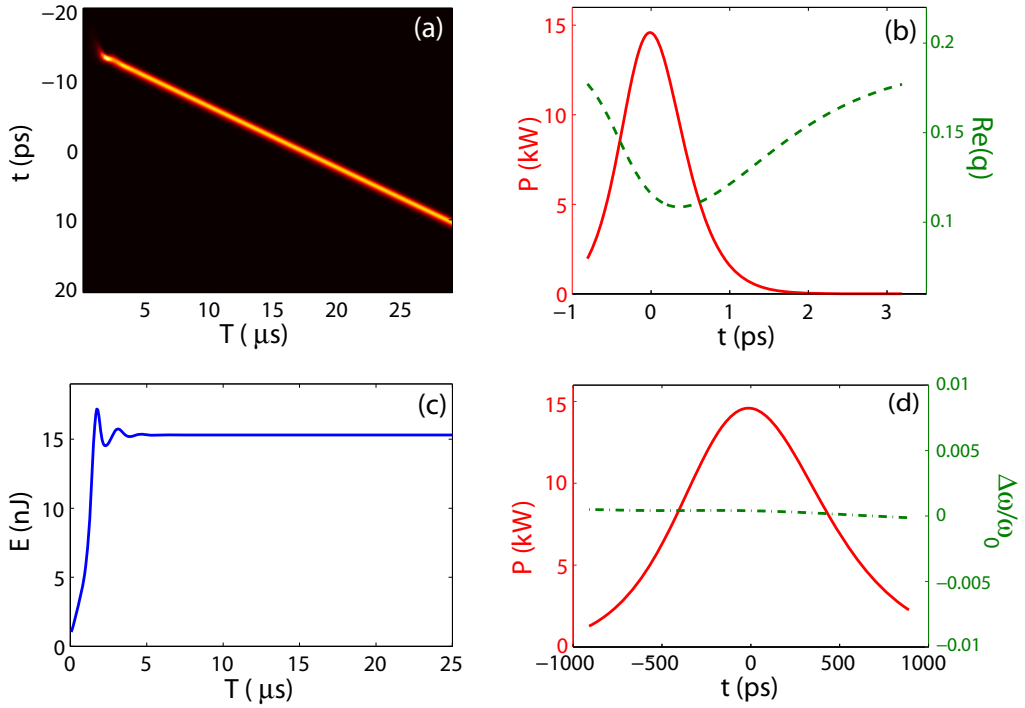

Figure 4.4.: Mode-locking behavior of Ho:YLF laser with SCHOTT glass N-BAK 4 doped with Au nanospheres smaller than 10 nm under soliton regime: (a)- pulse evolution, (b)- pulse profile and the dynamics of absorber loss, (c)- evolution of pulse energy, (d)- intensity and frequency profile. $D = -5000$ fs^2. In (a), T is the laboratory time and t is the local time (the time in the coordinate moving with group velocity).

In Fig. 4.4 we present a simulation result for the passive mode-locking behavior of Ho:YLF laser. The cross-section of beam on the metal nanocomposite absorber is taken to be 0.01 mm^2. The instant frequency change in Fig. 4.4(d) is calculated by using

$$\Delta\omega = -\frac{\partial\varphi}{\partial t}, \tag{4.28}$$

[197] where $\varphi(t,T) = \arg[A(t,T)]$. In Fig. 4.4(a), T is the laboratory time and t is the local time (the time in the coordinate moving with group velocity). Figures 4.4(a) and (c) show that the after the pulse energy is reached to a certain value, the pulse is rapidly stabilized. In this case the strong negative resonator dispersion partially compensates the nonlinear pulse broadening due to the Kerr effect in the gain crystal. The reason for the partial compensation is that the dynamic saturable absorber loss can also contribute to pulse shortening and stabilization. Especially, in the leading part of the pulse it is attenuated by the delayed response of the absorber (several hundreds femtoseconds) and it also partially contributes to the pulse shortening. This fact can be clarified by the ratio $R = -8\ln\left(\sqrt{2}+1\right)D/(\gamma E\tau_0)$, where τ_0 is the pulse duration (FWHM). If the value of R is exactly equal to 1 [190], the pulse can be considered to be ideal soliton. In this case, this

ratio has a value of about 0.63 and we can say that the contribution to the pulse shaping from the soliton formation is dominant. As Fig. 4.4(d) shows the instantaneous frequency is nearly zero as solitons. This fact can also be verified from the time-bandwidth product. In this case, the bandwidth of the pulse is about 0.46 THz (FWHM) and the pulse duration is 924.5 fs corresponding to time-bandwidth product of 0.43, which is 1.36 times of that for the perfect soliton pulse 0.315 [188] and we can regard it as a nearly bandwidth-limited hyperbolic pulse. In this case, the resultant pulse duration is much longer than 50-100 fs which is the principal limit calculated by the conventional rule for the soliton mode-locking. Unlike other saturable absorbers [190, 198], in the metal nanocomposites the rise time of transmittance is generally longer than 100 fs due to the slow equilibration of the electron system. In order to stabilize the soliton by the absorber, the maximal transmittance has to be not too much temporally shifted from the peak of pulse. This condition can be realized only for the pulses longer than the rise time. Therefore, the shortest pulse duration obtainable in this regime is several hundreds femtoseconds.

In Fig. 4.5 we show another regime of passive mode-locking. In this case, the GDD parameter has a very small but negative value of -10 fs^2. Clearly, in this case the influence of the intracavity dispersion on the pulse shaping dynamics is much weaker than in the former case. Nevertheless, the resultant pulse duration is much shorter than the former case and is about 100 fs. As Fig. 4.5(a) shows, the pulse duration rapidly decreases during the early stage of mode-locking and it is then stabilized.

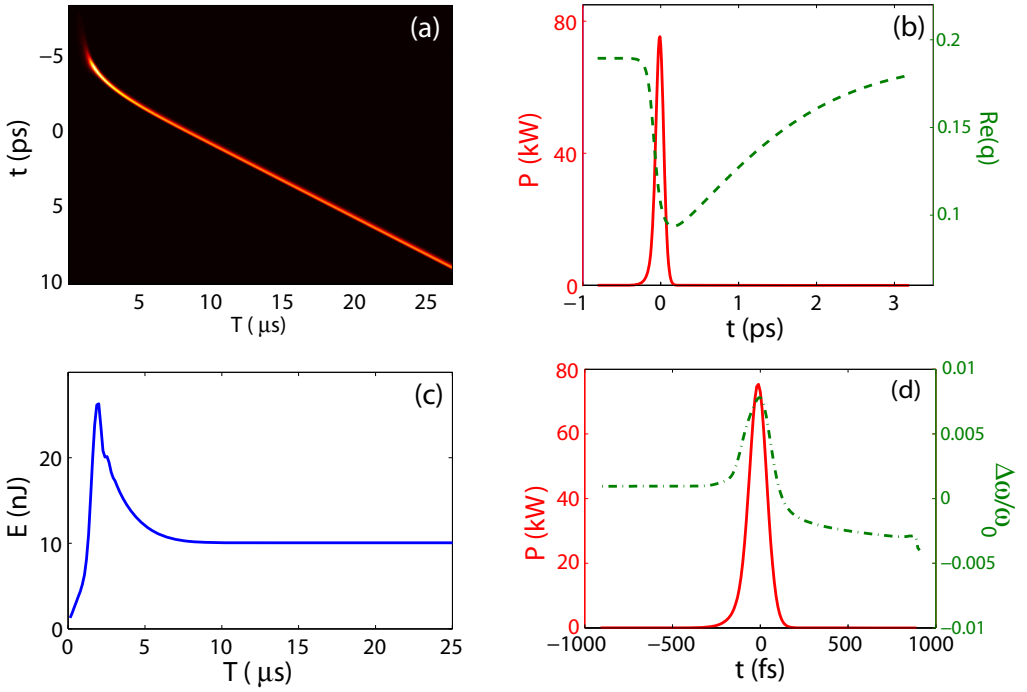

Figure 4.5.: Mode-locking behavior of Ho:YLF laser with SCHOTT glass N-BAK 4 doped with Au NPs smaller than 10 nm under non-soliton regime: (a)- pulse evolution, (b)- pulse profile and the dynamics of absorber loss, (c)- evolution of pulse energy, (d)- intensity and frequency profile. $D = -10$ fs^2.

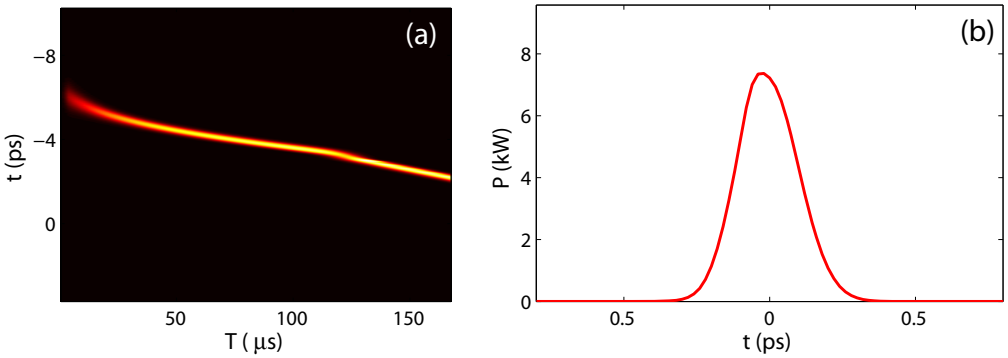

Figure 4.6.: Passively mode-locked operation of Ti:sapphire laser with silica glass film doped with Ag nanorods.

This pulse shortening mechanism is similar to the case of the traditional slow absorber without soliton formation[192]. However, the pulse duration in this case is much shorter than the self-shaping with traditional saturable absorbers [192, 193]. This is also attributed to the slow response of this material. If the absorber respond with less delay, the total pulse shortening in the leading part of the pulse becomes smaller. In contrast, for the delayed response as in the metal nanocomposites, we can expect strong pulse shortening in the leading part before the pulse is stabilized. The main difference from soliton regime is the prominent frequency chirp [see Fig. 4.5(d)]. In this case, the pulse is nonlinearly chirped and the central part has the highest frequency.

By tailoring the NPs shapes and sizes and host medium, we can change the SPR peaks in the frequency domain and applicable saturable absorption wavelength range. As an example, we present in Fig. 4.6 the passive mode-locking behavior of a Ti:sapphire laser at 800 nm. Here the optimal means the passive mode-locking regime providing the shortest pulse duration. The laser parameters are as follows: $g_0 = 0.07$, $l = 0.025$, $\gamma = 0.4$ MW^{-1}, resonator length of 1 m. To tune the SPR wavelength near the central lasing wavelength, we have taken Ag nanorods. The silica glass contains Ag nanorods with the diameter of 36 nm and the length of 90 nm, filling factor is 2×10^{-4}, the thickness (propagation length) is 1μm, and the beam area on the composite film is 1000 μm^2. The electron thermalization τ_{ee} and cooling τ_{ep} times are taken to be 100 fs and 1 ps. The resultant pulse duration is 178.6 fs and pulse energy is 1.93 nJ.

4.4.2. Mechanism of non-soliton mode-locking of solid-state laser

Though the pulse shortening process is already understood, the mechanism for the pulse stabilization in the non-soliton regime still has not been found. Especially, in our case the saturable absorber material exhibits a response different from the traditional saturable absorbers.

In Fig. 4.7 we present the influences of each component on the pulse profile and frequency chirp. For simplicity, we set the dispersion to be zero. In this case, the main components affecting the pulse evolution are the gain and intracavity filter dispersion $\Omega_{g,f}$, the Kerr nonlinearity δ, and the dynamic loss from the metal nanocomposite absorber $q(t,T)$.

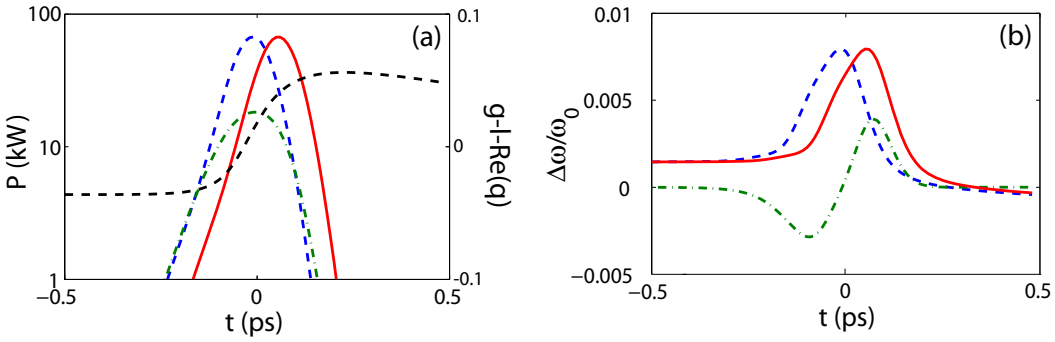

Figure 4.7.: Pulse stabilization mechanism in non-soliton (self-shaping) regime: All the changes of the pulse and frequency profiles are calculated for 20 round trip to be clearly distinguished from the initial state; the net gain in (a) corresponds to single round trip. Blue dashed and red solid lines correspond to the input and output pulse and frequency profiles, the green dash-dotted line is pulse profile affected by gain dispersion and the pulse profiles are all presented in the log scale, and black dashed line correspond to the gain. In (a) all the intensity profiles are represented in logarithmic scale. In (b) green dash-dotted line corresponds to the frequency change by the Kerr effect in the gain medium.

The gain and intracavity filter dispersion weakens the high and low frequency components. In Fig. 4.7(a) the central part of the pulse is attenuated by the gain and filter dispersion because the frequency in the central part is higher than in both the edges. It is temporally shifted by the dynamic net gain (black dashed line). The temporally shifted pulse has a profile identical to the initial pulse. We have shown the output pulse after 20 round trips, otherwise it is hard to distinguish the input and output pulses due to very slight change in one round trip because the gain coefficient is small.

The Kerr effect in the gain medium provides the negative frequency change in the leading edge and positive in the trailing edge of the pulse [green dash-dotted line in Fig. 4.7(b)]. As a result, the frequency chirp is also temporally forward-shifted. In particular, the temporal shifts in the pulse intensity and frequency profiles are exactly the same, meaning that the passive mode-locking process has already been stabilized.

If this parameter has a larger and positive value, the shorter frequency components in the central part of the pulse are forward-shifted and cause the pulse broadening.

4.4.3. Dependencies of pulse duration and energy on the dispersion and metal nanocomposite absorber parameters

In this subsection, we are going to investigate the dependencies of the pulse duration and energy on the parameters of the laser system: the cavity dispersion, laser beam diameter on the metal nanocomposite absorber, filling factor and so on.

The resonator dispersion is one of the important parameter affecting the mode-locking stability, pulse duration and energy. The simulations show that the pulse evolution is unstable for the GDD parameter value D from -55 fs^2 up to around -3200 fs^2 under the condition

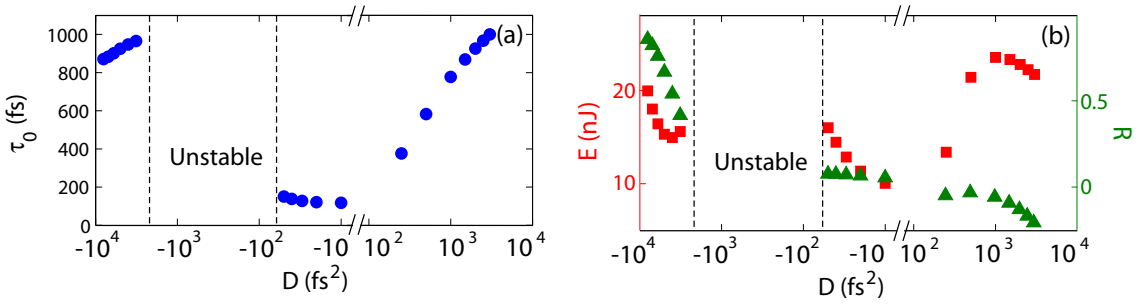

Figure 4.8.: Dependencies of pulse duration (a) and energy [red squares in (b)], and the ratio R [green triangles in (b)] on the magnitude of GDD parameter D. The beam area on the metal nanocomposite is 0.01 mm^2 and filling factor is 2×10^{-3}.

of the other parameters the same as in the above subsections. The physical origin responsible for the instability is attributed to the imbalance between the pulse delay due to the delayed loss response in the metal nanocomposite saturable absorber and pulse reshaping by the dispersion. In Fig. 4.8 we show the dependencies of the pulse duration and energy, and the ratio R (see Subsection 4.4.2) on the intracavity dispersion D for the beam area on the metal nanocomposite of 0.01 mm^2 and filling factor of 2×10^{-3}. As the dispersion increases, the pulse duration also increases regardless of the sign of dispersion. In the figure, the left side corresponds to the soliton-like pulse shaping regime and the right side to the non-soliton regime. The soliton-like pulse shaping regime does not work under the perfect soliton condition as evident from the value of R smaller than 1 (typically about 0.6). This fact is confirmed by the frequency chirp in Fig. 4.4(d). In this case, the frequency chirp is very small but it is not zero unlike that of perfect solitons.

The filling factor determines both the magnitude of the linear loss and the maximum loss change of the metal nanocomposite absorber. Figure 4.9 depicts the dependencies of pulse duration and energy on the filling factor for $D = -20$ fs^2 and the beam area on the metal nanocomposite 0.01 mm^2. Other conditions are the same as in the above figures. For small filling factor, we have the small maximum loss change leading to the longer pulse duration similarly to the traditional cases. For the filling factor smaller than 1.7×10^{-3}, the mode-locking becomes unstable. For the filling factor larger than 2.1×10^{-3}, the total linear loss by the saturable absorber exceeds the gain and the lasing itself becomes impossible.

In Fig. 4.10 we present the dependencies of the pulse duration and energy on the beam area for the metal nanocomposite absorber film with $D = -20$ fs^2 and $f = 2 \times 10^{-3}$. The beam area on the metal nanocomposite is directly related to intensity and determines the maximum loss change. However, it does not have the limit corresponding to the threshold for the laser oscillation because the maximum or linear loss on the metal nanocomposite saturable absorber does not depend on the intensity. In the figure, the mode-locking process is stable for the beam area larger than 0.1 mm^2 or smaller than 6000 μm^2 . The pulse duration increases with the beam area due to the reduced maximum loss change. The possible pulse duration range is from 110 fs to 1.31 ps.

Through the simulations, we have obtained the shortest pulse duration of 100.7 fs for $D = 0$, beam area 6000 μm^2, and filling factor 2×10^{-3}.

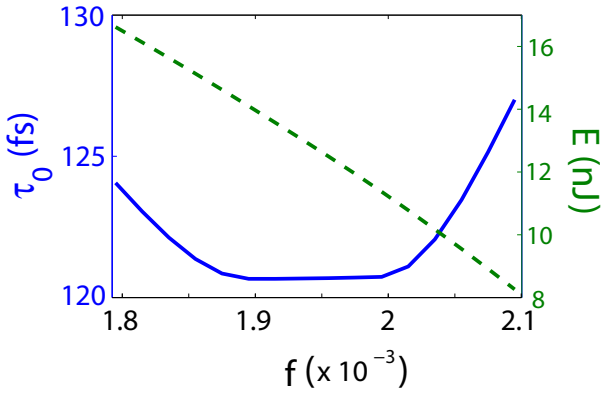

Figure 4.9.: Dependencies of pulse duration and pulse energy on filling factor. The beam area on the metal nanocomposite is 0.01 mm^2 and $D = -20$ fs^2.

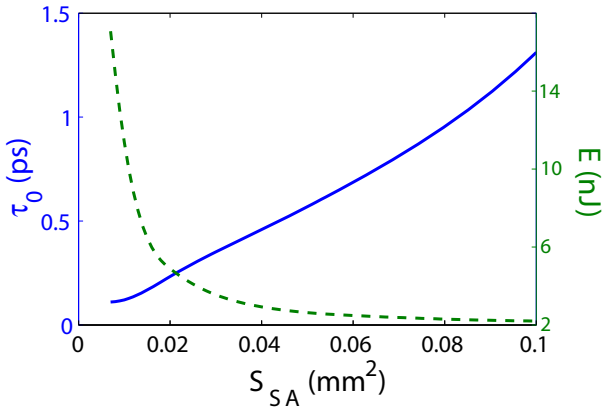

Figure 4.10.: Dependencies of pulse duration and energy, and the ratio R on the beam area on the metal nanocomposite saturable absorber. $D = -20$ fs^2 and $f = 2 \times 10^{-3}$.

In this section, we have investigated the passive mode-locking mechanisms and behavior of solid state lasers with metal nanocomposites as slow absorbers. There are two regimes responsible for the passive mode-locking: soliton and non-soliton regimes. In the soliton regime, the soliton-like pulse shaping is dominant but the resultant pulse is not a perfect soliton. In the non-soliton regime, the pulse shortening originates from the attenuation of the leading edge of the pulse due to the the slow response or transmittance rise due to the electron-electron scattering process. This pulse shaping mechanism is different from the case of the traditional saturable absorbers and provides the possibility of achievable pulse duration in the femtosecond range. The pulse stabilization is mainly contributed from the Kerr effect by the temporal forward-shift of the frequency chirp. The intracavity group delay dispersion contributes to the pulse broadening. The shortest pulse duration can be obtained in the non-soliton regime, and it is around 100 fs in Ho:YLF laser at 545 nm.

4.5. Mode-locking of short-wavelength semiconductor disk lasers with metal nanocomposites

In this section, we present a femtosecond pulse generation method by mode-locking of visible semiconductor disk lasers (SDLs) with metal nanocomposites as slow saturable absorbers. Unlike the solid state gain media, the semiconductors exhibit a dynamic gain in one round trip of the pulse in the resonator because of the large gain coefficient. This characteristic makes the process quite different from the mode-locked solid state lasers.

Passively mode-locked operation of the SDLs is described by the following master equation:

$$T_R \frac{\partial A(T,t)}{\partial T} = -iD\frac{\partial^2 A}{\partial t^2} + \left[(1-i\alpha)g - l + D_{g,f}\frac{\partial^2 A}{\partial t^2} - q(T,t)\right] A(T,t), \tag{4.29}$$

where α is the linewidth enhancement factor [170, 179]. In the above equation, the gain coefficient $g(t)$ is given by [179]

$$\frac{\partial g(t)}{\partial t} = -\frac{g(t)-g_0}{\tau_g} - g(t)\frac{|A(t)|^2}{E_g}, \tag{4.30}$$

where τ_g is the gain recovery time and E_g is the gain saturation energy dependent on the saturation fluence and the beam diameter on the gain medium. Such temporal dynamics of the gain leads to the pulse shortening from the trailing edge and this is absent in the case of solid state lasers due to the quasi-static gain.

As an example, we have taken the GaN-based SDL [169, 170] operating with the central lasing wavelength of 420 nm. The linear or small signal gain is taken to be $g_0 = 2$, the gain linewidth $\Omega_g = 2\pi \times 20.39$ THz, and the linewidth enhancement factor $\alpha = 2.8$ [169, 170]. The gain recovery time is approximately taken to be 1 ns [199, 200]. The saturation energy for the gain medium is taken to be 0.6 nJ. As a saturable absorber we have taken the silica glass film doped with Ag nanospheres smaller than 10 nm, the thickness of which is 1 μm. The filling factor is taken to be 7×10^{-3}. In this case, the SPR is located at 414 nm and the composite exhibits strong saturated absorption near 420 nm. The resonator length is taken to be 0.2 m.

In Fig. 4.11 we present an example of passively mode-locked operation of this laser with the cavity dispersion of $D = 100$ fs^2 and the beam area on the metal nanocomposite of 0.002 mm^2. Unlike the mode-locking of solid state lasers, in this case the pulse shortening happens in the very beginning of the process while the stabilization is achieved (in ~ 200 ns) much slower than the pulse shortening (in ~ 20 ns) but faster than in the solid state lasers (several μs). This is because semiconductor gain medium exhibits the dynamic gain unlike the solid state gain media. The resultant pulse duration is about 83 fs. Figure 4.11(d) shows both the intensity and frequency profile. As the figure shows, the pulse is positively chirped. This can be explained by the nonlinear index of gain and absorber. The nonlinear refraction in the gain medium originates from the linewidth enhancement due to the enhancement of the spontaneous emission into a lasing mode by the high cavity quality factor of the microcavity in the vertical cavity structure of the semiconductor disk gain medium [169]. In this case, gain medium dominantly contributes to the nonlinear phase

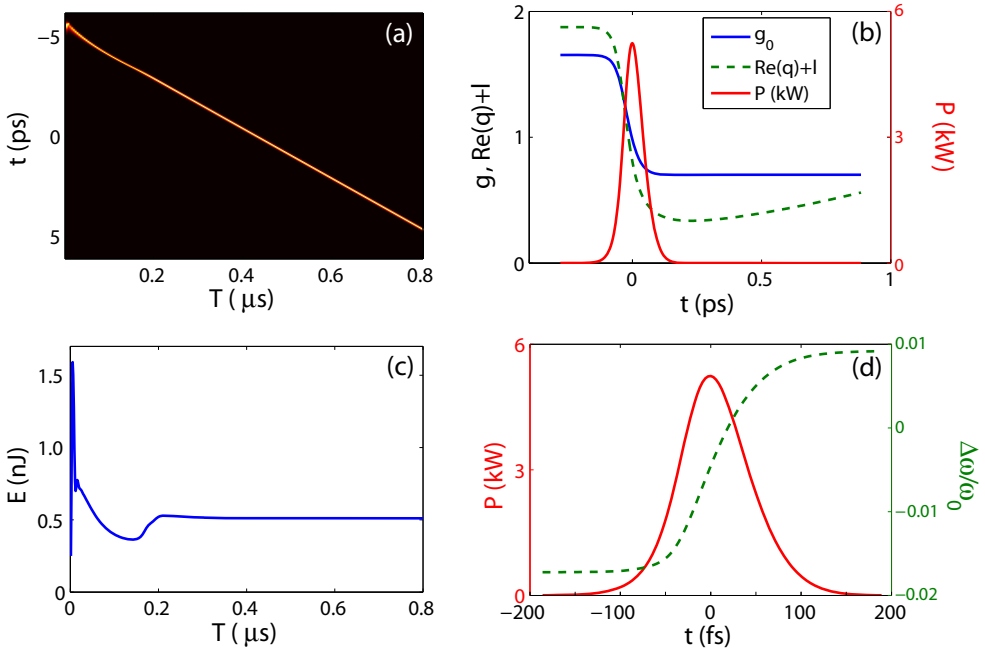

Figure 4.11.: Pulse evolution in the GaN-based semiconductor disk laser (420 nm) with silica glass doped with Ag NPs. $D = 100$ fs^2.

change of pulse. It is 6 times stronger than that from the metal nanocomposite absorber. As the nonlinear phase change is negative [see Eq. (4.29)], the total frequency chirp becomes positive. The positive frequency chirp is very similar to the case of SESAM-mode-locked semiconductor disk lasers and shows the same mode-locking mechanism [201, 202]: the balance between the pulse broadening by the dispersion and nonlinear index change by the gain through the linewidth enhancement due to the coexistence of both the stimulated and spontaneous emission in the lasing modes.

Figure 4.12 shows the dependencies of pulse duration and energy on the cavity dispersion D. The other parameters are the same as in Fig. 4.11. One can see that the pulse shaping is unstable for the range of small dispersion (from $D = -150$ fs^2 to 40 fs^2), regardless to the sign of dispersion. This is attributed to the imbalance between the dispersion-induced pulse broadening and compression by the dynamic gain and loss due to the slow response of metal nanocomposite materials. Due to the slow absorber response, the pulse shortening effect is stronger than in SESAMs and other traditional saturable absorbers. Under this condition, to realize the balance between the dispersion-induced pulse broadening and the above mentioned pulse shortening, we need the cavity dispersion larger than the traditional cases. The figure shows the achievable shortest pulse duration is about 54.0 fs for negative dispersion of $D = -160$ fs^2 and about 55.3 fs for positive dispersion of $D = 50$ fs^2. Note that the pulse duration for the positive D is marginally longer than that for the negative D with the same magnitude as former, because the pulse broadening effect is stronger for the positive D due to the positive frequency chirp.

For filling factor smaller than 6×10^{-3} due to the insufficient dynamic range of saturable

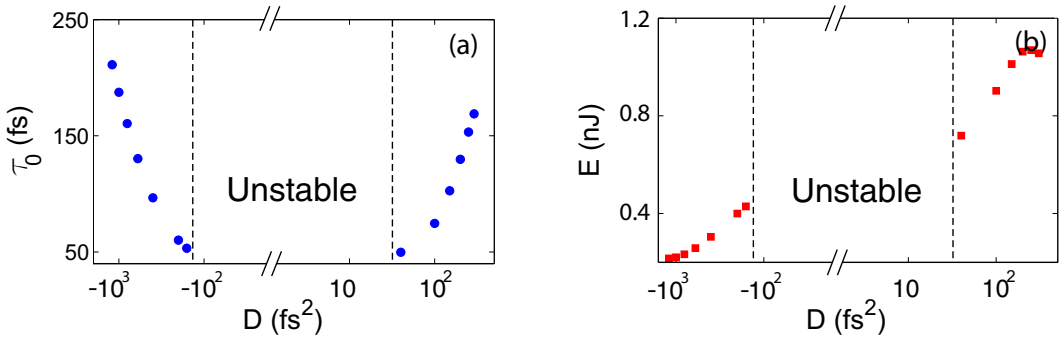

Figure 4.12.: Dependencies of pulse duration and energy on the group delay dispersion D in the GaN-based semiconductor disk laser (420 nm) with silica composite doped with Ag NPs. Beam area on the saturable absorber composite is 1000 μm^2.

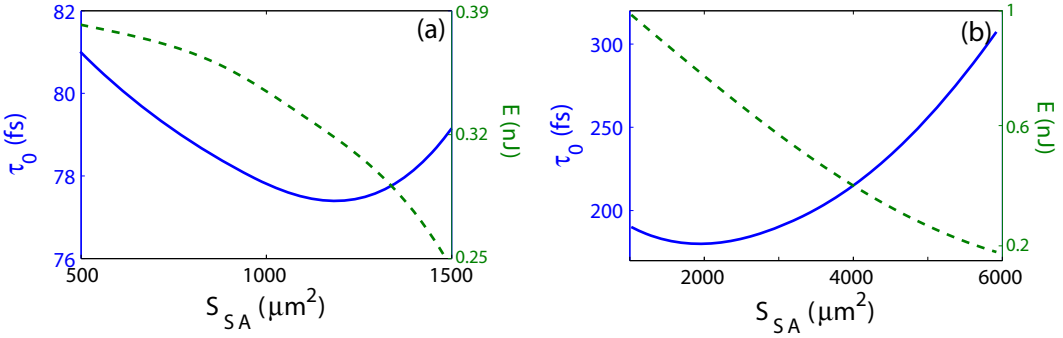

Figure 4.13.: Dependenices of pulse duration and energy on beam area on the silica glass doped with Ag NPs. In (a) $D = -300$ fs^2 and in (b) $D = 300$ fs^2.

loss the mode-locked operation becomes unstable. For filling factor larger than 7×10^{-3}, the lasing itself is impossible due to the negative small signal net gain. For $f = 6 \times 10^{-3}$, $\tau_0 = 87.14$ fs and $E = 0.69$ nJ and, for $f = 7 \times 10^{-3}$, $\tau_0 = 83.23$ fs and $E = 0.55$ nJ. These values are calculated for $D = -300$ fs^2. The other parameters are the same as in Fig. 4.11.

In Fig. 4.13 we show the dependenices of pulse duration and energy on the beam area on the metal nanocomposite absorbers for both cases of positive and negative cavity dispersions, -300 fs^{2}and 300 fs^2. The other parameters are the same as in Fig. 4.12. For the beam areas with the values other than illustrated in the figures, the mode-locked operation is unstable. The main difference from the case of solid state lasers in the preceding section, is that the pulse duration is not strongly changed for the different beam area. In particular, there is the optimal beam area for the same value of the dispersion. This phenomenon originates from the necessary condition for the balanced dynamic gain and loss.

The simulations show that the achievable shortest pulse duration is about 50 fs for $D =$ 50 fs^2 and $D = -160$ fs^2 in the GaN-based semiconductor disk laser with silica glass film doped with Ag nanospheres with very small sizes (smaller than 10 nm). The other parameters are the same as in Fig. 4.11.

To conclude, in this chapter we have theoretically demonstrated the mode-locking of solid state lasers and semiconductor disk lasers with metal nanocomposites as slow saturable absorbers. Prior to study the mode-locked operations, we have obtained a simplified equation for the nonlinear optical response of metal under the illumination of laser pulses. In combination with the effective medium approximation and the DDA, the transient nonlinear optical response of the composite materials doped with metal NPs of the different sizes and shapes can be calculated.

By using these approaches, we have investigated the mode-locked operation of solid-state lasers and semiconductor disk lasers.

In contrast to the other saturable absorbers, it is possible to obtain pulses much shorter than the plasmonic absorption recovery time under the non-soliton regime. The shortest pulse duration is about 100 fs in Ho:YLF laser lasing in the range of 545 nm. The mechanism responsible for the pulse stabilization in the non-soliton regime is the temporal forward-shift of the frequency peak the same as the shift of intensity profile by the Kerr-effect. The dependencies on the absorber parameters and cavity dispersion have been investigated.

Taking GaN-based semiconductor disk laser (lasing in the range of 420 nm) as an example, we have studied the passively mode-locked operation with silica glass doped with Ag NPs and have shown that the shortest pulse duration is about 50 fs. In this case, the pulse stabilization mechanism is the same as in cases of the traditional saturable absorbers. The dependencies of pulse duration and energy on the absorber parameters and dispersion have been investigated.

5. Slow light propagation in metal nanocomposites

In the preceding chapter, we have studied the transient nonlinear optical characteristics of the composites doped with metal NPs. These materials show good saturable absorption properties including a fast recovery time in the visible spectral range. Based on the result, we have investigated the mode-locked behaviors of visible solid state lasers, semiconductor disk lasers.

One of the main objective of this chapter is to investigate the nondegenerate nonlinearity of these materials. Here we should notice that the term "nondegenerate" is used to distinguish from the "purely" degenerate nonlinearity $\chi^{(3)}(\omega;\omega,-\omega,\omega)$, wavelengths of the waves taking part in which process are all the same. In the other words, we are interested here in the study of the effective nonlinear susceptibilities $\chi^{(3)}(\omega_2;\omega_1,-\omega_1,\omega_2)$ and $\chi^{(3)}(\omega_3;\omega_1,\omega_1,-\omega_2)$, where $\omega_3 = 2\omega_1 - \omega_2$.

The latter susceptibility is responsible for four-wave mixing and enables to achieve wavelength conversion. In the first section of this chapter, we present the general theory for this nonlinearity of metal and fundamental limitations of these materials for wavelength conversion.

One of the important applications of the saturable absorbers is the slow light phenomenon and the related technologies. Slow light in the saturable absorbers is related to the strong dispersion of the real part of the cross-modulation nonlinearity $\chi^{(3)}(\omega_2;\omega_1,-\omega_1,\omega_2)$. We address the question whether these materials exhibit the phenomenon of slowing-down the optical pulses. In the following sections we study the optical delay in these materials in detail.

5.1. Nondegenerate nonlinear susceptibility of metal nanocomposites

We consider the three coherent continuous waves with the different frequencies ω_1, ω_2 and $\omega_3 = 2\omega_1 - \omega_2$, respectively. The enhanced field amplitudes are E_1^{enh}, E_2^{enh} and E_3^{enh}, respectively, and they are given by the multiplication of the incident fields and the field enhancement factors at the individual frequencies: $E_j^{\mathrm{enh}} = x_j(\omega_j)E_j$, where $j = 1,2,3$, $x_j = x_j(\omega_j)$ and E_j are the corresponding field enhancement factors and incident field amplitudes, respectively. The total enhanced field can be written by

$$E^{\mathrm{enh}}(t) = \sum_j E_j^{\mathrm{enh}} e^{-i\omega_j t}. \tag{5.1}$$

On the other hand, for convenience we represent the nonlinear response of the dielectric

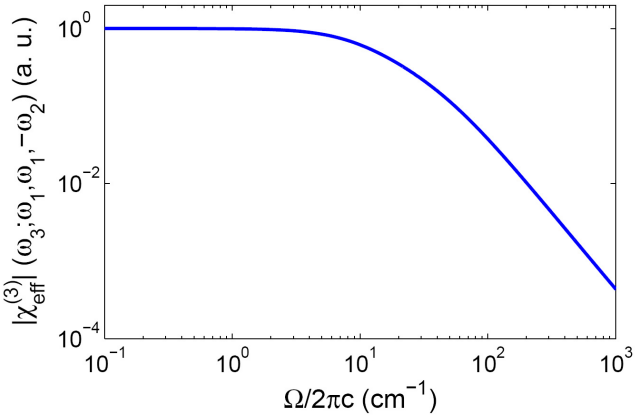

Figure 5.1.: Dependence of the magnitude of the nondegenerate third-order nonlinear susceptibility $\chi^{(3)}_{\rm eff}(\omega_3;\omega_1,\omega_1,-\omega_2)$ in silica glass doped with very small Au NPs with relaxation times of $\tau_{ee}=100$ fs and $\tau_{ep}=0.66$ ps, where $\Omega=\omega_1-\omega_2$. The result is consistent with the experimental data in Ref. [203].

function of metal given by Eq. (4.12) with the identical integral form:

$$\Delta\varepsilon_m(t)=\frac{\chi^{(3)}_m}{\tau_{ee}\tau_{ep}}\int_{-\infty}^{t}e^{-\frac{t-t'}{\tau_{ep}}}dt'\int_{-\infty}^{t'}e^{-\frac{t'-t''}{\tau_{ee}}}\left|E^{\rm enh}(t'')\right|^2dt'', \tag{5.2}$$

where

$$\Delta\varepsilon_m(t)=\varepsilon_m(t)-\varepsilon_{m0}, \tag{5.3}$$

and ε_{m0} is the linear dielectric function of metal. Note that the inherent nonlinear susceptibility of the metal $\chi^{(3)}_m$ in the above equation represents the pure degenerate third-order nonlinear susceptibility: $\chi^{(3)}_m=\chi^{(3)}_m(\omega;\omega,-\omega,\omega)$ and we assume that this value is nearly constant over the spectral range in consideration. From Eqs. (5.1, 5.2, and 5.3), we obtain

$$\chi^{(3)}_{\rm eff}(\omega_2;\omega_1,-\omega_1,\omega_2)=f\chi^{(3)}_m|x_1|^2x_2^2\left\{1+\frac{1}{[1+i(\omega_1-\omega_2)\tau_{ee}][1+i(\omega_1-\omega_2)\tau_{ep}]}\right\}, \tag{5.4}$$

$$\chi^{(3)}_{\rm eff}(\omega_3;\omega_1,\omega_1,-\omega_2)=f\chi^{(3)}_m\frac{x_1^2x_2^*x_3}{[1-i(\omega_1-\omega_2)\tau_{ee}][1-i(\omega_1-\omega_2)\tau_{ep}]}, \tag{5.5}$$

where f is the filling factor. The detailed derivations of Eqs. (5.4, 5.5) are given in Appendix C. Equation (5.4) corresponds to the third-order susceptibility responsible for the cross modulation and Eq. (5.5) for the four-wave mixing. The cross-nonlinear susceptibility (5.4) of the metal nanocomposites is responsible for the slow light, which will be considered in detail.

In this section, we focus on the four-wave mixing nonlinearity (5.5). From this equation, one can see that the magnitude of the effective nonlinear susceptibility decreases with the increase of the frequency difference $\omega_1-\omega_2$.

In Fig. 5.1 we show the dependence of the magnitude of $\chi^{(3)}_{\rm eff}(\omega_3;\omega_1,\omega_1,-\omega_2)$ on the

frequency difference $\Omega = \omega_1 - \omega_2$. The medium is silica glass doped with very small Au NPs. The pump wavelength corresponding to ω_1 is 532 nm. The result is also consistent with the experimental data reported in Ref. [203]. The figure shows that even for a very small frequency difference $\Omega/2\pi c$ of 1000 cm^{-1}, which corresponds to $\lambda_2 = 561.9$ nm and $\lambda_3 = 505.1$ nm, its magnitude decreases down to 4.4×10^{-4} of the maximum value. This fact shows explicitly that efficient wavelength far from the pump wavelength is impossible due to the narrow feature of the nonlinear susceptibility of $\chi^{(3)}_{\text{eff}}(\omega_3; \omega_1, \omega_1, -\omega_2)$. The width of the strong nonlinearity is determined by two time scales, τ_{ee} and τ_{ep}. In fact, an efficient wavelength conversion by using metal nanocomposites has not been demonstrated, although a number of experimental results has been published up to now and, importantly, the magnitude of the inherent degenerate third-order nonlinear susceptibility of metal is 6 orders larger than that of silica [155].

The cross-nonlinearity $\chi^{(3)}_{\text{eff}}(\omega_2; \omega_1, -\omega_1, \omega_2)$ exhibits a similar behavior – the narrow spectral feature. As the narrow spectral feature leads to the strong dispersion, we can expect slow-light phenomena in these materials.

5.2. Slow and fast light: physical basis and applications

Over the past decades, phenomena of slow or fast light propagation [204, 205] have attracted much attention [34, 206–209]. Slow light propagation is specifically fascinating phenomenon which promises applications in telecommunications including optical buffering [210] and data resynchronization [207], spectral enhancement of interferometers [211], efficiency enhancement of nonlinear optical processes [212], etc. This phenomenon is attributed to the large changes in group velocity because of the strong dispersion or very narrow dip in the absorption spectrum (or narrow peak in gain spectrum). There are several mechanisms responsible for slow light propagation: electromagnetically induced transparency (EIT), coherent population oscillation (CPO), stimulated Brillouin or Raman scattering (SBR or SRS), four-wave mixing, etc. CPO [213] is a quantum optical phenomenon in two-level systems exhibiting saturable or reverse saturable absorption or amplification. The Bragg resonance in plasmonic waveguides [214] has been proposed to be used for the demonstration of delayed propagation but the huge loss severely restricts the practical delay which requires the inclusion of gain [215]. A plasmonic analog of electromagnetically induced transparency (EIT) has been demonstrated in metamaterials with various metallic nanostructures [216, 217]. However, these structures require the expensive nanolithographic technology.

As we have discussed in the preceding chapters, the dielectric composites doped with metal NPs shows prominent saturable absorption properties. Naturally, we can have a question about the possibility of applications of these materials for all-optical delay through the slow-light phenomenon. To solve these problems, we first review the basic concept of slow light in the next paragraph before we study slow light in the metal nanocomposite materials.

The phase velocity of light field is given by

$$v_p(\omega) = \frac{c}{n(\omega)},$$

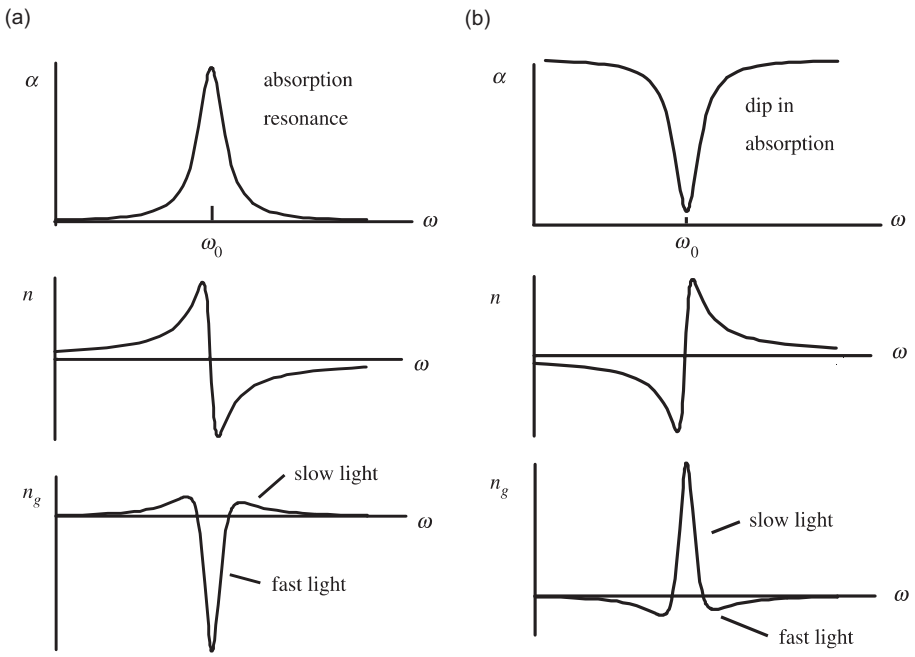

Figure 5.2.: Origin of slow and fast light for peaks and dips in absorption ad gain spectrum. The figure is taken from Ref. [34].

where $n(\omega)$ is the refractive index of the material for light frequency ω, and c is light velocity in vacuum. This is velocity of equiphase plane of light wave. On the other hand, the velocity of movement of the light pulse energy is described by group velocity

$$v_g(\omega) = \frac{c}{n_g(\omega)}, \tag{5.6}$$

where

$$n_g(\omega) = n(\omega) + \omega \frac{dn(\omega)}{d\omega}. \tag{5.7}$$

The above equation clearly shows that the group velocity can be significantly reduced in the materials with very strong dispersion so that $dn/d\omega \gg 1$. Nevertheless, in most cases, the dispersion of the optical materials are not so strong that group velocity is remarkably smaller than phase velocity. The only possibility can be given by resonances. On the other hand, if $-n/\omega < dn/d\omega < 0$, we can observe fast or superluminal light propagation. This is typical for reverse saturable absorbers, optical resonance, etc.

In Fig. 5.2 we show the conceptual illustration for slow and fast light. For the absorption peak, the refractive index shows strong anomalous dispersion and the corresponding group velocity has the narrow dip near the resonance. This leads to a pulse propagation faster than in vacuum. Contrary to these cases, for absorption dip formed by the saturation, the group velocity has a sharp peak near the resonance and slow light propagation can be realized. For a gain medium, the situation is opposite: for a gain peak slow light propagation can be realized and a gain dip fast light propagation. The basic principle is similar in all the resonant linear and nonlinear processes. In principle, the total optical delay or

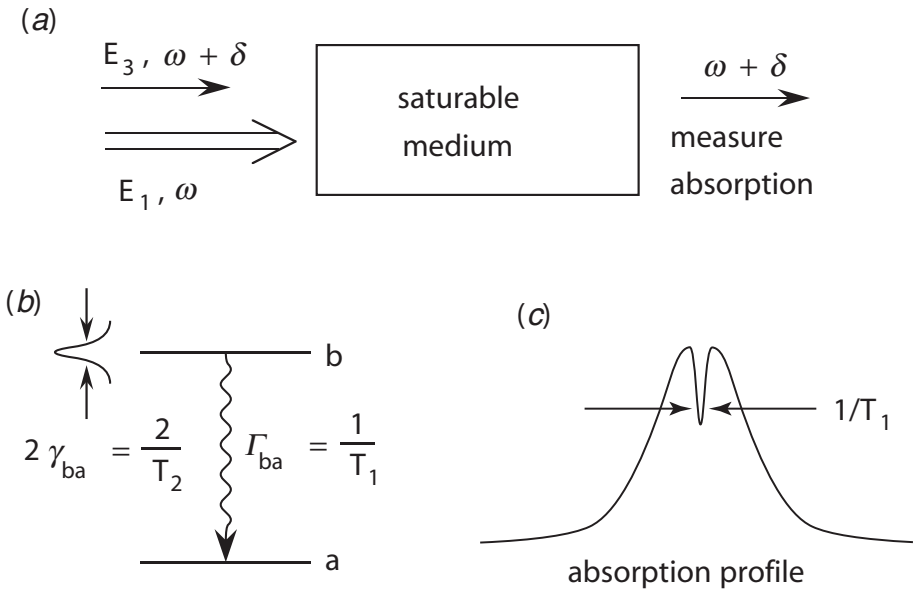

Figure 5.3.: Principle of CPO: (a)- configuration for study CPO, (b)- energy level diagram of typical saturable absorber, (c)- absorption profile in the presence of CPO. The figure is taken from Ref. [34].

advance increases with propagation length. Nonetheless, from a practical point of view, there are factors limiting these quantities such as residual absorption, pulse spreading and distortion, etc. One of the most severe problems is strong absorption near the resonances. Therefore, all the efforts to maximize these effects are focused on the reducing absorption or to find optical phenomena exhibiting gain with strong resonance. The optical effects in the former category include electromagnetically induced transparency (EIT) [218–221], coherent population oscillation (CPO) [213, 222–224], resonance in the photonic crystals [225–227], etc. As effects in the latter category, there are stimulated Raman [228] and Brillouin [229, 230] scattering (SRS and SBS), resonant gain in semiconductors, four-wave mixing in the materials with strong nondegenerate nonlinear susceptibility [222], etc. Another special example is to use a double resonance located in a narrow spectral interval [231] and this structure makes it possible to avoid the serious loss due to the exact resonance.

For a practical applications, we need a larger optical delay with cost-effective materials and inexpensive technique. Moreover, the compactness of the device is a key factor in practical applications.

EIT in atomic gases generally gives significantly slow light velocity down to 17 m/s, which is 17.6 million times slower than the normal speed of 300 million meters per second [220]. The researchers have achieved a total delay-bandwidth product of 14.1 corresponding to optical delay of 7.05 μs and a Rabi frequency of 2 MHz. Even though the dramatically large optical delay can be realized, the applicable pulse duration is limited to the μs range. In particular, this technique requires a complicated experimental set up and is difficult to use for practical purposes. Recently, Wu et al. have developed an EIT-based chip for slow light [221] and they realized the delay-bandwidth product of about 0.5. However,

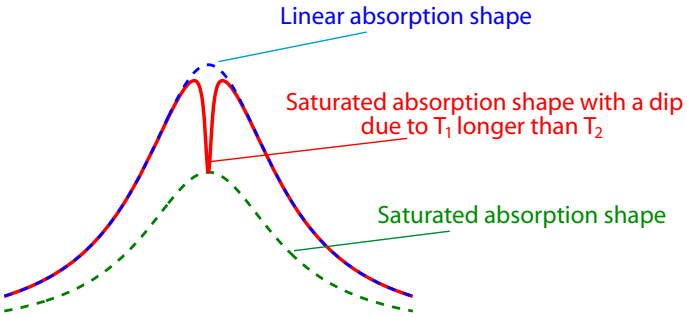

Figure 5.4.: Formation of narrow dip in absorption profile due to the longitudinal relaxation time T_1 much longer than dephasing time T_2.

this technique also requires a complicated device structure.

Stimulated Raman and Brillouin scatterings (SRS and SBS) with two light beams which have a frequency difference identical to the Raman or Brillouin frequency (optical or acoustic phonon frequencies), are important mechanisms responsible for the slow light phenomena in optical fibers [226]. The advantages of these techniques are the direct applicability at telecommunication wavelengths and large achievable optical delay. In Ref. [228], an optical delay of 80 % of the incident pulse width of 480 fs duration corresponding to the delay-bandwidth product of 3.44 has been obtained by using SRS. In Ref. [229], an optical delay of about 20 ns corresponding to delay-bandwidth product of 8.7 has been obtained. These facts show the stimulated scattering techniques can provide large amounts of optical delay in comparison with the pulse duration. Nonetheless, these methods also have the disadvantage of complicated optical systems. In addition, in case of SBS, the applicable pulse duration is significantly limited by Brillouin lifetime which is typically in nanosecond range.

Photonic crystals are easy to be integrated into a chip and slow-light in this structure is also widely investigated. The largest delay-bandwidth product ever achieved by using this structure is 0.35 [227] and the typical maximum group index is generally less than 100 [226].

The CPO-based technique provides the possibility of realization of slow light by using a compact structure with low cost. In these materials, the mechanism responsible for the slow light is a coherent population oscillation (Fig. 5.3). The material is illuminated by a strong pump and weak probe pulse, the central wavelength of which is slightly different from that of the pump. The population is driven coherently between the upper and lower states at the beat frequency of pump and probe beams. The resultant population oscillation leads to a dip in the absorption spectrum experienced by the probe. This phenomenon is called CPO or population pulsation. Correspondingly, the probe pulse is amplified in the process of propagation through the medium by two-wave coupling with pump light. The prerequisite for the CPO is a condition that the absorption linewidth given by the reciprocal of the transverse relaxation time T_2 has to be much larger than the reciprocal of longitudinal relaxation rate T_1. Otherwise, transparency dip in the absorption band can not be formed. To explicitly understand the principle of narrow dip formation in the absorption profile, let us see Fig. 5.4. The height of absorption spectrum with a linewidth equal to the

inverse of dephasing time T_2 is decreased by the pump-induced saturated absorption if T_1 has the same order as T_2 (see dotted green line in Fig. 5.4). Nevertheless, in the saturable absorber with T_1 much longer than T_2, due to the slow population difference the absorption saturation becomes inefficient around the zero frequency shift from the pump frequency, resulting in a narrow dip in the absorption spectral shape (see red line).

In the first experiment for the slow light by CPO [213], saturation of the green absorption band of ruby was used. Group velocity as low as 60 m/s was obtained. Nevertheless, the delay-bandwidth product which shows the capability of optical delay, was very small and about 0.022 because the relaxation rate $(T_1)^{-1}$ is 33.4 Hz with resultant delay of 0.612 ms. The theoretical limit in the obtainable maximum optical delay based on CPO in the traditional saturable absorbers is around 0.19 and an experimental result exceeding 0.1 has not yet been obtained [206].

Composite materials doped with metal NPs exhibit saturable absorption for moderate pump intensity (see Sections 3.3 and 3.4) and the relaxation time of nonlinear absorption saturation is in a few ps range [108, 114]. Moreover, the absorption linewidth due to the surface plasmon resonance (SPR) is in the range of 100 nm which is determined by the inverse of the plasmon decoherence time in the few femtoseconds range. From those facts, we can expect that the absorption spectrum might have a saturation dip, the width of which is determined by the inverse of the nonlinear absorption relaxation time and much narrower than the whole linewidth (several hundred times). To investigate the optical delay in these materials, we first introduce a concept of plasmonic pulsation corresponding to CPO.

5.3. Plasmonic pulsation as a classical counterpart of CPO

In this section, we show the basic principle of the slow light effect in metal nanocomposite materials. We consider metal nanocomposite materials illuminated by two pulses with a small frequency difference: pump and probe. The intensity of the pump is much higher than the peak intensity of the probe. Due to the interference of the two beams the intensity has a component oscillating with a beat frequency determined by the frequency difference of pump and probe. Correspondingly, the magnitude of the field enhancement factor, which determines the total absorption of the composite, also oscillates with the beat frequency because the inherent dielectric function contains a nonlinear contribution proportional to the intensity.

This is the plasmonic counterpart of CPO which leads to the oscillation of saturated absorption in two level-systems.

We assume that a metal nanocomposite is illuminated by a strong pump and a weak probe pulse with a frequency slightly different from that of pump which is in the range near the SPR. The total incident field is

$$E(t) = E_p^{\mathrm{enh}} e^{-i\omega_1 t} + E_{pr}^{\mathrm{enh}} e^{-i\omega_2 t}, \tag{5.8}$$

where E_p^{enh} andE_{pr}^{enh} are the enhanced field amplitude for pump and probe, which are defined in the same way as in section 5.1 and pump is much stronger than the probe: $\left|E_p^{\mathrm{enh}}\right|^2 \ll \left|E_{pr}^{\mathrm{enh}}\right|^2$. In addition, we assume that the frequency difference is much smaller

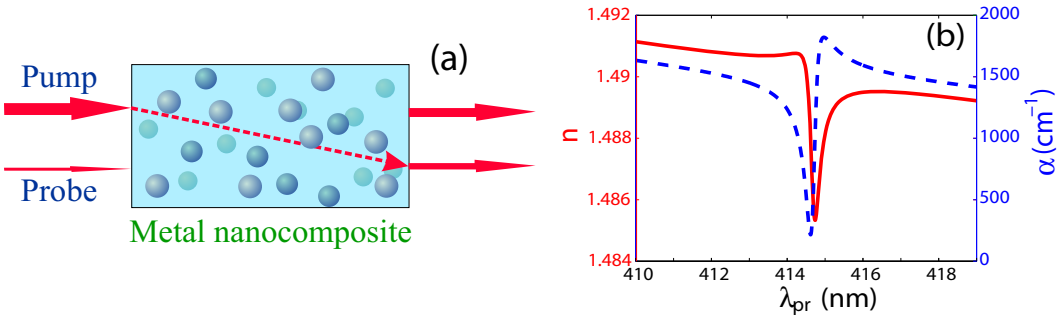

Figure 5.5.: Concept of plasmonic pulsation (a) and the absorption coefficient α (blue dashed line) and the effective index near the pump wavelength (red solid line) for the probe beam (b). Figure (a) shows that the probe transmittance is increased by the constructive coupling with the pump through the "plasmonic pulsation" represented by the temporal modulation of the field enhancement factor $x(t)$ with the beat frequency Ω. In (b), the material is silica glass doped with Ag nanospheres smaller than 10 nm with filling factor 3×10^{-3}. The intensity and wavelength of pump are 400 MW/cm^2 and 414.7 nm, respectively.

than τ_{ee} so that $|\Omega\tau_{ee}| \ll 1$, where $\Omega = \omega_p - \omega_{pr}$, from which a simplified equation

$$\Delta\varepsilon_m(t) = \frac{\chi_m^{(3)}}{\tau_{ep}} \int_{-\infty}^{t} e^{-\frac{t-t'}{\tau_{ep}}} \left|E^{\text{enh}}(t')\right|^2 dt', \tag{5.9}$$

can be applied. Under these assumptions and from Eq. (5.9), we obtain

$$\varepsilon_m(t) = \varepsilon_{m0} + \chi_m^{(3)} \left[\left(\left|E_p^{\text{enh}}\right|^2 + \left|E_{pr}^{\text{enh}}\right|^2 \right) + E_p^{\text{enh}*} E_{pr}^{\text{enh}} e^{i\Omega t} \left(1 + \frac{1}{1+i\Omega\tau_{ep}} \right) + c.c. \right] \tag{5.10}$$

For a very small filling factor, the total field enhancement factor is approximated by

$$x(t) = x_0 - \chi_m^{(3)} \frac{x_0^2}{3\varepsilon_h} \left|E_p^{\text{enh}}\right|^2 - \chi_m^{(3)} \frac{2x_0^2}{3\varepsilon_h} \left| \frac{E_p^{\text{enh}} E_{pr}^{\text{enh}}}{1+i\Omega\tau_{ep}} \right| \cos(\Omega t + \varphi), \tag{5.11}$$

where

$$x_0 = \frac{3\varepsilon_h}{\varepsilon_{m0} + 2\varepsilon_h} \tag{5.12}$$

is the linear field enhancement factor and

$$\varphi = \arg\left[E_p^{\text{enh}*} E_{pr}^{\text{enh}} / (1+i\Omega\tau_{ep}) \right]. \tag{5.13}$$

From Eq. (5.13), we can see that field enhancement factor oscillates in time with beat frequency Ω. In other words, the magnitude of the field enhancement factor representing the strength of SPR oscillates under the action of the two beams. The oscillation of field enhancement leads to the oscillation of the effective index of the composite material with the same frequency Ω [see Fig. 5.5(a)]. A part of pump beam energy is transferred to the

probe beam by the two-beam coupling mediated by the oscillating index. This principle shows a certain analogy with CPO in two level systems, but the essential difference here is that the two beam coupling arises from the nonlinear excitation of surface plasmons.

Up to now, we have assumed that both the pump and probe are the continuous waves. As the slow light is a pulse propagating with a small group velocity, we have to study the case of a pulsed probe. Taking into account this circumstance, we write the total enhanced field in metal NPs as follows:

$$E^{\text{enh}}(t) = E_p^{\text{enh}} e^{-i\omega_p t} + E_{\text{pr}}^{\text{enh}}(t)\, e^{-i\omega_{pr} t}. \tag{5.14}$$

The above equation can be rewritten by using the frequency domain probe amplitude $E_{\text{pr}}^{\text{enh}}(\Omega)$:

$$E^{\text{enh}}(t) = e^{-i\omega_p t}\left[E_p^{\text{enh}} + \int E_{\text{pr}}^{\text{enh}}(\Omega)\, e^{i\Omega t} d\Omega\right]. \tag{5.15}$$

In a similar way as we did in section 5.1, we obtain the dielectric functions of the metal at the pump and probe frequencies given by

$$\varepsilon_m(\omega_p) = \varepsilon_{m0} + \chi_m^{(3)} |x_p E_p|^2, \tag{5.16}$$

$$\varepsilon_m(\omega_p - \Omega) = \varepsilon_{m0} + \chi_m^{(3)} \left|x_p E_p^{\text{enh}}\right|^2 \left(1 + \frac{1}{1 + i\Omega\tau_{ep}}\right), \tag{5.17}$$

where $x_p = E_p^{\text{enh}}/E_p$ is the field enhancement factor for the pump depending on its intensity and is written by

$$x_p(\omega_p) = \frac{3\varepsilon_h}{\varepsilon_m(\omega_p) + 2\varepsilon_h}. \tag{5.18}$$

The detailed derivation is given in Appendix C. Applying the self-consistent approach as in Chapter 4 [see Eq. (3.9)] and considering that the probe is much weaker than the pump, we can approximately describe the nonlinear field enhancement factors by

$$x_p = \frac{3\varepsilon_{h1}}{\varepsilon_{m0} + 2\varepsilon_h + \chi_m^{(3)} |x_p E_p|^2}, \tag{5.19}$$

$$x_{pr}(\omega_p - \Omega) = \frac{3\varepsilon_{h2}}{\varepsilon_{m0} + 2\varepsilon_h + \chi_m^{(3)} \left(1 + \frac{1}{1+i\Omega\tau_{ep}}\right) |x_p E_p|^2}, \tag{5.20}$$

By using the Maxwell-Garnett formula (2.52), we find the effective dielectric function for probe

$$\varepsilon_{\text{eff}}(\omega_p - \Omega) = \frac{\varepsilon_h}{1-f}\left[1 + 2f - \frac{3 f x_0}{1 - f(1-x_0) + (1-f)\, q \left(1 + \frac{1}{1+i\Omega\tau_{ep}}\right) |x_p E_p|^2}\right], \tag{5.21}$$

where x_0 is the linear field enhancement factor given by Eq. (5.12) and

$$q = \frac{\chi_m^{(3)}}{\varepsilon_{m0} + 2\varepsilon_h}. \tag{5.22}$$

In CPO with a population relaxation time significantly longer than the dephasing time, the probe pulses can propagate with a slow and superluminal group velocity due to the strong dispersion of the refractive index in the narrow spectral range characterized by the relaxation time of the population inversion. Similar to the case of CPO, a narrow dip in the plasmonic absorption band can appear if the plasmon-mediated nonlinear relaxation time (here cooling time plays a role) is much longer than the dephasing time. Many theoretical and experimental results show that the electron cooling time τ_{ep} is characterized by a few picoseconds (see Subsection 2.2.4 and the references therein). This time scale is much longer than surface plasmon response time of few femtoseconds characterizing the total plasmonic absorption linewidths. In the frequency domain, this time scale is reflected in the dispersion of cross-nonlinear susceptibility $\chi_m^{(3)}[1+1/(1+i\Omega\tau_{ep})]$. With the increase of frequency detuning Ω, the nonlinear susceptibility decreases with a minimum $\chi_m^{(3)}$ and a maximum $2\chi_m^{(3)}$ and the spectral width of absorption dip is determined by τ_{ep}^{-1}.

In Fig. 5.5(b) we show an example of the absorption spectrum and the effective refractive index for the probe in silica glass doped with Ag NPs. The steep increase of the effective index with the probe wavelength as shown in Fig. 5.5(b) leads to a large group index and strong slowing down of the probe wave.

5.4. Slow light propagation in metal nanocomposites

5.4.1. Optical delay by plasmonic pulsation

We calculate the effective dielectric function of silica glass doped with very small Ag NPs with thickness 2 μm. The effective dielectric function is calculated by using the effective medium approximation and the field enhancement factor given by Eq. (5.20).

In Fig. 5.6 we show the refractive index, group index

$$v_g = \frac{c}{n+\omega dn/d\omega}, \tag{5.23}$$

transmittance, and the corresponding fractional delay T_{del}/T_0, where

$$T_{\mathrm{del}} = \frac{L(n_g-1)}{c} \tag{5.24}$$

is the delay time, L is the thickness of the medium, c is light propagation speed in vacuum. Pump wavelength is 414.7 nm corresponding to SPR peak. The pulse duration of the probe wave is 1.85 ps which is around 1.5 times longer than the electron cooling time, and the filling factor is 2.5×10^{-2}.

In Fig. 5.7 we show the maximum optical delays and the transmittance spectra for the different pump intensities as the functions of pump wavelength. The figure shows that the obtainable maximum delay is nearly the same as pulse duration which has the same order as the nonlinear relaxation time τ_{ep}.

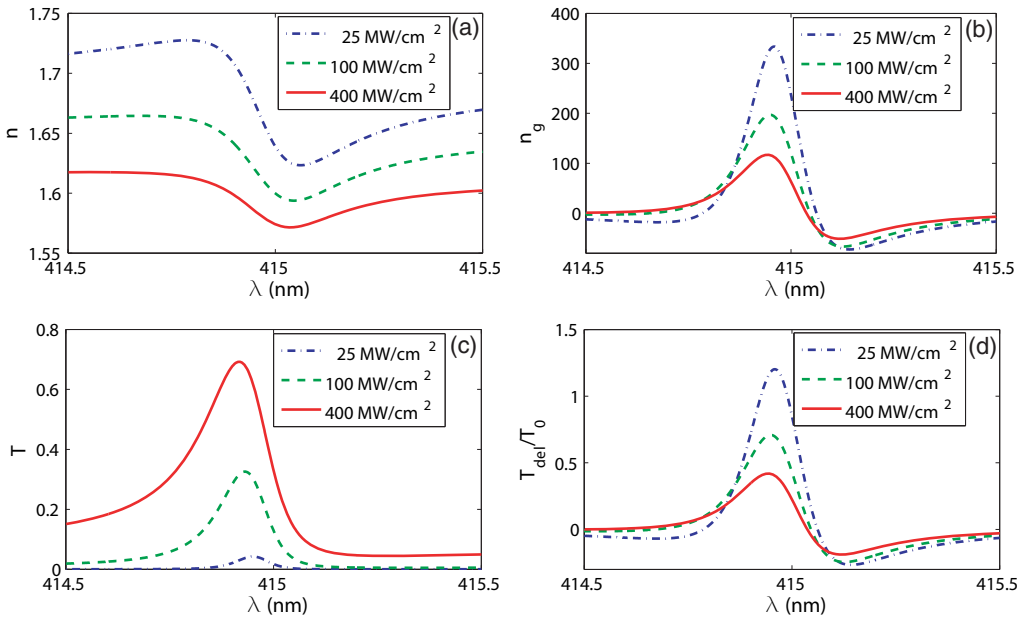

Figure 5.6.: Optical delay by plasmonic pulsation in the silica glass doped with small Ag nanospheres: λ is probe wavelength. (a)- refractive index, (b)- group index, (c)- transmittance, and (d)- fractional delay. The sample is silica glass doped with very small Ag nanospheres. Filling factor is 2.5×10^{-2} , pump intensities are 25, 100 and 400 MW/cm^2, and sample thickness is 2 μm.

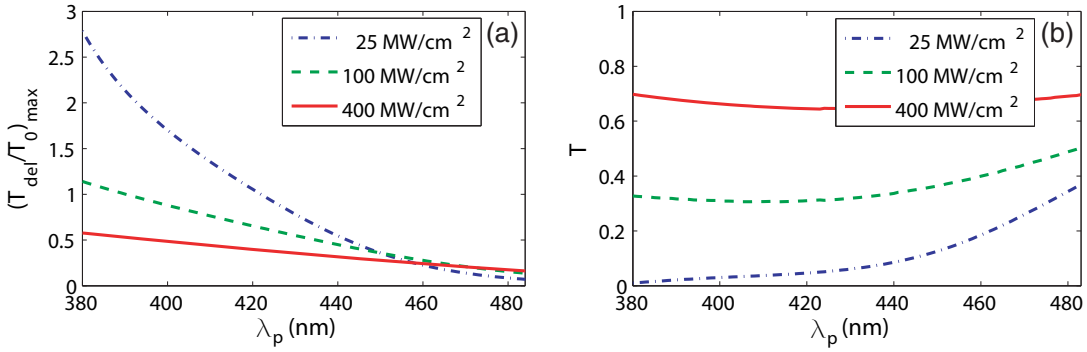

Figure 5.7.: Maximum optical delay in silica glass doped with Ag nanospheres smaller than 10 nm as the functions of pump wavelengths. Filling factor is 2.5×10^{-3} and the composite layer thickness is 2 μm. (a)- maximum fractional delay and (b)- the corresponding transmittance for various pump wavelengths.

5.4.2. Practical maximum delay

As we noticed in the preceding studies [206], the optical delay is not principally limited because the delay time is proportional to the propagation length. However, there is not any

ideally transparent material exhibiting the narrow resonance which is necessary for the optical delay. The residual absorption in those materials limits the practically achievable maximum optical delay. Here we analyze this quantity in metal nanocomposite saturable absorber materials.

From Eq. (2.52), we can approximately write the effective dielectric function for a small value of the filling factor at ω_2:

$$\varepsilon_{\text{eff},pr}(\omega_{pr}) = \varepsilon_h (1 + 3f - 3x_{pr} f). \tag{5.25}$$

Correspondingly, the effective complex index is given by

$$n_{\text{eff},pr} = \sqrt{\varepsilon_h}\left(1 + \frac{3f}{2} - \frac{3x_{pr} f}{2}\right). \tag{5.26}$$

From the definition of group index

$$n_g = \text{Re}\left\{\frac{d\left[\omega_{pr} n_{\text{eff},pr}(\omega_{pr})\right]}{d\omega_{pr}}\right\} = \text{Re}\left(n_{\text{eff},pr} - \omega_{pr}\frac{dn_{\text{eff},pr}}{d\Omega}\right), \tag{5.27}$$

we obtain

$$n_g|_{\Omega=0} = \text{Re}\left(n_{\text{eff},pr}\right) - \frac{3f\sqrt{\varepsilon_h}\omega_{pr}\tau_{ep}}{2}\text{Im}\left[\frac{x_0 q\left|E_p^{\text{enh}}\right|^2}{\left(1 + 2q\left|E_p^{\text{enh}}\right|^2\right)^2}\right]. \tag{5.28}$$

Considering that the effective index is much smaller than the group index at the nonlinear resonance dip, the time delay is written by

$$T_{del} = -\frac{3f\sqrt{\varepsilon_h}\omega_{pr}\tau_{ep}L}{2c}\text{Im}\left[\frac{x_0 q\left|E_p^{\text{enh}}\right|^2}{\left(1 + 2q\left|E_p^{\text{enh}}\right|^2\right)^2}\right], \tag{5.29}$$

On the other hand, the saturated absorption for $\Omega = 0$ is given by

$$\alpha|_{\Omega=0} = -\frac{3f\sqrt{\varepsilon_h}\omega_{pr}}{c}\text{Im}\left(\frac{x_0}{1 + 2q\left|E_p^{\text{enh}}\right|^2}\right). \tag{5.30}$$

The practical delay in saturable absorbers, in general cases, is limited by residual absorption in the materials. We take the maximum propagation length as the inverse of total absorption coefficient:

$$L_{\max} = -\frac{c}{3f\sqrt{\varepsilon_h}\omega_{pr}}\text{Im}\left(\frac{x_0}{1 + 2q\left|E_p^{\text{enh}}\right|^2}\right)^{-1}. \tag{5.31}$$

For this length, we obtain the maximum relative delay or delay-bandwidth product

$$\frac{(T_{del})_{\max}}{\tau_1} = \frac{\mathrm{Im}\left[x_0 q \left|E_p^{\mathrm{enh}}\right|^2 / \left(1+2q\left|E_p^{\mathrm{enh}}\right|^2\right)^2\right]}{\mathrm{Im}\left[x_0 / \left(1+2q\left|E_p^{\mathrm{enh}}\right|^2\right)\right]}. \tag{5.32}$$

The above equation shows that the maximum relative delay does not depend on the filling factor but depends on the intensity of the incident field and material parameters such as dielectric functions and third-order nonlinear susceptibility.

At SPR, considering that $\arg(x_{20}) = -\pi/2$ (see Eq. (3.7) and Ref. [156]) and that the imaginary part of third-order nonlinear susceptibility of metal is smaller than its real part, we obtain $\arg(q) \approx -\pi/2$. Therefore, Eq. (5.32) is transformed to

$$\frac{(T_{del})_{\max}}{\tau_{ep}} = \frac{2|q|^2 \left|E_p^{\mathrm{enh}}\right|^4}{1+4|q|^2 \left|E_p^{\mathrm{enh}}\right|^4}. \tag{5.33}$$

The above equation shows that the maximum limit in the delay-bandwidth product at the SPR is 0.5. This result is also consistent with the numerical results in Fig. 5.7. This limit is 2.5 times larger than that for the case of coherent population oscillation in saturable absorbers which is 0.19 [206].

Above described slow light scheme by pump-probe two beam coupling provides the all-optical delay of few picosecond optical signals with a fractional delay of more than 0.5. The advantage of this approach is the tailorability of light wavelength over wide spectral range from the visible to the infrared by changing the particle sizes and shapes and simple optical configuration. However, we need a strong pump intensity of higher than several hundreds of MW/cm^2 and relatively small fractional delay.

In the next section, we consider a scheme for slow light and high-fidelity all-optical delay of images by using the degenerate four-wave mixing (DFWM) in these materials with lower pump intensity.

5.5. Slow light and all-optical delay by degenerate four-wave mixing in metal nanocomposites

The degenerate four-wave mixing (DFWM) is a technique applied for a variety of purposes including ultrafast spectroscopy [232], optical phase-conjugation [233], and others. During the process of backward DFWM, a signal beam A_s propagates along the direction opposite to the probe beam A_{pr} by the holographic diffraction from the gratings formed by the interference with pump beams A_1 and A_2 [see Fig. 5.8(a)], resulting in optical phase conjugation [233]. This configuration has two-fold important features: phase matching condition is automatically satisfied and the signal beam is exactly the phase-conjugate with regard to probe.

Backward DFWM has been revealed as a powerful tool for the realization of slow light in dynamic holographic recording media such as photorefractive crystals [234–236]. The physical basis of this approach is in that the diffraction efficiency for the phase conjugate

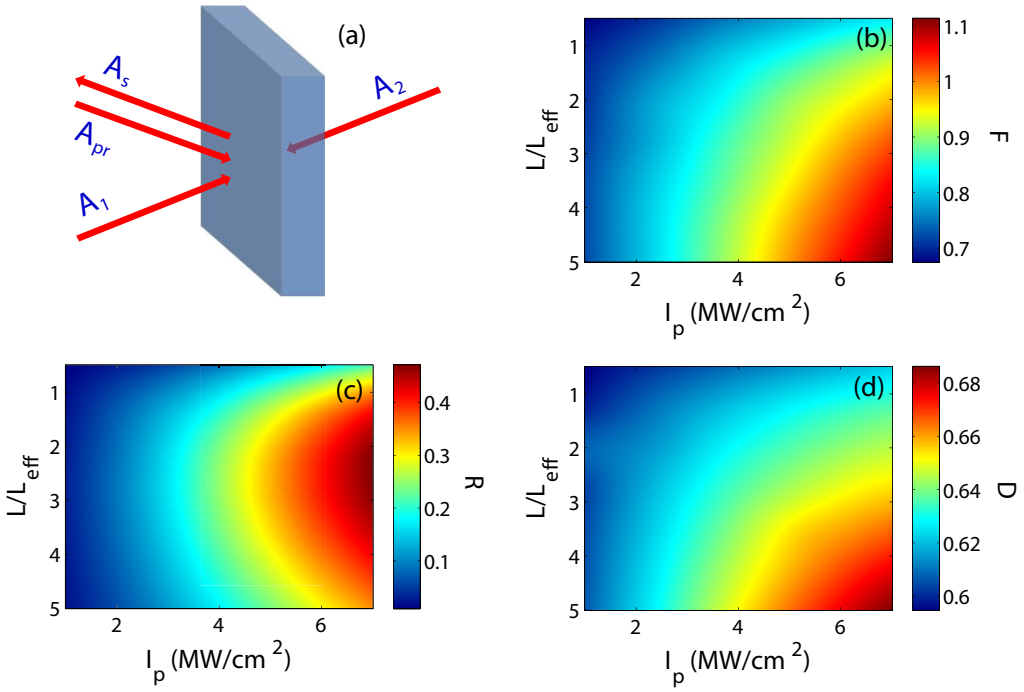

Figure 5.8.: Slow light by DFWM in TiO_2 layer containing Ag NPs smaller than 10 nm with filling factor of 10^{-4}: (a) configuration, (b) fractional delay F, (c) conjugate reflectivity R, (d) pulse distortion.

signal beam A_4 strongly depends on the frequency of probe beam A_3 due to the delayed nonlinear response of these materials. The main drawback of slow light by using the photorefractive materials is that they respond very slowly (up to several seconds), leading to severely limited bandwidth.

DFWM has been a long-term issue in the beginning of study on the plasmonic enhancement of third-order nonlinearity of metal nanocolloids. In this section, we study the slow light phenomenon in these materials using backward DFWM.

Under the approximation of undepleted pump intensity, we can describe the propagation of signal and probe pulses by using

$$\begin{cases} \partial A_s(\Omega,z)/\partial z = aA_s + bA_{pr}^* \\ \partial A_{pr}(\Omega,z)/\partial z = bA_s^* + aA_{pr} \end{cases}, \tag{5.34}$$

where $A_s(\Omega,z)$ and $A_{pr}(\Omega,z)$ are amplitudes of signal and probe pulses,

$$a = i\delta\left(|A_1|^2 + |A_2|^2\right)\left(1 + \frac{1}{1+i\Omega\tau_{ep}}\right) - \alpha/2, \tag{5.35}$$

$$b = 2i\delta A_1 A_2 \frac{1}{1-i\Omega\tau_{ep}}, \tag{5.36}$$

$$\delta = \frac{\omega_0 \chi_{\text{eff}}^{(3)}}{2c\text{Re}\sqrt{\varepsilon_{\text{eff}}(\omega_0)}\cos\theta}, \tag{5.37}$$

A_1 and A_2 are the amplitudes of continuous-wave counterpropagating pump waves,

$$\alpha = 2\text{Im}\sqrt{\varepsilon_{\text{eff}}(\omega_0)}\frac{\omega_0}{c}$$

is the linear absorption coefficient, and θ is a half of intersecting angle between pump A_1 and probe A_{pr}. The detailed derivations for Eqs. (5.35), (5.36), and (5.37) are given in Appendix C. The effective third-order susceptibility of metal nanocomposite is calculated by $\chi_{\text{eff}}^{(3)} = f\chi_m^{(3)}|x|^2x^2$ for spherical NPs with a diameter smaller than 10 nm, otherwise by the generalized effective medium approximation in combination with the discrete dipole approximation (see Section 3.1).

Figure 5.8(a) shows the slow light scheme using DFWM. In Fig. 5.8, the fractional delay (b), phase conjugate reflectivity (c), and pulse distortion (d) are shown as the functions of the medium length relative to the effective length L_{eff} and the pump intensity for pump intensity ratio of 1 at 625 nm with the probe pulse duration of 1 ps. In this case, the effective length was $L_{\text{eff}} = 90.2$ μm. We have taken TiO_2 composite containing silver NPs with diameters smaller than 10 nm exhibiting SPR at around 610 nm. Figure 5.8 shows that by using DFWM configuration the maximum fractional delay can be more than 1 with reflectivity up to more than 0.5 for the pump intensity lower than 8 MW/cm^2, which is much lower than that for the slow light scheme described in Section 5.4. The pulse distortion was evaluated by using the formula presented in Ref. [224] and was about 0.6. The pump intensity in this case was 200 MW/cm^2. This value is one order larger than for the case of small NPs presented in Fig. 5.8 and originates from the fact that the sauration intensity for the larger NPs higher than for the smaller NPs [see Section 3.4 and Fig. 3.11(d)].

One of the main advantages of backward DFWM is the realizability of optical phase conjugation [233], providing the exactly the same image as in the place of incident source and the possibility of parallel all-optical delay of multiple information. Figure 5.9 shows simulation result for delayed phase conjugate image (a) obtained by using this method (real size of picture 0.32 mm, pixel number 32×32, distance between incident picture plane and metal nanocomposite film 0.25 mm) in comparison with free-space-propagated

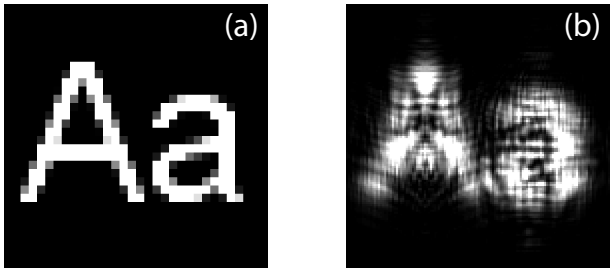

Figure 5.9.: Deleayed images: (a) phase conjugate image by degenerate FWM and (b) image formed after propagation in free-space with optical path the same as in (a).

image (b). We have chosen TiO_2 film containing Ag nanorods of 10 nm in diameter and 39 nm in length with a filling factor of 10^{-3}, providing the effective nonlinear susceptibility $\chi_{\text{eff}}^{(3)} = (6.62 - 7.61i) \times 10^{-16}$ m^{2}V^{-2} at the telecommunication wavelength 1550 nm. The resultant fractional delay was about 0.69, corresponding to effective total fractional delay of about 706.6 (0.69×32^2).

To conclude, in this chapter we proposed two slow-light schemes in composites doped with metal NPs. In two-beam coupling scheme, coupling between continuous wave pump beam and weak probe pulse with a duration of few picoseconds strongly dependent on the frequency, resulting in a significantly reduced group velocity. We have shown that employing these composites an ultra-compact slow-light device supports a delay-bandwidth product of 0.5 over a bandwidth of 300 GHz for probe pulses with a few ps duration. Fractional delay is comparable with other on-chip slow-light devices, but the scheme has the configuration much simpler compared with other techniques.

Under the backward degenerate FWM configuration, fractional delay of about unity can be realized. In particular, high-fidelity delayed image can be obtained by using this approach. As an example, at 1550 nm all-optical delay of an image of 1024 pixel number with fractional delay of 0.69 is revealed. Main advantage of this approach is high fidelity of delayed images compared with any other methods, tailorability of applicable wavelength range, short pulse duration in few picosecond range, cost-effectiveness of the material, and simple configuration.

6. Femtosecond plasmon pulse generation by mode-locking of a surface plasmon polariton laser

Recently, lasing and amplification of surface plasmon polaritons (SPPs) has attracted strong interest in nanophotonics mainly due to the strong loss of plasmon polaritons during their propagation (see Subsection 2.1.3 and references therein). For most applications of SPPs, it is important to examine the possibility of ultrashort plasmon polariton pulse generation, especially for ultrafast surface spectroscopy, informatics, and others.

In this chapter, we focus on the ultrashort plasmon pulse generation by mode-locking of a surface plasmon polariton laser. For this purpose, we consider a configuration (Fig. 6.1) with a dielectric layer c composed of a gain sublayer g and a sublayer with a saturable absorber sa adjacent to the metal film b. At the interface of the flat continuous metal film b SPPs can be excited which are confined to the proximity of the metal-dielectric interface and decay exponentially in both media. Optical pumping from below the dielectric layer c leads to a population inversion in the gain medium. Feedback in this scheme is realized by using a SPP grating at both end sides of the metal layer [237]. Passive mode-locking can be achieved by the combined action of slow saturable gain and slow saturable absorption in one round trip. Such a mode-locking mechanism is realized in standard dye lasers [141, 174, 175, 238] where both media exhibit different saturation intensities and different focusing. In a SPP laser considered here, the saturation in the absorber layer sa is stronger than in the gain sublayer g because of the stronger field localization of the SPP modes as shown in Fig. 6.1. Everywhere in the chapter below, we denote the quantities related to gain by subindex g and for saturable absorber by subindex q.

6.1. Surface plasmon polariton laser equation

In this section, we study the evolution of longitudinal SPP modes. First, we consider a passive SPP resonator. The dispersion relation for propagating SPPs is given by Eq. (2.42), where d is the thickness of the metal film, ε_a, ε_b and ε_c are dielectric functions of layers a, b and c taken from [151], and the constants α_a, α_b and α_c are directly related with the wavenumber K of propagating SPP by

$$\alpha_j^2 = K^2 - \varepsilon_j \frac{\omega^2}{c^2}, \tag{6.1}$$

where $j = a$, b and c, ω is the angular frequency of light and c is the light velocity in vacuum. For the passive SPP resonator in Fig. 6.1, the counterpropagating fields interfere

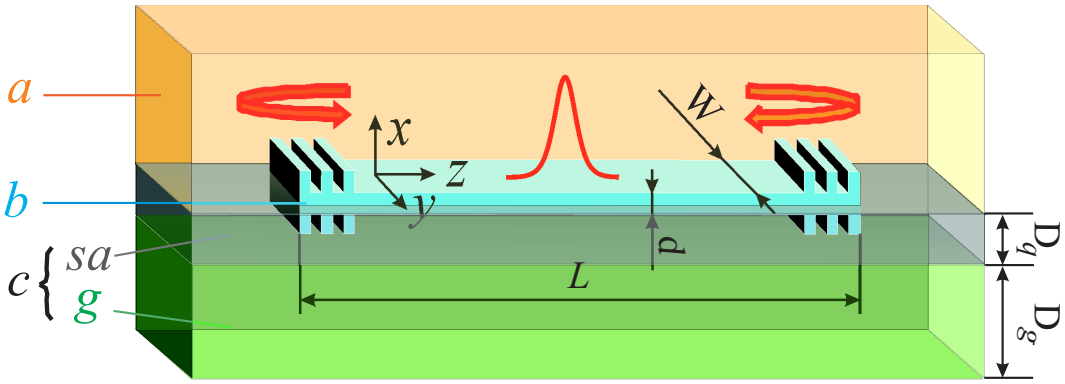

Figure 6.1.: Configuration of a SPP laser. The layer c is a dielectric layer with gain (green in the figure). For mode locking, we add a saturable absorber layer (gray-colored in the figure) into the layer c adjacent to the metal film layer b. The absorber and gain media are doped in the same host material with permittivity ε_c. For the feedback we take Bragg reflectors of SPPs as the resonator mirrors.

resulting in intracavity modes described as

$$\mathbf{E}_n = \mathbf{U}_n e^{-(\gamma_n + i\Omega_n)t}, \tag{6.2}$$

where indices n indicate longitudinal mode numbers and the mode function $\mathbf{U}_m(x,z)$ is given by

$$\begin{array}{ll} \mathbf{U}_n = A_{an}\mathbf{q}^-_{an}e^{-\alpha_{an}x} & (\infty > x \geq 0) \\ \mathbf{U}_n = A^+_{bn}\mathbf{q}^+_{bn}e^{\alpha_{bn}x} + A^-_{bn}\mathbf{q}^-_{bn}e^{-\alpha_{bn}x} & (0 > x \geq -d) \\ \mathbf{U}_n = A_{cn}\mathbf{q}^+_{cn}e^{\alpha_{cn}(x+d)} & (-d > x \geq -\infty) \end{array}, \tag{6.3}$$

$$\mathbf{q}^{\pm}_{jn} = (\hat{x}\sin K_n z \pm \hat{z}\,(\alpha_{jn}/K_n)\cos K_n z), \tag{6.4}$$

and A_j ($j = a$, b and c) are field amplitudes for each layers, $\hat{x}$ and $\hat{z}$ are unit vectors along the x and z axes, respectively,

$$K_n = n_{\mathrm{eff},n}\frac{\Omega_n}{c}, \tag{6.5}$$

$n_{\mathrm{eff},n}$ is the linear mode index and Ω_n is the angular frequency of the n-th longitudinal mode of the passive SPP resonator. From the field equations, we can see that SPP polarization direction is altered from normal to parallel at the interface in a half spatial period of longitudinal interferometric fringe of each mode. Nevertheless, normal components are dominant in layers a and c because $\left|\alpha_{jn}/K_n\right| \ll 1$, $j = a$, and c. The relations between the field amplitudes are given by (see Appendix D)

$$A_{an} = \frac{(\varepsilon_c\alpha_{bn} + \varepsilon_b\alpha_{cn})}{(\varepsilon_a\alpha_{bn} - \varepsilon_b\alpha_{an})}e^{\alpha_{bn}d}A_{cn}, \tag{6.6}$$

$$A^{\pm}_{bn} = \frac{(\varepsilon_c\alpha_{bn} \pm \varepsilon_b\alpha_{cn})}{2\varepsilon_b\alpha_{bn}}e^{\pm\alpha_{bn}d}A_{cn}. \tag{6.7}$$

In the expressions for mode fields the wavenumber K_n, the field attenuation factors in x-direction α_{jn} and the resonator loss γ_n obey the following relations:

$$K_n^2 = \alpha_{jn}^2 - \frac{\varepsilon_j}{c^2}\left(\gamma_n + i\Omega_n\right)^2, \tag{6.8}$$

where $j = a$, b and c. In fact, additional loss in the resonator arises due to the imperfect coupling and reflectance of the resonator mirrors which is included in the parameter γ_n. The additional modification of the modal structure and loss is related to the finite width of the waveguide in y direction. For a waveguide thickness much larger than d but smaller than a few μm there exist only one mode in this direction and its properties can be calculated using the effective index approach.

Next, we consider the evolution of modes in an active SPP resonator. The fields in layers a and b of the SPP resonator can be calculated from fields of the layer c by using the relations for the field amplitudes given by Eqs. (6.6, 6.7). The field in layer c is given by

$$\mathbf{E}_c = \frac{1}{2}\sum_n A_n(t)\left[\hat{x}\sin\left(K_n z\right) + \hat{z}\frac{\alpha_{cn}}{K_n}\cos\left(K_n z\right)\right] e^{\alpha_{cn}(x+d)-i\omega_n t} + c.c., \tag{6.9}$$

where ω_n is the angular frequency of n-th mode in the active resonator and we assume that $\omega_n \approx \Omega_n$. The induced polarization is described by the same expression replacing the field amplitude $A_n(t)$ with $P_n(t)$.

Substituting the above equation into Maxwell's equations for TM waves and using the slowly varying envelope approximation (SVEA) and the rotating-wave approximation for the induced polarization [239], we obtain the master equation for the SPP laser (see Appendix D)

$$\dot{A}_n + \gamma_n A_n = \frac{\sigma_g\sqrt{\varepsilon_c}\mathscr{D}_n\Gamma_g A_n}{M_n}\int_0^L\int_{-D_g-d_g}^{-d_g}|\mathbf{U}_n|^2 N_g dz dx, \tag{6.10}$$

where ρ_g is electric dipole moment of the gain,

$$\mathscr{D}_n = \frac{1}{\Gamma_g + i\left(\omega_L - \omega_n\right)}, \tag{6.11}$$

$T_{2g} = \Gamma_g^{-1}$ is the dephasing time,

$$\sigma_g = \frac{\rho_g^2\omega_n}{2\varepsilon_0\varepsilon_c\hbar\Gamma_g} \tag{6.12}$$

is the gain cross-section, $N_g = N_g(x,z,t)$ is a space-time dependent population inversion,

$$M_n = \int_0^L\int_{-\infty}^{\infty} dz dx\left|\mathbf{U}_n(x,z)\right|^2 n(x) \tag{6.13}$$

is a normalization factor, $n(x)$ is the refractive index different at each layer, L is the length of the SPP resonator, ε_0 is the vacuum permittivity, and $\hbar$ is Plank constant. In the above equation, the right hand determines the field source generated from the gain polarization induced by pumping.

We describe the right hand side of Eq. (6.10) as $g_n A_n$, where g_n is the transient nonlinear

mode gain. Using Eq. (6.3) we obtain

$$g_n = \beta_n \sigma_g \int_{-D_g-d_g}^{-d_g} \bar{N}_g(x,t)\, e^{\kappa(x+d)} dz dx, \tag{6.14}$$

where

$$\beta_n = \frac{\Gamma_g \mathscr{D}_n \left(1+|\alpha_{cn}/K_n|^2\right)\sqrt{\varepsilon_c}}{2M_n}, \tag{6.15}$$

$\kappa = 2|\mathrm{Re}[\alpha_c(\omega_L)]|$, ω_L is the lasing frequency, $\bar{N}_g(x,t) = \int_0^L N_g(x,z,t)\, dz/L$. The analogous procedure can be applied for the slow saturable absorber which yields similar expressions as above. For the study of mode-locking, below we consider the modes as a continuum by replacing ω_n, K_n, γ_n and $n_{\mathrm{eff},n}$ with ω, K, γ, and n_{eff}, respectively.

In difference to bulk mode-locked lasers, in the case of SPP lasers the mode field is confined in the vicinity of the metallic layer. Hence, the strength of gain and absorption saturation also depend on the position x because the SPP mode intensity is higher at the position closer to the metal surface. In addition, the pump intensity distribution is modulated in space due to the absorption of the pump in the gain sublayer and standing wave formation by the reflection from the metal film. Therefore we can not simply apply the relations or the master equations for passive mode-locking with saturable absorbers in bulk lasers, in which all the above given parameters do not depend on the transverse spatial coordinate [161, 240].

6.2. Master equation for mode-locked SPP lasers

Mode-locked dynamics can be understood more easily in the time domain rather than in the frequency domain. Here, we derive the master equation for mode-locked SPP lasers.

The SPP field in the laser resonator given by Eq. (6.9) can be written as the sum of forward and backward waves:

$$\mathbf{E}_c = \mathbf{E}_c^+ + \mathbf{E}_c^-,$$

where

$$\mathbf{E}_c^+ = \frac{1}{4}\sum_n A_n(t)\, e^{-i\omega_n t + K_n z}\left(-i\hat{x} + \frac{\alpha_{cn}}{K_n}\hat{z}\right) e^{\alpha_{cn}(x+d)} + c.c., \tag{6.16}$$

$$\mathbf{E}_c^- = \frac{1}{4}\sum_n A_n(t)\, e^{-i\omega_n t - K_n z}\left(i\hat{x} + \frac{\alpha_{cn}}{K_n}\hat{z}\right) e^{\alpha_{cn}(x+d)} + c.c. \tag{6.17}$$

Here we consider only the forward wave as the behavior of the two waves is identical. Equation (6.16) can be approximately written by

$$\mathbf{E}_c^+(x,z,t) = \frac{1}{4}\left(-i\hat{x} + \frac{\alpha_c}{K_L}\hat{z}\right) e^{\alpha_c(x+d)} \sum_n A_n(t)\, e^{-i\omega_n t + K_n z} + c.c. \tag{6.18}$$

For convenience, we rewrite the above equation:

$$\mathbf{E}_c^+(x,z,t) = \frac{1}{4}\left(-i\hat{x} + \frac{\alpha_c}{K_L}\hat{z}\right) e^{\alpha_c(x+d)} A(t,z)\, e^{-i\omega_L t + K_L z} + c.c.$$

One can see that the quantity

$$A(t,z) = \sum_n A_n(t)\, e^{-i(\omega_n-\omega_L)t+(K_n-K_L)z} \tag{6.19}$$

plays the role of the total amplitude of the SPP field with the central lasing frequency ω_L and wavenumber K_L. Therefore, we focus on the consideration of the evolution of the above amplitude. We neglect the discrete spectral structure and consider the SPP field as a continuum and rewrite Eq. (6.19) as follows:

$$A(t,z) = \int A(t,k)\, e^{-i\delta\omega t+ikz} dk, \tag{6.20}$$

where

$$k = K - K_L = \frac{n_{\text{eff}}}{c}(\omega - \omega_L), \tag{6.21}$$

$\delta\omega = \omega - \omega_L$, and $A(t,k)$ is the continuous form of the mode fields $A_n(t)$. In addition, we take coordinate transform by $T = t$, $\tau = t - v_g^{-1} z$, where T is the laboratory time, τ is the local time. Equation (6.20) is transformed into

$$A(T,\tau) = \int A(T,k)\, e^{-i[\omega(k)-v_g k]T+ikv_g\tau} dk, \tag{6.22}$$

We apply a coordinate transformation $T = t$, $\tau = t - v_g^{-1} z$, where T is the laboratory time, τ is the local time, γ *is* the frequency-dependent loss, T_R *is* the round trip time, and v_g *is* the group velocity of the SPPs. From Eqs. (6.10, 6.14), we obtain the following master equation of mode-locked SPP lasers (see Appendix D)

$$T_R \frac{\partial A}{\partial T} = [g(\tau) - q(\tau) - \gamma_0] A + \delta_1 \frac{\partial A}{\partial \tau} + \delta_2 \frac{\partial^2 A}{\partial \tau^2}, \tag{6.23}$$

where $g(\tau)$ and $q(\tau)$ are the total gain and absorber loss for a round trip given by multiplying the round trip time T_R to Eq. (6.14) but for ω_L instead ω_n, $\gamma_0 = \gamma|_{k=0}$ is the resonator loss for a round trip, δ_1 and δ_2 are first- and second-order dispersion coefficients. What we should stress here is that all the gain and losses are dimensionless quantities corresponding to those per one resonator round trip, but not the rate in unit s^{-1} as in the above section. The parameters in the above equation are given as follows. The dispersion coefficients are given by

$$\delta_1 = -\frac{i}{v_g} \left.\frac{\partial \gamma}{\partial k}\right|_{k=0} + \frac{g_i}{\Gamma_g} - \frac{q_i}{\Gamma_q}, \tag{6.24}$$

$$\delta_2 = \frac{g_i}{\Gamma_g^2} - \frac{q_i}{\Gamma_q^2} + \frac{1}{2v_g^2} \left[i \left(T_R + \frac{g_i}{\Gamma_g} - \frac{q_i}{\Gamma_q} \right) \frac{\partial^2 \omega}{\partial k^2} + \frac{\partial^2 \gamma}{\partial k^2} \right] \Bigg|_{k=0}. \tag{6.25}$$

Here the subscripts i for gain and loss represent the corresponding values just before the pulse.

For stable mode-locked operation, g_i must be partly recovered during one round trip.

The initial gain and loss rates are represented by

$$g_i = T_R \beta \int_{-D_g - D_q - d}^{-D_q - d} g_l^{'} e^{\kappa(x+d)} dx \tag{6.26}$$

and

$$q_i = T_R \beta \int_{-D_q - d}^{-d} q_l^{'} e^{\kappa(x+d)} dx, \tag{6.27}$$

respectively, where β is defined below Eq. (6.14) with the substitution $\omega_n \to \omega_L$, $g_l^{'}$ and $q_l^{'}$ are the initial nonlinear local gain and loss rates dependent on the spatial and temporal variables. The evolution of nonlinear local gain $g_l(x,\tau)$ and $q_l(x,\tau)$ are given by the equations [161]

$$\frac{\partial g_l}{\partial \tau} = -\frac{g_l - g_0(x)}{\tau_{0g}} - g_l \frac{|E_c(x,\tau)|^2}{A_{sg}^2 \tau_{0g}}, \tag{6.28}$$

$$\frac{\partial q_l}{\partial \tau} = -\frac{q_l - q_0(x)}{\tau_{0q}} - q_l \frac{|E_c(x,\tau)|^2}{A_{sq}^2 \tau_{0q}}, \tag{6.29}$$

where τ_{0g} and τ_{0q} are the upper-level lifetimes, A_{sg} and A_{sg} are the saturation fields for gain and absorber dyes, respectively.

The SPP field intensity distribution is nonuniform and the saturation at the position closer to metal surface is stronger. We do not use power expansion of the gain with intensity [161, 185, 240] but solve the combined Eqs. (6.23-6.29) self-consistently. For slow passive mode-locking the gain and absorber dyes exhibit a longer relaxation time compared with the pulse duration: τ_{0q}, $\tau_{0g} < \tau_0$. Besides, stable mode-locking operation is possible only if the conditions $0.1 \leq T_R/\tau_{0g} \leq 10$ and $\tau_{0q} < T_R$ are fulfilled [238]. The master equation for mode-locking of SPP lasers Eq. (6.23) can not be solved analytically because both the local gain and nonlinear absorption Eq. (6.28) depend on time and space, therefore we apply the split-step-Fourier method [197] to solve Eq. (6.23).

6.3. Design of long range SPP lasers

In this section, we discuss parameters of an appropriate gain and absorber medium and determine the main structural parameters supporting lasing of SPPs.

The dielectric layers a and c are assumed to be made of PMMA and we consider a metallic layer b made from silver. We restrict ourselves to the symmetric SPP mode [71] which has the smallest propagation loss. As explained in the above section, the conditions for the recovery times of gain and absorer molecules require a very short upper-state lifetime because the resonator length is, in our case, very short compared with conventional dye lasers. Therefore, we have selected dye IR-26 (Ref. [241]) as saturable absorber. As pump source for the dye gain media with an absorption band in the visible, we have chosen the SHG source of Nd-doped solid-state lasers at 532 nm. Besides, it is necessary to have an emission band of the gain dye which is extended to the absorption band of the saturable absorber. From the above conditions, we have selected Styryl-9 (Refs. [242–245]) as a dye for the gain. The PMMA polymer has been selected as a host medium.

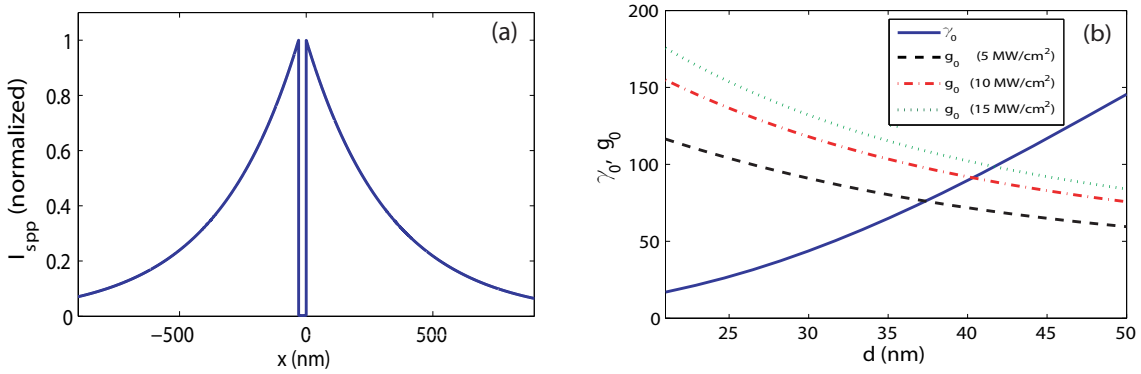

Figure 6.2.: Long range SPP intensity profile normalized by its maximum (a) and the dependence of attenuation γ_0 and linear gain g_0 on the metal film thickness d (b). Incident pump intensities 5, 10 and 15 MW/cm^2 were considered. Resonator length is 1 cm, Styryl-9 concentration is $N_g = 2.5 \times 10^{18}$ cm^{-3}, lasing wavelength is $\lambda_L = 900$ nm, the thicknesses of gain and absorber sublayers are $D_q = 400$ nm and $D_g = 5$ μm. The permittivities of each layer are $\varepsilon_a = \varepsilon_c = 2.20$ (PMMA) and $\varepsilon_b = -35.99 + 2.20i$ (silver), respectively.

Pumping and lasing wavelengths are taken to be 532 nm and 900 nm, respectively. The main parameters of the dyes are as follows: For the gain medium using Styryl-9, the cross-sections for stimulated emission at 900 nm and absorption at 532 nm are $\sigma_s = 1.8 \times 10^{-16}$ cm^2 and $\sigma_{ag} = 1.2 \times 10^{-16}$ cm^2, respectively, the upper-state relaxation time (or longitudinal relaxation time) is $\tau_{0g} = 400$ ps and the dephasing rate is $\Gamma_g = 3.3 \times 10^{13}$ Hz (see Ref. [241]). For saturable absorber molecules IR-26, the absorption cross-section is $\sigma_{aq} = 1.5 \times 10^{-16}$ cm^2 (Ref. [242]), the upper-state relaxation time (or absorber recovery time) is $\tau_{0q} = 22$ ps (Ref. [243, 244]) and the dephasing rate is $\Gamma_q = 2.5 \times 10^{13}$ Hz. All the SPP laser parameters can be calculated from the above quantities based on the formulas given in the last section. The concentrations of gain and saturable absorber molecules were taken to be 2.5×10^{18} cm^{-3} and 1×10^{17} cm^{-3}, respectively. Under the condition of CW pump operation, a severe problem in the use of dyes is the long-lived transient triplet-triplet absorption that gradually reduce the net gain and ultimately terminates the lasing process. In liquid dye lasers [246, 247], this problem is solved by a free-flying dye jets [248] and in solid dye lasers by a rotating disc [249–251]. Here we consider as an alternative a solid-state dye gain medium that is optically pumped with pulsed light sources with ns duration.

We choose a length of the SPP laser resonator of $L = 1$ cm and consider only the case of single mode guiding. From the model in Section 6.2, we can see that the upper limit of the SPP waveguide width for single mode guiding is ~ 2 μm for a thickness 30 nm of the Ag layer b [252, 253]. Here we take it to be 1.8 μm and obtain for the effective index and propagation loss $n_{\text{eff}} = 1.4988$ and $\gamma_0 = 44.78$, respectively.

The dispersion coefficient was calculated to be $\delta = (8.2 - 1.4i) \times 10^{-26}$ s^2, for the structure described above, . Below we determine the appropriate range of thicknesses for saturable absorber sublayer and metal layer b. In Fig. 6.2 we show the SPP intensity profile

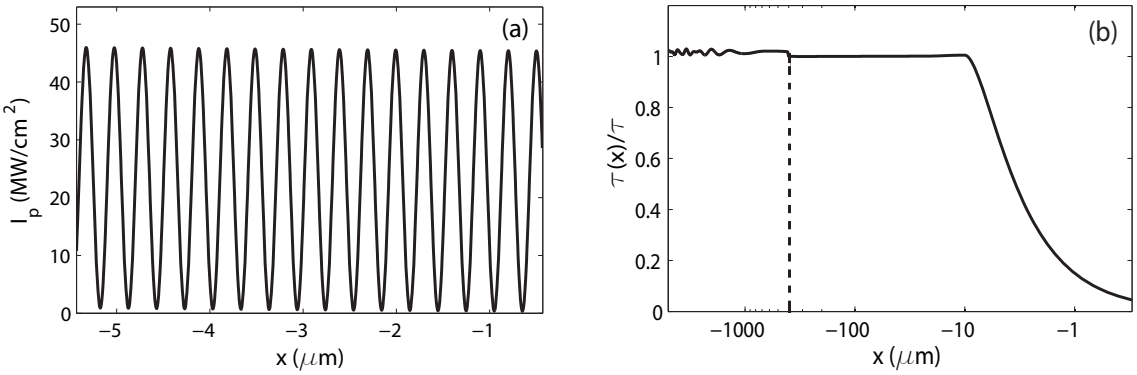

Figure 6.3.: Pump intensity distribution $I_p(x)$ in the gain sublayer (a) and normalized lifetime of upper state for both gain and saturable absorber sublayers. In (a), the intensity of incident pump beam is $I_{p0} = 15$ MW/cm^2. In (b) doted line shows the interface between gain (right) and absorber sublayers; the thickness of Ag layer b and saturable absorber sublayer are $d = 30$ nm and $D_q = 400$ nm, respectively.

(a) and the gain and loss quantities (b) for different metal layer thicknesses. In Fig. 6.2(a) we can see that the effective intensity confinement width is 227.8 nm (FWHM). This means that we must take the thickness of the absorber layer to be larger than this value if the saturation intensities for gain and absorber are nearly the same. Therefore, we take it to be 400 nm. In Fig. 6.2(b) the linear resonator loss and the unsaturated gain are shown in dependence on the film thickness d for pump intensity of 5, 10 and 15 MW/cm^2. With increasing metal film thickness the field energy becomes more concentrated towards the metal film. Therefore, we can expect that there is an upper limit of the metal film thickness for lasing. For a Ag film thicker than $d \sim 40$ nm at pump intensity 10 MW/cm^2 for $D_q = 400$ nm and $D_g = 5$ μm, the resonator loss is greater than the linear gain. Taking into account this fact, we choose the thickness of metal film as $d = 30$ nm for the consideration below.

In the final part of the section, we consider the influence of inhomogeneity of pump. The intensity of pump beam becomes inhomogeneous [see Fig. 6.3(a)] due to the absorption by the gain molecules and the formation of steady wave by the reflection from the metal film surface. The spatial modulation of pump beam is calculated by using the matrix formulation [90, 91, 254] and is taken into account in the all the simulations for mode-locking behavior. The pump absorption in saturable absorber layer, for this case, is negligible (see Fig. 6.3 in Ref. [242]). In addition the shortening of τ_{0g} due to the fluorescence quenching of gain molecules by the dipole energy transfer to metal layer [255, 256], is calculated by using the method represented in Refs. [91, 255, 256] [see Fig. 6.3(b)]. This effect is very weak because the gain sublayer is located 400 nm far from the metal film and quantum yield of Styryl-9 molecules is relatively small (0.05, see Ref. [241]). As for the saturable absorber, the decrease of upper level lifetime responsible for fluorescence accelerates the ground state recovery and makes the absorption to be recovered faster. However, the calculation shows that this effect is valid only in the sufficiently narrow region [~ 1 nm distance from metal surface, see Fig. 6.3(b)] because the fluorescence quantum yield of IR-26 dye is as small as $\sim 10^{-3}$ (Refs. [242–244]). Taking into account a very weak

lifetime shortening, we neglected this effect for both gain and absorber.

6.4. Numerical results and discussion

Figures 6.4 shows an example of our numerical study of the pulse evolution in mode-locked long range SPP lasers. Figure 6.4 shows the evolutions of gain and total loss (a), and the generated pulse profile at the position adjacent to the metal film in the dielectric layers (b).

For self-starting mode-locking, three conditions have to be satisfied [161, 238]: absorption saturation has to be stronger than gain saturation, the unsaturated net gain has to take a positive value and the net gain has to be negative before and after the pulse.

As mentioned above, for design parameters as discussed in Section 6.3 the absorber is stronger saturated than the gain because of the high confinement of the plasmon field. The unsaturated net gain per round trip is positive with a value of 59.6, while in the steady state of pulse formation, net gain before and after the pulse is negative and its value just before the pulse is about -2.02 (see Fig. 6.4(a)). The Figure 6.4(b) illustrates the dynamics of ultrashort pulse formation in the considered SPP laser: even though the response time of the gain and absorber medium is longer than the pulse duration in this regime a stable fs pulse regime is established because noise at the wings of the pulse is suppressed due to the negative net gain in this region.

In the initial stage of pulse formation the evolving pulse is shortened due to the different saturation behavior of the gain and the absorber because the absorber recovery is faster than that of the gain. This general scenario of passive mode-locking is analogous as in bulk femtosecond dye lasers [161, 238].

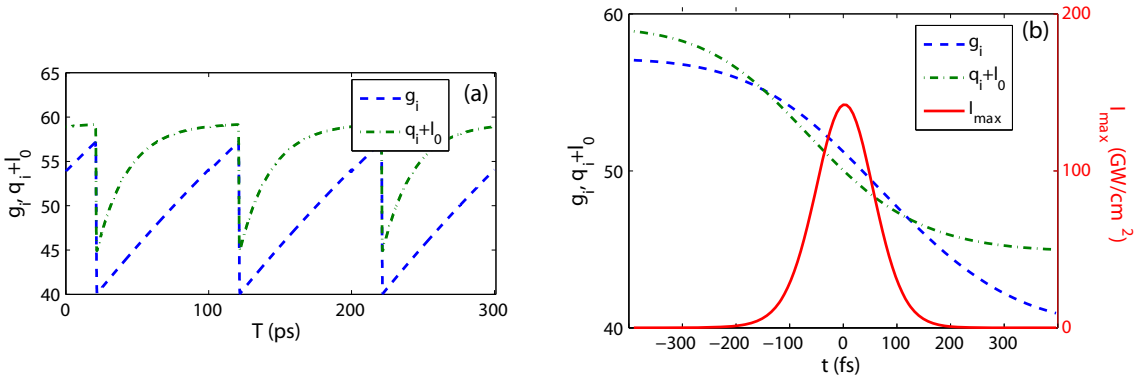

Figure 6.4.: The evolution of gain g_i and total loss $q_i + l_0$ (a), their detailed illustration near the pulse and pulse profile with maximum intensity $I_{\max}|_{x=-d}$ (at the position adjacent to Ag film in the dielectric layers a and c). The concentrations of gain and absorber molecules are $N_g = 2.5 \times 10^{18}$ cm^{-3} and $N_q = 1 \times 10^{17}$ cm^{-3}, respectively. The thicknesses of Ag film, gain and absorber sublayers are $d = 30$ nm, $D_q = 400$ nm and $D_g = 5$ μm, respectively. The intensity of incident pump beam is $I_{p0} = 10.26$ MW/cm^2.

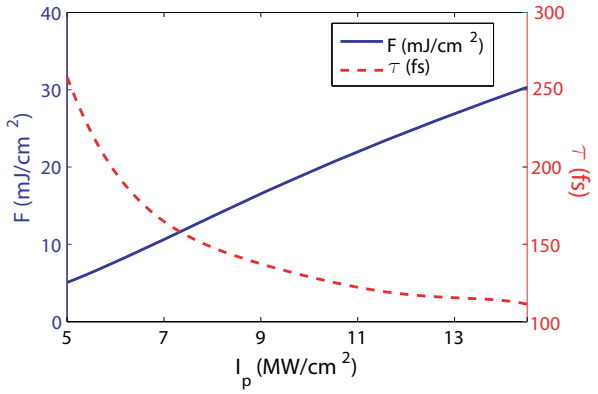

Figure 6.5.: Dependence of maximum pulse fluence $F_{\max}$ (at the position adjacent to Ag film) and duration τ on pump intensity I_p. The other parameters are the same as in Fig. 6.4.

In the example given in Fig. 6.4 for a SPP laser with a pump intensity of 10.26 MW/cm^2, a stable pulse train is formed with ~ 20 mJ/cm^2 maximum pulse fluence per pulse [at the positions adjacent to metal in the layers a and c, see Fig. 6.2 (a)]. In this case the pulse duration is 128.15 fs and the maximum peak intensity in the dielectric layers is $I_{\max} = 143$ GW/cm^2. Note that from Fig. 6.4(b) we can see that for the considered SPP laser parameters both the gain and the loss of the absorber are high and both are strongly saturated. This means that a simplified approach based on the assumption of small net gain and weak saturation [161] can not be applied for this case.

In Fig. 6.5 we show the dependence of output pulse fluence and the pulse duration, on the pump intensity. Figure 6.5 shows that the pulse fluence linearly increases and the pulse duration decreases in a nonlinear way with increasing pump intensity (see Fig. 6.5). Figure 6.5 shows that the pulse fluence linearly increases and the pulse duration decreases with increasing pump intensity. The limit for pulse shortening and growth of output fluence is set by damage threshold at roughly 1 J/cm^2 as well as by available pump sources.

To conclude, in this chapter we have studied the possibility of femtosecond plasmon pulse generation by mode-locking of long range SPP lasers. We developed a theory of passive mode-locking of SPP lasers with a Bragg resonator consisting of a silver film, a saturable absorber layer adjacent to the metal film, and a gain medium. For the specific example of solid dyes acting both as slow saturable gain medium and a slow saturable absorber the characteristic laser pulse parameters are calculated numerically. The results show that SPP femtosecond pulses with a maximum peak intensity in the range of ~ 143 GW/cm^2 and a shortest duration down to ~ 128 fs can be generated. We believe that mode-locked long range SPP lasers can find a variety of applications in ultrafast plasmonics.

7. High-order harmonic generation employing field enhancement by metallic fractal rough surfaces

In the preceding chapters, we have dealt with the interactions of ultrashort pulses and metallic nanostructures. In these cases, the pulse durations are in the range of more than tens of femtoseconds. In this chapter, we discuss an extreme nonlinear optical process in noble gases near metallic rough surfaces.

High-order harmonic generation (HHG) is an effective method for producing extreme ultraviolet (EUV) radiation and attosecond pulses, and finds applications in a wide range of fields [38]. This process can be explained by tunnel ionization of gaseous atoms in the intense laser field, the acceleration of the freed electrons in the strong electric field and finally the recombination of the electrons with the parent ion, accompanied by the emission of energetic photons.

Over several decades, techniques to increase the efficiency of HHG have been suggested. They include phase-matching in the nonadiabatic limit [257], quasi-phase matching by periodic structural modulation of hollow waveguides [258, 259], atomic density modulation [260], and phase modulation by quasi-cw counterpropagating light [261], etc. However, HHG still requires intensities higher than 10^{14} W/cm^2 available by complex and expensive femtosecond pulse amplifiers with repetition rates in the range of kHz. Recently a method of high-harmonic generation has been demonstrated that allows a significant reduction of the threshold pump power by using plasmon-assisted field enhancement in bow-tie metallic nanostructures [16] (note that some doubt on the interpretations of Ref. [16] was raised [262]). This arrangement requires only a MHz repetition rate femtosecond oscillator without amplifier. In Ref. [37], a theoretical model for HHG in noble gases near metallic tips or metallic bow-tie-shaped nanostructures has been developed which has shown good agreement with these experimental results. In the experiment reported in Ref. [16], the achieved field enhancement enabled the generation of up to the 21-th harmonic, but only a rather low conversion efficiency of about 10^{-9} in the plateau region of the harmonics has been realized by this configuration based on a bow-tie nanostructure. Therefore, the study of other configurations with larger total interaction volume of field enhancement and higher HHG efficiency is desirable.

In the present chapter, we study metallic rough surfaces [65], as an alternative to bow-tie structures, for the realization of plasmonic field enhancement for the HHG process in the vicinity of noble gas atoms. We show that the proposed self-affine fractal structure for a rough surfaces allows intensity enhancement factors larger than 10^3 and therefore permits corresponding low threshold pump intensities of about 100 GW/cm^2 for the generation of harmonics up to the order of 50. For grazing incidence of s-polarized pump pulses, the interaction volume in the HHG process can be increased and the efficiency of HHG in the

plateau is in the range of 10^{-7}.

7.1. Basics of HHG and Lewenstein model

In this section, we review the basic principle and general aspects of HHG through nonperturbative interactions between noble gas atoms and incident pulse. Next, we review the Lewenstein model as a theoretical tool for the consideration of this phenomenon.

For light pulses , the energy of which is much less than the ionization energy of the atom, the interactions between the atoms and light can be considered in the frame of perturbation theory. By using this approach, it is possible to describe the classical nonlinear optical processes including second-, third-harmonic generation, optical parametric generation and amplification, self- or cross-phase modulation, etc. In the classical nonlinear optics, the processes depend on the intensity of incident light but not on its phase.

For a very strong pulse, the interaction process cannot be considered in the perturbative approach, because the atoms in the light field can be ionized and this state is significantly changed from the initial state. This clearly can not be approximated by perturbative approach. Nonlinear optics in this regime is called extreme nonlinear optics. In extreme nonlinear optics, the process depends not only on the intensity of the incident pulse but also on the relative phase, the carrier-envelope phase (CEP).

7.1.1. Principle of HHG: three-step model

High-order harmonic generation (HHG) is one of the typical extreme nonlinear optical process. Basically, HHG process in atomic gases can be easily understood based on the classical three-step model [263]. In this model, the basic processes involved in HHG is can be divided by the three steps: tunnel ionization of the neutral atoms, acceleration of the ionized electrons far away from their nuclei, returning and recombination with them. This model is called three-step model and is widely accepted for the simple consideration for HHG process.

In the first step (I in Fig. 7.1), the strong field of light pulse reduces the Coulomb potential and the electron can be escaped from the nucleus to the continuum state through the tunneling. If the pump intensity is so high that the value of Keldysh parameter [264] is smaller than unity, tunneling ionization dominates over the multiphoton ionization.

In the second step, the electron is accelerated during the every first half cycle of pump light (II in Fig. 7.1). During this step, the electrons gain the kinetic energy named ponderomotive energy represented by

$$U_p = \frac{e^2 E^2}{4 m_e \omega_0^2}, \tag{7.1}$$

where e is the electron charge, E is the electric field intensity, m_e is electron mass and ω_0 is the central angle frequency of pump light. The above equation shows that the ponderomotive energy is proportional to the pump intensity for a given frequency.

In the third step, the electron changed its moving direction, collides and recombines to the parent ion during the second half cycle (III in Fig. 7.1). During this step, the

electron releases its kinetic energy and ionization energy to the harmonic photons. From this consideration, we can predict the maximum photon energy given by cutoff law:

$$\hbar\omega_{\max} = I_p + 3.2U_p, \tag{7.2}$$

where I_p is the ionization energy for the atom in consideration.

The above descriptions are valid only for the system satisfying the condition

$$\hbar\omega_0 \ll I_p \ll U_p. \tag{7.3}$$

This model gives a clear physical picture for HHG processes though the quantitative accuracy is not very high.

7.1.2. Lewenstein model

The Lewenstein model or strong field approximation [265] is a fully quantum mechanical model for the HHG process. This model is based on a nonperturbative approach and is also called strong field approximation. Below we introduce this theory presented in Ref. [265].

The time-dependent Schrödinger equation describing the process is given by

$$i\left|\Psi(\mathbf{r},t)\right\rangle = \left[-\frac{1}{2}\nabla^2 + \hat{V}(\mathbf{x}) - E(t)x\right]\left|\Psi(\mathbf{r},t)\right\rangle \tag{7.4}$$

in atomic unit, where $\hat{V}(\mathbf{x})$ is the Coulomb potential and $E(t)$ is the electric field of light.

Below we assume that the pump is polarized linearly and the considerations are limited to the case of single electron ionization (one atom can release only one electron). The ionization energy is assumed to be much larger than unit. Intermediate resonances are neglected because the pump intensity is very strong.

Upon ionization, the state of the electron is changed from the ground $|0\rangle$ to a continuum state $|\mathbf{v}\rangle$.

In this model, one assumes the following conditions [265]:

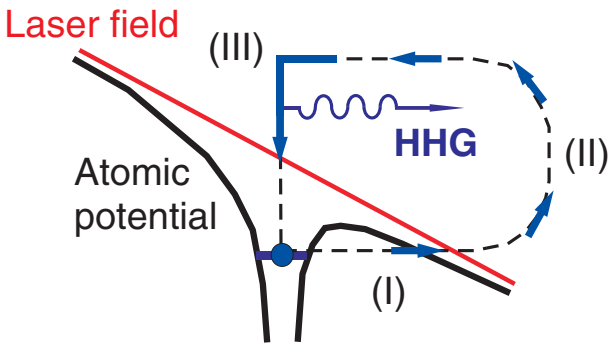

Figure 7.1.: Three-step model for HHG [263]: (I) Tunneling ionization, (II) Acceleration of electrons in the electric field, (III) recombination and emission of high-order harmonics.

i) The contribution to the evolution of the system in bound states except the ground state can be neglected.

ii) The depletion of the ground state can be neglected. This assumption means that the ponderomotive energy is not saturated by the pump because the pump intensity is not too high.

iii) The electrons in the continuum state can be dealt with as a free particle moving in the field with no effect caused by the potential $\hat{V}(\mathbf{x})$.

The wave function can be represented by superposition of the ground state $a(t)|0\rangle$ and all the continuum states $b(\mathbf{v},t)|\mathbf{v}\rangle$:

$$|\Psi\rangle = e^{iI_p t}\left[a(t)|0\rangle + \int d^3\mathbf{v}\, b(\mathbf{v},t)|\mathbf{v}\rangle\right]. \tag{7.5}$$

The exponential term in the above equation represents the oscillations of the ground state corresponding to the energy for the ionization. From the assumption (ii), $a(t) \approx 1$ and $\dot{a}(t) \approx 0$. Now the problem reduces to finding the continuum state amplitude $b(\mathbf{v},t)$. From the wave equation Eq. (7.4), it must satisfy the following equation

$$\dot{b}(\mathbf{v},t) = -i\left(\frac{\mathbf{v}^2}{2} + I_p\right) b(\mathbf{v},t) - E(t)\frac{\partial b(\mathbf{v},t)}{\partial v_x} + iE(t)\, d_x(\mathbf{v}). \tag{7.6}$$

In the above equation, $\mathbf{d}(\mathbf{v})$ is the dipole-matrix element for the bound-free transition and d_x is the parallel to the polarization axis.

The solution of Eq. (7.6) can be represented by

$$\begin{array}{c} b(\mathbf{v},t) = i\int_0^t dt' E(t')\, d_x(\mathbf{v}+\mathbf{A}(t)-\mathbf{A}(t')) \\ \times \exp\left\{-i\int_{t'}^t dt''\left[(\mathbf{v}+\mathbf{A}(t)-\mathbf{A}(t''))^2/2 + I_p\right]\right\} \end{array}, \tag{7.7}$$

where $\mathbf{A}(t) = \int_{-\infty}^t \mathbf{E}(t')\, dt'$is vector potential. The induced dipole moment is written by

$$x(t) = \int d^3\mathbf{v}\, d_x^*(\mathbf{v})\, b(\mathbf{v},t) + c.c. \tag{7.8}$$

In the above equation, we neglected the contribution from continuum-continuum part and have considered only the transitions from the continuum to the ground state. Now, we introduce a canonical momentum

$$\mathbf{p} = \mathbf{v} + \mathbf{A}(t). \tag{7.9}$$

After some math, we obtain the final expression for the dipole moment

$$\begin{array}{c} x(t) = i\int_0^t dt' \int d^3\mathbf{p} E(t')\, d_x(\mathbf{p}-\mathbf{A}(t')) \\ \times d_x^*(\mathbf{p}-\mathbf{A}(t)) \exp\left[-iS(\mathbf{p},t,t')\right] + c.c. \end{array}, \tag{7.10}$$

where

$$S(\mathbf{p},t,t') = \int_{t'}^t dt''\left(\frac{[\mathbf{p}-\mathbf{A}(t'')]^2}{2} + I_p\right) \tag{7.11}$$

is the classical action.

The first term in Eq. (7.10) $E(t')\,d_x(\mathbf{p}-\mathbf{A}(t'))$ is the probability amplitude for an electron to make the transition to the continuum at time t' with the canonical momentum $\mathbf{p}$. The exponential term including classical action in the above equation, describes the free moving of the electron. The complex conjugate term of the dipole matrix element $d_x^*(\mathbf{p}-\mathbf{A}(t))$ can be interpreted as the probability amplitude for a recombination of the electron and the parent ion at the moment t.

In Eq. (7.10), the main contribution to high harmonics comes from the electrons which escape from the nucleus through the tunneling ionization at time t and recombine to its parent ion at time t'. This condition can be represented by the equality $x(t)=x(t')$. In another way, this condition can also be written by

$$\nabla_{\mathbf{p}} S(\mathbf{p},t,t') = 0. \tag{7.12}$$

The above condition is identical to the condition for so called stationary point in mathematics. In other words, the above physical consideration is equal to apply the stationary point method for the calculation of integral in the right side of Eq. (7.10). This can be mathematically understood from the fact that the change of d is much slower than the classical action which is the precondition for the applicability of this approximation method.

By using the condition Eq. (7.12), we can rewrite Eq. (7.10) as follows:

$$\begin{array}{c} x(t) = i\int_0^\infty d\tau \left(\frac{\pi}{\varepsilon+i\tau/2}\right)^{1.5} d_x^*\left[p_{st}(t,\tau)-A_x(t)\right] \\ \times d_x\left[p_{st}(t,\tau)-A_x(t-\tau)\right] E(t-\tau)\exp\left[-iS_{st}(t,\tau)\right]+c.c. \end{array}, \tag{7.13}$$

where is a certain small constant, p_{st} and S_{st} are the canonical moment and classical action under the condition Eq. (7.12).

For hydrogen-like atoms, the ground state wave function is described by

$$\Psi(\mathbf{x}) = \left(\frac{\alpha^{3/4}}{\sqrt{\pi}}\right) e^{-\sqrt{\alpha}|\mathbf{x}|}, \tag{7.14}$$

where $\alpha = 2I_p$. In this case, the dipole matrix element for hydrogen-like atoms takes the form

$$\mathbf{d}(\mathbf{p}) = i\left(\frac{2^{7/2}\alpha^{5/4}}{\pi}\right)\frac{\mathbf{p}}{\left(\mathbf{p}^2+\alpha\right)^3}. \tag{7.15}$$

The quantities at the stationary points are given by:

$$p_{st}(t,\tau) = \frac{1}{\tau}\int_{t-\tau}^{t} dt' A(t'), \tag{7.16}$$

$$S_{st}(t,\tau) = \left(I_p - \frac{1}{2}P_{st}^2\right)\tau + \frac{1}{2}\int_{t-\tau}^{t} dt' A^2(t') \tag{7.17}$$

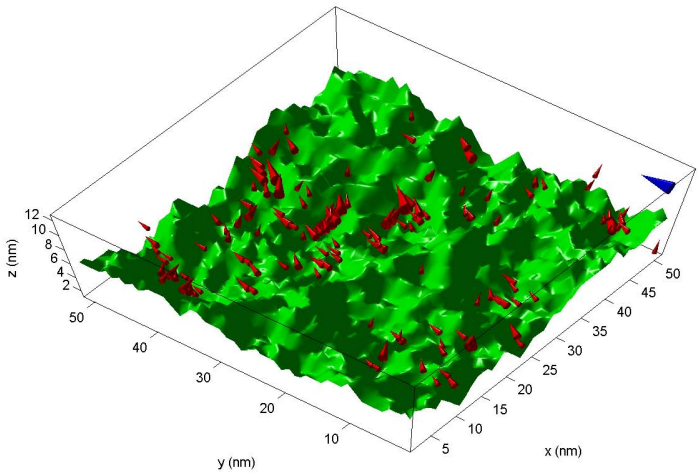

Figure 7.2.: Structure of the rough surface and enhanced field distribution. The surface structure is illustrated by green color and relative magnitudes and directions of enhanced field are shown by red cones. The blue cone shows the polarization of incident field at 800 nm. Voxel size of 1 nm and 50 nm $\times$ 50 nm samples were considered.

7.2. Highly efficient HHG near metallic fractal rough surface

Previously, the giant enhancement of local fields on thin metallic rough films of nanometer-sized roughness features in colloidal aggregates or other random nanocomposites has been studied in a large number of papers (see e.g. [65, 92, 266]). These results suggest that the metallic film surfaces obtained by deposition have self-affine fractal structures. These metallic random surfaces are not characterized by translational invariance but rather by scaling invariance.

Therefore surface-plasmon eigenmodes are excited being strongly localized in “hot spots” on subwavelength characteristic roughness scales. The local fields in the “hot spots” on a fractal rough surface are significantly enhanced in comparison with the input fields. Plasmon field-enhancement can be used for a multitude of highly efficient nonlinear processes, e. g., for second and third harmonic generation [13–15], and others. The main advantage of metallic rough surfaces as an inexpensive and strongly field-enhancing element is their applicability in processes which produce very weak signals or have a high threshold.

We describe a random metallic rough surface by the restricted solid-on-solid model [93] which very well describes the self-affine fractal structure typical for metal films produced by thermal evaporation or sputtering of metal onto an insulating substrate. In this model, particles are added one by one on top of the growing surface at random positions. These particles have a form of cubes (so-called voxels) and are added only when the newly created interface does not have steps higher than the size of one voxel.

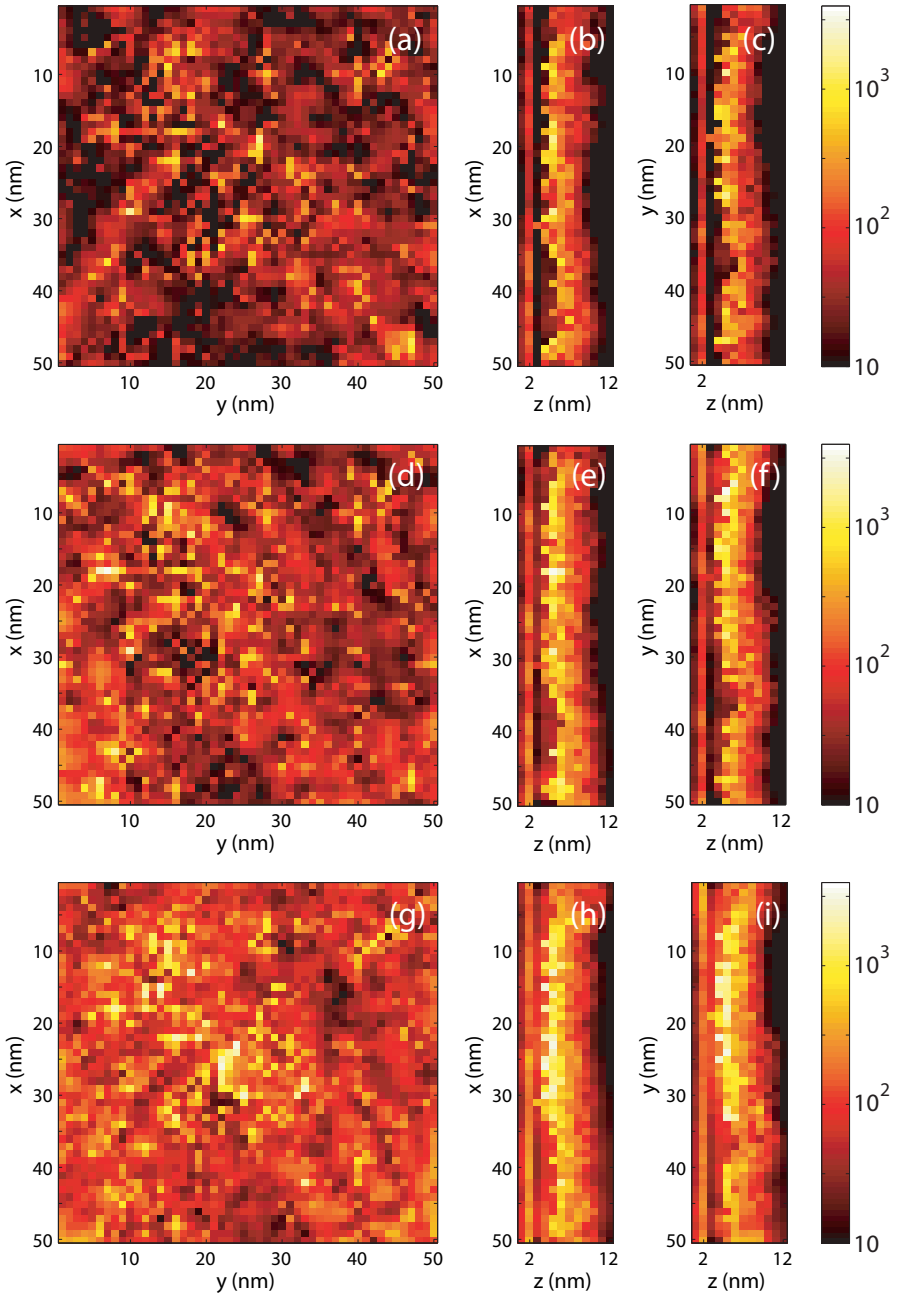

Figure 7.3.: Maximum intensity enhancement factor in different cross-sections for different wavelengths: 700 nm (a)-(c); 800 nm (d)-(f); 900 nm (g)-(i).

The enhanced field distribution for a silver fractal rough surface calculated by the discrete-dipole approximation [59] is shown in Fig. 7.2 by red cones together with the 800-nm incident field characterized by the blue cone. The cone directions indicate the polarization and the cone sizes the field enhancement factor. The figure shows that the enhanced field is localized at random positions due to the existence of localized modes on the fractal surface structure. Note that the calculated field has no "hot spots" at the boundaries of the

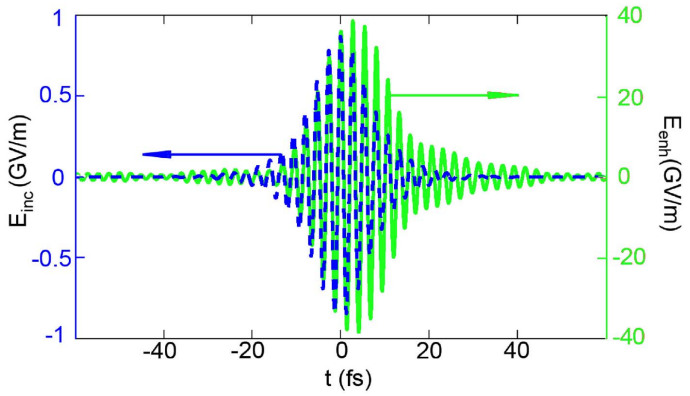

Figure 7.4.: Incident pulse (blue dotted line) and enhanced pulse (green line) profiles on the rough Ag surface for one of the realizations of random surface. Maximum field enhancement is more than 40 which corresponds to the instant intensity enhancement of ~ 2000.

computation domain which could arise by numerical artifacts. The simulation also shows that the physical size of voxels does not affect the maximum enhancement factor and the statistical characteristics of the field distribution.

For the study of HHG in a noble gas in the vicinity of the metallic rough surface, we have to calculate the field enhancement in the spectral range of the pump pulse. Here we consider 10 fs input pulses at central wavelength of 800 nm and calculate the field enhancement distribution in the spectral range of ~ 600 nm to ~ 1000 nm.

In Fig. 7.3, we show the maximum enhancement factor distribution for wavelengths at 700 nm, 800 nm and 900 nm. One can see that plasmonic hot-spots are formed at different locations depending on the wavelengths which is a typical feature of fractal surfaces [92]. The intensity enhancement factors range up to maximum values of ~ 5000, and the density of "hot spots" is higher for longer wavelengths, as found also in previous observations [92].

As we mentioned in the end of Subsection 2.2.4, for few femtosecond pulses with peak intensity of about 100 GW/cm^2 the nanostructured metal can be regarded as linearly responding medium and in this chapter we limit ourselves to the consideration of such pump pulses.

Using the wavelength-dependent field enhancement factors and the pump pulse spectrum, we reconstruct the temporal profile of the enhanced pulse by using the inverse Fourier transformation. In Fig. 7.4, we show an example of a pulse shape located at one of the "hot spots". The figure shows that the enhanced temporal pulse shape is delayed and stretched. This phenomenon is attributed to the dispersion of the plasmonic response on the surface.

In the calculation of the high harmonics we select only spots with a maximum intensity enhancement larger than 100 because other spatial positions do not contribute to HHG. For the calculation of HHG we apply the Lewenstein model [265]. The induced dipole moment for HHG is calculated by using the Lewenstein model (7.13). The only difference is that the field is replaced by the enhanced local field on the rough metal surface.

Next we perform simulations of the HHG spectrum and the efficiency by using the

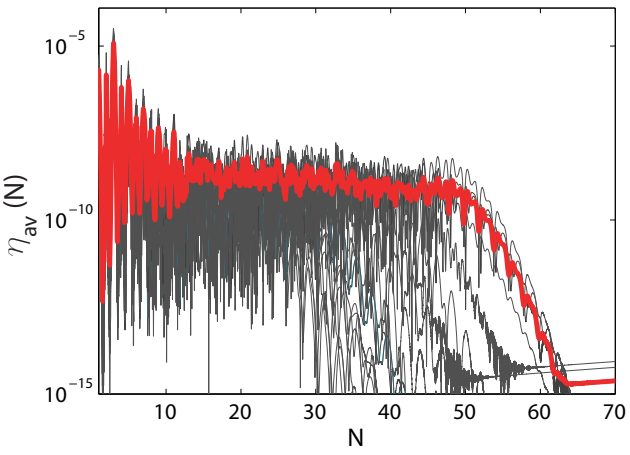

Figure 7.5.: The HHG efficiency $\eta_{\mathrm{av}}(N)$ as a function of harmonic orders N averaged over an ensemble of 20 random samples (thick red line) and for some of the individual samples (thin gray lines).

spectral distribution of the field enhancement factors for a 10 fs, 100 GW/cm^2 pump pulse with a central wavelength at 800 nm and substitute the local fields of this pulse in the "hot spots" into the expression Eq. (7.18) for the HHG dipole moment of surrounding argon atoms at a pressure of 0.18 atm.

The efficiency of harmonic generation is calculated by using the formula

$$\eta(N) = \omega^4 MT\left(12\pi\varepsilon_0 c^3 V\right)^{-1} \int |x(\omega)|^2 dV/\Phi, \tag{7.18}$$

where V is the volume of the space in consideration, $N = \omega/\omega_0$ is the harmonic order, $M = \omega_0/\Delta\omega$, ω_0 is the central frequency of the incident pulse, T and $\Delta\omega$ are the time window and frequency resolution of the numerically performed Fourier transformation, and Φ is the total pulse energy of the incident pulse propagating along the rough surface of the metallic substrate sample. The above equation has been obtained based on the theory of radiation power by a dipole. The reason for the occurrence of T and M in the above equation is as follows. Because the calculation is performed in a time window with a width of T and all the frequency components are harmonic in this window, the total energy for corresponding frequency must be multiplied with T. On the other hand, since $M = \omega_0/\Delta\omega$ and the numerical Fourier transform is performed with a frequency discretization of $\Delta\omega$, we have to add scaling factor M in Eq. (7.18).

In Fig. 7.5, we show the spectral distribution of the calculated HHG efficiency for perpendicular incidence of the pump with respect to the base plane of the rough surface as a function of harmonic order N. The spatial beam shape is approximated by a rectangular shape with constant intensity. The efficiency of several elementary samples are presented by the gray curves and the red curve is the averaged efficiency over an ensemble of 20 samples.

For harmonics in the plateau the efficiency is in the range of $10^{-8} \sim 10^{-9}$. In the case

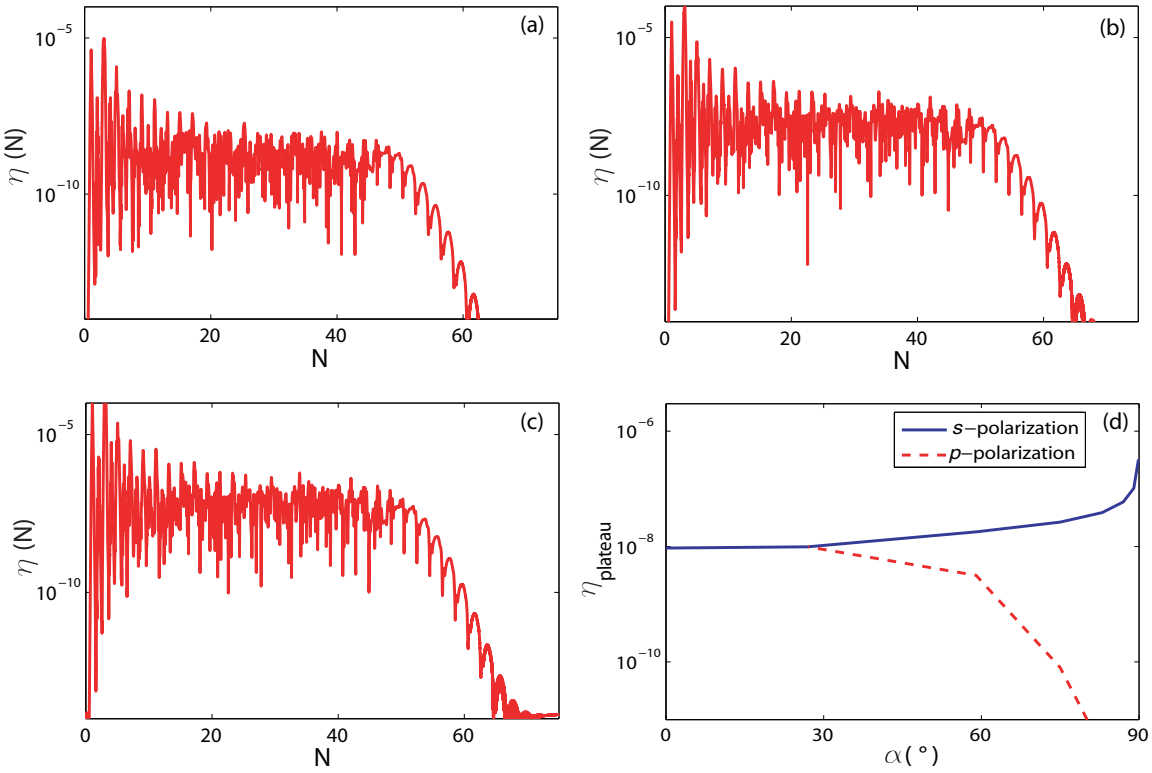

Figure 7.6.: The dependence of HHG efficiency on the incident angle for *s*- (blue curve) and *p*- (red curve) polarizations of the pump beam. HHG efficiency spectra for incident angles 0 °, 89 ° and 89.9 ° for *s*-polarization are shown in (a), (b) and (c), respectively. In (d), the HHG efficiencies in the range of plateau are shown.

of normal incidence of the pump pulses the interaction volume is restricted to the range of the beam spot size. This interaction volume can be significantly increased for grazing incidence of the pump.

In Fig. 7.6, we show the dependence of the spectral distribution of the efficiency for different incident angles and polarizations on the given fractal surface sample of Ag under the same pump condition as in Fig. 7.5. For the *p*-polarized pump pulse with grazing incidence, the main energy is contained in the component perpendicular to the base plane of the sample, leading to low enhancement factors and efficiency [92]. On the other hand, for grazing incident *s*-polarized pump, the pump field remains parallel to the surface and the interaction length is much longer than in the case of normal incidence. Under this arrangement, the HHG efficiency can be increased because the enhancement factors remain roughly the same for grazing incidence. In the case of *s*-polarization with incident angle of 89.9 °, the efficiency for harmonics in the plateau is increased by more than a factor of 30 compared with the case of normal incidence and is 1.1×10^{-7}which is approximately 2 orders of magnitude larger than the result in Ref. [16] obtained with a bow-tie gold nanostructure. In Fig. 7.6(d), the efficiencies are calculated for the harmonic spectrum

averaged over the plateau. The figure shows that the efficiency increases with the increase of incident angle for *s*-polarization and decreases for *p*-polarization.

In conclusion, we have studied plasmon-enhanced HHG in noble gases in the vicinity of metallic rough surfaces with a self-affine fractal structure. The enhanced pulse near the surface is calculated by using the discrete-dipole approximation. The results show that by using these surfaces, it is possible to achieve intensity enhancement factors in the range of 10^3. We predict that thanks to the corresponding reduction of the HHG threshold, laser pulses with peak intensity of only 100 GW/cm^2 and pulse duration of 10 fs can be used for the generation of extreme ultraviolet radiation with harmonic order up to 50. For grazing incidence of s-polarized pump beams, the efficiency for harmonics in the plateau is in the range of 10^{-7} and 2 orders of magnitude larger than the previous experimental result based on the utilization of bow-tie nanostructures.

8. Conclusion

This work is related to the nonlinear optical property of dielectric composites doped with metal nanoparticles, generation of ultrashort pulses and their high harmonics and controlling their propagation velocity in the metallic nanostructures.

The summarized results are as follows:

Nonlinear optical properties of metal nanocomposite and saturable absorption

• For very weak pump intensities, the magnitude of the effective degenerate third-order nonlinear susceptibility of metal nanocomposites is significantly increased near the surface plasmon resonance (SPR). For instance, for silica glass doped with Ag nanospheres with a diameter of 30 nm it was in the order of 10^{-15} m^2V^{-2} even for very low filling factor of 10^{-4}. Near SPR, its real part changes its sign and the imaginary part has a peak. Each main SPR has a corresponding peak of the effective third-order susceptibility. (Section 3.1)

• Based on the self-consistent formalism for the field enhancement factor, we have presented a method for obtaining the intensity-dependent dielectric function of metal nanocomposites. For spherical NPs smaller than 10 nm, saturable absorption appeared for a pump intensity higher than ~ 10 MW/cm^2. (Section 3.3)

For non-spherical nanoparticles, the field distribution is calculated by the modified discrete dipole approximation with self-consistently obtained enhancement factors and is applied for the calculation of intensity-dependent effective nonlinear dielectric function (Section 3.4). These materials exhibit the strong saturation near the surface plasmon resonance and this has been attributed to the blue spectral shift of the surface plasmon resonance peak depending on the pump intensity (see Section 3.2).

Ultrafast nonlinear optical response and non-degenerate susceptibility of metal nanocomposite

• From the semiclassical two-temperature model, we have obtained an explicit direct relation between the transient dielectric function of metal under the excitation with ultrashort pulse (Section 4.1) and have confirmed it by comparison with experimental data. (Section 4.2)

• We have presented the formula for the non-degenerate nonlinear susceptibility by using the above results for the transient response. (Section 5.1)

Femtosecond pulse generation by passive mode-locking of visible solid state lasers

and semiconductor disk lasers

• Taking a Ho:YLF laser lasing at 545 nm as an example, we have studied the behavior of the passively mode-locked solid state lasers with metal nanocomposite materials. In the non-soliton regime, the resultant pulse has the frequency peak in the central part. The dominant contribution is come from the Kerr-effect in the gain medium providing the temporal shift of frequency peak with the same extent as the intensity profile. The shortest pulse duration was about 120 fs. (Section 4.4)

• We have investigated the passive mode-locking behavior of the semiconductor disk lasers lasing in the visible range. The pulse is stabilized by the balance between the pulse shortening by the dynamic net gain and the nonlinear phase change in the gain. The shortest pulse duration was about 50 fs. (Section 4.5)

Slow light by plasmonic pulsation in the metal nanocomposites

• We have suggested the principle of a method for slowing down the probe pulses in metal nanocomposites. By the saturable absorption and the absorption recovery by electron-phonon relaxation, the absorption band exhibits a narrow dip under the illumination with a strong pump beam and a weak probe pulse. (Section 5.3)

• The achievable maximum bandwidth-delay product was 0.5, which is 2.5 times larger than that for the coherent population oscillation. (Section 5.4)

• We have suggested a scheme of slow light and all-optical delay of images using backward degenerate four-wave mixing. With low pump intensity up to 8 MW/cm^2, fractional delay of about unity has been confirmed for 1 ps pulses. This scheme could be applied for all-optical delay of images thanks to the optical phase conjugate feature of the reflected signal pulse. (Section 5.5)

Femtosecond plasmon pulse generation by mode-locking of long-range surface plasmon polariton lasers

• We have suggested a structure which can provide lasing of femtosecond long range surface plasmon polariton pulses. For a strong field confinement near the metal surface, the saturable absorber is saturated stronger than the gain which is a precondition for slow absorber mode-locking. (Section 6.1)

• We have developed a theoretical model for the passive mode-locking of the surface plasmon polariton. (Sections 6.2 and 6.3) The numerically obtained shortest pulse duration is 130 fs. (Section 6.4)

Plasmon-enhanced high-order harmonic generation on the metallic fractal rough surfaces

• The field enhancement factor on the metallic fractal rough surfaces was more than 3000, enabling high-order harmonic generation with pump peak intensity of 100 GW/cm^2

or even weaker, which is 3 orders lower than the traditional ones. In particular, for grazing incidence of s-polarized pump beams, the efficiency for harmonics in the plateau is in the range of 10^{-7} and 2 orders of magnitude larger than the previous experimental result based on the utilization of bow-tie nanostructures. (Chapter 7)

Appendices

A. Conjugate gradient method

For large scale linear equation system like Eq. (2.34), it is difficult to obtain the exact solutions. To obtain the approximate solution, the conjugate gradient method can be applied. Here, we introduce a modified conjugate gradient method for complex linear matrix equation applied by Draine [58]. For convenience, let us write the equation to be solved as follows: $Cx = y$, where C is the matrix, x is a vector to be solved, and y is a known vector. Let x to be the initial guess for x. First the following initial quantities are calculated.

$$z = C^{\dagger} y, \tag{A.1}$$

$$g_0 = z - C^{\dagger} C x, \tag{A.2}$$

$$p_0 = g_0, \tag{A.3}$$

$$w_0 = C x_0, \tag{A.4}$$

$$v_0 = C p_0, \tag{A.5}$$

where superscript † represents the Hermitian of a matrix: $\left(C^{\dagger}\right)_{jk} = \left(C_{kj}\right)^{*}$. Next iterate the following steps to improve the accuracy of the solution x_i:

$$\alpha_i = \frac{\langle g_i \mid g_i \rangle}{\langle v_i \mid v_i \rangle}, \tag{A.6}$$

$$x_{i+1} = x_i + \alpha_i p_i, \tag{A.7}$$

$$w_{i+1} = w_i + \alpha_i v_i, \tag{A.8}$$

$$g_{i+1} = z - C^{\dagger} w_{i+1}, \tag{A.9}$$

$$\beta_i = \frac{\langle g_{i+1} \mid g_{i+1} \rangle}{\langle g_i \mid g_i \rangle}, \tag{A.10}$$

$$p_{i+1} = g_{i+1} + \beta_i p_i, \tag{A.11}$$

$$v_{i+1} = Cg_{i+1} + \beta_i v_i. \tag{A.12}$$

B. Derivation of Eq. (3.13)

For convenience, we take the simplified notations

$$\xi = |x|^2,$$

$$y = |E_0|^2.$$

Then Eqs. (3.9, 3.12) become

$$x = \frac{x_0}{1+q\xi y} \tag{B.1}$$

and

$$\xi + (q+q*)\,\xi^2 y + |q|^2\,\xi^3 y^2 = |x_0|^2. \tag{B.2}$$

On the other hand, the effective dielectric function can be approximately expanded by the power series of y:

$$\varepsilon_{\text{eff}} = \varepsilon_h \frac{1+2\sigma f}{1-\sigma f} - \frac{3f\varepsilon_h}{(1-\sigma f)^2}\left.\frac{\partial x}{\partial y}\right|_{y=0} y$$

$$-\frac{3f\varepsilon_h}{(1-\sigma f)^4}\left[(1-\sigma f)^2\left.\frac{\partial^2 x}{\partial y^2}\right|_{y=0} - 2f(1-\sigma f)\left.\frac{\partial x}{\partial y}\right|_{y=0}^2\right] y^2 + \cdots. \tag{B.3}$$

Differentiating (B.1) , we obtain

$$\frac{\partial x}{\partial y} = -\frac{x_0 q\left(\frac{\partial \xi}{\partial y} y + \xi\right)}{(1+q\xi y)^2}, \tag{B.4}$$

$$\frac{\partial^2 x}{\partial y^2} = -x_0 q \frac{\left(\frac{\partial^2 \xi}{\partial y^2} y + 2\frac{\partial \xi}{\partial y}\right)(1+q\xi y)^2 - 2\left(\frac{\partial \xi}{\partial y} y + \xi\right)^2 (1+q\xi y)}{(1+q\xi y)^4}. \tag{B.5}$$

Eq. (B.2) leads to

$$\frac{\partial \xi}{\partial y} = -\frac{(q+q^*)\,\xi^2 + 2|q|^2\,\xi^3 y}{1+2(q+q^*)\,\xi y + 3|q|^2\,\xi^2 y^2}. \tag{B.6}$$

From Eqs. (B.4-B.6),

$$\left.\frac{\partial x}{\partial y}\right|_{y=0} = -x_0 q\xi, \tag{B.7}$$

$$\left.\frac{\partial^2 x}{\partial y^2}\right|_{y=0} = 2x_0 q\,(q+q^*)\,\xi^2, \tag{B.8}$$

For very low filling factor ($f \ll 1$), we obtain the approximation

$$\varepsilon_{\text{eff}} = \varepsilon_h \frac{1+2f\sigma}{1-f\sigma} + f\chi_m^{(3)} r |E_0|^2 - f\chi_m^{(3)} r |x_0|^2 (2q+q^*) |E_0|^4 ..., \tag{B.9}$$

where $\sigma = 1 - x_0$ and $r = x_0^2 |x_0|^2$.

C. Derivations of Eqs. (5.4, 5.5, 5.19, and 5.20)

• ***Derivation of Eqs. (5.4 and 5.5)***

The nonlinear polarization density is described by

$$P^{NL}(t) = \varepsilon_0 \Delta\varepsilon_m(t) E^{\text{enh}}(t). \tag{C.1}$$

Under the assumption that there are only the three field components with ω_1, ω_2 and ω_3, we can rewrite the above polarization as a sum of individual polarization components with the corresponding frequencies:

$$P^{NL}(t) = \sum_j P_j^{NL}(\omega_j) e^{-i\omega_j t}. \tag{C.2}$$

From Eqs. (5.1, 5.2), we have

$$\begin{aligned}
\Delta\varepsilon_m(t) = \chi_m^{(3)} \Bigg\{ & \left(\left|E_1^{\text{enh}}\right|^2 + \left|E_2^{\text{enh}}\right|^2 + \left|E_3^{\text{enh}}\right|^2 \right) + \\
& \frac{1}{[1+i(\omega_1-\omega_2)\tau_{ee}][1+i(\omega_1-\omega_2)\tau_{ep}]} E_1^{\text{enh}*} E_2^{\text{enh}} e^{i(\omega_1-\omega_2)t} + c.c. + \\
& \frac{1}{[1+i(\omega_1-\omega_3)\tau_{ee}][1+i(\omega_1-\omega_3)\tau_{ep}]} E_1^{\text{enh}*} E_3^{\text{enh}} e^{i(\omega_1-\omega_3)t} + c.c. + \\
& \frac{1}{[1+i(\omega_2-\omega_3)\tau_{ee}][1+i(\omega_2-\omega_3)\tau_{ep}]} E_2^{\text{enh}*} E_3^{\text{enh}} e^{i(\omega_2-\omega_3)t} + c.c. \Bigg\}
\end{aligned} \tag{C.3}$$

Substituting Eq. (C.3) into Eq. (C.2), considering Eq. (C.2) and the relation between the enhanced and incident field amplitudes, we obtain the Eq. (5.4) and Eq. (5.5).

To derive Eqs. (5.4, 5.5), we have applied the generalized effective medium approximation for the nonlinearity [see Eq. (2.60)]

$$E_i(\omega_i) \sum_{j,k,l} \chi_{\text{eff}}^{(3)}(\omega_i;\omega_j,\omega_k,\omega_l) E_j(\omega_j) E_k(\omega_k) E_l(\omega_l) = f P_j^{NL}(\omega_j) E_j^{\text{enh}}(\omega_j) \tag{C.4}$$

and assumed that the filling factor is much smaller than unity and the nonlinearity of the host is neglected.

• ***Derivation of Eqs. (5.19 and 5.20)***

Intensity of the total enhanced field is approximately described by

$$\left|E^{\text{enh}}(t)\right|^2 = \left|E_p^{\text{enh}}\right|^2 + E_p^{\text{enh}*}\int E_{\text{pr}}^{\text{enh}}(\Omega)\, e^{i\Omega t} d\Omega + c.c., \tag{C.5}$$

where we take into account that probe is much weaker than pump. From Eq. (5.2), we have

$$\varepsilon_m(t) = \varepsilon_{m0} + \chi_m^{(3)}\left[\left|E_p^{\text{enh}}\right|^2 + E_p^{\text{enh}*}\int \frac{E_{\text{pr}}^{\text{enh}}(\Omega)}{1+i\Omega\tau} e^{i\Omega t} d\Omega + E_p^{\text{enh}}\int \frac{E_{pr}^{\text{enh}*}(\Omega)}{1-i\Omega\tau} e^{i\Omega t} d\Omega\right]. \tag{C.6}$$

The electric displacement in metal NPs can be written by

$$D_m(t) = \varepsilon_m(t) E_{enh}(t)$$

$$= \left\{\varepsilon_{m0} + \chi_m^{(3)}\left[\left|E_p^{\text{enh}}\right|^2 + E_p^{\text{enh}*}\int \frac{E_{pr}^{\text{enh}}(\Omega)}{1+i\Omega\tau} e^{i\Omega t} d\Omega + E_p^{\text{enh}}\int \frac{E_{pr}^{\text{enh}*}(\Omega)}{1-i\Omega\tau} e^{-i\Omega t} d\Omega\right]\right\}$$

$$\times e^{-i\omega_p t}\left[E_p^{\text{enh}} + \int E_{pr}^{\text{enh}}(\Omega)\, e^{i\Omega t} d\Omega\right]$$

$$= e^{-i\omega_1 t}\left[\left(\varepsilon_{m0} + \chi_m^{(3)}\left|E_p^{\text{enh}}\right|^2\right) E_p^{\text{enh}} + \chi_m^{(3)}\left|E_p^{\text{enh}}\right|^2 \int \frac{E_{pr}^{\text{enh}}(\Omega)}{1+i\Omega\tau} e^{i\Omega t} d\Omega\right.$$

$$\left. + \chi_m^{(3)}\left(E_p^{\text{enh}}\right)^2 \int \frac{E_{pr}^{\text{enh}*}(\Omega)}{1-i\Omega\tau} e^{-i\Omega t} d\Omega + \left(\varepsilon_{m0} + \chi_m^{(3)}\left|E_p^{\text{enh}}\right|^2\right)\int E_{pr}^{\text{enh}}(\Omega)\, e^{i\Omega t} d\Omega\right] \tag{C.7}$$

In the equation, we neglected the square terms for the probe.

We can rewrite the above equation

$$D_m(t) = e^{-i\omega_p t}\left\{E_p^{\text{enh}}\left(\varepsilon_{m0} + \chi_m^{(3)}\left|E_p^{\text{enh}}\right|^2\right)\right.$$

$$+ \int E_{pr}^{\text{enh}}(\Omega)\left[\varepsilon_{m0} + \chi_m^{(3)}\left|E_p^{\text{enh}}\right|^2\left(1 + \frac{1}{1+i\Omega\tau}\right)\right] e^{i\Omega t} d\Omega$$

$$\left. + \chi_m^{(3)}\left(E_p^{\text{enh}}\right)^2 \int \frac{E_{pr}^{\text{enh}*}(\Omega)}{1-i\Omega\tau} e^{-i\Omega t} d\Omega\right\} \tag{C.8}$$

The term $\left(\varepsilon_{m0} + \chi_m^{(3)}\left|E_p^{\text{enh}}\right|^2\right)$ in the above equation corresponds to the pump frequency component and leads to Eq. (5.19). The term in the second line obviously corresponds to the probe frequency component and leads to Eq. (5.20). We write the central frequency of probe as ω_2. Considering that the central value of $\Omega = \omega_1 - \omega_2$, the third term in Eq. (C.8) is lie around the frequency $\omega_1 + \Omega = 2\omega_1 - \omega_2$ which is four-wave mixing component.

• ***Derivation of Eqs. (5.34-5.37)***

We suppose that there are two strong continuous plane wave pump beams $\mathbf{E}_1$ and $\mathbf{E}_2$, weak probe pulse $\mathbf{E}_{pr}$, and the signal pulse $\mathbf{E}_s$ with same central frequencies ω. All the beams are s-polarized (polarized perpendicular to incident plane). In this case, the total enhanced field in each metal NP is given by

$$\mathbf{E}^{\text{enh}}(\mathbf{r},t) = \mathbf{A}_1^{\text{enh}} e^{i\mathbf{k}_1\mathbf{r}-i\omega t} + \mathbf{A}_2^{\text{enh}} e^{i\mathbf{k}_2\mathbf{r}-i\omega t} + \mathbf{A}_{pr}^{\text{enh}}(z,t)\, e^{i\mathbf{k}_3\mathbf{r}-i\omega t} + \mathbf{A}_s^{\text{enh}}(z,t)\, e^{i\mathbf{k}_4\mathbf{r}-i\omega t}, \quad \text{(C.9)}$$

where we assumed that pump beams are so strong that they are not influenced by the probe and signal waves and they are constant both in the space and time (undepleted pump approximation). In the above equation, $\mathbf{A}_1^{\text{enh}}$, $\mathbf{A}_2^{\text{enh}}$, $\mathbf{A}_{pr}^{\text{enh}}$, and $\mathbf{A}_s^{\text{enh}}$ are the slowly varying amplitudes of each beams, which are enhanced by plasmonic response of metal NPs. If two pump beams propagate along the exactly opposite directions $\mathbf{k}_1 = -\mathbf{k}_2$, phase-matching condition is automatically satisfied and the signal wave becomes an accurate phase conjugate wave with regard to the probe: $\mathbf{k}_3 = -\mathbf{k}_4$.

By using Eq. (5.9) under the condition of pulse duration much longer than τ_{ee} as in Section 5.3, the transient nonlinear polarization of metal is given by

$$\mathbf{P}_m^{NL}(\mathbf{r},t) = \varepsilon_0 \chi_m^{(3)} \mathbf{E}^{\text{enh}}(\mathbf{r},t) \left\{ I_0 + \frac{1}{\tau_{ep}} \left[e^{i\mathbf{k}_i\mathbf{r}} \int_{-\infty}^{t} e^{-\frac{t-t'}{\tau_{ep}}} \left(\mathbf{A}_1^{\text{enh}} \mathbf{A}_{pr}^{\text{enh}*} + \mathbf{A}_2^{\text{enh}*} \mathbf{A}_s^{\text{enh}} \right) dt' \right.\right.$$
$$\left.\left. + e^{i\mathbf{k}_j\mathbf{r}} \int_{-\infty}^{t} e^{-\frac{t-t'}{\tau_{ep}}} \left(\mathbf{A}_1^{\text{enh}*} \mathbf{A}_s^{\text{enh}} + \mathbf{A}_2^{\text{enh}} \mathbf{A}_{pr}^{\text{enh}*} \right) dt' + c.c. \right] \right\}, \quad \text{(C.10)}$$

where $I_0^{\text{enh}} = \left|\mathbf{A}_1^{\text{enh}}\right|^2 + \left|\mathbf{A}_2^{\text{enh}}\right|^2$ is total enhanced pump intensity, and $\mathbf{k}_i = \mathbf{k}_1 - \mathbf{k}_3$ and $\mathbf{k}_j = -\mathbf{k}_1 - \mathbf{k}_3$. For convenience, let us write the nonlinear polarization as follows:

$$\mathbf{P}_m^{NL}(\mathbf{r},t) = \mathbf{P}_{m1}^{NL} e^{i\mathbf{k}_1\mathbf{r}-i\omega t} + \mathbf{P}_{m2}^{NL} e^{i\mathbf{k}_2\mathbf{r}-i\omega t} + \mathbf{P}_{m3}^{NL} e^{i\mathbf{k}_3\mathbf{r}-i\omega t} + \mathbf{P}_{m4}^{NL} e^{i\mathbf{k}_4\mathbf{r}-i\omega t}, \quad \text{(C.11)}$$

where $\mathbf{P}_{m1}^{NL}$, $\mathbf{P}_{m2}^{NL}$, $\mathbf{P}_{m3}^{NL}$, and $\mathbf{P}_{m4}^{NL}$ are the slowly varying amplitudes of induced nonlinear polarization. We are interested only in the third and fourth terms in Eq. (C.11), contributing to the probe and signal waves. From Eq. (C.10), we get

$$\mathbf{P}_{m3}^{NL}(z,t) = \varepsilon_0 \chi_m^{(3)} \left[I_0^{\text{enh}} \left(\mathbf{A}_{pr}^{\text{enh}} + \frac{1}{\tau_{ep}} \int_{-\infty}^{t} e^{-\frac{t-t'}{\tau_{ep}}} \mathbf{A}_{pr}^{\text{enh}} dt' \right) + 2\frac{\mathbf{A}_1^{\text{enh}} \mathbf{A}_2^{\text{enh}}}{\tau_{ep}} \int_{-\infty}^{t} e^{-\frac{t-t'}{\tau_{ep}}} \mathbf{A}_s^{\text{enh}*} dt' \right], \quad \text{(C.12)}$$

$$\mathbf{P}_{m4}^{NL}(z,t) = \varepsilon_0 \chi_m^{(3)} \left[I_0^{\text{enh}} \left(\mathbf{A}_s^{\text{enh}} + \frac{1}{\tau_{ep}} \int_{-\infty}^{t} e^{-\frac{t-t'}{\tau_{ep}}} \mathbf{A}_s^{\text{enh}} dt' \right) + 2\frac{\mathbf{A}_1^{\text{enh}} \mathbf{A}_2^{\text{enh}}}{\tau_{ep}} \int_{-\infty}^{t} e^{-\frac{t-t'}{\tau_{ep}}} \mathbf{A}_{pr}^{\text{enh}*} dt' \right], \quad \text{(C.13)}$$

where ε_0 is vacuum permittivity. Taking Fourier transform on the Eqs. (C.12, C.13), we obtain

$$\mathbf{P}_{m3}^{NL}(z,\Omega) = \varepsilon_0 \chi_m^{(3)} \left(1 + \frac{1}{1+i\Omega\tau_{ep}} \right) I_0^{\text{enh}} \mathbf{A}_{pr}^{\text{enh}}(z,\Omega) + \frac{2}{1-i\Omega\tau_{ep}} \mathbf{A}_1^{\text{enh}} \mathbf{A}_2^{\text{enh}} \mathbf{A}_s^{\text{enh}*}(z,\Omega), \quad \text{(C.14)}$$

$$\mathbf{P}_{m4}^{NL}(z,\Omega) = \varepsilon_0 \chi_m^{(3)} \left(1 + \frac{1}{1+i\Omega\tau_{ep}} \right) I_0^{\text{enh}} \mathbf{A}_s^{\text{enh}}(z,\Omega) + \frac{2}{1-i\Omega\tau_{ep}} \mathbf{A}_1^{\text{enh}} \mathbf{A}_2^{\text{enh}} \mathbf{A}_{pr}^{\text{enh}*}(z,\Omega). \quad \text{(C.15)}$$

For the pump intensity weaker than saturation intensity, we can apply perturbative approximation for the effective nonlinear polarization of the composite medium:

$$\mathbf{P}^{NL}_{3,\mathrm{eff}}(z,\Omega) = \varepsilon_0 \chi^{(3)}_m x^2 |x|^2 \left[\left(1 + \frac{1}{1+i\Omega\tau_{ep}} \right) I_0^{\mathrm{enh}} \mathbf{A}_{pr}(z,\Omega) + \frac{2}{1-i\Omega\tau_{ep}} \mathbf{A}_1 \mathbf{A}_2 \mathbf{A}^*_s(z,\Omega) \right], \tag{C.16}$$

$$\mathbf{P}^{NL}_{4,\mathrm{eff}}(z,\Omega) = \varepsilon_0 \chi^{(3)}_m x^2 |x|^2 \left[\left(1 + \frac{1}{1+i\Omega\tau_{ep}} \right) I_0^{\mathrm{enh}} \mathbf{A}_{s}(z,\Omega) + \frac{2}{1-i\Omega\tau_{ep}} \mathbf{A}_1 \mathbf{A}_2 \mathbf{A}^*_{pr}(z,\Omega) \right], \tag{C.17}$$

where $\mathbf{P}^{NL}_{3,\mathrm{eff}}$ and $\mathbf{P}^{NL}_{4,\mathrm{eff}}$ are the effective polarization amplitudes corresponding to the enhanced nonlinear polarizations $\mathbf{P}^{NL}_{m3}(z,\Omega)$ and $\mathbf{P}^{NL}_{m4}(z,\Omega)$, respectively. By using the propagation equation in frequency domain under the slowly varying envelope approximation, we obtain

$$2ik\cos\theta \frac{\partial A_{pr}}{\partial z}(z,\Omega) = -\mu_0 P^{NL}_{3,\mathrm{eff}}, \tag{C.18}$$

$$2ik\cos\theta \frac{\partial A_{s}}{\partial z}(z,\Omega) = \mu_0 P^{NL}_{4,\mathrm{eff}}, \tag{C.19}$$

where $k = \omega/c$, μ_0 is vacuum permeability, θ is a half of intersecting angle between two pump waves, and we assume that the beams propagate symmetrically with regard to the composite medium surface. Combining Eqs. (C.16-C.19), we obtain Eqs. (5.34-5.37).

D. Derivations of Eqs. (6.6, 6.7, 6.10, and 6.23)

• ***Derivation of Eqs. (6.6 and 6.7)***

Electromagnetic fields have to satisfy the following boundary conditions for continuity at each interfaces:

$$E_{az} = E_{bz}, \tag{D.1}$$

$$\varepsilon_a E_{ax} = \varepsilon_b E_{bx}, \tag{D.2}$$

$$E_{bz} = E_{cz}, \tag{D.3}$$

$$\varepsilon_b E_{bx} = \varepsilon_c E_{cx}, \tag{D.4}$$

where subscripts a, b, and c represents the individual components of electric field in layers a, b, and c, respectively. Substituting Eq. (6.3) into the above equations,

$$-A_{an}\frac{\alpha_{an}}{K_n} = A^+_{bn}\frac{\alpha_{bn}}{K_n} - A^-_{bn}\frac{\alpha_{bn}}{K_n}, \tag{D.5}$$

$$\varepsilon_a A_{an} = \varepsilon_b \left(A^+_{bn} + A^-_{bn} \right), \tag{D.6}$$

$$A^+_{bn}\frac{\alpha_{bn}}{K_n} e^{-\alpha_{bn} d} - A^-_{bn}\frac{\alpha_{bn}}{K_n} e^{\alpha_{bn} d} = A_{cn}\frac{\alpha_{cn}}{K_n}, \tag{D.7}$$

$$\varepsilon_b \left(A^+_{bn} e^{-\alpha_{bn} d} + A^-_{bn} e^{\alpha_{bn} d} \right) = \varepsilon_c A_{cn}. \tag{D.8}$$

From Eqs. (D.7, D.8),

$$A^+_{bn} e^{-\alpha_{bn} d} - A^-_{bn} e^{\alpha_{bn} d} = \frac{\alpha_{cn}}{\alpha_{bn}} A_{cn}, \tag{D.9}$$

$$A_{bn}^{+}e^{-\alpha_{bn}d}+A_{bn}^{-}e^{\alpha_{bn}d}=\frac{\varepsilon_c}{\varepsilon_b}A_{cn}. \tag{D.10}$$

Summing up the above two equations and multiplying both sides with $e^{\alpha_{bn}d}$, we obatin

$$A_{bn}^{+}=\frac{(\varepsilon_c\alpha_{bn}+\varepsilon_b\alpha_{cn})}{2\varepsilon_b\alpha_{bn}}e^{\alpha_{bn}d}A_{cn}. \tag{D.11}$$

Similarly, subtracting Eq. (D.9) from Eq. (D.10) and multiplying both sides with $e^{-\alpha_{bn}d}$, we obatin

$$A_{bn}^{-}=\frac{(\varepsilon_c\alpha_{bn}-\varepsilon_b\alpha_{cn})}{2\varepsilon_b\alpha_{bn}}e^{-\alpha_{bn}d}A_{cn}. \tag{D.12}$$

Above two euqations are identical to Eq. (6.7). From Eqs. (D.5, D.6),

$$\frac{\alpha_{an}}{\alpha_{bn}}A_{an}=-A_{bn}^{+}+A_{bn}^{-}, \tag{D.13}$$

$$\frac{\varepsilon_a}{\varepsilon_b}A_{an}=A_{bn}^{+}+A_{bn}^{-}. \tag{D.14}$$

Subtracting Eq. (D.13) from Eq. (D.14) and dividing both sides by

$$\frac{\varepsilon_a}{\varepsilon_b}-\frac{\alpha_{an}}{\alpha_{bn}},$$

we obtain Eq. (6.6).

• ***Derivation of Eq. (6.10)***

Maxwell's equations for TM wave is given by

$$\frac{\partial^2 E_x}{\partial z^2}-\frac{\partial^2 E_z}{\partial x\partial z}-\frac{\varepsilon}{c^2}\frac{\partial^2 E_x}{\partial t^2}=\mu_0\frac{\partial^2 P_x}{\partial t^2}, \tag{D.15}$$

$$\frac{\partial^2 E_z}{\partial x}-\frac{\partial^2 E_x}{\partial x\partial z}-\frac{\varepsilon}{c^2}\frac{\partial^2 E_z}{\partial t^2}=\mu_0\frac{\partial^2 P_z}{\partial t^2}, \tag{D.16}$$

where are the x- and z- components of the polarizations induced by the existence of gain and are defined similarly as the fields:

$$\mathbf{P}_c=\frac{1}{2}\sum_n P_n(t)\left[\hat{x}\sin(K_n z)+\hat{z}\frac{\alpha_{cn}}{K_n}\cos(K_n z)\right]e^{\alpha_{cn}(x+d)-i\omega_n t}+c.c., \tag{D.17}$$

Let us calculate the second derivatives for spatial and temporal variables:

$$\frac{\partial^2 E_{cx}}{\partial z^2}=-\frac{1}{2}\sum_n A_n K_n^2\sin(K_n z)\,e^{\alpha_{cn}(x+d)-i\omega_n t}+c.c., \tag{D.18}$$

$$\frac{\partial^2 E_{cz}}{\partial x\partial z}=-\frac{1}{2}\sum_n A_n\alpha_{cn}^2\sin(K_n z)\,e^{\alpha_{cn}(x+d)-i\omega_n t}+c.c., \tag{D.19}$$

$$\frac{\partial^2 E_{cx}}{\partial t^2}=\frac{1}{2}\sum_n\left(\ddot{A}_n-2i\omega_n\dot{A}_n-\omega_n^2 A_n\right)\sin(K_n z)\,e^{\alpha_{cn}(x+d)-i\omega_n t}+c.c., \tag{D.20}$$

In Eq. (D.20), the second derivative for time variable can be neglected in the frame of slowly varying envelope approximation. On the other hand,

$$\frac{\partial^2 P_x}{\partial t^2} = \frac{1}{2}\sum_n \left(\ddot{P}_n - 2i\omega_n \dot{P}_n - \omega_n^2 P_n\right) \sin\left(K_n z\right) e^{\alpha_{cn}(x+d)-i\omega_n t} + c.c. \tag{D.21}$$

In Eq. (D.21), the induced polarization is significantly smaller than the field and we neglect all the time derivatives. Substituing the above derivatives into Eq. (D.16), we obtain

$$\left(-K_n^2 + \alpha_{cn}^2 + \varepsilon_c \frac{\omega_n^2}{c^2}\right) A_n + 2i\frac{\varepsilon_c}{c^2}\omega_n \dot{A}_n = -\frac{\omega_n^2}{\varepsilon_0} P_n. \tag{D.22}$$

Considering Eq. (6.8) and assuming that lasing frequency is approximately the same as mode frequency of passive resonator $\omega_n \approx \Omega_n$, we have

$$-K_n^2 + \alpha_{cn}^2 + \varepsilon_c \frac{\omega_n^2}{c^2} = 2i\frac{\omega_n \gamma_n}{c^2}\varepsilon_c, \tag{D.23}$$

where we neglected the term containing γ_n^2 because the mode attenuation rate γ_n is much smaller than the mode frequency ω_n. Substituting the above euqation into Eq. (D.22), we obtain

$$\dot{A}_n + \gamma_n A_n = \frac{i\omega_n}{2\varepsilon_0 \varepsilon_c} P_n. \tag{D.24}$$

The same euqation can be obtained from Eq. (D.16).

On the other hand, from the rotating-wave approximation and the rate equation approximation, we obtain the induced polarization [239]

$$\mathbf{P}_c = -\frac{id_{12}^2 \mathscr{D} N_g\left(x,z,t\right)}{\hbar}\mathbf{E}_c, \tag{D.25}$$

where

$$\mathscr{D} = \frac{1}{\Gamma_g + i\left(\omega_L - \omega\right)} \tag{D.26}$$

is complex Lorentzian denominator, Γ_g is dephasing rate for gain, ω_L is central lasing frequency, $N_g\left(x,z,t\right)$ is a space-time dependent population inversion, $\hbar$ is plank constant, and d_{12} is the electric dipole component of gain molecule.

To figure out the individual components of the induced polarization, we calculate the integral

$$\int_0^L \int_{-\infty}^{\infty} \mathbf{P}_c \mathbf{U}_n^*\left(x,z\right) n\left(x\right) dzdx = \frac{1}{2} P_n e^{-i\omega_n t} \int_0^L \int_{-\infty}^{\infty} \left|\mathbf{U}_n\left(x,z\right)\right|^2 n\left(x\right) dzdx. \tag{D.27}$$

from Eq. (D.17), where

$$\mathbf{U}_n\left(x,z\right) = \left[\hat{x}\sin\left(K_n z\right) + \hat{z}\frac{\alpha_{cn}}{K_n}\cos\left(K_n z\right)\right] e^{\alpha_{cn}(x+d)}, \tag{D.28}$$

and $n\left(x\right)$ is space-dependent refractive index. In Eq. (D.27), for covenience we wrote only

the components of $e^{-i\omega_n t}$ (component of positive frequency). For simplicity, we introduce

$$M_n = \int_0^L \int_{-\infty}^{\infty} dzdx \left|\mathbf{U}_n(x,z)\right|^2 n(x). \tag{D.29}$$

On the other hand, from Eq. (D.25) we obtain the positive frequency component of $\int_0^L \int_{-\infty}^{\infty} \mathbf{P}_c \mathbf{U}_n^*(x,z)\, n(x)\, dzdx$:

$$-\frac{id_{12}^2 \mathscr{D}_n \sqrt{\varepsilon_c}}{2\hbar} e^{-i\omega_n t} \int_0^L \int_{-\infty}^{-d} N_g(x,z,t) \left|\mathbf{U}_n\right|^2 dzdx, \tag{D.30}$$

where $\mathscr{D}_n$ is $\mathscr{D}$ for mode frequency ω_n. In the above equation, we take integral only over the interval from $-\infty$ to $-d$ for x, in which the gain medium exists. Comparing Eq. (D.27) and Eq. (D.30), we obtain

$$P_n = -\frac{id_{12}^2 \mathscr{D}_n \sqrt{\varepsilon_c}}{M_n \hbar} \int_0^L \int_{-\infty}^{-d} N_g(x,z,t) \left|\mathbf{U}_n\right|^2 dzdx. \tag{D.31}$$

Substituting the above equation into Eq. (D.24), we obtain

$$\dot{A}_n + \gamma_n A_n = \frac{d_{12}^2 \mathscr{D}_n \sqrt{\varepsilon_c} A_n}{2\varepsilon_0 \varepsilon_c \hbar M_n} \int_0^L \int_{-D_g - d_g}^{-d_g} \left|\mathbf{U}_n\right|^2 N_g dzdx. \tag{D.32}$$

The above euqation is not other than Eq. (6.10) with the introduction of gain cross-section σ_g given by Eq. (6.12).

• ***Derivation of Eq. (6.23)***

From Eq. (6.20),

$$\frac{\partial A(t,z)}{\partial t} = \int \left[\frac{\partial A(t,k)}{\partial t} - i\delta\omega A(t,k)\right] e^{-i\delta\omega t + ikz} dk. \tag{D.33}$$

$\delta\omega$ can be expanded as follows:

$$\delta\omega = v_g k + \frac{1}{2} \left.\frac{\partial^2 \omega}{\partial k^2}\right|_{k=0} k^2 + \cdots \tag{D.34}$$

On the other hand, from Eq. (6.10, 6.14)

$$\frac{\partial A(t,k)}{\partial t} = \left[-\gamma(k) + g(t,k)\right] A(t,k), \tag{D.35}$$

where $\gamma(k)$ and $g(t,k)$ are continuous form of γ_n and $g_n(t)$. Passive resonator loss $\gamma(k)$ can be expanded as follows:

$$\gamma(k) = \gamma_0 + \left.\frac{\partial \gamma}{\partial k}\right|_{k=0} k + \frac{1}{2} \left.\frac{\partial^2 \gamma}{\partial k^2}\right|_{k=0} k^2 + \cdots \tag{D.36}$$

Frequency dependent gain is

$$g(t,k) = g(t)\, \mathscr{D}_n \Gamma_g, \tag{D.37}$$

where

$$g(t) = \beta \sigma_g \int_{-D_g - d_g}^{-d_g} \bar{N}_g(x,t)\, e^{\kappa(x+d)} dz dx, \tag{D.38}$$

where β is given by Eq. (6.15) at ω_L. From Eq. (D.37),

$$g(t,k) = g(t)\left[1 + \frac{i\delta\omega}{\Gamma_g} - \left(\frac{\delta\omega}{\Gamma_g}\right)^2 + \cdots\right]. \tag{D.39}$$

Considering Eq. (D.34), the above equation can be approximately rewritten by

$$g(t,k) = g(t)\left[1 + \frac{iv_g}{\Gamma_g}k - \left(\frac{i}{2\Gamma_g}\left.\frac{\partial^2\omega}{\partial k^2}\right|_{k=0} - \frac{v_g^2}{\Gamma_g^2}\right)k^2 + \cdots\right]. \tag{D.40}$$

Summarizing Eqs. (D.33, D.35, D.36, and D.40),

$$\begin{aligned}\frac{\partial A(t,z)}{\partial t} = \int \Bigg\{ & (g - \gamma_0) - i\left(\frac{i}{v_g}\left.\frac{\partial\gamma}{\partial k}\right|_{k=0} - \frac{g}{\Gamma_g} + 1\right)(v_g k) \\ & + \left[\frac{1}{2v_g^2}\left.\frac{\partial\gamma}{\partial k}\right|_{k=0} - g\left(\frac{i}{2\Gamma_g v_g^2}\left.\frac{\partial^2\omega}{\partial k^2}\right|_{k=0} - \frac{1}{\Gamma_g^2}\right) - \frac{i}{2v_g^2}\left.\frac{\partial^2\omega}{\partial k^2}\right|_{k=0}\right](v_g k)^2\Bigg\} \\ & \times A(t,k)\, e^{-i\delta\omega t + ikz} dk.\end{aligned} \tag{D.41}$$

We add the terms from the saturated absorber into Eq. (D.41) and multiply round trip time T_R on the both sides:

$$\begin{aligned}T_R\frac{\partial A(t,z)}{\partial t} = \int \Bigg\{ & (g' - q' - \gamma_0') - i\left(\frac{i}{v_g}\left.\frac{\partial\gamma'}{\partial k}\right|_{k=0} - \frac{g'}{\Gamma_g} + \frac{q'}{\Gamma_q} + T_R\right)(v_g k) \\ & + \left(\frac{g'}{\Gamma_g^2} - \frac{q'}{\Gamma_q^2} + \frac{1}{2v_g^2}\left[i\left(T_R + \frac{g'}{\Gamma_g} - \frac{q'}{\Gamma_q}\right)\frac{\partial^2\omega}{\partial k^2} + \frac{\partial^2\gamma'}{\partial k^2}\right]\Bigg|_{k=0}\right)(v_g k)^2\Bigg\} \\ & \times A(t,k)\, e^{-i\delta\omega t + ikz} dk,\end{aligned} \tag{D.42}$$

where dashes represent the quantities multiplied by T_R. In the above euqations the parameters for saturable absorer are defined in the same way as that for the gain. Now we introduce the coordinate transformation $T = t$, $\tau = t - v_g^{-1} z$, where T is the laboratory time, and τ is the local time. To simplify the above equation, we remember the properties of Fourier transform

$$-i\frac{\partial f(x)}{\partial x} = \int \xi F(\xi)\, e^{i\xi x} d\xi, \tag{D.43}$$

$$-\frac{\partial^2 f(x)}{\partial x^2} = \int \xi^2 F(\xi)\, e^{i\xi x} d\xi, \tag{D.44}$$

where

$$f(x) = \int F(\xi)\, e^{i\xi x} d\xi. \tag{D.45}$$

From Eqs. (D.42, D.43, and D.44), we obtain Eq. (6.23). What we have to notice here is

that we have changed gain and saturated loss in the dispersion terms δ_1 and δ_2 to the initial values assuming that the dispersion and saturation are not prominent.

Publications

Journal papers

1. Linear and nonlinear optical characteristics of composites containing metal nanoparticles with different sizes and shapes
   Kwang-Hyon Kim, Anton Husakou, and Joachim Herrmann
   Opt. Express **18**(7), 7488–7496 (2010)

2. Saturable absorption in composites doped with metal nanoparticles
   Kwang-Hyon Kim, Anton Husakou, and Joachim Herrmann
   Opt. Express **18**(21), 21918–21925 (2010)

3. High-order harmonic generation employing field enhancement by metallic fractal rough surfaces
   Kwang-Hyon Kim, Anton Husakou, and Joachim Herrmann
   Opt. Express **19**(21), 20910–20915 (2011)

4. Theory of plasmonic femtosecond pulse generation by mode-locking of long-range surface plasmon polariton lasers
   Kwang-Hyon Kim, Anton Husakou, and Joachim Herrmann
   Opt. Express **20**(1), 462–473 (2012)

5. Theory of passive mode-locking of solid-state lasers using metal nanocomposites as slow saturable absorbers
   Kwang-Hyon Kim, Uwe Griebner, and Joachim Herrmann
   Opt. Lett., in press.

6. Slow light in dielectric composite materials containing metal nanoparticless
   Kwang-Hyon Kim, Anton Husakou, and Joachim Herrmann
   Phys. Rev. Lett., submitted.

7. Passive mode-locking of semiconductor disk lasers in blue spectral range by metal nanocomposites
   Kwang-Hyon Kim, Uwe Griebner, and Joachim Herrmann
   Opt. Express, submitted.

8. All-optical delay of images by degenerate four-wave mixing in metal nanocomposites
   Kwang-Hyon Kim, Anton Husakou, and Joachim Herrmann
   Opt. Lett., in preparation.

Conference proceedings and talks

• Kwang-Hyon Kim, Anton Husakou, and Joachim Herrmann, "Saturable absorption and nonlinear refraction in composites doped with metal nanoparticles," Matheon Workshop, Photonic Devices, ZI Berlin, 18 February, 2011.

• Kwang-Hyon Kim, Anton Husakou, and Joachim Herrmann, "Saturable absorption and nonlinear refractive index in composites doped with metal nanoparticles," DPG Conference, Q29-5, TU Dresden, 16 March, 2011.

• Kwang-Hyon Kim, Anton Husakou, and Joachim Herrmann, "Theory of ultrashort plasmon pulse generation by mode-locked surface plasmon polariton lasers," DPG Conference, O41-5, TU Dresden, 16 March, 2011.

• Kwang-Hyon Kim, Anton Husakou, and Joachim Herrmann, "Theory of low-threshold high-order harmonic generation by using field enhancement near metallic fractal surfaces," 2nd International Workshop "Nonlinear Nanostructures for Ultrafast Laser Applications", Max-Born-Institute, Berlin, 20 May, 2011.

• Anton Husakou, Kwang-Hyon Kim, and Joachim Herrmann, "High harmonic generation assisted by the field enhancement near rough metallic surface," EJ.P.10 TUE, CLEO Europe-EQEC 2011, International Congress Center, München, 24 May, 2011.

• Kwang-Hyon Kim, Anton Husakou, and Joachim Herrmann, "Slow light in the dielectric composites doped with metal nanoparticles," Matheon Workshop, Photonic Devices, ZI Berlin, 23 February, 2012.

• Anton Husakou, Joachim Herrmann, and Kwang-Hyon Kim, "Efficient high-harmonic generation in a mixture of a noble gas and metal nanoparticles and on rough metal surfaces," HT4C.3, OSA congress “High-Intensity Lasers and High-Field Phenomena (HILAS)”, Laser Optics Berlin, Berlin, Germany, 20 March, 2012.

• Joachim Herrmann, Kwang-Hyon Kim, and Anton Husakou, "Slow light in metal nanocomposites," 3rd International Conference on Metamaterials, Photonic Crystals and Plasmonics META’12, 19-22 Apr. 2012, Paris, France.

• Joachim Herrmann, Anton Husakou, and Kwang-Hyon Kim, "Efficient high-harmonic generation in a mixture of a noble gas and metal nanoparticles and on rough metal surfaces," 3rd International Conference on Metamaterials, Photonic Crystals and Plasmonics META’12, 19-22 Apr. 2012, Paris, France.

Bibliography

[1] V. M. Shalaev and S. Kawata, *Nanophotonics with Surface Plasmons* (Elsevier, Amsterdam, 2007).

[2] S. A. Maier, *Plasmonics: Fundamentals and Applications* (Springer, Berlin, 2007), 2nd edn.

[3] D. Sarid and W. Challener, *Modern Introduction to Surface Plasmons* (Cambridge University Press, Cambridge, 2010).

[4] S. A. Maier and H. A. Atwater, "Plasmonics: Localization and guiding of electromagnetic energy in metal/dielectric structures," J. Appl. Phys. **98**, 011 101 (2005).

[5] S. M. Nie and S. R. Emory, "Probing single molecules and single nanoparticles by surface-enhanced Raman scattering," Science **275**, 1102–1106 (1997).

[6] Y. C. Cao, R. Jin, and C. A. Mirkin, "Nanoparticles with Raman spectroscopic fingerprints for DNA and RNA detection," Science **297**, 1536–1540 (2002).

[7] P. Alibizatos, "The use of nanocrystals in biological detection," Nature Biotech. **22**, 47–52 (2004).

[8] C. M. Cobley, S. E. Skrabalak, D. J. Campbell, and Y. Xia, "Shape-controlled synthesis of silver nanoparticles for plasmonic and sensing applications," Plasmonics **4**, 171–179 (2009).

[9] X. Huang, S. Neretina, and M. A. El-Sayed, "Gold nanorods: From synthesis and properties to biological and biomedical applications," Adv. Mater. **21**, 4880–4910 (2009).

[10] J. Valentine, S. Zhang, T. Zentgraf, E. Ulin-Avila, D. A. Genov, G. Bartal, and X. Zhang, "Three-dimensional optical metamaterial with a negative refractive index," Nature **455**, 376–379 (2008).

[11] S. Zhang, Y.-S. Park, J. Li, X. Lu, W. Zhang, and X. Zhang, "Negative refractive index in chiral metamaterials," Phys. Rev. Lett. **102**, 023 901 (2009).

[12] W. Cai, U. K. Chettiar, A. V. Kildishev, and V. M. Shalaev, "Optical cloaking with metamaterials," Nature Photon. **1**, 224–227 (2007).

[13] C. K. Chen, A. R. B. de Castro, and Y. R. Shen, "Surface-enhanced second-harmonic generation," Phys. Rev. Lett. **46**, 145–148 (1981).

[14] K. A. O'Donnell, R. Torre, and C. S. West, "Observations of second-harmonic generation from randomly rough metal surfaces," Phys. Rev. B **55**, 7985–7992 (1997).

[15] E. M. Kim, S. S. Elovikov, T. V. Murzina, A. A. Nikulin, O. A. Aktsipetrov, M. A. Bader, and G. Marowsky, "Surface-enhanced optical third-harmonic generation in Ag island films," Phys. Rev. Lett. **95**, 227 402 (2005).

[16] S.-C. Kim, J.-H. Jin, Y.-J. Kim, I.-Y. Park, Y. Kim, and S.-W. Kim, "High-harmonic generation by resonant plasmon field enhancement," Nature **453**, 757–760 (2008).

[17] F. Hache, D. Ricard, C. Flytzanis, and U. Kreibig, "The optical Kerr effect in small metal particles and metal colloids: The case of gold," Appl. Phys. **47**, 347–357 (1988).

[18] E. L. Falcao-Filho, C. B. de Araujo, and J. J. J. Rodrigues, "High-order nonlinearities of aqueous colloids containing silver nanoparticles," J. Opt. Soc. Am. B **24**, 2948–2956 (2007).

[19] L. A. Gomez, C. B. de Araujo, A. Brito-Silva, and A. Galembeck, "Solvent effects on the linear and nonlinear optical response of silver nanoparticles," Appl. Phys. B **92**, 61–66 (2008).

[20] D. Rativa, R. E. de Araujo, and A. S. Gomes, "One photon nonresonant high-order nonlinear optical properties of silver nanoparticles in aqueous solution," Opt. Express **16**, 19 244–19 252 (2008).

[21] N. Okada, Y. Hamanaka, A. Nakamura, I. Pastoriza-Santos, and L. M. Liz-Marzan, "Linear and nonlinear optical response of silver nanoprisms: Local electric fields of dipole and quadrupole plasmon resonances," J. Phys. Chem. B **108**, 8751–8755 (2004).

[22] S. C. Mehendale, S. R. Mishra, K. S. Bindra, M. Laghate, T. S. Dhami, and K. C. Rustagi, "Nonlinear refraction in aqueous colloidal gold," Opt. Commun. **133**, 273–276 (1997).

[23] J. E. Sipe and R. W. Boyd, "Nonlinear susceptibility of composite optical materials in the Maxwell-Garnett model," Phys. Rev. A **46**, 1614–1629 (1992).

[24] Z. W. Wilkes, S. Varma, Y.-H. Chen, H. M. Milchberg, T. G. Jones, and A. Ting, "Direct measurements of the nonlinear index of refraction of water at 815 and 407 nm using single-shot supercontinuum spectral interferometry," Appl. Phys. Lett. **94**, 211 102 (2009).

[25] Y. Sun and Y. Xia, "Shape-controlled synthesis of gold and silver nanoparticles," Science **298**, 2176–2179 (2002).

[26] A. R. Tao, S. Habas, and P. Yang, "Shape control of colloidal metal nanocrystals," Small **4**, 310–325 (2008).

[27] B. J. Wiley, Y. Chen, J. M. McLellan, Y. Xiong, Z.-Y. Li, D. Ginger, and Y. Xia, "Synthesis and optical properties of silver nanobars and nanorice," Nano Lett. **7**, 1032–1036 (2009).

[28] Y. Gao, X. Zhang, Y. Li, H. Liu, W. J. Y. Wang, Q. Chang, and Y. Song, "Saturable absorption and reverse saturable absorption in platinum nanoparticles," Opt. Commun. **251**, 429–433 (2005).

[29] L. D. Boni, E. L. Wood, C. Toro, and F. E. Hernandez, "Optical saturable absorption in gold nanoparticles," Plasmonics **3**, 171–176 (2008).

[30] C. Zheng, X. Y. Ye, S. G. Cai, M. J. Wang, and X. Q. Xiao, "Observation of nonlinear saturable and reverse-saturable absorption in silver nanowires and their silica gel glass composite," Appl. Phys. B **101**, 835–840 (2010).

[31] O. L. Muskens, N. D. Fatti, and F. Vallée, "Femtosecond response of a single metal nanoparticle," Nano Lett. **6**, 552–556 (2006).

[32] R. W. Boyd, *Nonlinear Optics* (Pergamon, San Diego, 2008), 3rd edn.

[33] A. Anderson, K. S. Deryckx, X. G. Xu, G. Steinmeyer, and M. B. Raschke, "Few-femtosecond plasmon dephasing of a single metallic nanostructure from optical response function reconstruction by interferometric frequency resolved optical gating," Nano Lett. **10**, 2519–2524 (2010).

[34] R. W. Boyd, "Slow and fast light: Fundamentals and applications," J. Mod. Opt. **56**, 1908–1915 (2009).

[35] M. I. Stockman, "Spasers explained," Nature Photon. **2**, 327–329 (2008).

[36] M. A. Noginov, G. Zhu, M. Mayy, B. A. Ritzo, N. Noginova, and V. A. Podolskiy, "Stimulated emission of surface plasmon polaritons," Phys. Rev. Lett. **101**, 226 806 (2008).

[37] A. Husakou, S.-J. Im, and J. Herrmann, "Theory of plasmon-enhanced high-order harmonic generation in the vicinity of metal nanostructures in noble gases," Phys. Rev. A **83**, 043 839 (2011).

[38] F. Krausz and M. Ivanov, "Attosecond physics," Rev. Mod. Phys. **81**, 163–234 (2009).

[39] M. Pelton, J. Aizpurua, and G. Bryant, "Metal nanoparticle plasmonics," Laser Photon. Rev. **2**, 136–159 (2008).

[40] J. Z. Zhang and C. Noguez, "Plasmonic optical properties and applications of metal nanostructures," Plasmonics **3**, 127–150 (2008).

[41] N. Liu, M. L. Tang, M. Hentschel, H. Giessen, and A. P. Alivisatos, "Nanoantenna-enhanced gas sensing in a single tailored nanofocus," Nature Mater. **10**, 631–636 (2011).

[42] A. V. Zayats, I. I. Smolyaninov, and A. A. Maradudinc, "Nano-optics of surface plasmon polaritons," Phys. Rep. **408**, 131–314 (2005).

[43] P. B. Johnson and R. W. Christy, "Optical constants of the noble metals," Phys. Rev. B **6**, 4370–4379 (1972).

[44] C. L. Haynes, A. D. McFarland, L. Zhao, R. P. V. Duyne, G. C. Schatz, L. Gunnarsson, J. Prikulis, B. Kasemo, and M. Kaell, "Nanoparticle optics: The importance of radiative dipole coupling in two-dimensional nanoparticle arrays," J. Phys. Chem. **107**, 7337–7342 (2003).

[45] D. P. Fromm, A. Sundaramurthy, P. J. Schuck, G. Kino, and W. E. Moerner, "Gap-dependent optical coupling of single 'bowtie' nanoantennas resonant in the visible," Nano Lett. **4**, 957–961 (2004).

[46] K. L. Kelly, E. Coronado, L. L. Zhao, and G. C. Schatz, "The optical properties of metal nanoparticles: The influence of size, shape, and dielectric environment," J. Phys. Chem. B **107**, 668–677 (2003).

[47] M. A. Ordal, L. L. Long, R. J. Bell, S. E. Bell, R. R. Bell, R. W. Alexander, and C. A. Ward, "Optical properties of the metals Al, Co, Cu, Au, Fe, Pb, Ni, Pd, Pt, Ag, Ti, and W in the infrared and far infrared," Appl. Opt. **22**, 1099–1119 (1983).

[48] R. Jin, Y. Cao, C. A. Mirkin, K. L. Kelly, G. C. Schatz, and J. G. Zheng, "Photoinduced conversion of silver nanospheres to nanoprisms," Science **294**, 1901–1903 (2001).

[49] D. J. Griffiths, *Introduction to Electrodynamics* (Prentice-Hall, New Jersey, 1957), 3rd edn.

[50] H. C. van de Hulst, *Light Scattering by Small Particles* (Jhon Wiley, New York, 1957).

[51] F. M. Kahnert, "Numerical methods in electromagnetic scattering theory," J. Quant. Spectrosc. Radiat. Transf. **79/80**, 775–824 (2004).

[52] M. Born and E. Wolf, *Principles of Optics: Electromagnetic Theory of Propagation, Interference and Diffraction of Light*, Vol. 2 (Pergamon, New York, 1964).

[53] H. Xu, "Multilayered metal core-shell nanostructures for inducing a large and tunable local optical field," Phys. Rev. B **72**, 073 405 (2005).

[54] M. Morgan and K. Mei, "Finite-element computation of scattering by inhomogeneous penetable bodies of revolution," IEEE Trans. Antennas Propag. **27**, 202–214 (1979).

[55] T.-R. Lin, S.-W. Chang, S. L. Chung, Z. Zhang, and P. J. Schuck, "Coating effect on optical resonance of plasmonic nanobowtie antenna," Appl. Phys. Lett. **97**, 063 106 (2010).

[56] S. Burger, L. Zschiedrich, J. Pomplum, and F. Schmidt, "Finite element method for accurate 3D simulation of plasmonic waveguides," Proc. SPIE **7604**, 76 040F (2010).

[57] S. Zaiba, F. Lerouge, A.-M. Gabudean, M. Focsau, J. Lerme, T. Gallavardin, O. Maury, C. Andraud, S. Parova, and P. L. Baldeck, "Transparent plasmonic

nanocontainers protect organic fluorophores against photobleaching," Nano Lett. **11**, 2043–2047 (2011).

[58] B. T. Draine, "The discrete-dipole approximation and its application to interstellar graphite grains," Astrophys. J. **333**, 848–872 (1988).

[59] B. T. Draine and P. J. Flatau, "Discrete-dipole approximation for scattering calculations," J. Opt. Soc. Am. A **11**, 1491–1499 (1994).

[60] J. J. Goodman, B. T. Draine, and P. J. Flatau, "Application of fast-Fourier-transform techniques to the discrete-dipole approximation," Opt. Lett. **16**, 1198–1200 (1991).

[61] T. Jensen, L. Kelly, A. Lazarides, and G. C. Schatz, "Electrodynamics of noble metal nanoparticles and nanoparticle clusters," J. Cluster Sci. **10**, 295–317 (1999).

[62] M. A. Yurkin and A. G. Hoestra, "The discrete dipole approximation: An overview and recent developments," J. Quant. Spectrosc. Radiat. Transfer **106**, 558–589 (2007).

[63] W.-H. Yang, G. C. Schatz, and R. P. V. Duyne, "Discrete dipole approximation for calculating extinction and Raman intensities for small particles with arbitrary shapes," J. Chem. Phys. **103**, 869–875 (1995).

[64] E. Hao and G. C. Schatz, "Electromagnetic fields around silver nanoparticles and dimers," J. Chem. Phys. **120**, 357–366 (2004).

[65] V. M. Shalaev, *Nonlinear Optics of Random Media: Fractal Composites and Metal-Dielectric Films* (Springer, Berlin, 2000).

[66] R. P. Feynman, R. B. Leighton, and M. Sands, *The Feynman Lectures on Physics* (Addison-Wesley, Reading, 1964), 2nd revised edn.

[67] H. Raether, *Surface Plasmons on Smooth and Rough Surfaces and on Gratings* (Springer, New York, 1988), 2nd edn.

[68] Y. R. Shen, *The Principles of Nonlinear Optics* (Wiley, New York, 1984).

[69] N. Rotenberg and J. E. Sipe, "Analytic model of plasmonic coupling: Surface relief gratings," Phys. Rev. B **83**, 045 416 (2011).

[70] L. Wendler and R. Haupt, "Long-range surface plasmon-polaritons in asymmetric layer structures," J. Appl. Phys. **59**, 3289–3291 (1986).

[71] P. Berini, "Long-range surface plasmon polaritons," Advances in Optics and Photonics **1**, 484–588 (2009).

[72] P. Berini, "Long-range surface plasmon-polariton waveguides in silica," J. Appl. Phys. **102**, 053 105 (2007).

[73] J. Seidel, S. Grafstroem, and L. Eng, "Stimulated emission of surface plasmons at the interface between a silver film and an optically pumped dye solution," Phys. Rev. Lett. **94**, 177 401 (2005).

[74] M. Ambati, S. H. Nam, E. Ulin-Avila, D. A. Genov, G. Bartal, and X. Zhang, "Observation of stimulated emission of surface plasmon polaritons," Nano Lett. **8**, 3998–4001 (2008).

[75] I. D. Leon and P. Berini, "Amplification of long-range surface plasmons by a dipolar gain medium," Nature Photon. **4**, 382–387 (2010).

[76] M. C. Gather, K. Meerholz, N. Danz, and K. Lesson, "Net optical gain in a plasmonic waveguide embedded in a fluorescent polymer," Nature Photon. **4**, 457–461 (2010).

[77] K. Li, X. Li, M. I. Stockman, and D. J. Bergman, "Surface plasmon amplification by stimulated emission in nanolenses," Phys. Rev. B **71**, 115 409 (2005).

[78] M. T. Hill, M. Marell, E. S. P. Leong, B. Smalbrugge, Y. Zhu, M. Sun, P. J. van Veldhoven, E. J. Geluk, F. Karouta, Y.-S. Oei, R. Noetzel, C.-Z. Ning, and M. K. Smit, "Lasing in metal-insulator-metal sub-wavelength plasmonic waveguides," Opt. Express **17**, 11 107–11 112 (2009).

[79] M. A. Noginov, G. Zhu, A. M. Belgrave, R. Bakker, V. M. Shalaev, E. E. Narimanov, S. Stout, E. Herz, T. Suteewong, and U. Wiesner, "Demonstration of a spaser-based nanolaser," Nature **460**, 1110–1112 (2009).

[80] R. F. Oulton, V. J. Sorger, T. Zentgraf, R.-M. Ma, C. Gladden, L. Dai, G. Bartal, and X. Zhang, "Plasmon lasers at deep subwavelength scale," Nature **461**, 629–632 (2009).

[81] D. J. Bergman and M. I. Stockman, "Surface plasmon amplification by stimulated emission of radiation: Quantum generation of coherent surface plasmons in nanosystems," Phys. Rev. Lett. **90**, 027 402 (2003).

[82] I. E. Protsenko, A. V. Uskov, O. A. Zaimidoroga, V. N. Samoilov, and E. P. O'Reilly, "Dipole nanolaser," Phys. Rev. A **71**, 063 812 (2005).

[83] J. A. Gordon and R. W. Ziolkowski, "The design and simulated performance of a coated nano-particle laser," Opt. Express **15**, 2622–2653 (2007).

[84] S.-W. Chang, C.-Y. A. Ni, and S.-L. Chuang, "Theory for bowtie plasmonic nanolasers," Opt. Express **16**, 024 301 (2008).

[85] M. Wegener, J. L. Garcia-Pomar, N. M. C. M. Soukoulis, M. Ruther, and S. Linden, "Toy model for plasmonic metamaterial resonances coupled to two-level system gain," Opt. Express **16**, 19 785–19 798 (2008).

[86] Z.-G. Dong, H. Liu, T. Li, Z.-H. Zhu, S.-M. Wang, J.-X. Cao, S.-N. Zhu, and X. Zhang, "Resonance amplification of left-handed transmission at optical frequencies by stimulated emission of radiation in active metamaterials," Opt. Express **16**, 20 974–20 980 (2008).

[87] A. Fang, T. Koschny, M. Wegener, and C. M. Soukoulis, "Self-consistent calculation of metamaterials with gain," Phys. Rev. B **79**, 241 104 (2009).

[88] M. I. Stockman, "The spaser as a nanoscale quantum generator and ultrafast amplifier," J. Opt. **12**, 024 004 (2010).

[89] G. Winter, S. Wedge, and W. L. Barnes, "Can lasing at visible wavelengths be achieved using the low-loss long-range surface plasmon-polariton mode?" New J. Phys. **8**, 211 102 (2006).

[90] I. D. Leon and P. Berini, "Theory of surface plasmon-polariton amplification in planar structures incorporating dipolar gain media," Phys. Rev. B **78**, 161 401 (2008).

[91] I. D. Leon and P. Berini, "Modeling surface plasmon-polariton gain in planar metallic structures," Opt. Express **17**, 20 191–20 202 (2009).

[92] V. M. Shalaev, R. Botet, J. Mercer, and E. B. Stechel, "Optical properties of self-affine thin films," Phys. Rev. B **54**, 8235–8242 (1996).

[93] P. Meakin, P. Ramanlal, L. M. Sander, and R. C. Ball, "Ballistic deposition on surfaces," Phys. Rev. A **34**, 5091–5103 (1986).

[94] J. M. Kim and J. M. Kosterlitz, "Growth in a restricted solid-on-solid model," Phys. Rev. Lett. **62**, 2289–2292 (1989).

[95] M. Moskovits, "Surface-enhanced spectroscopy," Rev. Mod. Phys. **57**, 783–826 (1985).

[96] D. Stroud, "The effective medium approximations: Some recent developments," Superlattices Microstruct. **23**, 567–573 (1998).

[97] D. Stroud and P. M. Hui, "Nonlinear susceptibilities of granular matter," Phys. Rev. B **37**, 8719–8724 (1988).

[98] H. I. Elim, J. Yang, J.-Y. Lee, J. Mi, and W. Ji, "Observation of saturable and reverse-saturable absorption at longitudinal surface plasmon resonance in gold nanorods," Appl. Phys. Lett. **88**, 083 107 (2006).

[99] U. Gurudas, E. Brooks, D. M. Heiroth, T. Lippert, and A. Wokaun, "Saturable and reverse saturable absorption in silver nanodots at 532 nm using picosecond laser pulses," J. Appl. Phys. **104**, 073 107 (2008).

[100] R. Ganeev, A. Ryasnyanskii, A. Stepanov, and T. Usmanov, "Nonlinear absorption of visible light in silicate glasses doped with copper nanoparticles," Quantum Electron. **33**, 1081–1084 (2003).

[101] R. Ganeev, A. Ryasnyanskii, A. Stepanov, and T. Usmanov, "Saturated absorption and nonlinear refraction of silicate glasses doped with silver nanoparticles at 532 nm," Opt. Quantum Electron. **36**, 949–960 (2004).

[102] P. V. Kamat, M. Flumiani, and G. V. Hartland, "Picosecond dynamics of silver nanoclusters. Photoejection of electrons and fragmentation," J. Phys. Chem. B **102**, 3123–3128 (1998).

[103] Y. Hamanaka, A. Nakamura, N. Hayashi, and S. Omi, "Dispersion curves of complex third-order optical susceptibilities around the surface plasmon resonance in Ag nanocrystal-glass composites," J. Opt. Soc. Am. B **20**, 1227–1232 (2003).

[104] N. C. Kothari, "Effective-medium theory of a nonlinear composite medium using the T-matrix approach: Exact results for spherical grains," Phys. Rev. A **41**, 4486–4492 (1990).

[105] X.-Y. Liu and Z.-Y. Li, "High-order nonlinear susceptibilities of composite medium," Solid state communications **96**, 981–985 (1995).

[106] K. T. Tsen, *Non-Equilibrium Dynamics of Semiconductors and Nanostructures* (CRC, New York, 2005).

[107] R. W. Schoenlein, W. Z. Lin, J. G. Fujimoto, and G. L. Eesley, "Femtosecond studies of nonequilibrium electronic processes in metals," Phys. Rev. Lett. **58**, 1680–1683 (1987).

[108] T. S. Ahmadi, S. L. Logunov, and M. A. El-Sayed, "Picosecond dynamics of colloidal gold nanoparticles," J. Phys. Chem. **100**, 8053–8056 (1996).

[109] N. D. Fatti, R. Bouffanais, F. Vallée, and C. Flytzanis, "Nonequilibrium electron interactions in metal films," Phys. Rev. Lett. **81**, 922–925 (1998).

[110] Y. Hamanaka, N. Hayashi, A. Nakamura, and S. Omi, "Ultrafast relaxation dynamics of electrons in silver nanocrystals in glass," J. Luminescence **77**, 221–225 (1998).

[111] H. Inouye, K. Tanaka, I. Tanahashi, and K. Hirao, "Ultrafast dynamics of nonequilibrium electrons in a gold nanoparticle system," Phys. Rev. B **57**, 11 334–11 340 (1998).

[112] V. Halte, J. Guille, J.-C. Merle, I. Perakis, and J.-Y. Bigot, "Electron dynamics in silver nanoparticles: Comparison between thin films and glass embedded nanoparticles," Phys. Rev. B **60**, 11 738–11 746 (1999).

[113] V. Halte, J.-Y. Bigot, B. Palpant, M. Broyer, B. Prevel, and A. Perez, "Size dependence of the energy relaxation in silver nanoparticles embedded in dielectric matrices," Appl. Phys. Lett. **75**, 3879–3801 (1999).

[114] S. Link and M. A. El-Sayed, "Spectral properties and relaxation dynamics of surface plasmon electronic oscillations in gold and silver nanodots and nanorods," J. Phys. Chem. B **103**, 8410–8426 (1999).

[115] N. D. Fatti, C. Voisin, M. Achermann, S. Tzortzakis, D. Christofilos, and F. Vallée, "Nonequilibrium electron dynamics in noble metals," Phys. Rev. B **61**, 16 956–16 966 (2000).

[116] J. H. Hodak, A. Henglein, and G. V. Hartland, "Photophysics of nanometer sized metal particles: Electron-phonon coupling and coherent excitation of breathing vibrational modes," J. Phys. Chem. B **104**, 9954–9965 (2000).

[117] C. Voisin, N. D. Fatti, D. Christofilos, and F. Vallée, "Ultrafast electron dynamics and optical nonlinearities in metal nanoparticles," J. Phys. Chem. B **105**, 2264–2280 (2001).

[118] M. Hu and G. V. Hartland, "Heat dissipation for Au particles in aqueous solution: Relaxation time versus size," J. Phys. Chem. B **106**, 7029–7033 (2002).

[119] J. S. Melinger, V. D. Kleiman, D. McMorrow, F. Groehn, B. J. Bauer, and E. Amis, "Ultrafast dynamics of gold-based nanocomposite materials," J. Phys. Chem. B **107**, 3424–3431 (2003).

[120] E. Carpene, "Ultrafast laser irradiation of metals: Beyond the two-temperature model," Phys. Rev. B **74**, 024 301 (2006).

[121] S. Lysenko, J. Jimenez, G. Zhang, and H. Liu, "Nonlinear optical dynamics of glass-embedded silver nanoaprticles," J. Electron. Mater. **35**, 1715–1721 (2006).

[122] M. Halonen, A. A. Lipovskii, and Y. P. Svirko, "Femtosecond absorption dynamics in glass-metal nanocomposites," Opt. Express **15**, 6840–6845 (2007).

[123] V. V. Kruglyak, R. J. Hicken, P. Matousek, and M. Towrie, "Spectroscopic study of optically induced ultrafast electron dynamics in gold," Phys. Rev. B **75**, 035 410 (2007).

[124] N. Rotenberg, A. D. Bristow, M. Pfeiffer, M. Betz, and H. M. van Driel, "Nonlinear absorption in Au films: Role of thermal effects," Phys. Rev. B **75**, 155 426 (2007).

[125] J. Wang and C. Guo, "Effect of electron heating on femtosecond laser-induced coherent acoustic phonons in noble metals," Phys. Rev. B **75**, 184 304 (2007).

[126] Y. Guillet, M. Rashidi-Huyeh, and B. Palpant, "Influence of laser pulse characteristics on the hot electron contribution to the third-order nonlinear optical response of gold nanoparticles," Phys. Rev. B **79**, 045 410 (2009).

[127] R. Rangel-Rojo, J. McCarthy, H. T. Bookey, A. K. Kar, L. Rodriguez-Fernandez, J. C. Cheang-Wong, A. Crespo-Sosa, A. Lopez-Suarez, A. Olibier, V. Rodriguez-Iglesias, and H. G. Silva-Rereyra, "Anisotropy in the nonlinear absorption of elongated silver nanoparticles in silica, probed by femtosecond pulses," Opt. Commun. **282**, 1909–1912 (2009).

[128] W. G. Ma, H. D. Wang, X. Zhang, and W. Wang, "Experiment study of the size effects on electron-phonon relaxation and electrical resistivity of polycrystalline thin gold films," J. Appl. Phys. **108**, 064 308 (2010).

[129] K. Puech, F. Henari, W. Blau, D. Duff, and G. Schmid, "Investigation of the ultrafast dephasing time of gold nanoparticles using incoherent light," chem Phys. Lett. **247**, 13–17 (1995).

[130] C. Voisin, D. Christofilos, P. A. Loukakos, N. D. Fatti, F. Vallée, J. Lerme, M. Gaudry, E. Cottancin, M. Pellarin, and M. Broyer, "Ultrafast electron-electron

scattering and energy exchanges in noble-metal nanoparticles," Phys. Rev. B **69**, 195 416 (2004).

[131] O. P. Varnavski, T. G. III, M. B. Mohamed, and M. A. El-Sayed, "Femtosecond excitation dynamics in gold nanospheres and nanorods," Phys. Rev. B **72**, 235 405 (2005).

[132] N. D. Fatti, D. Christofilos, and F. Vallée, "Optical response of a single gold nanoparticles," Gold Bull. **41**, 147–158 (2008).

[133] H. Baida, D. Mongin, D. Christofilos, G. Bachelier, A. Crut, P. Maioli, N. D. Fatti, and F. Vallée, "Ultrafast nonlinear optical response of a single gold nanorod near its surface plasmon resonance," Phys. Rev. Lett. **107**, 057 402 (2011).

[134] H. Baida, D. Christofilos, P. Maioli, A. Crut, N. D. Fatti, and F. Vallée, "Ultrafast nonlinear spectroscopy of a single silver nanoparticle," J. Raman Spectrosc. p. in print (2011).

[135] J. Jayabalan, "Origin and time dependence of higher-order nonlinearities in metal nanocomposites," J. Opt. Soc. Amer. B **28**, 2448–2455 (2011).

[136] C.-K. Sun, F. Vallée, L. H. Acioli, E. P. Ippen, and J. G. Fujimoto, "Femtosecond-tunable measurement of electron thermalization in gold," Phys. Rev. B **50**, 15 337–15 348 (1994).

[137] K. Wundke, S. Poetting, J. Auxier, A. Schuelzgen, N. Peyghambarian, and N. F. Borrelli, "PbS quantum-dot doped glasses for ultrashort-pulse generation," Appl. Phys. Lett. **76**, 10–12 (2000).

[138] A. M. Malyarevich, K. V. Yumashev, and A. A. Lipovskii, "Semiconductor-doped glass saturable absorbers for near-infrared solid-state lasers," Appl. Phys. Lett. **103**, 081 301 (2008).

[139] U. Keller, K. J.Weingarten, F. X. Kaertner, D. Kopf, B. Braun, I. D. Jung, R. Fluck, C. Hoenninger, N. Matuschek, and J. A. der Au, "Semiconductor saturable absorber mirrors (SESAMs) for femtosecond to nanosecond pulse generation in solid-state lasers," IEEE J. Sel. Top. Quantum Electron. **2**, 435–453 (1996).

[140] P. M. W. French, J. A. R. Williams, and J. R. Taylor, "Passively mode locked c.w. dye lasers operating from 490 nm to 800 nm," Revue Phys. Appl. **22**, 1651–1655 (1987).

[141] A. Penzkofer, "Passive Q-switching and mode-locking for the generation of nanosecond to femtosecond pulses," Appl. Phys. B **46**, 43–60 (1988).

[142] C. Ropers, D. R. Solli, C. P. Schulz, C. Lienau, and T. Elsaesser, "Localized multiphoton emission of femtosecond electron pulses from metal nanotips," Phys. Rev. Lett. **98**, 043 907 (2007).

[143] C. Lemell, X.-M. Tong, F. Krausz, and J. Burgdörfer, "Electron emission from metal surfaces by ultrashort pulses: Determination of the carrier-envelope phase," Phys. Rev. Lett. **90**, 076 403 (2004).

[144] A. Apolonski, P. Dombi, G. G. Paulus, M. Kakehata, R. Holzwarth, T. Udem, C. Lemell, K. Torizuka, J. Burgdörfer, T. W. Hänsch, and F. Krausz, "Observation of light-phase-sensitive photoemission from a metal," Phys. Rev. Lett. **92**, 073 902 (2004).

[145] C. Ropers, T. Elsaesser, G. Cerullo, M. Zavelani-Rossi, and C. Lienau, "Ultrafast optical excitations of metallic nanostructures: from light confinement to a novel electron source," New J. Phys. **9**, 397 (2007).

[146] R. Bormann, M. Gulde, A. Weismann, S. V. Yalunin, and C. Ropers, "Tip-enhanced strong-field photoemission," Phys. Rev. Lett. **105**, 147 601 (2010).

[147] S. V. Yalunin, M. Gulde, and C. Ropers, "Strong-field photoemission from surfaces: Theoretical approaches," Phys. Rev. B **84**, 195 426 (2011).

[148] C. Kern, M. Zürch, J. Petschulat, T. Pertsch, B. Kley, T. Käsebier, U. Hübner, and C. Spielmann, "Comparison of femtosecond laser-induced damage on unstructured vs. nano-structured Au-targets," Appl Phys A **104**, 15–21 (2011).

[149] G. Mie, "Beiträge zur Optik trüber Medien, speziell kolloidaler Metallösungen," Annal. Phys. **330**, 377–445 (1908).

[150] J. C. M. Garnett, "Colours in metal glasses and in metallic films," Phil. Trans. R. Soc. London **203**, 385–420 (1904).

[151] D. W. Lynch and W. R. Hunterg, "Comments on the optical constants of metals and an introduction to the data for several metals," in *Handbook of Optical Constants of Solids*, E. Palik, ed. (Academic, Orlando, Fla., 1985).

[152] K. Tanabe, "Field enhancement around metal nanoparticles and nanoshells: A systematic investigation," J. Phys. Chem. C **112**, 15 721–15 728 (2008).

[153] R. Driben, A. Husakou, and J. Herrmann, "Supercontinuum generation in aqueous colloids containing silver nanoparticles," Opt. Lett. **34**, 2132–2134 (2009).

[154] R. Driben, A. Husakou, and J. Herrmann, "Low-threshold supercontinuum generation in glasses doped with silver nanoparticles," Opt. Express **17**, 17 989–17 995 (2009).

[155] E. L. Falcao-Filho, C. B. de Araujo, A. Galembeck, M. M. Oliveira, and A. J. Zarbin, "Nonlinear susceptibility of colloids consisting of silver nanoparticles in carbon disulfide," J. Opt. Soc. Am. B **22**, 2444–2449 (2005).

[156] D. D. Smith, G. Fischer, R. W. Boyd, and D. A. Gregory, "Cancelation of photoinduced absorption in metal nanoparticles composites through a counterintuitive consequence of local field effects," J. Opt. Soc. Am. B **14**, 1625–1631 (1997).

[157] R. Remmert, *Theory of Complex Functions* (Springer, Berlin, 1991).

[158] L. Hoermander, *An Introduction to Complex Analysis in Several Variables* (North-Holland, Amsterdam, 1990).

[159] J. Nocedal and S. J. Wright, *Numerical Optimization* (Springer, Berlin, 2006), 2nd edn.

[160] F. X. Kaernter, *Few-Cycle Laser Pulse Generation and Its Application* (Springer, Berlin, 2004).

[161] A. M. Weiner, *Ultrafast Optics* (Jhon Wiley, Hoboken, New Jersey, 2008).

[162] Y.-C. Chen, N. R. Raravikar, L. S. Schadler, P. M. Ajayan, Y.-P. Zhao, T. M. Lu, G.-C. Wang, and X.-C. Zhang, "Ultrafast optical switching properties of single-wall carbon nanotube polymer composites at 1.55 μm," Appl. Phys. Lett. **81**, 975–977 (2002).

[163] A. Schmidt, S. Rivier, G. Steinmeyer, J. H. Yim, W. B. Cho, S. Lee, F. Rotermund, M. C. Pujol, X. Mateos, M. Aguilo, F. Diaz, V. Petrov, and U. Griebner, "Passive mode locking of Yb:KLuW using a single-walled carbon nanotube saturable absorber," Opt. Lett. **33**, 729–731 (2008).

[164] H. Zhang, Q. Bao, D. Tang, L. Zhao, and K. Loh, "Large energy soliton erbium-doped fiber laser with a graphene-polymer composite mode locker," Appl. Phys. Lett. **95**, 141 103 (2009).

[165] R. A. Ganeev, R. I. Tugushev, and T. Usmanov, "Application of the nonlinear optical properties of platinum nanoparticles for the mode locking of Nd:glass laser," Appl. Phys. B **94**, 647–651 (2009).

[166] F. Cornacchia, A. D. Lieto, M. Tonelli, A. Richter, E. Heumann, and G. Huber, "Efficient visible laser emission of GaN laser diode pumped Pr-doped fluoride scheelite crystals," Opt. Express **16**, 15 932–15 941 (2008).

[167] T. Günn, P. Metz, and G. Huber, "Power scaling of laser diode pumped P^{3+}:LiYF4 cw lasers: Efficient laser operation at 522.6 nm, 545.9 nm, 607.2 nm, and 639.5 nm," Opt. Lett. **36**, 1002–1004 (2011).

[168] B. Xu, P. Camy, J.-L. Doualan, Z. Cai, and R. Moncorgé, "Visible laser operation of Pr^{3+}-doped fluoride crystals pumped by a 469 nm blue laser," Opt. Express **19**, 1191–1197 (2011).

[169] T.-C. Lu, J.-T. Chu, S.-W. Chu, S.-W. Chen, B.-S. Cheng, H.-C. Kuo, and S.-C. Wang, "Lasing behavior, gain property, and strong coupling effects in GaN-based vertical-cavity surface-emitting lasers," Jpn. J. Appl. Phys. **47**, 6655–6659 (2008).

[170] T.-C. Lu, J.-T. Chu, S.-W. Chu, S.-W. Chen, B.-S. Cheng, H.-C. Kuo, and S.-C. Wang, "Temperature dependent gain characteristics in GaN-based vertical-cavity surface-emitting lasers," Opt. Express **17**, 20 149–20 154 (2009).

[171] J.-Y. Bigot, V. Halté, J.-C. Merle, and A. Daunois, "Electron dynamics in metallic nanoparticles," Chem. Phys. **251**, 181–203 (2000).

[172] H. A. Haus, "Mode-locking of lasers," IEEE J. Sel. Top. Quantum Electron. **6**, 1173–1185 (2000).

[173] G. H. C. New, "Mode-locking of quasi-continuous lasers," Opt. Commun. **6**, 188–192 (1972).

[174] J. Herrmann, F. Weidner, and B. Wihelmi, "Theory of passive mode-locking of CW dye lasers with contacted and non-contacted absorbers," Appl. Phys. B **26**, 197–202 (1981).

[175] J. Herrmann and F. Weidner, "Theory of passively mode-locked cw dye lasers," Appl. Phys. B **27**, 105–113 (1982).

[176] H. J. Polland, T. Elsaesser, A. Seilmeier, W. Kaiser, M. Kussler, N. J. Marx, B. Sens, and K. H. Drexhage, "Picosecond dye laser emission in the infrared between 1.4 and 1.8 μm," Appl. Phys. B **32**, 53–57 (1983).

[177] U. Keller and A. C. Tropper, "Passively modelocked surface-emitting semiconductor lasers," Phys. Rep. **429**, 67–120 (2006).

[178] E. U. Rafailov, M. A. Cataluna, and W. Sibbett, "Mode-locked quantum-dot lasers," Nature Photon. **1**, 351–401 (2007).

[179] E. J. Saarinen, R. Herda, and O. G. Okhotnikov, "Dynamics of pulse formation in mode-locked semiconductor disk lasers," J. Opt. Soc. Am. B **24**, 2784–2790 (2007).

[180] P. Klopp, F. Saas, M. Zorn, M. Weyers, and U. Griebner, "290-fs pulses from a semiconductor disk laser," Opt. Express **16**, 5770–5773 (2008).

[181] A.-R. Bellancourt, D. J. H. C. Maas, B. Rudin, M. Golling, T. Suedmeyer, and U. Keller, "Modelocked integrated external-cavity surface emitting laser," IET Optoelectronics **3**, 61–72 (2009).

[182] A. H. Quarterman, K. G. Wilcox, V. Apostolopoulos, Z. Mihoubi, S. P. Elsmere, I. Farrer, D. A. Ritchie, and A. Tropper, "A passively mode-locked external-cavity semiconductor laser emitting 60-fs pulses," Nature Photon. **3**, 729–731 (2009).

[183] P. Klopp, U. Griebner, M. Zorn, A. Klehr, A. Liero, M. Weyers, and G. Erbert, "Mode-locked InGaAs-AlGaAs disk laser generating sub-200-fs pulses, pulse picking and amplification by a tapered diode amplifier," Opt. Express **17**, 10 820–10 834 (2009).

[184] P. Klopp, U. Griebner, M. Zorn, and M. Weyers, "Pulse repetition rate up to 92 GHz or pulse duration shorter than 110 fs from a mode-locked semiconductor disk laser," Appl. Phys. Lett. **98**, 071 103 (2011).

[185] H. A. Haus, "Theory of mode locking with a fast saturable absorber," J. Appl. Phys. **46**, 3049–3058 (1975).

[186] T. Brabec, C. Spielmann, P. F. Curley, and F. Krausz, "Kerr lens mode locking," Opt. Lett. **17**, 1292–1294 (1992).

[187] J. Herrmann, "Theory of Kerr-lens mode locking: Role of self-focusing and radially varying gain," J. Opt. Soc. Am. B **11**, 498–512 (1994).

[188] R. Paschotta, *Encyclopedia for Photonics and Laser Technology* (Wiley-VCH, Weinheim, Germany, 2008).

[189] F. X. Kaertner, D. Kopf, and U. Keller, "Solitary-pulse stabilization and shortening in actively mode-locked lasers," J. Opt. Soc. Am. B **12**, 486–496 (1995).

[190] F. X. Kaertner, I. D. Jung, and U. Keller, "Soliton mode-locking with saturable absorbers," IEEE J. Sel. Top. Quantum Electron. **2**, 540–556 (1996).

[191] D. Li, U. Demirbas, J. R. Birge, G. S. Petrich, L. A. Kolodziejski, A. Sennaroglu, F. X. Kaertner, and J. G. Fujimoto, "Diode-pumped passively mode-locked GHz femtosecond Cr:LiSAF laser with kW peak power," Opt. Lett. **35**, 1446–1448 (2010).

[192] R. Paschotta and U. Keller, "Passive mode locking with slow saturable absorbers," Appl. Phys. B **73**, 653–662 (2001).

[193] U. Keller, "Ultrafast solid-state laser oscillators: A success story for the last 20 years with no end in sight," Appl. Phsy. B **100**, 15–18 (2010).

[194] F. X. Kaertner, J. A. der Au, and U. Keller, "Mode-locking with slow and fast saturable absorbers - What's the difference?" IEEE J. Sel. Top. Quantum Electron. **4**, 159–168 (1996).

[195] B. M. Walsh, N. P. Barnes, and B. D. Bartolo, "Branching ratios, cross sections, and radiative lifetimes of rare earth ions in solids: Application to Tm^{3+} and Ho^{3+} ions in LiYF4," J. Appl. Phys. **83**, 2772–2787 (1998).

[196] B. M. Walsh, N. P. Barnes, M. Petros, J. Yu, and U. N. Singh, "Spectroscopy and modeling of solid state lanthanide lasers: Application to trivalent Tm^{3+} and Ho^{3+} in YLiF4 and LuLiF4," J. Appl. Phys. **95**, 3255–3271 (2004).

[197] G. P. Agrawal, *Nonlinear Fiber Optics* (Elsevier, Amsterdam, 2007), 4th edn.

[198] W. H. Knox, D. S. Chemla, G. Livescu, J. E. Cunningham, and J. E. Henry, "Femtosecond carrier thermalization in dense Fermi seas," Phys. Rev. Lett. **61**, 1290–1293 (1988).

[199] Y.-K. Song, H. Zhou, M. Diagne, A. V. Nurmikko, R. P. Schneider, C. P. Kuo, M. R. Krames, R. S. Kern, C. Carter-Coman, and F. A. Kish, "A quasicontinuous wave, optically pumped violet vertical cavity surface emitting laser," Appl. Phys. Lett. **76**, 1662–1664 (2000).

[200] I. V. Smetanin, P. P. Vasil'ev, and D. L. Boiko, "Theory of the ultrafast mode-locked GaN lasers in a large-signal regime," Opt. Express **19**, 17 114–17 120 (2011).

[201] R. Paschotta, R. Häring, A. Garnache, S. Hoogland, A. Tropper, and U. Keller, "Soliton-like pulse-shaping mechanism in passively mode-locked surface-emitting semiconductor lasers," Appl. Phys. B **75**, 445–451 (2002).

[202] M. Hoffmann, O. D. Sieber, D. J. H. C. Maas, V. J. Wittwer, M. Golling, T. Südmeyer, and U. Keller, "Experimental verification of soliton-like pulse-shaping mechanisms in passively mode-locked VECSELs," Opt. Express **18**, 10 143–10 153 (2010).

[203] N. N. Lepeshkin, W. Kim, V. P. Safonov, J. G. Zhu, R. L. Armstrong, C. W. White, R. A. Zuhr, and V. M. Shalaev, "Optical nonlinearities of metal-dielectric composites," J. Nonlinear Opt. Phys. Mater **8**, 191–210 (1999).

[204] P. W. Milonni, *Fast Light, Slow Light and Left-Handed Light* (Institute of Physics Publishing, Bristol, 2005).

[205] J. B. Khurgin and R. S. Tucker, *Slow Light: Science and Applications* (CRC Press, Boca Raton, 2008).

[206] R. W. Boyd, D. J. Gauthier, A. L. Gaeta, and A. E. Willner, "Maximum time delay achievable on propagation through a slow-light medium," Phys. Rev. A **71**, 023 801 (2005).

[207] R. W. Boyd and D. J. Gauthier, "Controlling the velocity of light pulses," Science **326**, 1074–1077 (2009).

[208] F. Arrieta-Yanez, O. G. Calderon, and S. Melle, "Slow and fast light based on coherent population oscillations in erbium-doped fibres," J. Optics **12**, 104 002 (2010).

[209] L. Thevenaz, "Slow and fast light in optical fibres," Nature Photon. **2**, 474–481 (2008).

[210] F. Xia, L. Sekaric, and Y. Vlasov, "Ultracompact optical buffers on a silicon chip," Nature Photon. **1**, 65–71 (2007).

[211] Z. Shi, R. W. Boyd, D. J. Gauthier, and C. C. Dudley, "Enhancing the spectral sensitivity of interferometers using slow-light media," Opt. Lett. **32**, 915–917 (2007).

[212] B. Corcoran, C. Monat, C. Grillet, D. J. Moss, B. J. Eggleton, T. P. White, L. O'Faolain, and T. F. Krauss, "Grating-assisted phase matching in extreme nonlinear optics," Nature Photon. **3**, 206–210 (2009).

[213] M. S. Bigelow, N. N. Lepeshkin, and R. W. Boyd, "Observation of ultraslow light propagation in a ruby crystal at room temperature," Phys. Rev. Lett. **90**, 113 903 (2003).

[214] M. Sandtke and L. Kuipers, "Slow guided surface plasmons at telecom frequencies," Nature Photon. **1**, 573–576 (2007).

[215] E.-P. Fitrakis, T. Kamalakis, and T. Sphicopoulos, "Slow light in insulator-metal-insulator plasmonic waveguides," J. Opt. Soc. Am. B **28**, 2159–2164 (2011).

[216] S. Zhang, D. A. Genov, Y. Wang, M. Liu, and X. Zhang, "Plasmon-induced transparency in metamaterials," Phys. Rev. Lett. **101**, 047 401 (2008).

[217] N. Liu, L. Langguth, T. Weiss, J. Kaestel, M. Fleischhauer, T. Pfau, and H. Giessen, "Plasmonic analogue of electromagnetically induced transparency at the Drude damping limit," Nature Mater. **8**, 758–762 (2009).

[218] M. Fleischhauer, A. Imamoglu, and J. P. Marangos, "Electromagnetically induced transparency: Optics in coherent media," Rev. Mod. Phys. **77**, 633–673 (2005).

[219] M. M. Kash, V. A. Sautenkov, A. S. Zibrov, L. Hollberg, G. R. Welch, M. D. Lukin, Y. Rostovtsev, E. S. Fry, and M. O. Scully, "Ultraslow group velocity and enhanced nonlinear optical effects in a coherently driven hot atomic gas," Phys. Rev. Lett. **82**, 5229–5232 (1999).

[220] L. V. Hau, S. E. Harris, Z. Dutton, and C. H. Behroozi, "Light speed reduction to 17 metres per second in an ultracold atomic gas," Nature **397**, 594–598 (1999).

[221] B. Wu, J. F. Hulbert, E. J. Lunt, K. Hurd, A. R. Hawkins, and H. Schmidt, "Slow light on a chip via atomic quantum state controln," Nature Photon. **4**, 776–779 (2010).

[222] G. P. Agrawal, "Population pulsations and nondegenerate four-wave mixing in semiconductor lasers and amplifiers," J. Opt. Soc. Am. B **5**, 147–159 (1988).

[223] M. S. Bigelow, N. N. Lepeshkin, and R. W. Boyd, "Superluminal and slow light propagation in a room-temperature solid," Science **301**, 200–202 (2003).

[224] H. Shin, A. Schweinsberg, G. Gehring, K. Schwertz, H. J. Chang, R. W. Boyd, Q.-H. Park, and D. J. Gauthier, "Reducing pulse distortion in fast-light pulse propagation through an erbium-doped fiber amplifier," Opt. Lett. **32**, 906–908 (2007).

[225] Y. A. Vlasov, M. O'Boyle, H. F. Hamann, and S. J. McNab, "Active control of slow light on a chip with photonic crystal waveguides," Nature **438**, 65–69 (2005).

[226] T. Baba, "Slow light in photonic crystals," Nature Photon. **2**, 465–473 (2008).

[227] R. Hao, E. Cassan, X. L. Roux, D. Gao, V. D. Khanh, L. Vivien, D. Marris-Morini, and X. Zhang, "Improvement of delay-bandwidth product in photonic crystal slow-light waveguides," Opt. Express **18**, 16 309–16 319 (2010).

[228] J. Sharping, Y. Okawachi, and A. Gaeta, "Wide bandwidth slow light using a Raman fiber amplifier," Opt. Express **13**, 6092–6098 (2005).

[229] Y. Okawachi, M. S. Bigelow, J. E. Sharping, Z. Zhu, A. Schweinsberg, D. J. Gauthier, R. W. Boyd, and A. L. Gaeta, "Tunable all-optical delays via Brillouin slow light in an optical fiber," Phys. Rev. Lett. **94**, 153 902 (2005).

[230] A. Zadok, A. Eyal, and M. Tur, "Stimulated Brillouin scattering slow light in optical fibers [Invited]," Appl. Opt. **50**, E38–E49 (2011).

[231] R. M. Camacho, M. V. Pack, j. C. Howell, A. Schweinsberg, and R. W. Boyd, "Wide-bandwidth, tunable, multiple-pulse-width optical delays using slow light in cesium vapor," Phys. Rev. Lett. **98**, 153 601 (2007).

[232] S. Mukamel, *Principles of Nonlinear Optical Spectroscopy* (Oxford Univ. Press, New York, 1995).

[233] G. S. He, "Optical phase conjugation: Principles, techniques, and applications," Progress in Quantum Electron. **26**, 131–191 (2002).

[234] B. Sturman, E. Podivilov, and M. Gorkunov, "Deceleration and shape-transformation of light pulses during phase conjugation in photorefractive media," Appl. Phys. B **95**, 545–549 (2009).

[235] B. Sturman, P. Mathey, R. Rebhi, and H.-R. Jauslin, "Nonlinear pulse deceleration using photorefractive four-wave mixing," J. Opt. Soc. Amer. B **26**, 1949–1953 (2009).

[236] P. Mathey, G. Gadret, and K. Shcherbin, "Slow light with photorefractive four-wave mixing," Phys. Rev. A **84**, 063 802 (2011).

[237] J.-C. Weeber, Y. Lacroute, A. Dereux, E. Devaux, T. Ebbesen, C. Girard, M. Gonzalez, and A. Baudrion, "Near-field characterization of Bragg mirrors engraved in surface plasmon waveguides," Phys. Rev. B **70**, 235 406 (2004).

[238] J. Herrmann and B. Wilhelmi, *Lasers for Ultrashort Light Pulses* (North-Holland, Amsterdam, 1987).

[239] P. Meystre and M. S. III, *Elements of Quantum Optics* (Springer, Berlin, 2007), 4th edn.

[240] H. Haus, "Theory of mode locking with a slow saturable absorber," IEEE J. Quantum electron. **11**, 736–746 (1975).

[241] P. Sperber, W. Spangler, B. Meier, and A. Penzkofer, "Experimental and theoretical investigation of tunable picosecond pulse generation in longitudinally pumped dye laser generators and amplifiers," Opt. Quantum Electron. **20**, 395–431 (1988).

[242] Y.-C. Chen, N. R. Raravikar, L. S. Schadler, P. M. Ajayan, Y.-P. Zhao, T. M. Lu, G.-C. Wang, and X.-C. Zhang, "Diode-pumped dye laser analysis and design," Appl. Opt. **31**, 7034–7041 (1992).

[243] B. Kopainsky, P. Qiu, W. Kaiser, B. Sens, and K. H. Drexhage, "Lifetime, photostability, and chemical structure of IR heptamethine cyanine dyes absorbing beyond 1 μm," Appl. Phys. B **29**, 15–18 (1982).

[244] A. A. Ishchenko, "Laser media based on polymethine dyes," Quantum Electron. **24**, 87–172 (1994).

[245] V. I. Bezrodnyi and A. A. Ishchenko, "High efficiency lasing of a dye-doped polymer laser with 1.06 μm pumping," Appl. Phys. B **73**, 283–285 (2001).

[246] B. H. Soffer and B. B. McFarland, "Continuously tuable, narrow band organic dye lasers," Appl. Phys. Lett. **10**, 266–267 (1967).

[247] A. Costela, I. Garcia-Moreno, and C. Gomez, "Efficient and stable dye laser action from modified dipyrromethene BF_2 complexes," Appl. Phys. Lett. **79**, 305–307 (2001).

[248] P. Runge and R. Rosenberg, "Unconfined flowing-dye films for CW dye lasers," IEEE J. Quantum Electron. **8**, 910–911 (1972).

[249] A. Costela, I. Garcia-Moreno, R. Sastre, D. W. Coutts, and C. E. Webb, "High-repetition-rate polymeric solid-state dye lasers pumped by a copper-vapor laser," Appl. Phys. Lett. **79**, 452–454 (2001).

[250] I. G. Kytina, V. G. Kitin, and K. Lips, "High power polymer dye laser with improved stability," Appl. Phys. Lett. **84**, 4092–4904 (2004).

[251] R. Bornemann, U. Lemmer, and E. Thiel, "Continuous-wave solid-state dye laser," Opt. Lett. **31**, 1669–1671 (2006).

[252] M. J. Adams, *An Introduction to Optical Waveguides* (John Wiley and Sons, Chichester-New York-Brisbane-Toronto, 1981).

[253] K. Kawano and T. Kitoh, *Introduction to Optical Waveguide Analysis* (John Wiley and Sons, New York, 2001).

[254] P. Yeh, *Optical Waves in Layered Media* (Jhon Wiley, New York, 1998).

[255] G. Ford and W. Weber, "Electromagnetic interactions of molecules with metal surfaces," Phys. Rep. **113**, 195–287 (1984).

[256] W. L. Barnes, "Fluorescence near interfaces: The role of photonic mode density," J. Mod. Opt. **45**, 661–699 (1998).

[257] M. Geissler, G. Tempea, and T. Brabec, "Phase-matched high-order harmonic generation in the nonadiabatic limit," Phys. Rev. A **62**, 033 817 (2000).

[258] I. P. Christov, H. C. Kapteyn, and M. M. Murnane, "Quasi-phase matching of high-harmonics and attosecond pulses in modulated waveguides," Opt. Express **7**, 362–367 (2000).

[259] A. Paul, R. A. Bartels, R. Tobey, H. Green, S. Weiman, I. P. Christov, M. M. Murnane, H. C. Kapteyn, and S. Backus, "Quasi-phase-matched generation of coherent extreme-ultraviolet light," Nature **421**, 51–54 (2003).

[260] T. Auguste, B. Carre, and P. Salieres, "Quasi-phase-matching of high-order harmonics using a modulated atomic density," Phys. Rev. A **76**, 011 802 (2007).

[261] O. Cohen, X. Zhang, A. L. Lytle, T. Popmintchev, M. M. Murnane, and H. C. Kapteyn, "Grating-assisted phase matching in extreme nonlinear optics," Phys. Rev. Lett. **99**, 053 902 (2007).

[262] M. Sivis, M. Duwe, Y. Liu, K. Siefermann, B. Abel, and C. Ropers, "Nanostructure-enhanced Atomic Line Emission from Noble Gases driven by Low-Energy, Few-Cycle Laser Pulses," in *Research in Optical Sciences, OSA Technical Digest* (Optical Society of America, 2012), p. HW4C.3.

[263] P. B. Corkum, "Plasma perspective on strong-field multiphoton ionization," Phys. Rev. Lett. **71**, 1994–1997 (1993).

[264] L. V. Keldysh, "Ionization in the field of a strong electromagnetic wave," Sov. Phys. JETP **20**, 1307–1319 (1965).

[265] M. Lewenstein, P. Balcou, M. Y. Ivanov, A. L'Huillier, and P. B. Corkum, "Theory of high-harmonic generation by low-frequency laser fields," Phys. Rev. A **49**, 2117–2132 (1994).

[266] E. Y. Poliakov, V. A. Markel, V. M. Shalaev, and R. Botet, "Nonlinear optical phenomena on rough surfaces of metal thin films," Phys. Rev. B **57**, 14 901–14 913 (1998).

List of Figures

Acknowledgement

This work has been performed under the scientific supervision of Dr. habil. Joachim Herrmann, the head of theory group. His long-time experiences in this field, especially, mode-locking of lasers and ultrafast nonlinear optics, have been the source of the creative ideas presented in the thesis. I am sincerely grateful for his positive acceptance of my research proposal, scientific and organizational support over three years of my study.

I would like to thank my supervisor Prof. Dr. Thomas Elsässer, diretor of Max Born Institute for Nonlinear Optics and Short Pulse Spectroscopy, for his organization for my research stay and the comprehensive lectures on ultrafast optics and spectroscopy.

My special thanks go to Dr. Anton Husakou for his critical and also constructive arguments and comments on the related works. During the work, he has always been ready to discuss for the improvement of papers and has helped me so much as possible. I appreciate his help for the numerics and the careful proof-reading of the thesis.

I wish to express my gratitude to Dr. Uwe Griebner for the discussions for passive mode-locking of lasers.

I am also thankful for the support from the Daimler Benz Foundation on the initial step of my work and my special thanks go to Dr. Jörg Klein for his efforts for my research stay here.

I thank all the colleagues of A3 group who have contributed to this work and helped me in my research activities.

Selbständigkeitserklärung

Ich erkläre, dass ich die vorliegende Arbeit selbständig und nur unter Verwendung der angegebenen Literatur und Hilfsmittel angefertigt habe.

Berlin, den 24. Januar 2012 Kwang-Hyon Kim